

FOG

Freiberg Online Geology

FOG is an electronic journal registered under ISSN 1434-7512



2014, VOL 37



Robert Sieland

Hydraulic Investigations of the Salar de Uyuni, Bolivia

208 pages, 118 figures, 36 tables, 165 references



Table of contents

<i>I</i>	<i>Acknowledgments</i>	<i>iii</i>
<i>II</i>	<i>Abstract</i>	<i>v</i>
<i>III</i>	<i>Zusammenfassung</i>	<i>vii</i>
<i>IV</i>	<i>Resumen</i>	<i>ix</i>
<i>V</i>	<i>List of Figures</i>	<i>xi</i>
<i>VI</i>	<i>List of Tables</i>	<i>xv</i>
<i>VII</i>	<i>List of Abbreviations</i>	<i>xvi</i>
<i>VIII</i>	<i>Terms and definitions</i>	<i>xviii</i>
1	Introduction	1
1.1	Structure of the thesis	1
1.2	Economical background of lithium.....	2
1.3	Lithium resources worldwide.....	2
1.4	Motivation and objectives of the thesis.....	4
1.5	Investigation area	6
1.5.1	Geological and hydrological setting of the Altiplano.....	6
1.5.2	Climate conditions	7
1.5.3	Description of the Salar de Uyuni	8
2	Literature Review	11
2.1	Research history of lithium resources	11
2.2	General stratigraphy and Quaternary evolution of the Uyuni salt flat	12
2.3	Hydrogeology and hydraulic behavior of other salt flats worldwide	15
2.3.1	Hydraulic parameters of salt flats.....	15
2.3.2	Groundwater level fluctuations in arid basin aquifers	17
2.3.3	Density-driven brine flow and free convection	19
3	Methodology	21
3.1	Field methods.....	21
3.1.1	Drilling procedure and sampling.....	21
3.1.2	Well constellation and well casing.....	23
3.1.3	Pumping tests	25
3.1.4	Long-term observation of brine-level fluctuations	34
3.2	Laboratory methods.....	37
3.2.1	Physical properties of the brine	37
3.2.2	Permeability determination by flow-through experiments.....	39
3.2.3	Gas permeability measurement.....	41
3.2.4	Geochemical analyses of lithium concentrations.....	41

3.2.5	Radiocarbon dating on brine samples.....	42
3.2.6	X-ray diffraction (XRD).....	43
3.2.7	Porosity determination	43
3.3	Data Evaluation	52
3.3.1	Resource estimation	52
3.3.2	Time series analyses	55
4	Results and Interpretation	56
4.1	Porosity determination and lithium reservoir estimation	57
4.1.1	Results and discussion of micro-CT analyses	57
4.1.2	Pore structure and pore size distribution.....	61
4.1.3	Total porosity of salt core samples by direct measurement	66
4.1.4	Effective porosity determination.....	68
4.1.5	Overall porosity distribution of the upper salt crust of Salar de Uyuni.....	69
4.1.6	Lithium reservoir estimation	74
4.2	Permeability and flow conditions within the salt crust.....	85
4.2.1	Physical properties of the brine	85
4.2.2	Pumping tests in a highly saline environment	90
4.2.3	Experimental permeability determination on core samples	106
4.2.4	Radiocarbon dating as brine tracer	108
4.3	Natural brine level fluctuations	111
4.3.1	Short-term brine level records.....	111
4.3.2	Time-series analyses of long-term data records.....	114
4.3.3	Mean daily fluctuation	121
4.3.4	Determination of the barometric efficiency	123
4.3.5	Interpretation of diurnal variations in data records	124
4.3.6	Temporal behavior of the Rio Grande river level	130
5	Final Discussion and Conclusions	137
6	References.....	143
	Appendix	152

I Acknowledgments

I would like to express my very great appreciation to my supervisor Prof. Broder Merkel, Institute of Geology (TU Bergakademie Freiberg), for his patient guidance, ongoing encouragement and all-encompassing scientific support through the course of my thesis. A deep sense of gratitude, I also want to express to Dr. habil. Jörg Hammer and Dr. Michael Schramm, Federal Institute of Geosciences and Natural Resources (BGR), for their cordial supervision and enriching scientific discussions. I am very grateful for their absolute support in taking the task of second reviewer.

This work would not have been completed without the help and support of many experts, colleagues and friends. I would like to thank everyone who helped me along the way, in particular:

- Prof. Wolfgang Voigt (TUBAF), initiator and leader of the German-Bolivian lithium-project “Salar de Uyuni”, who allowed me to be a part of a very exciting international research project and who gave me great confidence in situations of the project in Bolivia.
- Un gran agradecimiento a los miembros de la Universidad “Tomás Frías” en Potosi por el gran apoyo en la realización de los investigaciones en el Salar de Uyuni entre 2009 y 2012. En particular, me gustaría dar las gracias a Dr.-Ing. Jaime Claros Jimenez, Ing. Pedro Lopez Cortez, Ing. Juan Carlos Equizia, Ing. Hernan Rios, Ing. Agustin Perez, los conductores y los estudiantes de Geologia y Medio Ambiente. Después de todo, sus gran empleo y entusiasmo en el Salar han permitido exitosos investigaciones.
- Milton Lerida y su compañeros de la Universidad Boliviana de Litio en Llica por sus apoyo logístico y sus gran interés en este trabajo.
- Dr. Jana Hubalkova and Dr. Uta Balaschk (Institute of Ceramics, Glass and Construction Materials, TUBAF) for CT-measurements of salt cores and patiently answering my numerous questions concerning the data evaluation.
- Dr. Carsten Freese and Angelika Liedke (Institute of Drilling Engineering and Fluid Mining, TUBAF) for realizing permeability analysis and their interest to support this thesis.
- Dr. Peter Fröhlich (Institute of Technical Chemistry, TUBAF) for allowing me to use laboratory equipment for measuring the brine viscosity.
- Dipl.-Chem. Kurt Herklotz (IÖZ, TUBAF) for providing data from the meteorological station “Reiche Zeche”.
- Prof. Gerhard Heide (Institute of Mineralogy, TUBAF), Dr. Peter Szymczak (G.E.O.S. Ingenieurgesellschaft mbH), Dr. Thomas Wilsnak (IBeWa, Freiberg), Dipl.-Geol., Dipl.-Krist. Christoph Jahnke (BTU Cottbus), Dr. Ines Görz (Institute for Geophysics and Geoinformatics, TUBAF) and Dr.-Ing. Rhena Wulff (Thermodynamics and Heat

Transfer, TUBAF) for their willing to pass on their knowledge and to help me with their expertise. Thank you for all the inspiring scientific discussions.

- Dr. Catherine Alexandrakis (Institute of Geophysics and Geoinformatics, TUBAF) for her kind willingness to spend many days for English proof-reading which considerably improved the manuscript.
- Not to forget all of my colleagues from the Department of Hydrogeology for always listening to my problems and giving me valuable advices and having inspiring scientific discussions!
- Nadja, Judith, Ariane, Micha and Vanessa for their excellent work and support in the field as well as in the laboratory.
- My friends Dr. Hendrik Lamert, Dr. Christoph Ehrler and Dr. Mandy Schipek for the exchange of scientific experiences, helpful advice and also fruitful discussions.
- Thanks to Anna and Reynaldo for their very kind hospitality and friendship during my time in Bolivia.
- Finally, my dear Madeleine for endless patience, constant encouragement and for her entire love.

Above all, I want to thank God, the Lord, for guiding me and protecting me during my time in Bolivia and for giving me power and endurance all the time of my work.

II Abstract

With a surface area of about 10,000 km², the Salar de Uyuni is the largest salt flat in the world. It is located at an altitude of 3,653 m on the Altiplano, a high plateau in the south of the Bolivian Andes. The Salar de Uyuni consists of an alternating sequence of highly porous salt layers (mainly composed of halite) and lacustrine clay sediments. The pore volume of the uppermost salt layer which has a thickness of up to 11 m is filled by brine. The brine contains high amounts of Mg, K, Li and B. The element lithium is an especially important raw material for the production of batteries. Thus, it plays an important role for the development of the electric mobility.

With this background, extensive hydrogeological exploration activities were carried out at the Salar de Uyuni in the context of this dissertation. The hydraulic properties of the uppermost salt crust and the physical properties (density and viscosity) of the brine must be characterized. In order to do this, several core drillings were made, observation wells were installed, brine samples were taken and pumping tests were conducted between 2009 and 2012.

The stratigraphic documentation of the obtained sediment cores provided insights about the deposit structure and the upper salt layer thickness. The determination of the salt core porosity was carried out by three different methods: (a) by using X-ray computed tomography, (b) gravimetrically by saturation with 2-octanol and (c) by completion of the core volume with plasticine and calculation of the porosity under consideration of the particle density of the salt.

The laboratory investigations showed a depth-dependent porosity distribution in the upper salt layer. The uppermost 2 m were characterized by very high porosity values between 30 and 39%. However at greater depth, the total porosity decreases on average to 13.5%.

Geochemical analyses of brine samples confirmed the general spatial distribution of the lithium concentrations as already published by previous studies. On the basis of the lithium distribution in the brine, the thickness of the upper salt layer and the depth-dependent porosity distribution, the total lithium deposit in the Salar de Uyuni was calculated to be about 7 million tons.

The evaluation of the pumping tests under consideration of the density and viscosity of the pumped brine showed that the salt has a very high permeability in the horizontal direction. In contrast, flow-through experiments on drill cores indicated a clear vertical anisotropy of the permeability. This is caused by the inhomogeneous sediment stratification for instance by interbedded fine gypsum or clay lamina. Thus, horizontal brine movements are possible, but a deep vertical flow component can hardly be expected. This assumption is confirmed by radiocarbon dating the brine samples from different salt depths.

The influence of annual floods during the rainy season could be observed by long-term brine level measurements. Throughout the time-series analysis, distinct periodic brine

fluctuations of a few centimeters per day could be identified during the dry season. These daily fluctuations indicated an impermeable crust probably formed by the evaporation of near-surface brine and subsequent crystallization of salts in the pore volume. Thus, daily temperature and atmospheric pressure changes could directly affect the brine level.

Due to the extensive hydrogeological investigations, this dissertation contributes to the essential understanding of the hydraulic conditions in the Salar de Uyuni.

III Zusammenfassung

Mit einer Fläche von rund 10.000 km² ist der Salar de Uyuni die größte Salz-Ton-Ebene der Welt. Er befindet sich in einer Höhe von 3653 m NN im Altiplano, einer Hochebene im Süden der bolivianischen Anden. Der Salar de Uyuni besteht aus einer Wechsellagerung von hochporösen Salzschieben (überwiegend aus Halit bestehend) und lakustrinen Tonsedimenten. Die Porenräume der obersten bis zu 11 m mächtigen Salzschiebe sind mit einer Sole gefüllt, die hohe Gehalte an Mg, K, Li und B aufweist. Insbesondere das Element Lithium ist ein wichtiger Rohstoff u.a. für die Herstellung von Batterien und spielt damit eine bedeutende Rolle bei der Entwicklung der Elektromobilität.

Vor diesem Hintergrund wurden im Rahmen der vorliegenden Dissertation umfassende hydrogeologische Erkundungsarbeiten am Salar de Uyuni durchgeführt, um die hydraulischen Eigenschaften der obersten Salzkruste sowie die physikalischen Eigenschaften (Dichte und Viskosität) der Sole zu charakterisieren. Dazu wurden zwischen 2009 und 2012 zahlreiche Kernbohrungen abgeteuft, Beobachtungsbrunnen installiert, Soleproben entnommen und Pumpversuche durchgeführt.

Die stratigraphische Dokumentation der gewonnenen Bohrkerne lieferte Erkenntnisse zur Ablagerungsstruktur und zur Mächtigkeitsverteilung der obersten Salzschiebe. Die Bestimmung der Porosität der Salzkerne erfolgte mit drei verschiedenen Methoden: (a) mittels Computertomographie, (b) gravimetrisch durch Aufsättigung mit 2-Oktanol und (c) durch Volumenergänzung der Kernproben mit Plastilin und Berechnung der Porosität unter Einbeziehung der Reindichte des Salzes.

Die Laboruntersuchungen zeigten eine tiefenabhängige Porositätsverteilung in der obersten Salzschiebe. Während die obersten 2 m durch sehr hohe Porositäten zwischen 30 und 39% gekennzeichnet sind, nimmt die Gesamtporosität in größerer Tiefe auf durchschnittlich 13.5% ab.

Geochemische Analysen von Soleproben bestätigten die grundsätzliche räumliche Verteilung der Lithium-Konzentrationen, wie sie bereits durch frühere Studien veröffentlicht wurde.

Auf Basis der Lithium-Verteilung in der Sole, der Mächtigkeit der oberen Salzschiebe sowie der tiefenabhängigen Porositätsverteilung wurde ein Lithium-Vorkommen im Salar de Uyuni von rund 7 Millionen Tonnen berechnet.

Die Auswertung der Pumpversuche unter Berücksichtigung der Dichte und Viskosität der geförderten Sole zeigte, dass das Salz eine sehr hohe Permeabilität in horizontaler Richtung aufweist. Allerdings zeigten Durchströmungsversuche an Bohrkernen eine deutliche vertikale Anisotropie der Permeabilität, was auf die inhomogene Sedimentschichtung durch z.B. eingeschaltete feine Gips- oder Tonschichten zurückzuführen ist. Somit sind zwar horizontale Solebewegungen möglich, jedoch ist kaum mit einer tiefgreifenden vertikalen Strömungskomponente in der Salzschiebe zu

rechnen. Diese Vermutung wird durch ^{14}C -Altersdatierungen von Soleproben aus unterschiedlichen Tiefen des Salzes bestätigt.

Der Einfluss der jährlichen Überschwemmungen während der Regenzeit konnte anhand von Langzeitmessungen des Solespiegels beobachtet werden. Im Zuge der Zeitreihen-Analyse zeigten sich zudem ausgeprägte periodische Tageschwankungen von einigen Zentimetern während der Trockenzeit. Diese deuten darauf hin, dass durch Verdunstung oberflächennaher Sole und damit einhergehender Kristallisation von Salzen im Porenraum eine undurchlässige Kruste entsteht. Dadurch haben tägliche Temperatur- und Luftdruckschwankungen direkten Einfluss auf den Solespiegel.

Die vorliegende Dissertation trägt aufgrund der umfangreichen hydrogeologischen Untersuchungen wesentlich zum Verständnis der hydraulischen Verhältnisse im Salar de Uyuni bei.

IV Resumen

Con una superficie de aproximadamente 10.000 kilómetros cuadrados el Salar de Uyuni es el mayor lago de sal en el mundo. Se encuentra a una altura de 3.653 m sobre el nivel del mar en el altiplano en el sur de los Andes bolivianos. El Salar de Uyuni consiste en una alternancia de capas de sal altamente porosa (que consiste predominantemente de halita) y lacustre sedimentos de arcilla. La capa superior de sal tiene un espesor de hasta 11 metros. Los espacios de poros del sal se llenan con una salmuera que contiene altos contenidos de Mg, K, Li y B. En particular, el elemento litio constituye una importante materia prima para la producción de baterías que son utilizadas en la construcción de vehículos eléctricos.

Bajo estos antecedentes y en el contexto de la presente tesis, se han desarrollado extensas actividades de exploración hidrogeológica en el Salar de Uyuni. Las propiedades hidráulicas de la corteza de sal superior y las propiedades físicas (densidad y viscosidad) de la salmuera debían caracterizadas. Para ello, entre 2009 y 2012 se realizaron varias perforaciones con la finalidad de obtener muestras de núcleos, se instalaron pozos de supervisión, se realizaron pruebas de bombeo y se tomaron muestras de salmuera.

La documentación estratigráfica de los núcleos de perforación proporciona conocimientos para la estructura de los depósitos y para el espesor de la superior capa de sal. La porosidad de los núcleos de sal fue determinada por medio de tres métodos diferentes: (a) por tomografía computarizada (TC), (b) gravimétricamente mediante la saturación con 2-octanol y (c) mediante de compleción del volumen del núcleo con plastilina y computación de la porosidad en atención a la densidad real del sal.

Las investigaciones de laboratorio demostraron una distribución de la porosidad dependiente de la profundidad en la capa superior de sal. Mientras que la parte superior 2 m se caracterizan por altas porosidades entre el 30 y 39%, la porosidad total decae en una profundidad mayor a un promedio de 13,5%.

Los análisis geoquímicos de muestras de salmuera confirmó la distribución espacial fundamental de las concentraciones de litio, como ya se ha publicado por estudios anteriores. A base de la distribución de litio en la salmuera, el espesor de la capa superior de sal, y la porosidad dependiente de la profundidad determinaron que todos los recursos minerales de litio en el salar de Uyuni son alrededor de 7 millones de toneladas.

La evaluación de las pruebas de bombeo en consideración de la densidad y la viscosidad de la salmuera transmitido mostró que la sal generalmente tiene una permeabilidad muy alta. Pero, las pruebas de flujo en muestras de núcleo mostró una anisotropía significativa de la permeabilidad con la profundidad, que se debe a una estratificación de sedimentos no homogénea debido las láminas finas de yeso o arcilla intercaladas. Por lo tanto, es correcto que los movimientos de salmuera horizontales son posibles, pero es poco probable que movimientos verticales de salmuera ocurran.

Esta hipótesis se ve confirmada por la datación por radiocarbono de muestras de salmuera de diferentes profundidades de la sal.

El impacto de las inundaciones anuales durante la estación lluviosa se puede observar a partir de las mediciones a largo plazo del nivel de salmuera. En el curso del análisis de series de tiempo también mostraron pronunciadas variaciones diarias periódicas de unos pocos centímetros en la estación seca. Esto sugiere que hay una corteza impermeable que se forma por evaporación de salmuera cerca de la superficie y la cristalización de sales en el espacio de los poros. En esta manera, las fluctuaciones diarias de temperatura y de presión de aire influyen directamente el nivel de salmuera. Gracias a las extensas investigaciones hidrogeológicas realizadas, la presente tesis contribuye significativamente a la comprensión de las condiciones hidráulicas en el Salar de Uyuni.

V List of Figures

Figure 1: Main parts of the results and interpretation (chapter 4)	1
Figure 2: Satellite image of the northern and central Altiplano bordered by the eastern and western Cordillera and schematic map of the Altiplano with its main lakes, salars and rivers.....	7
Figure 3: Average monthly precipitation and temperature of the Uyuni weather station for a 10-year time period between 2001-2011.	8
Figure 4: Polygon structure of the salt surface with salt efflorescences along the cracks.	10
Figure 5: Brine pools found in the central part of the salt flat	10
Figure 6: Spring activity in the marshy marginal zone in the north of the Salar de Uyuni.	10
Figure 7: Lithium iso-concentrations in the Salar de Uyuni modified after Ballivian and Risacher (1981).....	12
Figure 8: Paleolake level history of the Altiplano illustrated by a NS schematic section.	14
Figure 9: Schematic view of free convection in an arid desert basin triggered by high mountain groundwater recharge and evaporation induced density differences within the salt flat.	19
Figure 10: Topographic map of the Salar de Uyuni and the adjacent Salar de Coipasa in the north as well as the Salar de Empexa in the west.....	22
Figure 11: Drill rig set-up connecting it to the ground surface using (a) a board, tie bars and (b) the load of a car.	22
Figure 12: Determination of the barometric coefficient BE at site 08-CEN in 2011 by means of the curve of sums of the increments of atmospheric pressure $[\Sigma\Delta p]$ and natural brine level fluctuations $[\Sigma\Delta h]$	27
Figure 13: Example of mean absolute daily brine level fluctuations at investigation site 08-CEN.	28
Figure 14: Brine level data correction for the 08-CEN pumping test in observation well B on Nov. 03, 2010	29
Figure 15: Brine level depression and recovery during a pumping test at site 05-TAH.....	33
Figure 16: Installation of the Cera-Divers in shallow depth in the Uyuni salt crust.....	35
Figure 17: Preparation of a boulder for the installation of the CTD-Diver in the Rio Grande for long-term monitoring of the river level.	35
Figure 18: Atmospheric pressure and air temperature measured with the Baro-Diver in comparison with the atmospheric pressure recorded by the Baro Transmitter of the weather station Reiche Zeche (TUBAF) for a time period of 14 days.....	36
Figure 19: Time series of air temperature and atmospheric pressure difference between data records from Baro-Diver (Schlumberger) and a Baro Transmitter B-278-1/2T of the meteorological station of the Reiche Zeche.	36
Figure 20: Principle of the flow-through experiments on the salt cores.	40
Figure 21: Sketch of brine sample preparation in a vacuum extraction line for radiocarbon dating analysis.	42
Figure 22: Sketch of the prepared salt core sample	48
Figure 23: Completion of the cylindrical shape of the salt core in order to determine gravimetrically the total porosity of the core sample.....	51
Figure 24: Variogram $\gamma(h)$ of the lithium concentrations in the Uyuni brine and the adapted spherical model.....	53

Figure 25: Schematic example illustrating the computation of different salt layers in ArcGIS.	55
Figure 26: Pore size classification modified after Mays (2007) and applied methods of porosity quantification.	56
Figure 27: Example of CT-gray scale images of a core sample.	57
Figure 28: Comparison of the porosity determined by the Otsu algorithm and visual thresholding technique	59
Figure 29: Porosity distribution with depth for 08-CEN and 03-INC samples arising from X-ray computed tomography analysis.	61
Figure 30: 3D CT-images from core samples from 03-INC	62
Figure 31: Logarithmic plot of the frequency distribution of single pore object volumes of the core samples from drilling 08-CEN-A	64
Figure 32: Logarithmic plot of the percentage of each pore size classes on the total pore volume of the samples from drilling 08-CEN-A	65
Figure 33: Horizontal representation of a defect analysis of the core sample CEN-08-1a.	66
Figure 34: Total porosity determined by direct measurement of core samples from 4 different drilling sites.	67
Figure 35: Results of gravimetric porosity determination according to the method of saturation with 2-octanol.	68
Figure 36: Porosity distribution of the upper salt crust of Salar de Uyuni based on the evaluation of core samples from 5 different drillings using three different methods.	71
Figure 37: 3-inch (left) and 8-inch (middle) salt core samples from 0 – 1 m depth of the salt crust at drilling site 08-CEN.	72
Figure 38: Porosity distribution with depth in Quaternary salt-deposits.	74
Figure 39: Comparison of lithium concentrations according to TUBAF and Risacher and Fritz (1991) for proximal sampling locations.	75
Figure 40: Landsat TM satellite image (channel 1, 2, 3) showing the dry river bed through the pampas east of the “Intersalar”.	76
Figure 41: Lithium distribution map obtained by interpolation of lithium concentration data from own investigations (TUBAF) using ordinary kriging with spherical semi-variogram.	77
Figure 42: Lithium distribution map created by ordinary kriging with spherical semi-variogram based on logarithmic transformed lithium concentration data from TUBAF and Risacher and Fritz (1991).	77
Figure 43: Thin, hard gypsum layer found in different drillings at different depth.	78
Figure 44: Drilling profiles showing the general stratigraphy of the Uyuni salt flat down to a depth of 13 meters from north to south (top) and from east to west (bottom).	80
Figure 45: Salt thickness of the upper salt layer of Salar de Uyuni	81
Figure 46: Model for the lithium-reservoir estimation at the Salar de Uyuni.	82
Figure 47: 3-dimensional visualization of the Uyuni basin showing the distribution of the lithium reserves in the brine within the upper salt layer in kg/m ² .	84
Figure 48: Temperature profiles in five different wells.	86
Figure 49: Box plots of brine sample density measurements from different locations at 25°C temperature condition.	87
Figure 50: Dynamic viscosity of brine samples depending on temperature conditions during the measurement.	88

Figure 51: Brine level behavior and atmospheric pressure for a time period of about 12 days at investigation site 02-LLI in 2011.....	92
Figure 52: Semi-log plot of the time-drawdown relationships of three observation wells showing confined (05-TAH-B), leaky (02-LLI-D) and unconfined (06-NOR-C) aquifer conditions.	92
Figure 53: Logarithmic drawdown of three observation wells showing confined (05-TAH-B), leaky (02-LLI-D) and unconfined (06-NOR-C) aquifer conditions.	93
Figure 54: Semi-logarithmic brine level drawdown in three observation wells at pumping test site 05-TAH.	96
Figure 55: Pumping test data from 02-LLI.....	99
Figure 56: Measured drawdown at pumping site 02-LLI (2012).....	101
Figure 57: Measured drawdown at pumping site 08-CEN (2012).....	101
Figure 58: Intrinsic permeability of the Salar de Uyuni upper salt crust at five different sites.....	102
Figure 59: Storage coefficients determined from pumping test data in 2010 and *2012.....	105
Figure 60: Intrinsic permeability versus depth of samples from five different drillings.....	107
Figure 61: Pressure curves in the input and output chamber during the gas permeability measurement of the gypsum layer.	108
Figure 62: ¹⁴ C activity in the atmosphere during the Holocene based on data from tree rings and corals	109
Figure 63: Calibrated radiocarbon ages of Uyuni brine samples from different depth.....	110
Figure 64: 12-day brine-level records of three wells in comparison with the atmospheric pressure.....	111
Figure 65: Flooded salt crust close to Incahuasi island in the central part of the Uyuni salt flat.....	112
Figure 66: (A) Mean daily atmospheric pressure, (B) daily brine level fluctuation in the three monitoring wells, (C) brine temperature variations	113
Figure 67: Brine level time-series from Dec. 19, 2011 to Sept. 12, 2012.....	116
Figure 68: Enlargement of the brine level time-series showing the characteristic daily brine level variations during the dry season at the three observation stations.	117
Figure 69: Time-series of brine level, brine temperature, air pressure and air temperature at site 03-INC.	118
Figure 70: Fourier analysis of the brine level time-series during the dry season.	120
Figure 71: Fourier analysis of the time-series of brine level and brine temperature from site 06-NOR in comparison with atmospheric pressure, air temperature and synthetic earth tide (WDD) for the Salar de Uyuni.....	120
Figure 72: Moving Window spectrum of the brine level data from site 08-CEN.....	121
Figure 73: Mean daily brine level and brine temperature fluctuations during the dry season at site 08-CEN in comparison with the mean daily atmospheric pressure and air temperature.	122
Figure 74: Principle of the salt breeze effect induced by different thermodynamic properties of the salt surface and the surrounding landmass at day and night.....	125
Figure 75: Linear correlation of the daily moving-averages of the air temperature and the brine level at observation site 03-INC.....	127
Figure 76: Illustration of the brine level, brine temperature, atmospheric pressure and air temperature at site 03-INC during the dry period between May 12 – September 12, 2012.....	128

Figure 77: Correlation between daily moving averages of brine level and air temperature for the sites 03-INC, 06-NOR and 08-CEN.....	129
Figure 78: Anomaly of (A) water level, (B) water temperature and (C) specific conductivity in the Rio Grande data records between June 21 and July 8, 2012.....	131
Figure 79: Water level, water temperature and electrical conductivity of the Rio Grande de Lipez between Dec. 19, 2011 and Sept. 13, 2012.	132
Figure 80: Mean daily fluctuations in water level, water temperature and specific conductivity of the Rio Grande River in the dry season.	133
Figure 81: Mean diurnal water level fluctuation of the Rio Grande in response to evapotranspiration.....	135
Figure 82: Sketch of the daily brine level fluctuations in consequence of a temperature effect	141

VI List of Tables

Table 1: Well constellation at the different investigation sites: Distances and directions of the different drillings/wells.	23
Table 2: Summary of the well specifications.	24
Table 3: Physical properties of 2-octanol used for flow-through experiments.	39
Table 4: Advantages and disadvantages of the applied methods for porosity determination.	45
Table 5: Comparison of porosity results arising from different segmentation techniques. ...	59
Table 6: Results of micro-CT-analysis of selected core samples.	60
Table 7: Key figures of pore morphology.	62
Table 8: Particle density of representative salt core samples analyzed by helium pycnometry	66
Table 9: Comparison of methods for porosity determination.	70
Table 10: Mineral composition of selected sediment samples determined by XRD analysis.	79
Table 11: Results of lithium-reservoir calculations in ArcGIS® for separate layers of the model.	83
Table 12: Dynamic viscosity η of Uyuni brine samples from different locations at standard temperature $T = 25^\circ\text{C}$	89
Table 13: Density and dynamic viscosity of the brine under field temperature conditions during pumping test completion.	89
Table 14: Overview of the main settings of the pumping tests.	94
Table 15: Intrinsic permeability K [m^2] obtained from pumping tests performed in 2010 on partly penetrating wells and in 2012 on fully penetrating wells.	97
Table 16: Storage coefficients S [-] determined from pumping tests performed in 2010 on partly penetrating wells and in 2012 on fully penetrating wells.	104
Table 17: Comparison of hydraulic conductivity k_f from different salt flats in the world.	105
Table 18: Conventional radiocarbon ages of Uyuni brine samples from different depths from *Nov. 2010 and Dec. 2011.	109
Table 19: Phase lags between brine level and the other parameters obtained from signal correlation in Tsoft software package.	123
Table 20: Barometric efficiency for short-term and long-term brine level records at different sites on the salt flat.	124
Table 21: Heat capacity c and thermal conductivity λ of relevant rock and fluid types at 20°C	125

VII List of Abbreviations

¹⁴ C	Radiocarbon isotope
a.g.l.	Above ground level
a.s.l.	Above sea level
b.g.l.	Below ground level
BE	Barometric efficiency
BGR	Federal Institute of Geosciences and Natural Resources
BOT	Bolivian Time
COMIBOL	Corporación Minera de Bolivia (Bolivian Mining Company)
CON	Condition-function used in ArcGIS
cpd	Cycles per day
CT	Computed tomography
DSI	Discrete Smooth Interpolation
ET	Evapotranspiration
EV	Electric vehicle
EVI	Electric vehicle initiative of the Clean Energy Ministerial
EVs	Electric Vehicles
FFT	Fast Fourier Transformation
GNRE	Gerencia Nacional de Recursos Evaporiticos (National Management of Evaporite Resources)
GPR	Ground penetrating radar
HU	Hounsfields units
IBF	Institute of Drilling Engineering and Fluid Mining
ICP-MS	Inductive coupled plasma – mass spectrometry
IEA	International Energy Agency
IKGB	Institute of Ceramics, Glass and Construction Materials
IÖZ	Interdisciplinary Ecological Center
MIP	Mercury intrusion porosimetry
N	Number of objects (e.g. measurements or samples)
n.d.	Not determined
N-S	North-South
∅	Diameter
p	p-value / level of significance
PDB	Pee Dee Belemnite (standard for δ ¹³ C values/carbon isotopes)
PE	Polyethylene
pMC	Percent modern carbon
PT	Pumping test
PVC	Polyvinyl chloride
r	Correlation coefficient
R ²	Coefficient of determination
RMSE	Root mean squared error
Rpm	Rotations per minute
SF	Shape factor
SPSS	Statistic software package
SQM	Sociedad Quimica y Minera de Chile S.A.

SRTM	Shuttle Radar Topography Mission
STD	Standard deviation
STFT	Short-time Fourier transform
TUBAF	Technische Universität Bergakademie Freiberg
UP32	Software for pumping test evaluation
USGS	U.S. Geological Survey
UTC/GMT	Universal Time, Coordinated/Greenwich Mean Time
UTM	Universal Transverse Mercator (coordinate system)
WC	Water column
WDD	Synthetic earth tide (calculated in Tsoft)
WGS 84	World Geodetic System established in 1984
XRD	X-ray diffraction
yr BP	Years before present

VIII Terms and definitions

Brine level	The term “brine level” as used in this thesis describes the position of the brine surface referred to an arbitrary reference point which is determined by the position of the Diver data-logger.
Drainable porosity	Only a certain part of the totally saturated porosity might be drained under gravity (Houston et al. 2011).
Effective porosity (n_{eff})	Some pores are isolated and therefore do not contribute to the drainage. Therefore, only those pores which are in mutual contact with each other belong to the interconnected porosity which is the effective porosity (Houston et al. 2011).
Hydraulic conductivity (k_f)	It is “defined as the volume of water that will move through a porous medium in unit time under a unit hydraulic gradient through a unit area measured at right angles to the direction of flow” (Kruseman and de Ridder, 2000). The hydraulic conductivity depends on the permeability of the porous medium and also on the properties of the fluid which flows through the medium (Batu, 1998).
Permeability, intrinsic	Describes the permeability of a certain porous medium depending on the character of the pore system. It is independent of the fluid properties (density and viscosity) of the medium filling the pores (Hölting and Coldeway, 2013).
Reserve	“That part of the reserve base which could be economically extracted or produced at the time of determination. The term reserves need not signify that extraction facilities are in place and operative. Reserves include only recoverable materials” (USGS, 2012).
Reserve base	“That part of an identified resource that meets specified minimum physical and chemical criteria related to current mining and production practices, including those for grade, quality, thickness, and depth. The reserve base is the in-place demonstrated (measured plus indicated) resource from which reserves are estimated. It may encompass those parts of the resources that have a reasonable potential for becoming economically available within planning horizons beyond those that assume proven technology and current economics” (USGS, 2012).
Resource	“A concentration of naturally occurring solid, liquid, or gaseous material in or on the Earth’s crust in such form and amount that economic extraction of a commodity from the concentration is currently or potentially feasible” (USGS, 2012). Identified resources are those “whose location, grade, quality, and quantity are known or estimated from specific geologic evidence” (USGS, 2012).
Salar	The term is used in South America for salt-encrusted playas in internally drained continental basins formed under arid to semi-arid climatic conditions. Similar terms are salt flat or salt pan (Stoertz and Ericksen, 1974).

Specific yield (S_y)	It is “the volume of water that an unconfined aquifer releases from storage per unit surface area of aquifer per unit decline of the water table”. It is sometimes interchangeably used with the effective porosity (Kruseman and de Ridder, 2000).
Storage coefficient (S)	It describes the volume of water that is released from the storage of a saturated confined aquifer “per unit surface area of the aquifer per unit decline in the component of hydraulic head normal to that surface. [...] Its values in confined aquifers range between $5 \cdot 10^{-5}$ to $5 \cdot 10^{-3}$ (Kruseman and de Ridder, 2000).
Total porosity (n)	Comprises the volume of pore space contained within a certain unit of rock or aquifer material (Houston et al. 2011).
Transmissivity (T)	“Transmissivity is the product of the average hydraulic conductivity k_f and the saturated thickness of the aquifer. Consequently, transmissivity is the rate of flow under a unit hydraulic gradient through a cross-section of unit width over the whole saturated thickness of the aquifer” (Kruseman and de Ridder, 2000).

1 Introduction

1.1 Structure of the thesis

The thesis is structured into five chapters. After an introduction of the economic background and the motivation behind the thesis, an overview about the study area is given in chapter 1. The literature review that follow in chapter 2 summarizes previous studies on the hydrogeology and formation of the Uyuni salt flat as well as hydraulic properties and characteristic phenomena with regard to brine level fluctuations known from other salt flats in the world. Afterwards, all field investigations, laboratory experiments and analyses as well as methods of data evaluation are described in chapter 3 (Methodology).

The results and interpretations of this thesis are presented in chapter 4, which is subdivided into three main parts (Figure 1):

- I The first part aims to re-evaluate the total lithium resources in Uyuni salt flat. For this, the porosity properties of the upper salt crust will be presented in detail. Furthermore, the general stratigraphy and the lithium distribution in the brine of the upper salt layer will be considered in order to create a two-layer model for resource estimation.
- II The second part focuses on the permeability properties determined by pumping tests in the field and laboratory flow-through experiments. Additionally, physical brine parameters such as temperature, dynamic viscosity and density will be evaluated. Radiocarbon dated brine samples are used as a natural tracer for brine dynamics within the salt crust.
- III In the third part, long-term observations of the brine level of the Salar de Uyuni are presented and evaluated using time-series analysis.

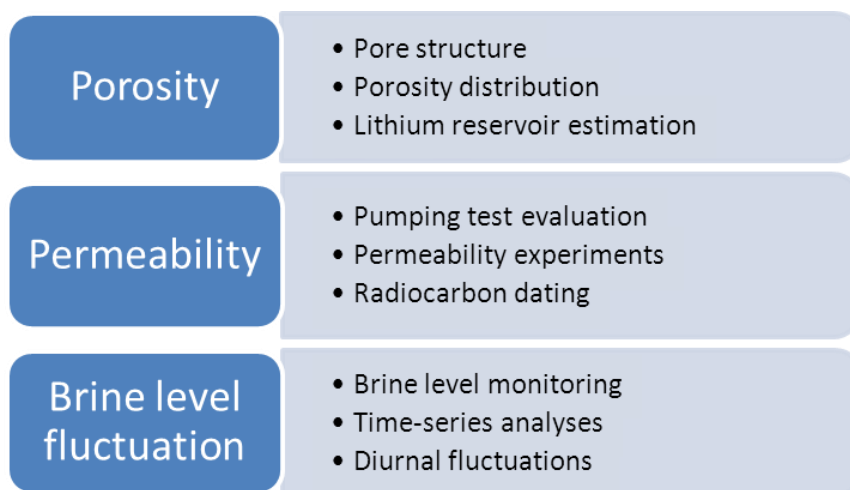


Figure 1: Main parts of the results and interpretation (chapter 4)

Finally, chapter 5 discusses the main outcomes and conclusions of the study and gives recommendations for future research.

1.2 Economical background of lithium

Since several years economic experts presume big changes in the technology of mobility. At the present time, electric cars (Electric Vehicles = EVs) are expected to be the future mode of transportation. Even the German government is convinced and therefore created a plan to have about 1 million electric cars on German roads by the year 2020 (Bundesregierung, 2009). The Electric Vehicles Initiative (EVI) is a multi-governmental policy forum which is launched under the Clean Energy Ministerial. With its currently 15 member government as well as the International Energy Agency (IEA) they held more than 90% of the world's electric vehicle stock in 2012. By the year 2020, the ambitious intention of the group is to put about 20 million EV passenger cars (EVs are battery-electric vehicles, plug-in hybrid vehicles and fuel cell electric vehicles) on worldwide roads (OECD/IEA, 2013). In the meantime, many automobile manufacturers (e.g. BMW, Ford, Nissan, Renault, Toyota among others) already produce electric cars in large series (Orecchini et al., 2014).

In order to produce electric cars and to store energy, high-capacity batteries are needed. The most prominent present day technology is lithium-ion batteries. The main lithium compound which enters the production of this kind of batteries is lithium carbonate (Li_2CO_3) in high purity (>99%). An average battery pack of 300 kg for one electric vehicle needs an input of about 12 kg Li_2CO_3 (Stamp et al., 2012).

The current development in the mobility sector is summarized by Tahil (2007) with the possibility that future lithium carbonate demand could exceed 3% of the global Li_2CO_3 recoverable reserves per annum. Estimates from SQM (Sociedad Quimica y Minera de Chile S.A.) – currently the world's largest lithium producer – assumed that the annual demand for lithium carbonate will increase from 85,000 tons in 2007 to 160,000 tons in 2015 when 5 million electric vehicles/year will be produced (Evans, 2008b).

Lithium is the lightest element, beside hydrogen and helium (Vine, 1980), and is characterized by the lowest standard electrode potential of -3.07 V which makes it to the most electropositive metal. "It thus can generate the greatest electrical power per unit weight or volume of any metal" (Garrett 2004). Therefore, lithium is perfectly suited to manufacture (rechargeable) batteries for energy storage. Beside its use for the production of batteries (25%) it is further used in lubricating greases (12%), frits (10%), glass (8%) and air conditioners (6%) among others (Yaksic and Tilton 2009).

1.3 Lithium resources worldwide

The Salar de Uyuni in the Bolivian highlands is a lithium-rich brine deposit with estimated lithium resources ranging between 5.4 million tons (Ballivian and Risacher, 1981, Tahil, 2007, Evans, 2008a), 9 million tons (Risacher and Fritz, 1991, USGS, 2014), and up to 10.2 million tons (Gruber et al., 2011). Despite the strong discrepancy in the

published estimates and their uncertainties, Bolivia holds in fact one of the largest known lithium deposits in the world. The media often describe lithium as the “Resource of the future” or the “White gold/treasure of the Andes” (e.g. Heise Online¹, Handelsblatt², Süddeutsche Zeitung³, Hamburger Abendblatt⁴). Moreover, Bolivia is even expected to become the “Saudi Arabia of lithium of the electric car era” (The New Yorker⁵, 3sat⁶).

However, lithium is a comparatively rare element in the Earth’s crust (20 ppm, Vine, 1980). In fact, there is a large number of lithium containing rocks and brine deposits but only a few of them are of actual or commercial value (Garrett, 2004).

Brines are “currently the most important and cheapest sources of lithium” (Yaksic and Tilton, 2009). They are associated with salt lakes such as the Salar de Atacama (Chile) or the Salar de Hombre Muerto (Argentina). The other type of resource from which lithium is currently extracted comprises hard rock deposits. The predominant form of lithium containing rocks are pegmatites which are coarse grained igneous rocks formed by the crystallization of post-magmatic fluids (Garrett, 2004). The principle lithium pegmatite minerals that have economic values are spodumene, lepidolite and petalite (Yaksic and Tilton, 2009). Lithium at elevated concentrations can be also found in geothermal brines and oil-field waters, or can be extracted from clays (especially hectorite) and seawater as potential source of supply (Abell et al., 2008, Evans, 2008a, Yaksic and Tilton, 2009).

The total lithium resources in minerals, brines and clays are estimated to about 64 million tons of lithium equivalent, whereby the lithium brine deposits alone account for 52.3 mill t. The recoverable amount of Li worldwide is estimated by Evans (2008b) with about 29.79 mill t (or about 157.3 mill t lithium carbonate).

In 2013 about 35,000 metric tons of lithium was recovered mainly from brine salt flats. The main producers of lithium are Chile (38.6%), Australia (37.1%), China (11.4%), Argentina (8.6%), Zimbabwe (3.1%) and the USA (no data published) (USGS, 2014).

According to different lithium resource estimates worldwide (Tahil, 2007, Evans, 2008a, Gruber et al., 2011, USGS, 2014) the Salar de Uyuni is the largest lithium resource on the planet, but currently no economical extraction of lithium exists.

¹ Heise Online: <http://www.heise.de/newsticker/meldung/Bolivien-Der-Lithium-Schatz-im-Salzsee-968713.html> (accessed on 19-12-2013)

² Handelsblatt: <http://www.handelsblatt.com/finanzen/rohstoffe-devisen/rohstoffe/zukunftsstoff-lithium-wie-bolivien-groesster-schatz-ungehoben-bleibt/3559778.html> (11-10-2010, access data: 19-12-2013)

³ Süddeutsche Zeitung: <http://www.sueddeutsche.de/wirtschaft/lithium-rausch-in-bolivien-salziges-gold-1.35122> (accessed on 19-12-2013)

⁴ Hamburger Abendblatt: <http://www.abendblatt.de/ratgeber/wissen/article2203671/Groesstes-Lithiumvorkommen-der-Welt-lagert-unter-Salzsee.html> (accessed on 19-12-2013)

⁵ New Yorker: http://www.newyorker.com/reporting/2010/03/22/100322fa_fact_wright (accessed on 19-12-2013)

⁶ 3Sat: TV documentation, <http://www.3sat.de/mediathek/?mode=play&obj=23172> (28:41 min) (accessed on 19-12-2013)

Meridian International Research (2008) even reduced the estimate of recoverable reserves in the salt flat to about 300,000 tons of lithium because economically interesting concentrations of more than 2,000 mg/L only occur in a limited area of 200 km² in the southern fringe of the salt flat close to the delta of the main tributary Rio Grande de Lipez.

Since 2008, the Bolivian government implemented a strategy to industrialize the natural evaporite resources of the Uyuni salt flat by the Bolivian mining company COMIBOL. This national strategy comprised three stages (COMIBOL, 2011):

- (1) Production of lithium carbonate (Li₂CO₃) in a pilot plant and semi-industrial production of potassium chloride (KCl)
- (2) Implementation of industrial production of Li₂CO₃ and KCl
- (3) Fabrication of lithium batteries.

Certainly, some natural challenges make the lithium extraction from Salar de Uyuni difficult in comparison with the world's largest currently active lithium production from Salar de Atacama in Chile (USGS, 2014, Gruber et al., 2011). Annual flooding of large areas of the Bolivian salt flats may not allow or at least restrict a continuous production of lithium carbonate using large evaporation ponds. Furthermore, high magnesium concentrations in the brine impede the separation of lithium because of the similar chemical behavior of both elements. While the Mg to Li ratio of Atacama brines are about 6.4, Uyuni brines are characterized by Mg/Li-ratios around 18.6 (Tahil, 2007, Yaksic and Tilton, 2009).

1.4 Motivation and objectives of the thesis

With this background, in 2007 the *Lithium Initiative* of the TU Bergakademie Freiberg started a research project in collaboration with the Bolivian university "Tomàs Frías" in Potosí with the aim of exploiting of the lithium-resources in the Salar de Uyuni. The lithium project comprised three investigation parts:

- Hydrogeological and geochemical exploration of the Uyuni salt flat
- The concentration of lithium in the brine using self-developed intense evaporation cones
- Development of an appropriate extraction technology to extract lithium carbonate as well as potassium, boron and other chemical components from the pre-concentrated brine.

The present study is based on the first part of the project and is focused upon the hydrogeological investigation of the Salar de Uyuni. The main purpose of the exploration work is a general characterization of the hydraulic properties of the salt

layers and the brine.⁷ Hydraulic and geochemical properties are necessary information for the evaluation of the lithium-brine deposit and its possible future utilization.

Almost all data available in the literature which are related to the hydrogeological characterization of the Salar de Uyuni arise from older field studies in the 1970s and 1980s (compare chapter 2). Therefore, an update of the knowledge and a verification of the old data are indispensable when dealing with resource estimation. Also, as a consequence of the wide span of published lithium-resource estimations, the total lithium resources in the brine of Salar de Uyuni will be re-evaluated based on the porosity of the salt layer, the lithium distribution in the brine as well as the general stratigraphy of the upper salt aquifer. Additionally, the permeability of the salt layer is characterized by pumping tests and laboratory experiments. Radiocarbon dating on selected brine samples should serve as tracer for brine circulation and recharge in the Uyuni salt flat. Insights in the hydrology of the salt flat over time with focus on annual flooding and the influence of characteristic climatic conditions should be gained by long-term observation of the brine level.

Consequently, the following hypotheses will be examined in this thesis:

- (1) The porosity of the upper salt layer is inhomogeneously distributed and decreases with depth.
- (2) The total lithium resources in the brine are significantly lower than estimated by previous studies with 9 - 10.2 million tons (e.g. in Gruber et al., 2011, USGS, 2012, Risacher and Fritz, 1991).
- (3) The permeability of the salt aquifer is high but also determined by strong anisotropy due to the formation history of the sediment stratigraphy.
- (4) Horizontal brine flow may dominate within the salt layer, but significant vertical circulation or mixing is unlikely.
- (5) Seasonal brine level fluctuations are caused by annual flooding due to precipitation and surface runoff from the catchment area.
- (6) Diurnal brine level fluctuations are triggered by daily temperature and atmospheric pressure variations.

⁷ Aspects regarding the geochemical distribution of elements in the brine phase as well as their origin and accumulation will be issued in the doctoral thesis of my colleague Mrs. Nadja Schmidt and are not comprised in detail in this thesis.

1.5 Investigation area

The Salar de Uyuni is located in the Southwestern part of Bolivia (20°S 68°W) on the Altiplano, a high plateau of the Andes, at an altitude of 3,653 m a.s.l. (above sea level). With a surface area of more than 10,000 km² the salt flat of Uyuni is stated to be the largest salt flat in the world (e.g. Svendsen, 2003, Chepstow-Lusty et al., 2005). It mainly belongs to the province of Daniel Campos with a minor part in the province of Nor Lipez, both in the department of Potosi (Carpio, 2007).

1.5.1 Geological and hydrological setting of the Altiplano

The Bolivian Altiplano is an north-south elongated undrained basin of about 200,000 km² bordered by the eastern and the western Cordillera of the Central Andes (Donselaar et al., 2013, Fornari et al., 2001). The Eastern Cordillera is typified by palaeocoic sediments (sandstone, shales) and granitic plutons. The basement of the Altiplano is also formed by Palaeozoic formations which are covered by huge strata of continental sediments from the Cretaceous and Tertiary ages (sandstones, claystones, mudstones, shales and evaporates). On the contrary, the western and southern Altiplano was influenced by intense volcanic activity during Plio-Quaternary times. The Western Cordillera is mostly of volcanic origin (Risacher and Fritz, 1991, Kussmaul et al., 1977).

More than 75 salt pans lie in the closed basin at altitudes of more than 3800 m a.s.l. (Rettig et al., 1980). The Altiplano can be subdivided into a set of evaporitic basins (compare Figure 2). The northern basin is occupied by lake Titicaca (8,560 km², 3810 m a.s.l.) which is a permanent 285 m deep fresh water lake (Donselaar et al., 2013). The outflow from lake Titicaca is discharged via the Rio Desaguadero southward into the lake Poopó [2,500 km²; 3,686 m a.s.l. (Rettig et al., 1980, Grove et al., 2003)].

The central trough of the Altiplano in the south is covered by the giant salt crust of the Salar de Uyuni which is separated by low terrain from the smaller basins of the Salar de Coipassa (2225 km², 3656 m a.s.l.) and lake Poopó to the north (Grove et al., 2003).

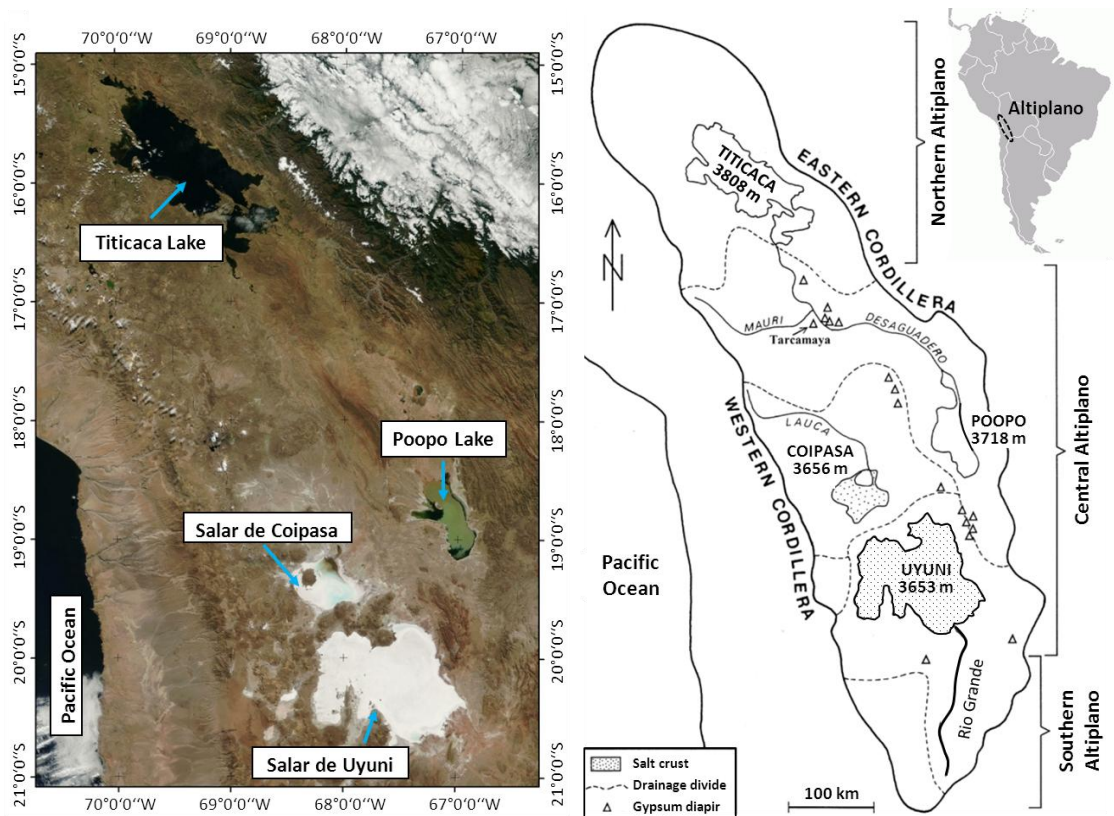


Figure 2: Satellite image of the northern and central Altiplano bordered by the eastern and western Cordillera (left picture, source: NSSL⁸) and schematic map of the Altiplano with its main lakes, salars and rivers (right picture, modified from Risacher and Fritz, 2000).

1.5.2 Climate conditions

The Altiplano is characterized by semi-arid to arid climatic conditions with mean annual precipitation that drops from 800 mm around lake Titicaca in the north down to less than 100 mm in the south. The mean annual temperature is 10°C in the north and 4°C in the south (Figure 3). Progressively drier conditions appear in the hydrographic basins from north to south (Donselaar et al., 2013).

The study area of the Salar de Uyuni has a mean annual temperature of about +7.7°C and average annual rainfall of about 200 mm (Figure 3, Ministerio de Medio Ambiente y Aqua, 2012). Thereby, air temperatures may vary between +20°C during daytime in summer and -20°C at night in winter (Fornari et al., 2001). Most of the precipitation occurs in a short rainy season between December and March which is caused by the South American summer monsoon. During that time the salt flat is extensively flooded to a depth between 0 and 75 cm. In the dry season during winter months, almost the entire surface of the salt flat dries up (Garrett, 2004, Risacher and Fritz, 1991).

⁸ NSSL National Severe Storms Laboratory:
<http://www.nssl.noaa.gov/projects/pacs/salljex/web/T11.html> (accessed on 25-05-2014)

The potential evaporation is estimated between 1,500 – 1,700 mm/a. Therefore, it greatly exceeds the annual precipitation (Risacher and Fritz, 2009, Carpio, 2007).

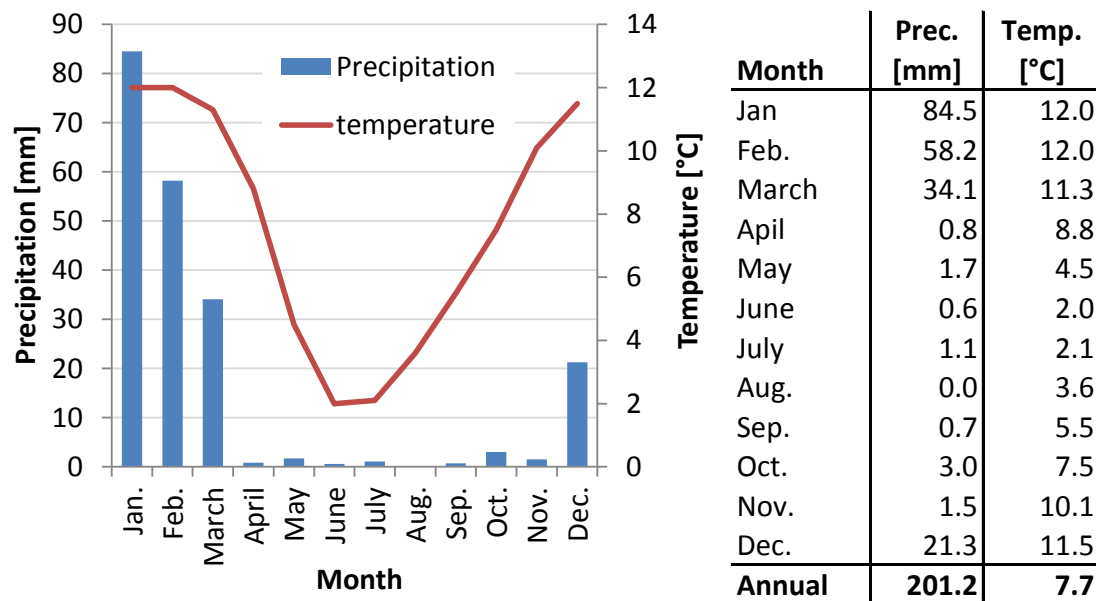


Figure 3: Average monthly precipitation and temperature of the Uyuni weather station for a 10-year time period between 2001-2011 (data from Ministerio de Medio Ambiente y Aqua, 2012).

1.5.3 Description of the Salar de Uyuni

The Salar de Uyuni is a salt-crusted saline pan (or playa or salt flat) at an altitude of more than 3,600 m a.s.l (Warren, 2006). It forms the deepest point of an inland drainage basin (terminal lake) that covers 46,000 km² in the south of the Altiplano Basin (Svendsen, 2003). Because this basin is a hydrological closed basin which only receives water from rainfall and river inflow but which does not have any outflow except evaporation or probable seepage into deeper layers, huge amounts of evaporites could accumulate over time within the Salar de Uyuni (Warren, 2010).

The large surface area of the Uyuni salt flat extends about 140 km in W-E direction and about 110 km on average (maximum 160 km) in N-S direction. In the north, the area is bordered by the *Serrania Intersalar* and in the south by the Cordillera Lipez and Cordillera de Chocaya, which is where the main tributaries of the salt flat come from. To the west, the basin is bordered by N-S running young volcanic mountain ranges that form parallel elements to the high cordillera. To the east, the salt flat is also limited by a N-S trending mountain range which is previously located to the Cordillera Chichas from where several rivers and creeks flow into the Altiplano (Wolf, 2010).

For most of the year the salt flat is completely dry. After the rain season almost the entire surface area is episodically flooded and forms an ephemeral saline lake (Warren, 2010). The main surface-water inflow into the Salar de Uyuni is the Rio Grande de

Lipez to the south which drains a catchment area of app. 25,000 km² to the south of the salt flat (Orris, 1995).

Even when no surface brine occurs in the dry season, a large brine body can be found within the porous halite crust which has a maximum thickness of about 10 m (Rettig et al., 1980). The brine is characterized by salinities of more than 300 g/L and high concentrations of Mg, K, Li and B (Risacher and Fritz, 1991).

The surface of the Salar de Uyuni is a hard and smooth halite crust with relief of only a few centimeters. It is characterized by desiccation polygons that range between 1 and 4 m in diameter (Figure 4). Along the cracks salt efflorescences are formed due to evaporation of near-surface brine which rises to the surface by capillary pressure (Risacher et al., 2006, Goodall et al., 2000).

Additionally, in the north-central part of the salt flat steep-sided “brine pools” occur in the salt. They appear either in form of irregular tube-like openings along the boundaries of desiccation polygons (Figure 5, left) or as circular pools of in part more than 1 meter in diameter (Figure 5, right). The pools are filled with clear or turbid brine up to the salt surface. Ericksen and Salas (1987) attribute the formation of such brine pools to the dissolution of salt due to the renewed activity of springs in lacustrine sediments beneath the thick halite-layer. The outer rim of the salt flat is limited by narrow marshy or muddy marginal zones with the occurrence of springs (Figure 6). Locally, thin layers of ulexite or gypsum occur (Ericksen et al., 1977).



Figure 4: Polygon structure of the salt surface with salt efflorescences along the cracks (photos made by Judith Heinrich, 2010).



Figure 5: Brine pools found in the central part of the salt flat (close to 08-CEN site, 19K 0649590, UTM 7774480, photos made by Judith Heinrich, 2010)



Figure 6: Spring activity in the marshy marginal zone in the north of the Salar de Uyuni (near the village Tahua, photo made by Robert Sieland, 2011).

2 Literature Review

2.1 Research history of lithium resources

Already in the 1970s, American scientists intensively discussed the question of global lithium resource estimates in order to secure the demand for lithium in the future. The role of lithium as a key factor in the production of batteries for storing energy for electric mobility was already expected and forecasted by Brobst and Pratt (1973). They published a very early estimate of global lithium resources in brines and pegmatites of about 6.5 million short tons (=5.9 million metric tons).

The most important lithium-rich brine deposits in the United States are Searles Lake (0.015% Li₂O), Silver Peak (300 ppm Li), Great Salt Lake (60 ppm), and the Salton Sea geothermal brine (210 ppm). The Silver Peak deposit was estimated to hold about 2.27 million metric tons of lithium under the assumption that the brine occupies 40% of the total volume and an average lithium concentration of 300 ppm (Brobst and Pratt, 1973).

First systematic investigations of the salars in the Central Andes started in the early 1960s (Ericksen and Salas, 1987, Stoertz and Ericksen, 1974). The most prominent studies on the Salar de Uyuni were completed in 1976 by the Bolivian Geological Survey (GEOBOL) and the U.S. Geological Survey (USGS) who made a first systematic sampling (Ericksen et al., 1977, Ericksen et al., 1978). At the same time a French group of scientists from ORSTROM (Office de la Recherche Scientifique et Technique Outre-Mer) investigated the lithium distribution in the brine of the upper salt layer, which revealed a thickness of up to 11 meters (Risacher and Fritz, 1991, Rettig et al., 1980, Ballivian and Risacher, 1981).

The first lithium distribution maps were published by Ballivian and Risacher (1981) as well as Davis et al. (1982). Later on they were refined by Risacher and Fritz (1991). These maps are still today the base for all lithium-resource estimates of the Salar de Uyuni (Figure 7).

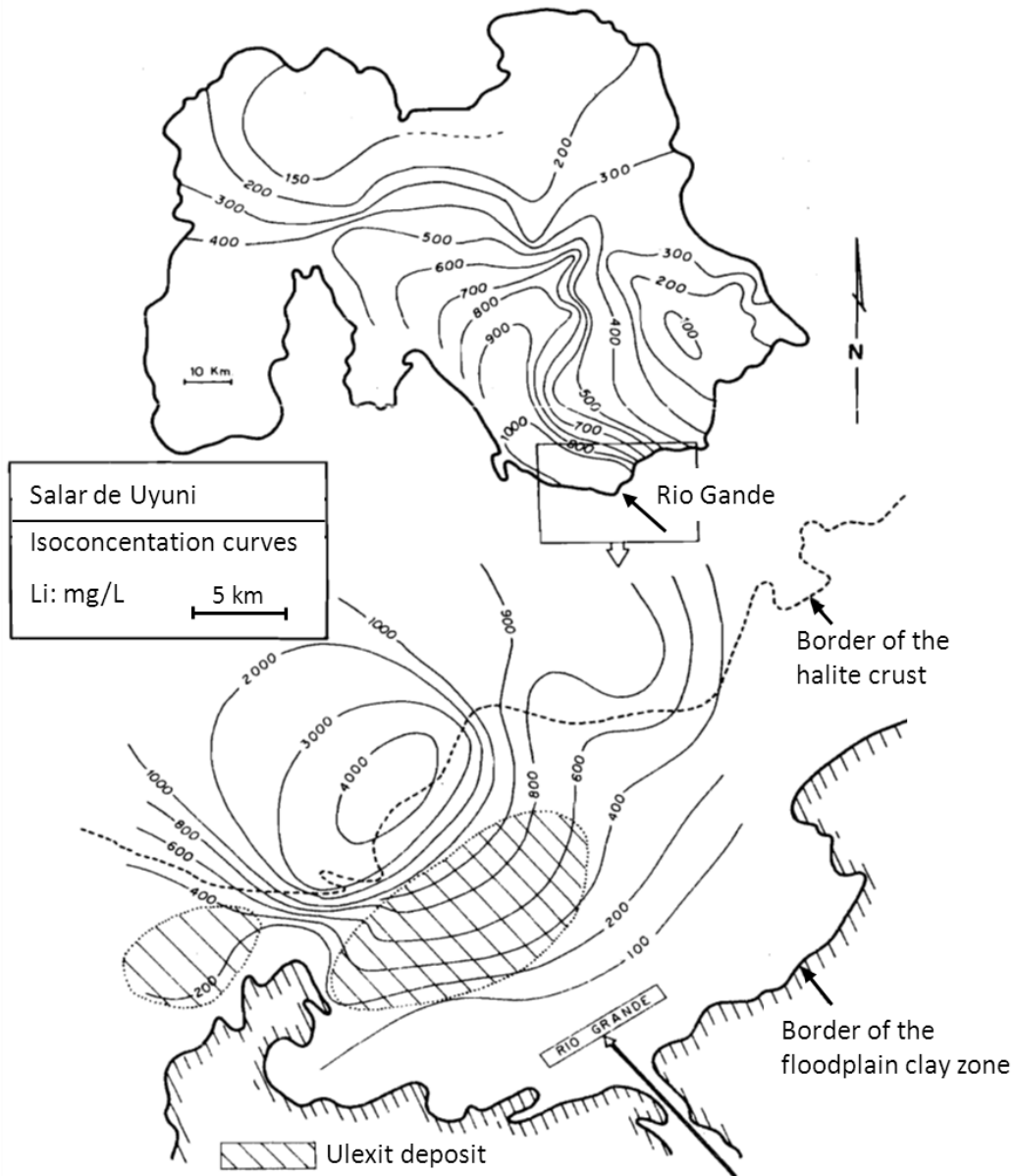


Figure 7: Lithium iso-concentrations in the Salar de Uyuni modified after Ballivian and Risacher (1981)

2.2 General stratigraphy and Quaternary evolution of the Uyuni salt flat

The upper salt crust of Salar de Uyuni has a maximum thickness of 11 m and consists mainly of layered porous halite (~95%) with a small amount of fine-grained gypsum (~5%). The average porosity of the whole crust was estimated to be 30-40% based on analyses of hard samples, which are not further explained (Risacher and Fritz, 1991). The porous salt contains interstitial brine. Only the uppermost 10-20 cm below the surface is not filled with brine. The brine evaporates during the dry season either by capillary forces or water vapor transport through the topmost 10 to 20 centimeters of the salt crust. Therefore, the crust is cemented into a very compact and hard

pavement which consequently limits evaporation from the brine. Below the salt crust impermeable lacustrine sediments occur, which are finely laminated and are made of detrital material, microcrystalline gypsum, calcite, organic matter and minor amounts of clay minerals (smectite and illite).

In the Rio Grande di Lipez delta region to the south of the Salar, fluviodeltaic sediments are interbedded in the salt crust on an area of about 300 km². This delta area is also characterized by the largest borate (ulexite) deposits of Bolivia (Risacher and Fritz, 1991).

In 1986, an initial drilling project in the salt flat down to a depth of 121 m was conducted in the central part of the Salar de Uyuni. The recovered sediment core was characterized by an alternating sequence of 12 salt layers interrupted by 11 lacustrine sediment layers (clayey lake sediments) reflecting the alternating dry and wet climatic periods during Quaternary times (Fornari et al., 2001).

It was further found that the thickness of the mud layers increase with time. In combination with ¹⁴C data from shells or algal bioherms (diatoms) from palaeo-shorelines or lacustrine outcrops and U/Th analyses on carbonate samples it was suggested that the duration of lacustrine events in the central Altiplano increased during the Pleistocene (e.g. Wirmann and Mourguiart, 1995, Sylvestre et al., 1999).

In 1999, another drilling near the island Pescado, which was completed by the Duke University (USA), reached a depth of approximately 220 m and ended in a salt horizon. Down-hole logging using natural gamma radiation confirmed the alternating sequence of mud and salt layers down to 188 m depth (Baker et al., 2001). Additionally, radiocarbon dating on total organic carbon content of mud and salt samples from the upper 31 m of the core was accomplished in order to understand the hydrologic variations on the southern Altiplano over the last 170,000 years (Fritz et al., 2004). It was found that the wet periods on the millennial and orbital timescale on the Altiplano are correlated with the surface temperature of the high-latitude North Atlantic and are therefore triggered by a common factor (Baker et al., 2001, Fritz et al., 2004, Placzek et al., 2013).

Between 1999 and 2002 geophysical investigations were performed by the University of Delaware (USA) in order to study the stratigraphy and palaeoclimate of the Altiplano and the extent to which the Quaternary lake stratigraphy is affected by neo-tectonic deformation. High-resolution seismic reflection experiments observed high-velocities down to depths of at least 300 m. However, no data are available about the final depth of the Uyuni salt deposits (McGeary et al., 2000, McGeary, 2001, McGeary et al., 2003).

The formation of the Salar de Uyuni started in Quaternary times and continues still today. Since about 1.8 million years the Altiplano was occupied several times by large paleolake bodies which were characterized by alternating extension and desiccation periods due to climatic changes. These paleolake periods correspond, from the oldest to the youngest, with lakes Mataro, Cabana, Ballivian, Minchin and Tauca (Clapperton et al., 1997, Wirmann and Mourguiart, 1995). The latter two palaeolake phases, **Tauca**

(12,000 – 16,000 yr BP) and **Minchin** (30,000 – 73,000 yr BP) correspond with the uppermost two major mud layers of the Uyuni stratigraphy. These layers are well studied and dated by several authors using U/Th dating (Baker et al., 2001, Fritz et al., 2004) and ^{14}C -dating on diatoms (Sylvestre et al., 1996) or on carbonates from paleo-shorelines (Sylvestre et al., 1999, Placzek et al., 2006). The reconstructed lake levels of the palaeolake stages on the Altiplano are illustrated in Figure 8.

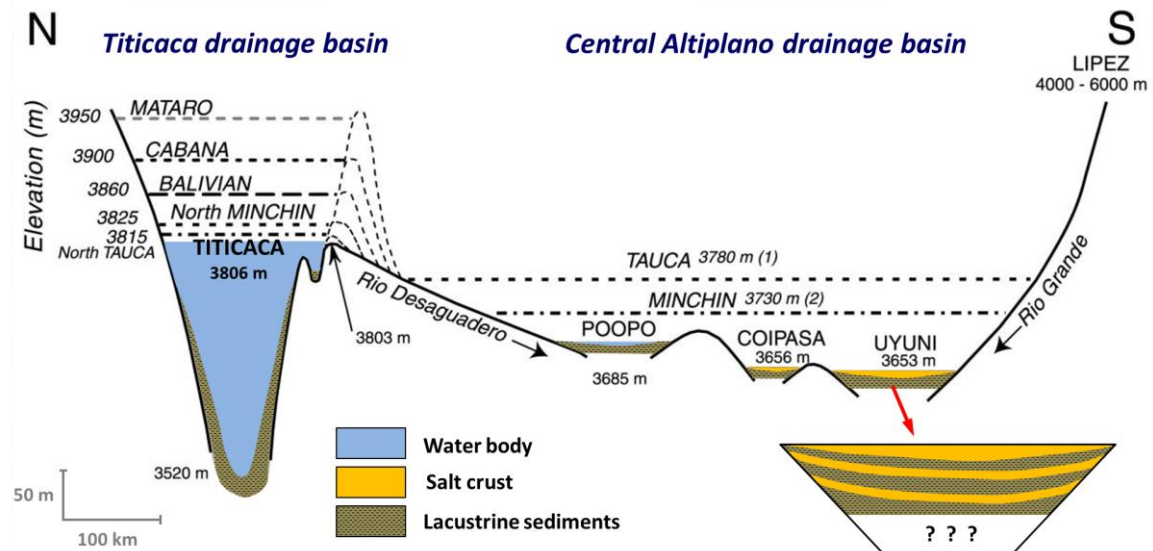


Figure 8: Paleolake level history of the Altiplano illustrated by a NS schematic section (modified after Fornari et al., 2001). The sediment stratigraphy is characterized by an alternating sequence of salt crusts and lacustrine sediments as illustrated exemplarily for Uyuni (the final depth of the Uyuni salt flat is still unknown).

Many other studies of the Altiplano deal with paleohydrology and paleoclimatology (Argollo and Mourguiart, 2000, Baker, 2001, Chepstow-Lusty et al., 2005, Cross et al., 2001, Gosling et al., 2008, Rigsby et al., 2005, Wirmann and Mourguiart, 1995). Based on multiproxy isotope studies on lake waters and sediment cores, uranium-series and radiocarbon dating of lake carbonates and of peat associated with glacial and glacialfluvial sediments, it was found that the maximum extend of the glaciers on the Bolivian Altiplano temporally correspond with the lake level highstand during the Tauca phase. Both events are correlated with increased effective moisture and cooler climatic conditions (Clapperton et al., 1997, Fritz et al., 2007, Abbott et al., 2000).

Between 1964 and 1985 Manfred Wolf investigated the geology and geochemistry of the Altiplano salt flats. In contrast to previously published studies, which stated that the Altiplano is one large hydrologic system where all sub-basins are interconnected with each other, Wolf (2010) postulates four independent hydrologic systems on the Altiplano: (1) Lake Titicaca and lake Poopó, (2) Salar de Coipasa, (3) Salar de Uyuni and

(4) the internal drainage basin within the volcanic edifices in the very south of the Bolivian Altiplano at an average altitude of about 4500 m a.s.l.

The formation of the Salar de Uyuni and other salt flats in arid and semi-arid environments depends on the salt pan cycle which comprises four different stages according to Lowenstein and Hardie (1985) and Wolf (2010):

- 1) Desiccation stage marked by desert soil weathering
- 2) Flooding stage: The beginning of the rainy season is dominated by dissolution, erosion and transport of salt. Wide areas are flooded in association with differentiated sedimentation and pre-concentration.
- 3) Evaporative concentration stage: Main concentration and crystallization as a result of intense evaporation
- 4) Return to desiccation stage

2.3 Hydrogeology and hydraulic behavior of other salt flats worldwide

2.3.1 Hydraulic parameters of salt flats

Previously, Turk et al. (1973) studied intensively the hydrogeological properties of the lacustrine sediments of Bonneville salt flat (Utah, USA) by conducting numerous pumping tests as well as wet and dry bulk density measurements for porosity determination. The aquifers have an average porosity of 45%. The transmissivity ranged between $7 \cdot 10^{-5}$ and $7 \cdot 10^{-3}$ m²/s, whereby very high hydraulic conductivities were found only in the uppermost part of the salt flat sediments. Furthermore, the vertical brine flow was negligible under the observed hydraulic gradients.

The most important lithium-reservoir in recent times in terms of world lithium production is the Salar de Atacama in Chile. According to Bobst et al. (2001), the Chilean company SQM performed altogether 38 drillings between July and August 1986. However, until 1997 these drillings were under lock. Then, one of these drill cores was uncovered for paleontological research. The core bottom at 100 m depth was dated to about 106 ka using U/Th-dating (Bobst et al., 2001). Carmona et al. (2000) estimated the total depth of the Salar de Atacama to about 1,000 m but drillings reached a maximum depth of only 500 m.

Extensive investigations of the hydraulic parameters of the Salar de Atacama and adjacent lagoons were published by Salas et al. (2010). They performed various pumping tests and also reinterpreted other pumping test data which were previously recorded by the company SQM. For the nucleus of the Atacama salt flat which is comparable with the Uyuni salt flat, they determined permeabilities ranging between 10 m/d and 100 m/d.

Further pumping test studies on the Salar de Huasco (northern Chile) or the Salar de Rincon (Argentina) as well as on a sabkha in Saudi Arabia showed similar high permeabilities or even higher values up to several hundred meters per day (Ovejero

Toledo et al., 2009, Acosta and Custodio, 2008, Sabtan and Shehata, 2003). However, nowhere in the above mentioned publications it is mentioned whether the obtained permeability values are corrected with regard to the density and viscosity properties of the pumped brine.

The salt layer porosity was estimated from the grain size distribution of the sediments or the storage coefficient calculated from the pumping test data. Ovejero Toledo et al. (2009) gives a porosity range for the Salar de Rincon (Argentina) from 10% to more than 30%. As well, the Salar de Atacama was characterized by an average overall porosity of 18% within the upper 25 m of the halite crust (Garrett, 2004). Also the halite-dominated strata of the Qarhan Playa in the Quaidam Basin (China) are characterized by porosities between 20 and 30% (Yu et al., 2013). However, for the Salar de Hombre Muerto (Argentina) the porosity of halite was estimated by Goldfrey et al. (2013) to only about $9 \pm 3\%$.

In general, it is known that the porosity of modern salt deposits worldwide is very high in the uppermost part (up to more than 50%) but decreases with depths to nearly zero at depths below about 45 m (Casas and Lowenstein, 1989). Responsible processes for the porosity loss with depth are post-depositional diagenetic cementation and compaction of the sediments (Baar, 1977).

The porosity of the Uyuni salt crust was first estimated by Ballivian and Risacher (1981) as well as Risacher and Fritz (1991) to be on average between 30 and 40%. Their estimates were based on soil type characterization and several porosity determinations on hard samples which yield only 20-30%. However, no further details are given about the measurement procedure. In addition, they found friable salt layers whose porosity was assumed to be significantly higher at about 40-50%.

Contrary to these publications, Wolf (2010) reported porosity measurements of two Uyuni salt rock samples of about 3.2% and 4.7%, respectively, which are based on mercury high-pressure porosimetry.

Investigations concerning the permeability properties of the Uyuni salt flat have not been done or published before this study.

According to Houston (2011) the Salar de Uyuni can be classified as an immature clastic salt flat. An alternating sequence of fine-grained sediments and evaporitic layers of halite define the stratigraphy of those salt flats. Due to the generally high inhomogeneity and anisotropy of clastic sediments, permeability highly depends on the lithology. Thus, the permeability may vary somewhere between 10^{-2} and 10^{+2} m/d even if fissures mostly do not occur. With increasing depth the permeability only slightly declines (Houston et al., 2011).

Due to the presence of interbedded or underlying sediment layers of different permeability fresher water can be transmitted from outside the salar margins through the sediments to the center of the salt flat. In the center, the density differential of the inflowing water with the nucleus brine causes an increasing tendency of upward flow of the brine with the proviso that the confining layers have sufficient permeability to allow such leakage (Houston et al., 2011).

2.3.2 Groundwater level fluctuations in arid basin aquifers

Groundwater levels may be influenced by different reasons. Indeed, changes in groundwater level do not always indicate groundwater recharge or discharge and fluctuations can occur on different time-scales. Long-term fluctuations over several years to decades might be attributed to climate changes or anthropogenic activities (e.g. pumping activity, changes in land usage, irrigation, etc.). Seasonal fluctuations often occur in response to the seasonality of precipitation, evaporation, irrigation activity or surface-water fluctuations of lakes and rivers connected with the groundwater system. Finally, short-term fluctuations can be induced by rainfall, barometric pressure fluctuations, ocean tides or earth tides, evapotranspiration, temperature variations or pumping (Healy and Cook, 2002, Gonthier, 2007). The relationships between water-level fluctuations, barometric pressure changes and earth tides can be evaluated using time-series analyses. To accomplish this task, various signal analysis methods can be applied, i.e. trend analyses, spectral analyses using Fast Fourier Transformation (FFT) and different filter techniques as well as cross-correlation (Bernard and Delay, 2008). Using these methods, cycles and periodic components can be identified within the time series. Phase lags between two parameters can be discovered by cross-correlation analyses (Acworth and Brain, 2008).

Using different time-series techniques, Bernard and Delay (2008) compared water level data with atmospheric pressure and tidal effects. Based on the effects of earth's tides on groundwater level data they computed the storage capacity and porosity of the aquifer. The results of the storage capacity were in good agreement with those obtained from petrophysical measurements or pumping test evaluations. In contrast, porosity values revealed by time-series analyses were greatly underestimated.

The barometric effects of atmospheric pressure fluctuations on confined aquifers can be estimated by different methods. Clark (1967) developed a procedure to determine the barometric coefficient (barometric efficiency) BE including the possibility to eliminate subjective errors. The procedure is based on a test which determines the sign of the incremental water-level changes Δh compared to the sign of the incremental atmospheric pressure changes Δp (Langguth and Voigt, 2004). Thus, water level changes that occur when there is no change in the atmospheric pressure are not considered in the calculation of the barometric efficiency so that external factors are excluded. Gonthier (2007) published a graphical method for estimating the barometric efficiency on continuous data. When plotting the daily-moving averages of the atmospheric pressure versus the daily-moving averages of the water-level, elliptical loops are formed for each daily cycle. The barometric efficiency can be estimated graphically from the preferred slope of all loops of a certain time-period.

Diurnal and semi-diurnal water level fluctuations were observed in (arid) groundwater systems by several authors (e.g. White, 1932, Acworth and Brain, 2008, Gribovszki et al., 2010, Zhu et al., 2011, Healy and Cook, 2002, Lautz, 2008, Tyler et al., 2006, Turk,

1975). However, two different types of diurnal fluctuations and related processes can be distinguished:

- **Type 1:** Diurnal fluctuations which are caused by evapotranspiration (ET) in extremely shallow groundwater generally show a minimum water-level between 18:00 and 19:00 and maximum in the early morning between 07:00 and 09:00. The minimum follows a period of drawdown during the daytime caused by water consumption by vegetation. At night, transpiration is minimal and recharge by net influx of groundwater occurs (Lautz, 2008). The daily consumption of groundwater as a result of evapotranspiration by vegetation can be estimated from the magnitude of diurnal ground-water level fluctuation (White, 1932, Lautz, 2008, Yin et al., 2013). For ET estimation, the specific yield is further needed, which is the most difficult parameter to determine (Lautz, 2008).

For instance, from the riparian zone of the Red Creek Canyon (USA), maximum daily fluctuations in the range of 1 – 32 mm were observed in the vegetation period between May and October (Lautz, 2008).

Besides shallow groundwater systems, type 1 diurnal fluctuations were also observed in stream flows. Gribovszki et al. (2010) gives an excellent summary of evapotranspiration-induced diurnal signal studies.

- **Type 2:** Turk (1975) observed diurnal fluctuations in the Bonneville Salt Flats (Utah, USA) which were characterized by highest water levels in the late afternoon between 16:00 and 18:00 and lowest levels occurring in the mid-morning. This is exactly the opposite of type 1 diurnal fluctuations triggered by evapotranspiration (Turk, 1975).

Turk (1975) found a significant correlation between the brine-level in the salt flat and the temperature as well as atmospheric pressure. A combination of three temperature-induced effects could be detected and confirmed also by laboratory experiments.

- (1) “As temperature increases, the volumetric air content can be increased due to thermal expansion of trapped air, resulting in a rise of the water table when the water table is close to the land surface.” (Tyler et al., 2006)
- (2) Another suggestion is based on the reduction in surface tension of water at higher temperatures leading to a release of water from the unsaturated zone that can quickly drain to the water table and rises the groundwater level during the hottest part of the day (Turk, 1975).
- (3) When air temperatures increase, the atmospheric pressure will decrease. Consequently, the total pressure of the salt crust and the aquifer will also decrease. Entrapped air in the unsaturated zone of the salt can expand and capillary water will be extruded into the groundwater leading to a rising water level (Turk, 1975).

Healy and Cook (2002) describe another effect on groundwater levels which they call the “Lisse” effect. During intense rain, air might be entrapped in the pores of the vadose zone. Due to the rise in atmospheric pressure, soil water from the unsaturated zone will be released from pores leading to a rising groundwater level immediately after precipitation.

2.3.3 Density-driven brine flow and free convection

The density of brines strongly depends on the concentration of dissolved elements and/or temperature. Variations of these parameters can cause fluid density gradients which play an important role in the transport of solutes. Any kind of density differences between two distinct brine phases may induce density-driven fluid flow in the form of fingers or lobe-shaped instabilities (Simmons et al., 2001).

Holzbecher (2005) gives an excellent summary of previous numerical modeling studies on density-driven groundwater flow in the vicinity of salt lakes. Figure 9 illustrates a schematic view of the flow pattern and hydraulic conditions under steady state conditions in accordance with Fan et al. (1997) and Holzbecher (2005). The model region comprises the area from the center of a closed desert basin covered by a salt lake to the surrounding mountains. Two competing flow regimes are supposed to determine the groundwater flow pattern. On the one side, groundwater recharge occurs in the surrounding mountains either by precipitation or by snow melting. The ambient flow regime is thus determined by regional groundwater flow from the mountains to the deepest point in the basin (forced convective flow). On the other hand, intense evaporation within the center of the arid basin induces density gradients characteristic for the buoyancy regime (Holzbecher, 2005). Brine with higher density overturns and sinks down. Thus, large-scale convection cells are triggered in the deep aquifer. At the margins of the salt lake the cells rise up and mix with the fresh groundwater from the mountains (Tyler et al., 2006). The “hinge” (Figure 9) represents the border between net recharge in the mountains and net discharge by evaporation in the basin (Fan et al., 1997).

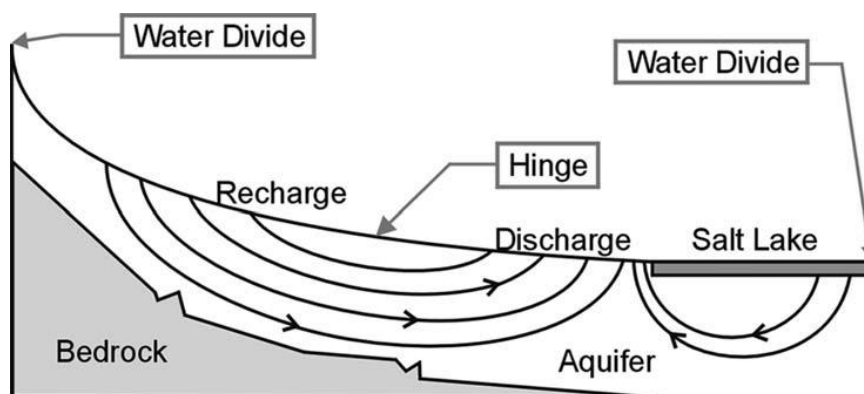


Figure 9: Schematic view of free convection in an arid desert basin triggered by high mountain groundwater recharge and evaporation induced density differences within the salt flat (according to Fan et al., 1997, Holzbecher, 2005).

Fan et al. (1997) investigated free convection of brines in closed basins. They made extensive field studies in Pilot Valley, Nevada, by measuring salinity differences and performing stable isotope analyses on water samples. Stable isotopic composition was used to identify free convection by identifying different sources or processes (meteoric water, geothermal influence, evaporation process). Furthermore, salinity profiles were measured over a longer period of time (9 months) to observe temporal changes in the spatial density distribution.

Free convection depends on the Rayleigh number. This in turn is affected by the permeability k and the porosity n . For instance, clay with a lower k and a higher n can cause a higher density gradient for free convection to occur (Fan et al., 1997).

Based on a literature review of field studies from several closed basins within the Great Basin (USA) as well as locations in Australia, Fan et al. (1997) summarized the necessary conditions for free convection to occur:

- (1) Playa wetness influences the hydraulic connection between the playa and deep groundwater leading to groundwater discharges at the regional base level of the playa. Concentrating brines provide the source and driving force of free convection.
- (2) Differences in the permeability of playa sediments might lead to slow solute transport into the subsurface caused by diffusion whereby free convection is limited due to smoothing out the density front.
- (3) Regional climate and climate history determine precipitation and evaporation and thus the formation of brines on the playa surface. When salinity becomes high enough, free convection can be triggered. Periodic basin filling and drying caused by fluctuations in climate may therefore cause a cycle of switching off-on the playa and groundwater interaction.

3 Methodology

The study of the hydraulic and geochemical properties of the Salar de Uyuni required the application of various analyses and experimental procedures. The first section of the following chapter describes all field investigations such as exploration drillings and well construction, pumping test realization and evaluation, as well as long-term brine level monitoring. Laboratory experiments and analyses conducted on salt core or brine samples are presented in the next section. Finally, methods of data evaluation are explained in the last section.

3.1 Field methods

3.1.1 Drilling procedure and sampling

During three field campaigns in 2009, 2010 and 2012 exploration drillings were conducted on 11 different sites all over the salt flat of Uyuni (Figure 10, the geographic coordinates are listed in Table 2).

A rotary drilling machine DK32S from DIAMASA Diamantbohrtechnik GmbH & Co. KG (Grimma, Germany) was used for core drillings. The technical specifications are summarized in Table B – 1. The drill rig was attached to a wooden board which in turn was fixed to the salt surface using tie bars as well as the load of a car on one side of the board (compare Figure 11). The drill was powered by a gasoline-driven generator (HONDA, 5.5 kW, estimated power loss at an altitude of 3,600 m a.s.l. due to lower air pressure and lower oxygen partial pressure is about 30%).

Brine served as the drilling fluid, which was pumped by a manual pressure pump via the rotating swivel into the drill rod. The drilling fluid was extruded from the bottom of the drill rod and removed cuttings and mud from the drill bit.

A tripod was used to facilitate the manual extraction of the drill bit, containing the sediment core, together with the drill rods from the borehole after each meter of drilling progress.

The sediment cores were extracted with a diameter of 62 mm and were placed on a plastic tarpaulin in order to dry the core samples in the sun and to document the stratigraphy in detail.

3. Methodology

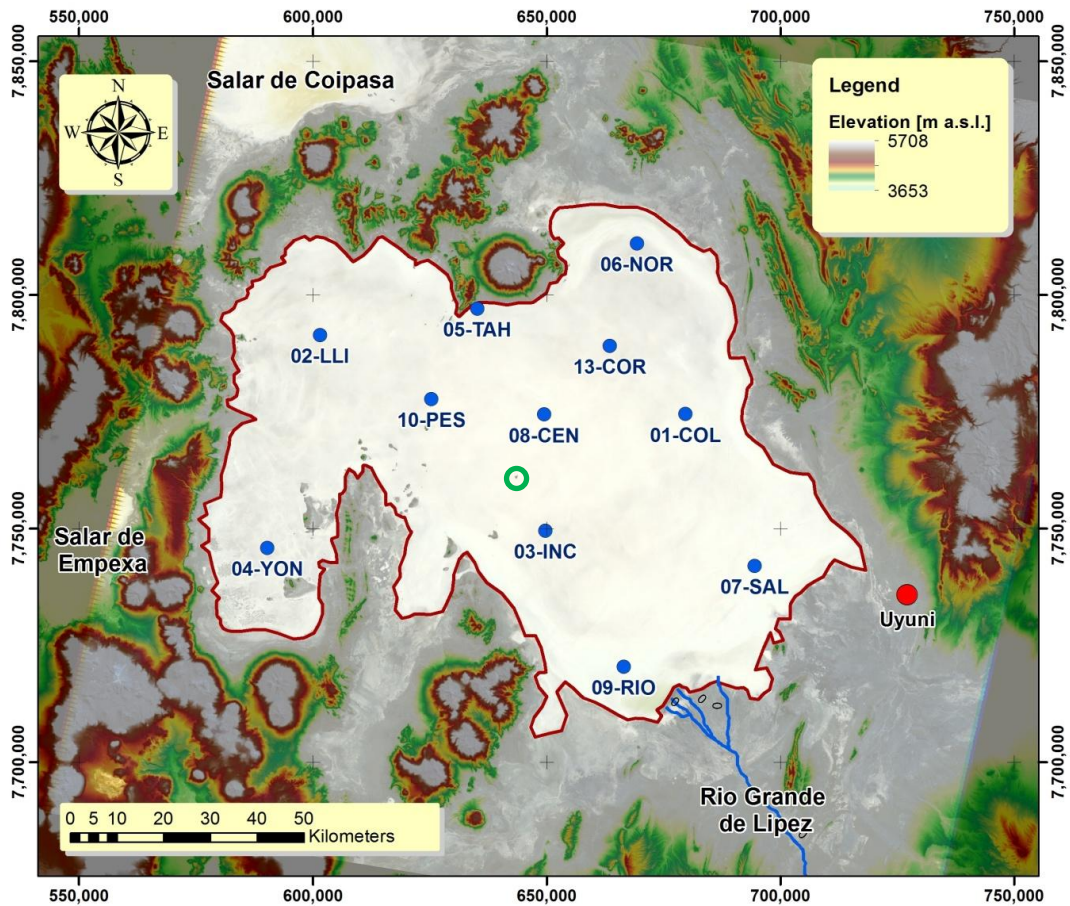


Figure 10: Topographic map of the Salar de Uyuni and the adjacent Salar de Coipasa in the north as well as the Salar de Empexa in the west showing the investigation sites (blue points) and the island Inkahuasi in the center of the Salar de Uyuni (green circle) [data base for map generation: SRTM and Landsat satellite data from USGS Earth Explorer⁹].

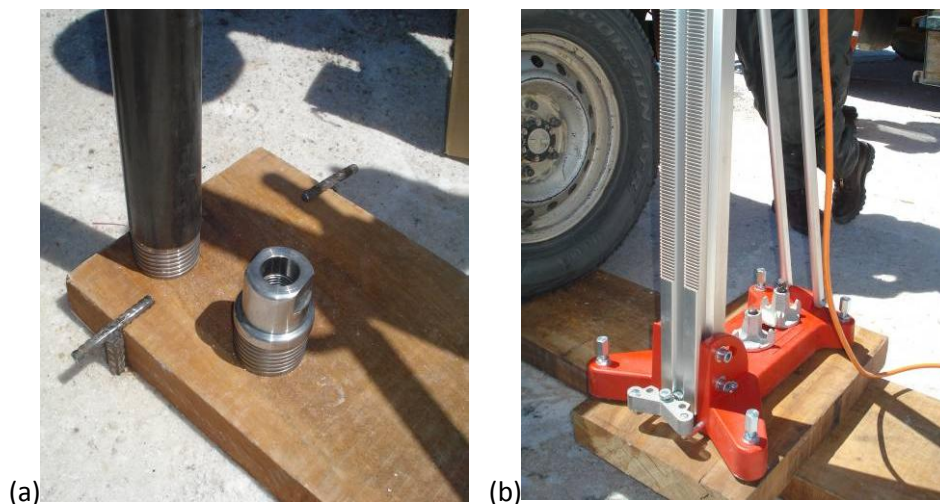


Figure 11: Drill rig set-up connecting it to the ground surface using (a) a board, tie bars and (b) the load of a car (Sieland et al., 2011).

⁹ USGS Earth Explorer: <http://earthexplorer.usgs.gov> (accessed on 03-08-2010). SRTM data: 90x90 m, recorded in March 2007; Landsat satellite data: 30x30 m, recorded in June 2002, band combination: 1, 2, 3 (red, green, blue).

3.1.2 Well constellation and well casing

Drillings were performed at a total of 11 different sites all over the salt flat. In order to perform pumping tests, several boreholes were drilled in different distances and directions to each other at seven sites (compare Table 1, Figures A – 1 to A – 3). At the other four sites only one borehole per site was drilled in order to obtain sediment cores for stratigraphic documentation as well as for porosity measurements.

Table 1: Well constellation at the different investigation sites: Distances and directions of the different drillings/wells (modified according to Sieland et al., 2011).

Distance							
[m]	01-COL	02-LLI	03-INC	05-TAH	06-NOR	08-CEN	09-RIO
A-B	2.76	2.95	3.00	3.10	2.10	3.08	3.48
A-C	2.51	2.02	5.00	4.16	3.15	4.04	1.88
A-D	-	3.95	-	1.87	5.00	1.92	4.02
A-E	12.33	2.10	10.00	-	-	1.16	-
A-F	7.74	1.55	-	-	-	-	-
Direction	01-COL	02-LLI	03-INC	05-TAH	06-NOR	08-CEN	09-RIO
A-B	70°NE	158°SE	268°SW	306°NW	30°N	315°NW	257°W
A-C	145°SE	289°NW	53°NE	63°NE	280°W	80°E	28°N
A-D	-	57°NE	-	170°S	180°S	220°SW	150°SE
A-E	169°SE	138°SE	163°SE	-	-	140°SE	-
A-F	260°SW	35°NE	-	-	-	-	-

All boreholes were equipped as wells using PE-tubes which were closed at the bottom by a cap. Screens were manually produced by cutting slits into the PE-tubes with a metal saw because industrial manufactured screens were locally not available. The resulting slot size was about 1 mm.

Usually, each well was equipped with only one meter screen in different depths (in order to take brine samples from different depths). However, in 2012 the wells 02-LLI-F and 08-CEN-E were screened completely over the total depth of the aquifer (see Table 2).

The annular space between the borehole wall, casing and screen, respectively, was back-filled with filter gravel produced by sieving gravel from a nearby river to a grain size between 2 and 4 mm. In case of the penetration of a mud or clay layer during drilling, the annular space in the borehole was back-filled with clay. For this, boulders of clay from a local clay pit outside of the salt flat were hashed and crushed into fine grained sediment. Afterwards, it was suspended with fresh water to form a clay mud.

3. Methodology

Table 2: Summary of the well specifications [b.g.l. – below ground level, a.g.l. – above ground level, *wells 02-LLI-B and E were filtered in the second salt layer separated by ~4 m thick lacustrine sediment strata from the upper salt layer] (modified according to Sieland et al., 2011).

Well notation	Coordinates (UTM, WGS 84)		Drilled depth	Well depth	Tube length	Screen length	Date of drilling	
	Easting	Northing	[m]	b.g.l. [m]	a.g.l. [m]	b.g.l. [m]		
01-COL	A	679821	7774578	12.50	12.00	0.56	11.7 – 12.3	Sep-2009
	B	679825	7774576	6.00	5.74	0.59	4.5 – 5.5	Sep-2009
	C	679820	7774576	8.50	8.33	0.59	7.0 – 8.0	Sep-2009
	E	679827	7774565	8.00	7.70	0.48	6.4 – 7.4	Sep-2009
	F	679813	7774576	3.50	3.30	0.54	2.0 – 3.0	Sep-2009
02-LLI	A	601593	7791495	7.90	7.86	0.86	0.28 - 1.08	Nov-2010
	B*	601594	7791492	9.70	9.23	0.79	8.0 - 9.0	Nov-2010
	C	601595	7791492	4.00	ca. 4.00	0.80	2.80 - 3.80	Nov-2010
	D	601597	7791496	2.00	ca. 2.00	0.60	0.80 - 1.80	Nov-2010
	E*	601594	7791493	10.00	9.29	0.58	7.5 - 9.0	Nov-2012
	F	601594	7791496	4.00	4.00	n.d.	0 - 4.0	Nov-2012
03-INC	A	649798	7749639	11.80	9.00	0.85	4.3 – 5.3	Sep-2009
	B	649796	7749639	4.70	5.00	0.86	3.5 – 4.5	Sep-2009
	C	649802	7749642	3.70	4.00	0.61	2.5 - 3.5	Sep-2009
	E	649801	7749633	2.70	3.00	0.75	1.5 – 2.5	Sep-2009
04-YON	590267	7745962	9.20	9.05	1.15	6.85 - 7.85	Nov-2010	
05-TAH	A	635277	7797118	12.50	1.20	0.75	0.0 - 0.7	Oct-2010
	B	635276	7797121	3.00	1.04	0.94	0.0 - 0.7	Oct-2010
	C	635278	7797115	2.00	1.76	0.13	0.0 - 0.6	Oct-2010
	D	635277	7797116	4.00	3.62	0.14	2.82 - 3.62	Oct-2010
06-NOR	A	669419	7811070	13.00	1.10	0.73	0.20 - 0.90	Oct-2010
	B	669419	7811072	5.00	5.10	0.95	2.75 - 3.75	Oct-2010
	C	669416	7811072	3.00	3.00	1.19	1.8 - 2.8	Oct-2010
	D	669419	7811065	2.00	2.00	0.98	0.80 - 1.80	Oct-2010
07-SAL	694555	7742069	10.70	9.79	0.78	7.09 - 8.09	Nov-2010	
08-CEN	A	649559	7774478	13.00	11.30	1.25	7.5 - 9.5	Nov-2010
	B	649557	7774483	5.00	5.00	1.00	3.8 – 4.8	Nov-2010
	C	649562	7774482	3.00	3.00	1.08	1.8 - 2.8	Nov-2010
	D	649557	7774480	8.00	8.00	0.96	4.5 - 5.5	Nov-2010
	E	649560	7774477	8.50	7.50	0.27	0 - 7.5	Nov-2012
09-RIO	A	666568	7720469	10.00	6.96	0.12	2.0 - 3.0	Nov-2010
	B	666565	7720468	3.00	2.70	0.15	1.47 - 2.47	Nov-2010
	C	666569	7720471	4.00	3.95	0.07	2.75 - 3.75	Nov-2010
	D	666570	7720466	2.00	1.96	0.14	0.74 - 1.74	Nov-2010
10-PES	625164	7777644	10.00	9.70	0.65	5.0 - 6.0	Nov-2010	
13-COR	663549	7788949	9.70	9.34	0.49	5.05 - 6.05	Nov-2010	

3.1.3 Pumping tests

Pumping tests were performed at 5 different sites on the salt flat in 2010 and 2012 and lasted for about 3.5 to 5 hours. In 2010 the pumping was accomplished by a submersible Cromatic CH 291 W(A) pump from Homa. In order to accommodate the pump in the well (the submersible pump has a diameter of 176 mm), the normal exploratory borehole had to be enlarged from 76 mm to 206 mm diameter using a larger drill bit. However, enlargement was only possible to a maximum depth of 1 m. For the pumping tests in 2012, a gasoline driven suction pump with a 2.5 inch (6.3 mm) diameter hose was used.

The constant pumping rates of the different pumping tests varied between 1.07 and 2.47 L/s. The extracted brine water was discharged via a 50 m PE-tube connection or a 100 m flexible tube onto the salt flat.

Observation wells screened at different depths were available at various distances around the pumping well (Table 1 and Table 2, Figures A – 1 to A – 3).

The piezometric levels were measured during drawdown and recovery in the observation wells using CeraDiver® data loggers from Schlumberger Water Services (10 m water column (WC), 0.05%/10 m; -20...+80°C ±0.1 K). All data records of the CeraDivers represent pressure values in relation to normal fresh water. Hence, these raw data needs to be processed and corrected prior to any further evaluation.

Additionally, the maximum drawdown was low (approx. 10 cm) because of the high permeability of the salt crust and the rather low pumping rate. Therefore, special requirements have to be considered for processing the recorded drawdown data.

3.1.3.1 Data correction

Pressure data recorded by the data loggers in the wells were converted to brine level values before starting the actual pumping test evaluation. Additionally, seasonal or short-term cyclic fluctuations may overlap the drawdown values during the pumping test (Langguth and Voigt, 2004) and have to be considered in the data processing procedure:

- **Barometric compensation:** Because the divers in the wells always detect the total pressure (i.e. water pressure and air pressure) barometric compensation of the data must be done:

$$p_{\text{comp}} = p_{\text{Diver}} - p_{\text{air}} \quad (3.1)$$

where p_{comp} – Barometric compensated pressure
 p_{Diver} – Pressure of the brine above the Diver
 p_{air} – Barometric pressure

Barometric pressure data were obtained by using Baro-Divers (Schlumberger Water Services, 150 cm WC, 0.03%/150 cm WC; -20...+80°C ± 0.1 K; 0.03%/150 cm WC) which were installed within the above ground well tubes.

- **Density correction:** For pure water with a density $\rho_{H_2O} = 1 \text{ g/cm}^3$ the following relation is valid:

$$h_{\text{comp}} = p_{\text{comp}} \quad (3.2)$$

where h_{comp} – Water level in cm above the diver

However, due to density differences between the pumped brine and pure water, barometric compensated pressure values cannot easily be used as ‘cm water level’ but they have to be converted into ‘cm brine level’ (h_{brine}):

$$h_{\text{brine}} = \frac{h_{\text{comp}}}{\rho_{\text{field temp.}}} \quad (3.3)$$

where $\rho_{\text{field temp.}}$ – Density of the brine at field temperature conditions during the pumping test

The density was measured from brine samples from each pumping test site as described in chapter 3.2.1, and converted to local brine temperature, which was recorded simultaneously by the Cera-Divers, according to equation 3.4.

$$\rho_{\text{field temp.}} = \frac{\rho_{25^\circ\text{C}}}{1 + v \cdot (T - 25^\circ\text{C})} \quad (3.4)$$

where $\rho_{25^\circ\text{C}}$ – Density of the brine measured in the laboratory at 25°C
 v – Cubic thermal expansion coefficient (see chapter 3.2.1, equation 3.26)
 T – Brine temperature (°C) under field conditions

The cubic thermal expansion coefficient was determined according to equation 3.26 in chapter 3.2.1.

- **Discontinuities:** In some data sets discontinuities in the pressure head occurred due to unscheduled disturbance of the attachment of the pressure sensor in the piezometer by another person. These discontinuities were adjusted manually by adding/subtracting the difference of the gap in the data.
- **Influence of atmospheric pressure changes on confined brine levels**
In the case of confined aquifer conditions, changes in atmospheric pressure influence the brine levels measured by the piezometers. In order to remove these fluctuations a barometric coefficient (BE) was determined according to a statistical procedure developed by CLARK (1967). For this procedure only records were used which were obviously not influenced by pumping test action or any seasonal changes of the salt crust properties due to precipitation or flooding.

Therefore, a sign test is performed on Δh compared to the sign of Δp for each time step according to certain rules given by CLARK, 1967 (cited in Langguth and Voigt, 2004). Then, the sums of the changes in brine level $\Sigma\Delta h$ were plotted versus the sums of the corresponding changes in atmospheric pressure $\Sigma\Delta p$ (Figure 12). The barometric coefficient BE can now be calculated from the slope of the resulting regression line ($\Sigma\Delta h/\Sigma\Delta p$) and the specific weight (γ) according to equation 3.5 (Kruseman and de Ridder, 2000).

$$BE = \gamma \cdot \frac{\Sigma\Delta h}{\Sigma\Delta p} \quad (3.5)$$

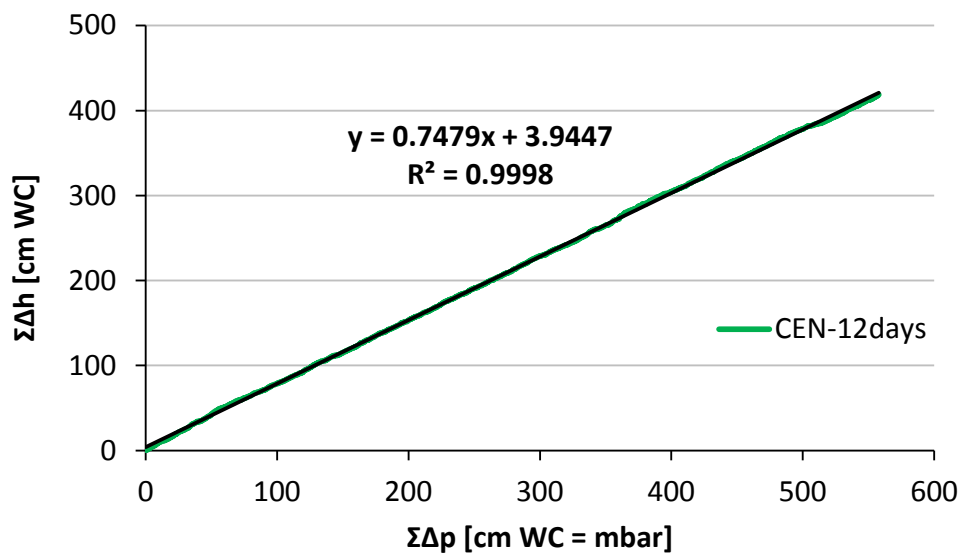


Figure 12: Determination of the barometric coefficient BE at site 08-CEN in 2011 by means of the curve of sums of the increments of atmospheric pressure [$\Sigma\Delta p$] and natural brine level fluctuations [$\Sigma\Delta h$] in the time period from Dec. 4, 2011 until Dec. 18, 2011 (not influenced by pumping test activity).

Beside atmospheric pressure changes also other factors or natural processes may influence the brine level leading to natural fluctuations which in turn disturb the brine level records during the pumping tests (e.g. tidal influence, temperature variations, or evaporation).

Even if the reasons for the non-rhythmic brine level fluctuations cannot be explained with certainty (a detailed discussion is given in chapter 4.3) an appropriate data correction of the pumping test data is necessary. Therefore, a statistical evaluation of long-term brine level records was applied.

- **Mean daily brine level fluctuations:**

Due to a limited number of pressure sensors (Cera-Diver data loggers) it was not possible to measure the undisturbed, natural brine level in the vicinity of the test sites while the pumping test was conducted.

However, long-term brine level records (between 12 and 269 days) from different sites indicated periodic brine level fluctuations. During the dry season, brine levels in all observed piezometers showed characteristic daily diurnal patterns (independently from the absolute brine head). Therefore, absolute mean daily brine levels were calculated from dry season data (compare Figure 13). Further details to this procedure are explained in chapter 3.3.2.

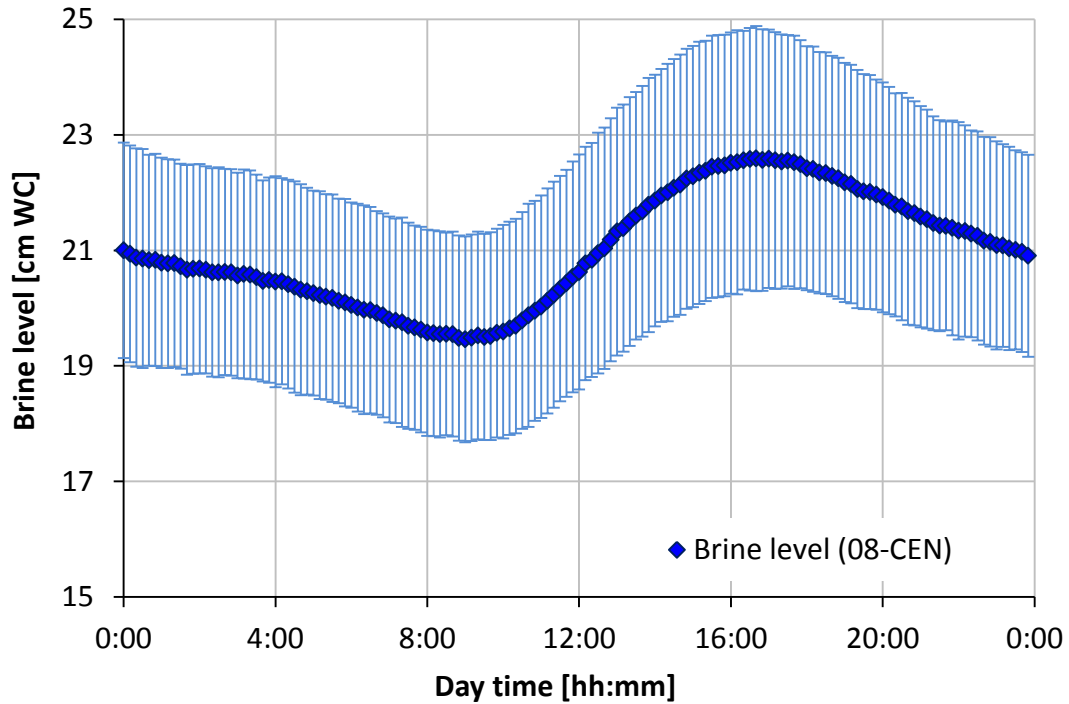


Figure 13: Example of mean absolute daily brine level fluctuations at investigation site 08-CEN. Data records from 167 days in the dry season of 2012 (June 29 – September 12, 2012) are averaged in time steps of 10 min. The standard deviations are also shown in light blue error bars.

In order to correct the pumping test data, the dry season absolute daily brine level fluctuations h_{mean} for each investigation site were used since all pumping tests were conducted when the salt flat was completely dry at the end of the dry season (between October and beginning of December; compare Figure 14).

$$h_{\text{PT}} = h_{\text{brine}} - h_{\text{mean}} \quad (3.6)$$

where h_{PT} – Theoretical brine level [cm] during the pumping test after subtracting the daily natural brine level fluctuation (h_{mean})

h_{brine} – Brine level recorded during the pumping test (equation 3.3)

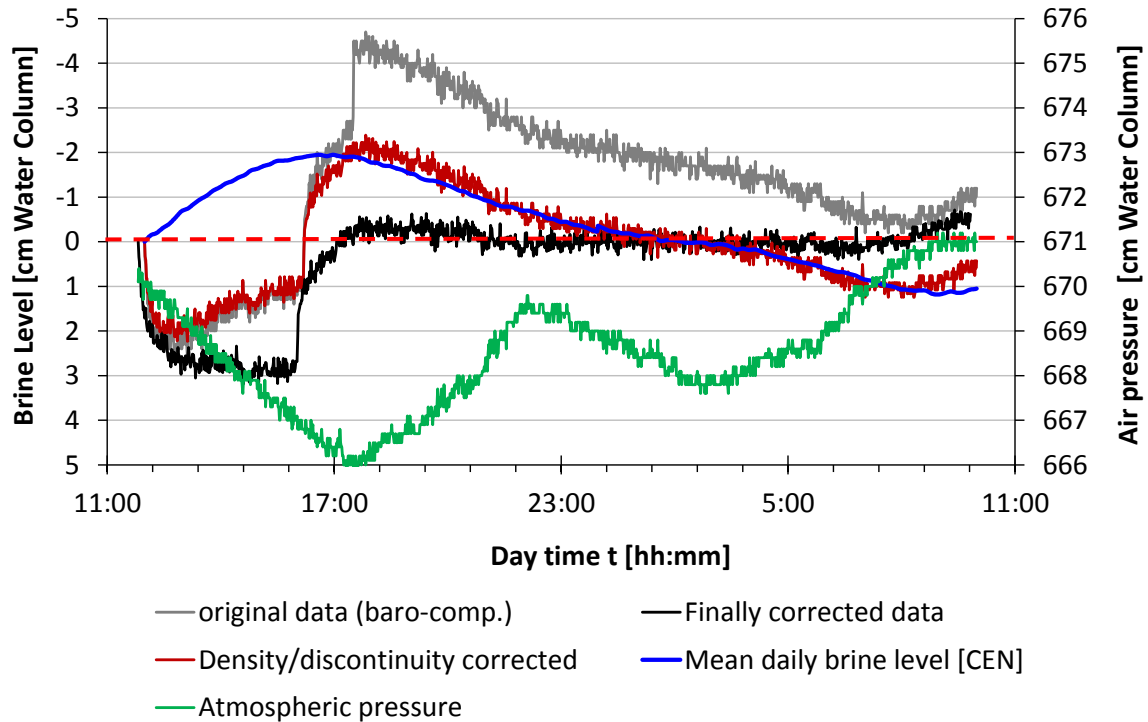


Figure 14: Brine level data correction for the 08-CEN pumping test in observation well B on Nov. 03, 2010: Barometric compensated original data measured by Cera-Diver are shown as gray line, the dark red line indicates the density corrected data (including correction of the unwanted discontinuity due to changes in the position of the data logger in the well), the blue line describes the absolute mean daily brine level fluctuation observed at 08-CEN, and the black line represents the final corrected brine level behavior during the pumping test. Additionally, the air pressure is plotted as green curve.

- **Calculation of drawdown:** Finally, the actual drawdown s [m] during the test was calculated for each time step ($t = i$) in relation to the initial brine level h_{PT} immediately before starting the pumping test ($t = 0$ s):

$$s = h_{PT,t=i} - h_{PT,t=0} \quad (3.7)$$

for i = Time steps during the pumping test

3.1.3.2 Evaluation of drawdown

➤ *Transmissivity*

All pumping tests were evaluated based on the assumption of confined aquifer conditions due to the inverse relationship between air pressure and brine level fluctuation. However, air pressure alone does not explain the undisturbed brine level fluctuations. There must be another influence which will be discussed separately in chapter 4.3.

The unsteady-state brine level depressions during the pumping tests were first evaluated using the COOPER & JACOB straight-line procedure (Langguth and Voigt, 2004) for **fully penetrating pumping wells** (i.e. pumping tests at sites O2-LLI (pumping well F) and O8-CEN (pumping well E) performed in 2012, compare Table 2). The COOPER-JACOB-procedure is a simplification of the THEIS method under the assumption that the integration variable u of the THEIS well function is smaller than 0.02 which reflects a maximum error <1%.

$$u = \frac{r^2 \cdot S}{4 \cdot T \cdot t} \quad (3.8)$$

where u – Euler constant
 r – Distance of the piezometer to pumping well
 S – Storage coefficient
 T – Transmissivity
 t – Time

From this, the drawdown values were plotted versus the logarithm of the time. A logarithmic regression line is constructed for the part of the curve where the coefficient of determination (R^2) is maximum. The slope of the regression equation corresponds to Δs which is needed for the calculation of the transmissivity T according to equation 3.9:

$$T = \frac{2.3 \cdot Q}{4\pi \cdot \Delta s} \quad (3.9)$$

where Q – Pumping rate or well discharge [m^3/s]
 Δs – Brine level depression over a logarithmic time decade

Alternatively, the **THEIS curve matching procedure** was applied using the software UP32 (version 1.1.10.5) within the ‘Umweltinformationssystem Sachsen’ (UIS, Sächsisches Landesamt für Umwelt, Landwirtschaft und Geologie). UP32 serves as graphical and numerical evaluation tool for pumping tests, especially in order to determine the transmissivity, storage coefficient as well as leakage factor (Szymczak and Behnke, 2009). Data input was completed in UHYDRO32 which is a front end program designed for data acquisition from outcrops and boreholes as well as from pumping tests.

The basic equation for UP32 pumping test evaluation is the HANTUSH equation 3.10 which “exactly describes the temporal change of the groundwater pressure head in consequence of a time-constant water discharge from a fully penetrating single well without self-capacitance in an endless, horizontal flat, confined aquifer and leakage from lying or overhanging layers” (Szymczak and Behnke, 2009). The leakage effect is represented by the leakage factor B .

At the initial phase of the pumping test (for the conditions $s > 2r/B$ and $t > B \cdot R \cdot S / 8T$) and if no leakage occurs, the equation simplifies to the THEIS well equation 3.13 (Szymczak and Behnke, 2009).

$$s = \frac{Q}{4 \cdot \pi \cdot T} \cdot W\left(\sigma, \frac{r}{B}\right) \quad (3.10)$$

$$\sigma = \frac{r^2 \cdot S}{4 \cdot t \cdot T} \quad (3.11)$$

$$B = \frac{\overline{T \cdot d}}{k_v} \quad (3.12)$$

$$s = \frac{Q}{4 \cdot \pi \cdot T} \cdot W(\sigma) \quad (\text{THEIS equation}) \quad (3.13)$$

where

- s – Depression [m]
- Q – Pumping rate/discharge [m³/s or L/s, respectively]
- T – Transmissivity [m²/s]
- W – Well function according to HANTUSH or THEIS
- r – Distance of the observation well to the well axis of the pumping well [m]
- S – Storage coefficient [-]
- t – Pumping time [s or min]
- σ – Argument of the well function (compare equation 3.10)
- B – Leakage factor [m] ($1 < B < 9.99 \cdot 10^9$ m)
- d – Thickness of the lying or overhanging layer [m]
- k_v – Vertical filtration coefficient of the semi-permeable lying/overhanging layer [m/s]

However, in case of only **partly penetrating pumping wells** the requirement of a horizontal flow regime is not given especially in the vicinity of the pumping well. This leads to lower permeability values. Therefore, all pumping tests performed in 2010 (only partly filtered pumping wells) are evaluated according to the procedure described in the guideline TGL 23864/08 (1973) for confined, isotropic aquifers.

The drawdown equation is expressed by

$$s = \frac{0.183 \cdot Q}{T} \left[\lg \frac{2.25}{r^2} + \lg t + 2 \cdot \delta \left(\frac{r}{M}, \frac{z}{M} \right) \right] \quad (3.14)$$

where

- Q – Pumping rate [m³/s]
- T – Transmissivity [m²/s]
- t – Pumping time [s]
- δ(r/M, z/M) – Correction function
- r – Distance of the piezometer from the pumping well [m]
- z – Mean depth of the filter screen [m]
- M – Thickness of the aquifer [m]

The correction function value δ(r/M, z/M) was taken from table values. If necessary, a graphical interpolation between the table values was done.

The transmissivity was calculated according to equation 3.15.

$$T = \frac{0.183 \cdot Q}{\alpha_t} \quad (3.15)$$

where α_t – Slope of the constructed straight-line

An auxiliary variable/correction value for drawdown (influenced by incomplete filtering of the pumping well) needs to be calculated according to following relation.

$$\Delta s = \frac{0.366 \cdot Q}{T} \cdot \delta\left(\frac{r}{M}, \frac{z}{M}\right) \quad (3.16)$$

t_0 is the intersection of the straight-line with the horizontal line $s = \Delta s$ or calculated by

$$t_0 = \frac{t_1}{10^{\frac{(s_1 - \Delta s)}{\alpha_t}}} \quad (3.17)$$

where t_1, s_1 – Coordinates of an arbitrary point on the straight-line

➤ *Storage coefficient*

The calculation of the storage coefficient S was performed for all pumping tests, no matter if the pumping wells are partly or completely penetrating, using the time t_0 (for $s = 0$) and the distance of the piezometer to the pumping well r according to equation 3.18.

$$S = \frac{2.25 \cdot T \cdot t_0}{r^2} \quad (3.18)$$

After the calculation of T and S , the range of validity needs to be checked by

$$t \geq 3.8 \cdot a \cdot r^2 \quad (3.19)$$

where $a = S/T$

➤ *Intrinsic permeability*

The relation between transmissivity T and permeability k_f depends on the water-filled thickness of the aquifer M :

$$T = k_f \cdot M \quad (3.20)$$

Based on density and viscosity properties of the brine, the resulting k_f -values have to be converted into the intrinsic permeability K [m^2] by equation 3.21 in order to receive a fluid-independent parameter for the salt crust.

$$K = \frac{k_f \cdot \eta}{\rho \cdot g} \quad (3.21)$$

where η – Dynamic viscosity of the brine at field temperature [$Pa \cdot s = kg/(m \cdot s)$]

ρ – Density of the pumped brine at field temperature [kg/m^3]

g – Gravitational acceleration ($9.81 m/s^2$)

3.1.3.3 Evaluation of recovery according to JACOB (1963) and DRISCOLL (1986)

The evaluation of the brine level recovery after a period of constant-discharge can be done for example by the straight-line procedures from JACOB (1963) or by the extended procedure from DRISCOLL (1986) for both cases if the pumping well is fully or only partly penetrating the aquifer.

The recovery starts when the pump is stopped at the time $t'=0$. Now it is assumed that instead of a pumping well there is an injection well with the same discharge power as the pumping well before. In accordance with JACOB (1963), the residual depression has to be plotted versus the logarithm of the ratio of t/t' . For one logarithmic cycle the difference of the residual depression Δs_r can be taken from the plot and used to calculate the transmissivity T according to equation 3.22 (Langguth and Voigt, 2004):

$$T = \frac{2.3 \cdot Q}{4\pi \cdot \Delta s_r} \quad (3.22)$$

where Δs_r – Residual depression after stopping the pump ($t' = 0$)

However, the storage coefficient cannot be determined using this procedure.

On the contrary, according to DRISCOLL (1986), the difference between the extrapolated drawdown from the discharge period s and the residual depression during recovery s_r has to be calculated (compare Figure 15) and plotted versus the logarithm of t' . Transmissivity T and storage coefficient S can now be calculated with equation 3.23 and 3.24, respectively.

$$T = \frac{2.3 \cdot Q}{4\pi \cdot \Delta(s-s_r)} \quad (3.23)$$

where $\Delta(s-s_r)$ – Difference for a logarithmic cycle between extrapolated depression from discharge period s and residual depression during recovery s_r

$$S = \frac{2.25 \cdot T \cdot t'_0}{r^2} \quad (3.24)$$

where t'_0 – Reverse extended abscissa of the straight-line for $(s-s_r) = 0$

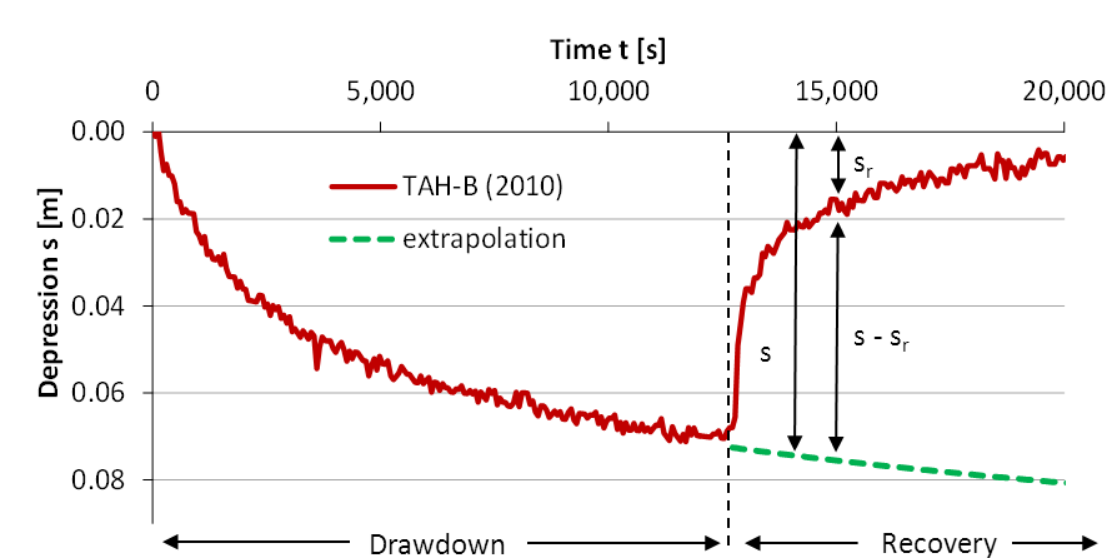


Figure 15: Brine level depression and recovery during a pumping test at site 05-TAH. Green dashed line indicates extrapolated depression behavior.

3.1.4 Long-term observation of brine-level fluctuations

In order to describe and understand the annual flooding behavior of the salt flat during and after the rain season, brine-level changes were observed over a time period of about nine months using CeraDiver® data loggers (Schlumberger Water Services, compare chapter 1.1.1). Three different locations from north to south (06-NOR, 08-CEN, 03-INC, compare Figure 10) were selected for long-term monitoring. Data loggers were installed at a depth of about 30 cm in the salt by drilling a little hole using a Bosch drilling hammer. In order to minimize corrosion of the data loggers over time, they were enclosed in plastic bags filled with distilled water (Figure 16). Afterwards, the sensors were covered with salt grit to avoid destructions or illegal removal. The data recording took place in 10 min time intervals.

Additionally, a Baro-Diver was placed on Incahuasi island, located within the salt flat (compare Figure 10), under a cover of some rocks in order to record air pressure fluctuations in 20 min time steps.

Also, the water level of the main tributary Rio Grande de Lipez was monitored during the same time period using a CTD-Diver (Schlumberger Water Services; 0...120 mS/cm, 1%/conductivity measurement value; 10 m water column, 0.1%/10 m; -10...+40°C ±0.1 K) which also allows the measurement of electrical conductivity. Before installation in a boulder that was placed in the Rio Grande (Figure 17), the diver was calibrated using 0.01 M KCl buffer solution with an electrical conductivity of 1413 µS/cm.

3.1.4.1 *Discussion of temperature effect on reliability of pressure sensors*

In order to check if there are any systematic temperature effects on the pressure measurements of the Divers, a series of tests were conducted at the meteorological station Reiche Zeche in Freiberg (TU Bergakademie Freiberg). The atmospheric pressure was measured in 2 min intervals over a time period of about two weeks using on the one side a Baro-Diver, which was also applied in Bolivia (as described in chapter 3.1.3.1), and on the other side a Baro Transmitter B-278-1/2T (from Thies Clima, accuracy without heating at -40°C to +65°C: ±1 hPa = 1 mbar)¹⁰.

Since both barometric devices were exposed to the same atmospheric pressure changes at the same time and location, the differences at each time step should result in a constant line if both devices measure correctly (data of the Baro Transmitter are related to mean sea level; data of the Baro-Diver are absolute on-site values).

Indeed, Figure 19 shows variations of the barometric pressure differences between -1 and +1 cm WC (= mbar). Additionally, the air temperature variations to which the Baro-Diver was exposed are plotted for comparison (Figure 19). Statistical analyses in SPSS

¹⁰ Data from the Baro Transmitter of the meteorological station were provided by Herklotz, Kurt: TU Bergakademie Freiberg, Interdisciplinary Ecological Center, personal communication from March 26, 2014.

3. Methodology

for Windows show that the differences in the atmospheric pressure measurements have a correlation with the air temperature which can be best explained by a quadratic regression ($R^2 = 35.8\%$, $p < 0.001$).



Figure 16: Installation of the Cera-Divers in shallow depth in the Uyuni salt crust.



Figure 17: Preparation of a boulder for the installation of the CTD-Diver in the Rio Grande for long-term monitoring of the river level.

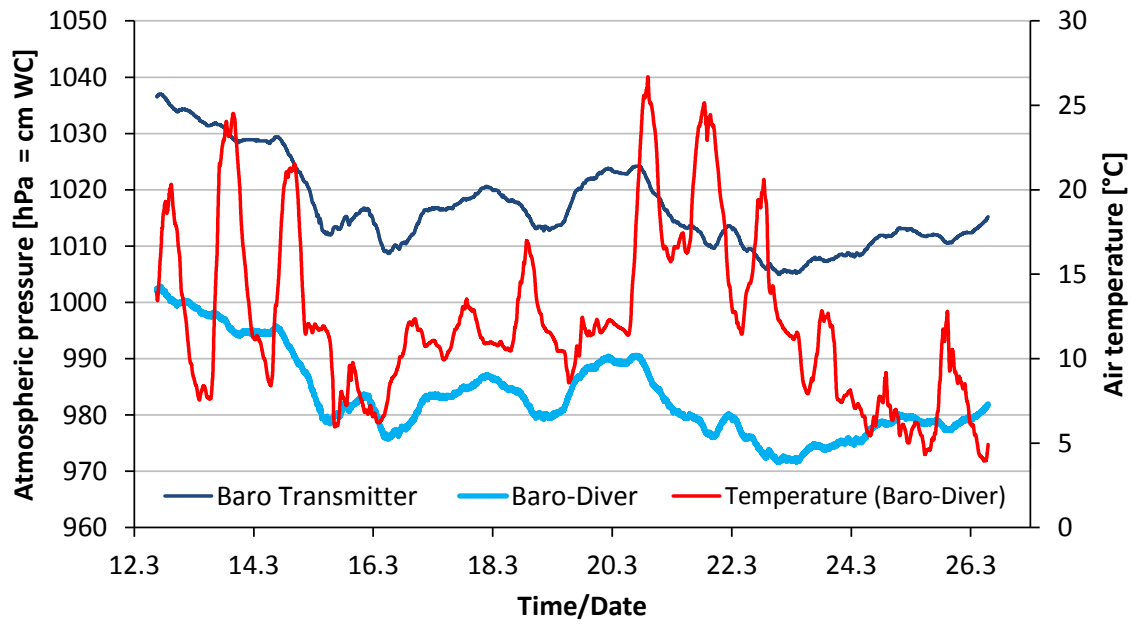


Figure 18: Atmospheric pressure and air temperature measured with the Baro-Diver in comparison with the atmospheric pressure recorded by the Baro Transmitter of the weather station Reiche Zeche (TUBAF) for a time period of 14 days. Atmospheric pressure data of the Baro Transmitter are related to mean sea level whereby data of the Baro-Diver are absolute on-site values.

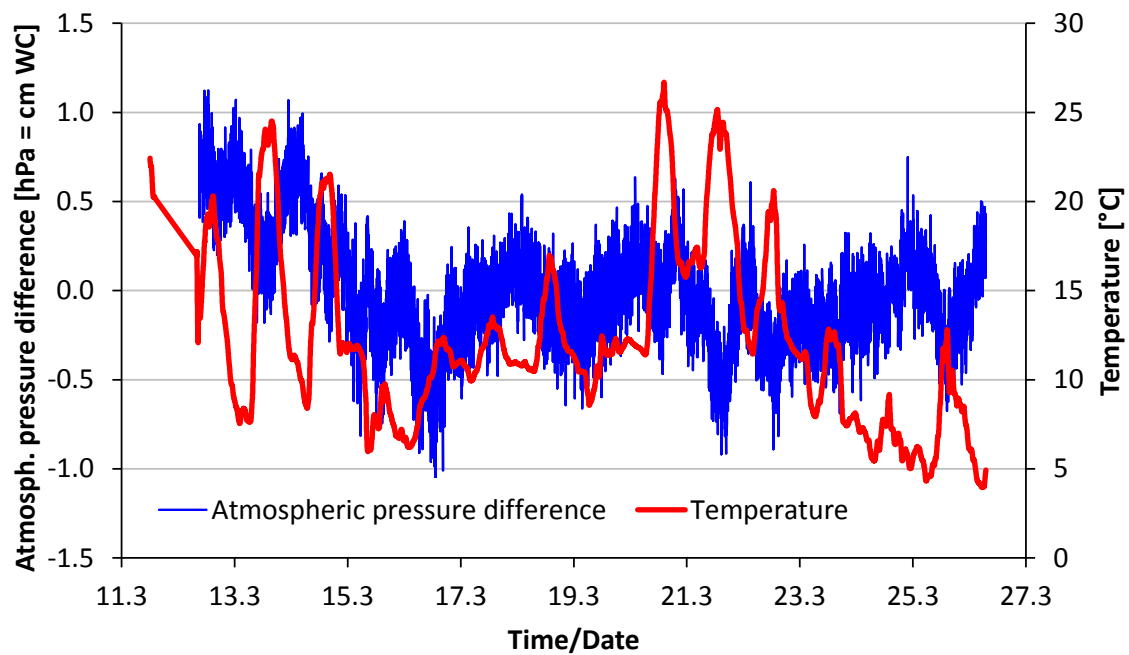


Figure 19: Time series of air temperature and atmospheric pressure difference between data records from Baro-Diver (Schlumberger) and a Baro Transmitter B-278-1/2T of the meteorological station of the Reiche Zeche [time steps = 2 min].

Though, the accuracy of the Baro Transmitter from the meteorological station is given by manufacturer as only ± 1 mbar, a much higher accuracy can be assumed due to very small total temperature variations at the location of the measuring device on the garret of the Reiche Zeche building (14° - 17°C).¹¹

In fact, the pressure measurement depends strongly on temperature. This effect is actually internally compensated for each diver by a “footprint” matrix. The “footprint” is determined by the manufacturer for temperatures ranging between -20° and $+80^{\circ}\text{C}$ and pressures between zero and the maximum measuring range of the respective Diver.¹² Nevertheless, a low temperature influence on the pressure measurement is still observable under natural temperature conditions.

3.2 Laboratory methods

3.2.1 Physical properties of the brine

In order to precisely determine the hydraulic properties of the salt crust, the physical properties of the brine have to be considered, too. In the following chapter the methods of temperature, density and viscosity measurement are described.

Temperature

Brine temperature measurements were performed in-situ with CeraDiver® data loggers from Schlumberger Water Services (accuracy: 0.05%/10 m, $\pm 0.1^{\circ}\text{C}$) during pumping tests as well as for long-term monitoring. In addition, a GMH 3350 temperature measurement device (Greisinger Electronics) connected with a temperature sensor (NiCr/Ni-thermo element, type K, 0°C till $+1100^{\circ}\text{C}$, $\pm 1.5^{\circ}\text{C}$) via a 40 m long cable was used. Temperature-depth profiles in the wells were measured in each case twice downward and upward in order to be aware of hysteresis effect due to instruments' adaptation time to the surrounding temperature conditions in the brine.

Density

The density of the brine samples from all wells were determined using a pycnometer DMA 38 at 25°C according to DIN EN ISO 2811-1 (2011) in the laboratory of the Federal Institute for Geosciences and Natural Resources (BGR) in Hannover. The density conversion depending on different field temperatures during the pumping tests was accomplished according to equation 3.25 from Hering et al. (2009).

¹¹ Herklotz, Kurt: TU Bergakademie Freiberg, Interdisziplinäres Ökologisches Zentrum, 09599 Freiberg, personal communication from May 14, 2014.

¹² Oestreicher, Ralf: UTK – EcoSens GmbH, 06712 Zeitz, personal communication from May 13, 2014.

$$\rho_1 = \frac{\rho_2}{(1+\gamma \cdot \Delta T)} \quad (3.25)$$

where ρ_1 – Density at field temperature
 ρ_2 – Density at standard temperature (25°C)
 γ – Cubic thermal expansion coefficient [K⁻¹]
 ΔT – Temperature difference [K]

Due to the strong dependency of the *thermal expansion coefficient* γ on the chemical composition, literature data could not be found for Uyuni brines. Therefore, the thermal expansion coefficient was determined experimentally in the laboratory. Two volumetric flasks were filled with 100 ml of brine at room temperature. One flask was heated in a drying cabinet to about 30°C and the other flask was cooled in a refrigerator to about 10°C. The volume excess in the warm flask was precisely removed by an Eppendorf pipette; whereas the volume deficit of the cooled flask was filled with brine of the same temperature. Rapid operation was necessary in order to minimize major uncertainties due to temperature changes of the samples during pipetting. The thermal expansion coefficient was then calculated using the differences in temperature and volume of both flasks according to equation 3.26 from Eichler et al. (2001).

$$V_t = V_0 \cdot [1 + \gamma \cdot t - t_0] \quad \rightarrow \quad \gamma = \left(\frac{V_t}{V_0} - 1 \right) \cdot \frac{1}{\Delta T} \quad (3.26)$$

where V_t, V_0 – Volume of brine at high and low temperature conditions
 t, t_0 – High and low temperatures

Kinematic and dynamic viscosity

The *kinematic viscosity* ν of the brine was measured at ambient pressure conditions (1013.25 hPa) and varying temperatures ranging between 15°C and 22°C using a UBBELOHDE capillary viscometer (Schott-Geräte GmbH, size I, Ia or II) at the Institute of Technical Chemistry (TU Bergakademie Freiberg) according to DIN 51562-3 (1985). During the measurements, the viscometer was immersed in an insulated, continuously stirred water bath. Temperature was regulated via continuous flowing tap water with an electrical heater and a precision temperature controller. Temperature was measured using a mercury thermometer with an uncertainty of 0.2 K.

Each sample was measured 10 times, and reported as an average of at least successive flow times (Widegren and Magee, 2007). Using the average flow time the kinematic viscosity was calculated according to equation 3.27.

$$\nu = k \cdot (t_{\text{mean}} - \Theta) \quad (3.27)$$

where ν – Kinematic viscosity [mm²/s]
 k – Capillary constant [mm²/s]
 t_{mean} – Mean flow time for traversing the path from the upper to the lower reading point [s]
 Θ – Hagenbach-Couette correction

The *dynamic viscosity* η [$mPa \cdot s$] is needed for the evaluation of flow-through experiments in the lab as well as for the calculation of the intrinsic permeability derived from pumping tests. The dynamic viscosity resulted from the multiplication of the kinematic viscosity ν with the density of the brine ρ [g/cm^3] at corresponding temperature:

$$\eta = \nu \cdot \rho \quad (3.28)$$

According to Busch et al. (1993) the viscosity decreases with increasing temperature, but increases with increasing mineralization. Therefore, laboratory experiments were conducted for each sample at two different temperatures in order to be able to interpolate/extrapolate to field temperature conditions.

3.2.2 Permeability determination by flow-through experiments

The permeability or hydraulic conductivity of the saturated salt cores was determined in the laboratory with a constant-head apparatus according to Klute and Dirksen (1986). In order to avoid any dissolution of the salt cores, organic liquids were used for the experiment instead of water.

Table 3: Physical properties of 2-octanol used for flow-through experiments (*experimentally determined using an UBBELOHDE capillary viscosimeter, compare chapter 3.2.1, viscosity measurements have been conducted for temperatures T of 18.2°C, 25°C and 30°C)

Organic substance	2-octanol
Density (25°C)	0.8170 g/cm ³ (Yaws, 2009)
Dynamic viscosity (25°C)	5.324 mPa·s*

2-octanol was used as the fluid because it is not harmful, poisonous or dangerous to the environment.

Core samples (solid salt rock) were encapsulated in heat-shrink tubes connected with PVC reducers connected with a PE hose. Samples were saturated with 2-octanol from the bottom to the top in order to expel air bubbles from the core. The organic fluid (2-octanol) was pumped in a circle from a storing tank into the constant head tank via a peristaltic pump. From there, the excess fluid was conducted back into the storing tank (Figure 20).

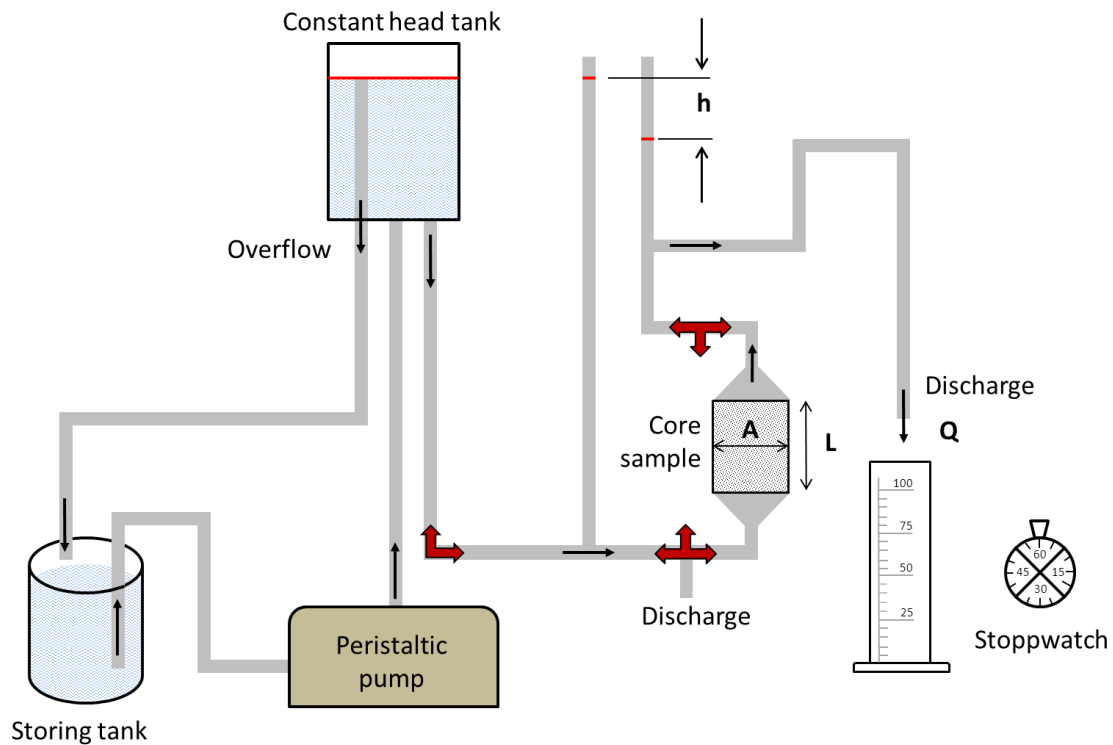


Figure 20: Principle of the flow-through experiments on the salt cores.

The conductivity was calculated based on Darcy's Law by the equation (modified from Busch et al., 1993):

$$k_f = \frac{Q \cdot L}{A \cdot h} \quad (3.29)$$

- where Q – Discharge rate of 2-octanol through the salt core (volume of 2-octanol ΔV /time Δt)
- A – Cross-section of the core sample
- L – Length of the core sample
- h – Hydraulic gradient of 2-octanol (Figure 20)

For each hydraulic gradient, the discharge rate was determined in replicates. Finally, the experimentally determined conductivity values based on 2-octanol were converted into intrinsic conductivities K [m^2] according to equation 3.21 (chapter 3.1.3.2) but can be converted as well into brine-related permeability.

The temperature dependence of the density ρ [$g/ml = g/cm^3$] of liquid-organic compounds can be described by the general equation 3.30 (Yaws, 2009):

$$\rho = \frac{A}{B \left(1 - \frac{T}{C}\right)^n} \quad (3.30)$$

- where A, B, C, n are regression coefficients for 2-octanol: $A = 0.27770, B = 0.27272, C = 637.15, n = 0.29430$ (from Yaws, 2009)

When calculating the 2-octanol density for different temperature values T , a regression equation (3.31) was deduced.

$$\rho_{2\text{-octanol}} = 0.836 - 0.00076 \cdot T \quad (3.31)$$

The dynamic viscosity of 2-octanol was determined experimentally using the UBBELOHD capillary viscosimeter as it is described above in chapter 3.2.1. Linear regression of the measured dynamic viscosity values at three different temperatures ($T = 18.2^\circ\text{C}$, 25.0°C , 30.0°C) gives the following relation:

$$\eta_{2\text{-octanol}} = 11.4146 - 0.237354 \cdot T, \quad R^2 = 0.9907 \quad (3.32)$$

3.2.3 Gas permeability measurement

The permeability of one conspicuously hard and dense sediment sample (which was identified as a gypsum layer, compare chapter 4.1.6.2) was analyzed at the Institute of Drilling Engineering and Fluid Mining (TU Bergakademie Freiberg) using a self-made unsteady-state two-chamber procedure (described in Amro et al., 2012). The sample was cut into a specimen with a diameter of 40 mm and a length of 15 mm in order to fit into the gas chamber of the device. The intrinsic permeability can be calculated from the temporal gas pressure profile. The lower detection limit of this procedure is about 10^{-21} m^2 (Amro et al., 2012).

3.2.4 Geochemical analyses of lithium concentrations

For geochemical analyses of lithium concentrations, brine samples were taken from all bore holes using a submersible COMET Geo-Dublo-Plus pump with a pumping rate of 17 L/min ($\sim 280 \text{ ml/s}$). In the field, each brine sample was prepared for the measurement in the laboratory by filtration and acidification with ultra-pure HNO_3 .

The chemical composition of the brine with special emphasis on lithium concentrations was analyzed using ICP-MS (inductive coupled plasma mass spectrometry, X Series 2, Thermo Scientific) in the laboratory of the Department of Hydrogeology (TUBAF). For this, filtered and acidified samples were measured in dilutions of 1:200. Each 10 ml of diluted sample had 100 μL of internal standard (5 mg/L Ge, and each 1 mg/L of Re and Rh) added to it. Measurements took place in normal mode on the mass 7 for lithium. Quantification of the concentrations deviated from the determination of the peak areas for each sample under consideration of the standard calibration (detection limit for 1:200 diluted samples: 20 $\mu\text{g/L}$ Li). The analytical accuracy of ICP-MS measurements including sampling and dilution accounts for $\pm 10\%$.

For more details about the geochemical aspects of Uyuni brines including on-site parameters, chemical composition and isotopic signatures, the reader is referred to Schmidt (2010) and Heinrich (2012).

3.2.5 Radiocarbon dating on brine samples

Brine samples taken from different depths (i.e. from different wells each filtered in certain depth, compare chapter 3.1.2) were prepared for radiocarbon dating by means of a vacuum extraction line (Figure 21). Carbon was extracted from approximately 1 L samples by converting all carbon species dissolved in the brine into CO_2 by adding concentrated (65%) phosphoric acid. The released CO_2 was collected in a special glass vial (ampule) which was previously flushed several times with ultra-pure nitrogen (N_2 5.0 / 99.999% N_2) and evacuated by a vacuum pump (from Edwards) to -980 mbar. The CO_2 extraction was stopped once the system reached a final pressure of -200 mbar and the glass vial was closed by melting using a glassblower.

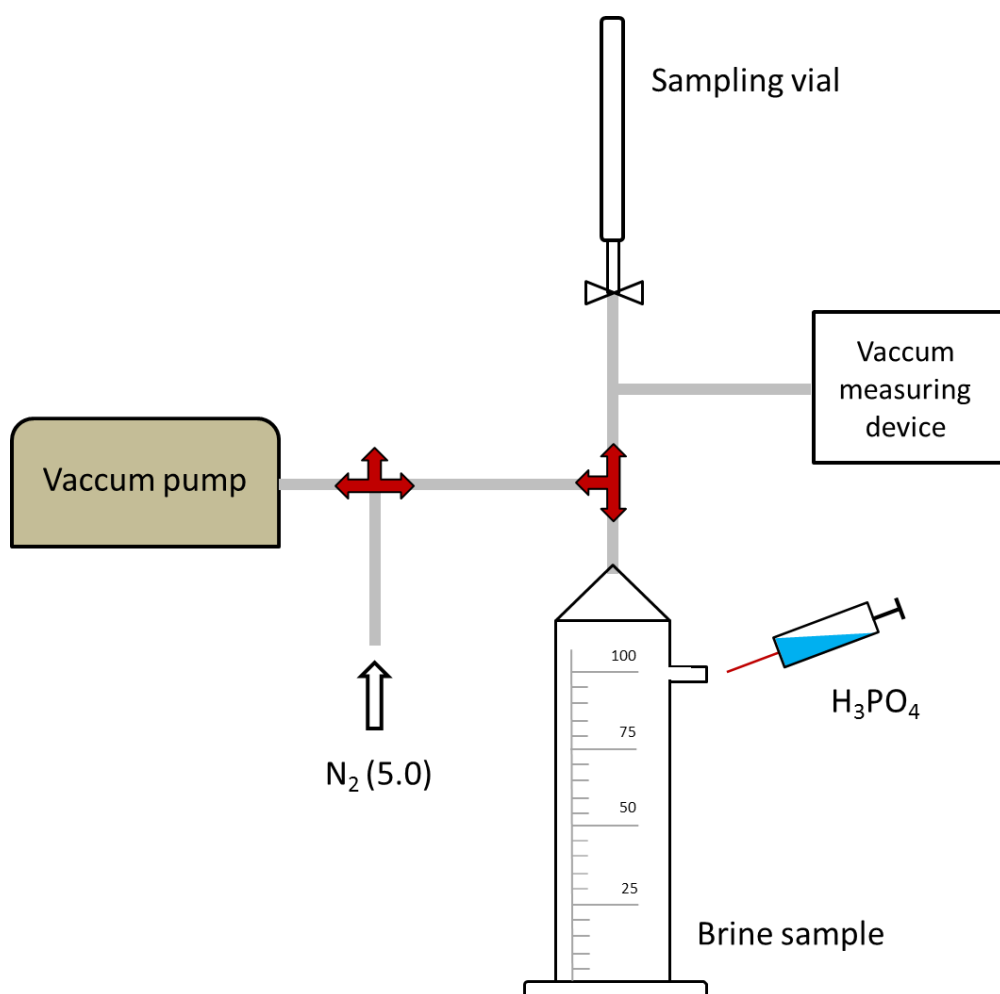


Figure 21: Sketch of brine sample preparation in a vacuum extraction line for radiocarbon dating analysis.

The prepared CO₂ gas samples were analyzed at the Poznan Radiocarbon Laboratory for ¹⁴C/¹²C and ¹³C/¹²C ratios by accelerator mass spectrometry technique using a 1.5 SDH-Pelletron Model "Compact Carbon AMS" (ser. no. 003, produced in 2001 by the National Electrostatics Corporation, Middleton, USA). The measured sample ratios were compared to the ratios measured in an international ¹⁴C standard (Oxalic Acid II). The ¹⁴C/¹²C ratios in the samples were also fractionation-corrected using δ¹³C values measured in the samples expressed with respect to the fractionation-corrected ¹⁴C/¹²C ratio in the "modern standard". The results are given in pMC (per cent modern carbon). The ¹⁴C ages of the brine samples were reported as conventional radiocarbon ages according to equation 3.33 assuming an initial ¹⁴C concentration of 100 pMC.¹³

$$\text{Age} = -8033 \cdot \ln\left(\frac{\text{pMC}}{100}\right), \quad (T_{1/2} = 5568 \text{ years}) \quad (3.33)$$

3.2.6 X-ray diffraction (XRD)

The mineral composition of some selected sediment samples was analyzed using X-ray diffraction (XRD) at the Federal Institute of Geosciences and Natural Resources (BGR) in Hannover using a X-ray diffractometer X'Pert PRO from PANalytical. The diffractograms for each sample are attached in Figures A – 4 to A – 6.

3.2.7 Porosity determination

The classical methods for porosity characterization (e.g. Mercury intrusion porosimetry, thin-section and microscopic porosity quantification, helium pycnometry, buoyancy method) are not suitable for describing the salt core porosity from the Salar de Uyuni because of several reasons which are explained below.

Mercury intrusion porosimetry (MIP) is actually the classical experimental method for determining the pore size distribution and porosity of a porous material, e.g. sedimentary rocks. However, the maximum sample size which can be investigated using a mercury porosimeter is limited to only view cm³ by restricted dimensions of the penetrometer cell of common instruments. Therefore, only small pores on order of nm- to μm-scale can be characterized (Vergés et al., 2011, Kumar and Bhattacharjee, 2004, De Las Cuevas, 1997). Salt core samples from the Salar de Uyuni are determined by high total porosity as well as quite large pore objects of several mm to cm in size. When cutting specimens of the size predefined by the penetrometer cell of the Hg porosimeter most of the natural pore objects could not be captured. Therefore, this technique is not suitable for determining the overall average porosity of Uyuni salt core samples.

¹³ Goslar, Tomasz: Poznan Radiocarbon Laboratory, 61612 Poznan, Poland, personal communication from July 29, 2014.

Another method is the *microscopic evaluation and image analysis* of thin-sections of core samples. Certainly, this technique does not give precise appraisals of the porosity (De Las Cuevas, 1997). Moreover, the preparation of thin sections from salt rock samples is extremely complex and time-consuming because it requires kerosene lubricant in order to avoid any dissolution of the salt (Casas et al., 1992). Furthermore, several hundreds of thin-sections would be necessary to precisely determine the porosity of an average salt core sample 6 cm in diameter and 10 cm long (Zauner, 2012).

Alternatively, *helium pycnometry* can be used for porosity determinations. Actually, this method is predominantly used for matrix or particle density determination. Most available commercial helium pycnometers have sample chambers varying between 1 and 135 cm³ (Flint and Flint, 2002). So, here the maximum measurable sample size is again small compared with the total porosity and the size of some pore objects of salt samples in this study. Therefore, this method is not appropriate to determine representative porosity values.

The simple *saturation-buoyancy method of Archimedeian* (Trautwein, 2005) could also not be applied to the Uyuni salt core samples due to high solubility of salt in water. Even when using an organic liquid in order to avoid dissolution during the measurement, problems arise from the intrusion of the liquid in large outer pore objects. In order to avoid this effect core samples have to be encapsulated. Due to sharp crystals and the irregular outer shape of the core samples (especially the breaking edge) it is not an applicable procedure.

Thus, the porosity and the pore structure were investigated by three alternative methods:

- (1) X-ray computed tomography (micro-CT)
- (2) Gravimetrically on saturated core samples
- (3) Directly computed on dried salt core samples using the geometry and mass of the core samples (complement method) and the particle density of the salt which was previously determined by helium pycnometry.

Table 4 gives a general comparison of the advantages and disadvantages of the applied methods of this study.

3. Methodology

Table 4: Advantages and disadvantages of the applied methods for porosity determination (*percentage deviation of porosity values determined by the visual thresholding technique from those determined by the automated Otsu algorithm; **error estimation according to DIN V ENV 13005 (1999), compare Texts C-1, C-3 and C-4 in the appendix).

Criteria	Method 1 (micro-CT)	Method 2 (saturation)	Method 3 (completion)
Sample preparation	no	encapsulation in heat-shrink tube	drying in cabinet dryer (180 – 300 h)
Measurement time	quick (~15 min/sample)	very time-consuming (1 h to >24 h/sample)	time-consuming (~0.5 h/sample)
Data-processing	complex and time-consuming	minor corrections	no
Accuracy/Error estimation	pore size resolution 76x76x76 μm ; uncertainty of binning: 1.1 to 35.1%*	average error: $\pm 61\%^{**}$	average error: $\pm 20.7\%^{**}$
Total porosity	yes	no	yes
Effective porosity	(subjective estimation possible)	yes	no
Pore size distribution	yes	no	no
Costs	expensive (~200 – 400,- €/sample)	cheap (~100,- € for 5 L of 2-octanol)	very cheap (~10,- € for plasticine)

3.2.7.1 Method 1: X-ray computed tomography (micro-CT)

X-ray computed tomography is a 3D imaging technology which can be used to visualize the internal pore structure of the salt cores without destruction of the samples. Nine salt core samples from drilling 08-CEN-A (taken in 2010) and two core samples from drilling 03-INC-A (taken in 2009) were analyzed using X-ray computed tomography at the Institute of Ceramics, Glass and Construction Materials (IKGB, TU Bergakademie Freiberg).

Scanning and reconstruction of CT images

The salt core samples were scanned using a CT-Alpha 225 (technical specifications are listed in Table B – 2). The applied micro-CT laboratory machine consists of a micro-focus direct beam tube with a stationary detector while the sample is rotated within the X-ray cone-beam by 360°. In order to reach the highest possible image resolution, the maximum length of the sample core was limited to about 10 cm. Therefore, the spatial resolution for a voxel (volume element or 3D pixel) reached about 76.5 μm .

In principle, transmitted X-rays penetrate the core sample and are diminished to varying degree depending on the composition and density of the sample material (Cnudde and Boone, 2013). The residual X-ray intensity reaches the detector where it is detected three times per angle and averaged (in total the sample is scanned from 400 angles, Table B – 2).

The reconstruction of a voxel model from the 3D micro-CT scanned images was done with the software Voxel 6.0 (Fraunhofer EZRT/Entwicklungszentrum Röntgentechnik) and is based on a filtered back projection (FBP) according to the FELDKAMP's volumetric cone beam algorithm (Armbrecht et al., 2006). During this procedure the attenuation values are converted to CT-values which are expressed on an internationally standardized scale called HOUNSFIELDS units (HU, Taud et al., 2005):

$$CT = \frac{\mu - \mu_w}{\mu_w} \cdot 1000 \quad (3.34)$$

where μ_w – Attenuation coefficient of water

For calibration, water is defined by 0 HU and air by –1000 HU (Jacobs et al., 1995). Finally, these CT-values are displayed as gray values for each voxel in a series of 16-bit encoded 2D images in X-Y, X-Z and Y-Z direction. The difference between two neighboring image slices equals the resolution of a voxel.

Artifacts, i.e. image errors, due to the arrangement during the measuring procedure could not be found in the CT images.

Image processing and pore object identification

Materials absorb X-rays to different extents because of variations in their densities (Landis and Keane, 2010). Different values in the CT-image can therefore distinguish between salt matrix and air-filled pores within the core sample. For instance, salt with high density is imaged in white whereas air filled pores appear black (see chapter 4.1.1, Figure 27). The spatial resolution of the CT-images is determined by the voxel size. A voxel is the smallest detectable 3-dimensional unit with an edge length (in this study) of 76.5 μm . The voxel size in turn defines the resolution of the border between pore objects and the salt matrix.

The identification of pores in the salt samples and the calculation of the total or effective porosity require several steps of image processing which was done with the software MAVI 1.4.0 (Modular Algorithms for Volume Images, created by Fraunhofer Institute for Industrial Mathematics ITWM, 2006). These steps of image processing will be described in the following.

a. Cropping

The original 3D CT-image also includes the surroundings of the actual core sample which do not belong to the “real” pore space inside the salt core and therefore had to be removed by cropping. Hence, a square body was defined from the 3D image which completely comprised of the inner part of the cylindrical shaped salt core.

b. Filtering

A linear low-pass filter (Weighted Mean Filter 2) was applied to the CT-images in order to remove random noise or outliers for better pore object identification.

c. Segmentation and binning

The most challenging step in image processing is the differentiation (segmentation) between foreground and background of an image which corresponds to the definition of salt matrix and pore space. During binning the gray-scale image is transformed into a 1-bit image representing two phases: salt matrix in white (solid phase) and pore space in black. For this, a threshold has to be set to define which values belong to the pore space and which one to the salt matrix.

Usually, in geological practice the segmentation of CT images is done by a thresholding technique which applies a **visually interpreted threshold**. The user defines whether a pixel with a certain value belongs to the pore space or the background (matrix). Uncertainties exist in the classification of voxels having values close to the threshold level or by the partial volume effect. This effect is caused by voxels that contain a mixture of multiple gray values which occur at the pores boundary or corresponds to pore objects smaller than the voxel resolution (sub-voxel pores) (Vergés et al., 2011). As a consequence, different results emerge from the application of this visual interpreted threshold technique to the same data leading to an uncertainty of the porosity measurement (Taud et al., 2005, Baveye et al., 2010).

Hence, the computation of the segmentation threshold was done by an automatic thresholding technique according to the **OTSU-method**. Otsu (1979) assumes a bimodal distribution of the voxel intensity histogram (foreground and background values). The global OTSU-algorithm tries to minimize the variance of the values within one class and to maximize the variance of values between the two classes during binning. Mathematical principles are described in detail in Otsu (1979). According to Otsu (1979), after binning, the complement image has to be calculated in order to continue with labeling.

d. Classification by reconstruction (labeling)

Labels are assigned to all pixels which belong to the pore space class. Those pixels which are connected within one component will get the same label. Whether two pixels belong to one component is determined by the selected neighborhood system (26-6-neighborhood system).

e. Analysis of object features

Every pore object of the salt core can now be identified by its label. Via the analysis function, parameters such as volume, surface, diameter and shape factor can be calculated for each pore object (Armbrecht et al., 2006).

3.2.7.2 Method 2: Saturation using 2-octanol

For some salt samples, porosity measurement was realized in the laboratory through the method of saturation as described in Fallico et al. (2010). This method only allows the quantification of open and connected pore space; closed pores cannot be saturated.

However, saturation of the dried core samples was performed with 2-octanol during the flow-through experiments as described in chapter 3.2.2. For that purpose, three-way valves at the top and the bottom of the encapsulated salt cores were closed in order to avoid any leakage of 2-octanol when removing the core setting from the apparatus (compare Figure 20 and Figure 22).

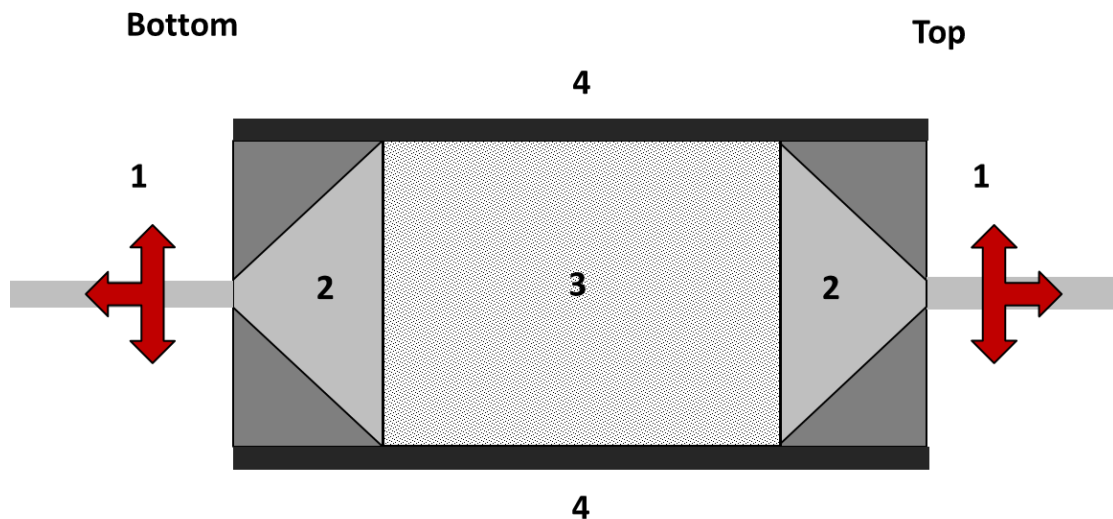


Figure 22: Sketch of the prepared salt core sample (3) encapsulated in a heat shrink tube (4) and connected via PE reductions (2) with flexible tubes which can be closed by 3-way valves (1). The inner volume of the PE reductions (2) should not be considered for porosity calculations and therefore has to be removed from the total mass of 2-octanol necessary for complete saturation of the whole setting.

In the classical saturation procedure for porosity determination, samples are treated in a saturation chamber capable of sustaining vacuum in order to avoid air filled pores which could not completely be saturated (e.g. DIN EN 993-1, 1995, Dane and Topp, 2002). However, the application of vacuum was not able in this case because of technical limitations.

Alternatively, saturation was accomplished by vertically streaming the fluid from the bottom to the top of the core in order to press out remaining air from the pore space.

However, it cannot be ruled out that dead-end pore spaces (“Sackporen”) are not completely saturated with 2-octanol due to trapped remaining air.

The dry salt core was weighted in the setting described in Figure 22 (m_{dry}) and again after saturation in the setting (m_{sat}). The mass difference yields the mass of 2-octanol which is necessary to completely saturate the effectively interconnected pores of the salt core sample.

$$m_{octanol} = m_{sat.} - m_{dry} \quad (3.35)$$

where $m_{octanol}$ – Mass of 2-Octanol saturating the open pore space
 $m_{sat.}$ – Mass of the saturated core sample
 m_{dry} – Mass of the dry core sample

$$V_{pores} = \frac{m_{octanol}}{\rho_{octanol}} - V_{res} \quad (3.36)$$

where V_{pores} – Volume of saturated pores
 m_{core} – Mass of the salt core encapsulated in heat shrink tube including PE reductions and flexible tubes with 3-way valves
 m_{sat} – Mass of m_{core} plus mass of 2-octanol for saturation
 $\rho_{octanol}$ – Density of octanol at ambient room temperature during the experiment
 V_{res} – Residual volume of 2-octanol in the PE-reductions and the flexible tubes which does not belong to the actual porosity of the salt core (= 2x25 ml)

Subsequently, the effective porosity was calculated using the cylindrical bulk volume of the core sample (equation 3.36) according to equation 3.37.

$$V_{core} = \pi \cdot r^2 \cdot L \quad (3.37)$$

where V_{core} – Volume of the core sample
 r – Radius of the salt core
 L – Length of the salt core

$$n_{eff} \% = \frac{V_{pores}}{V_{core}} \cdot 100\% \quad (3.38)$$

3.2.7.3 Method 3: Direct measurement – completion method

An alternative method to determine the total porosity of salt core samples was the direct measurement using a dimension and weighing method. For this, the dry weight, the bulk volume as well as the particle density of the salt material is needed.

Initially, salt cores were dried in a drying cabinet at 70°C until the weight loss within the last 100 hours of drying was less than 1% of the initial salt core weight. Afterwards, they were cooled down to room temperature in a desiccator in order to avoid the

reuptake of air humidity by the hygroscopic salt. The resulting weight of the dried salt core is the initial weight for further calculations.

The bulk volume of the porous salt sample was determined by measuring the length and diameter of the cores.

However, due to the mostly irregular shape of the broken planes, the core was reconstructed to an ideal cylindrical body for which it was easier to calculate the volume. For this, the irregular ends of the core sample were encapsulated with Perspex® tubes and modeled with plasticine™ (Figure 23 a+b). Finally, overlapping plasticine was cut with a knife in order to create a geometrically flat surface. The length of the total core, including plasticine extensions, was measured afterwards (Figure 23 c+d).

Now, the weight of the used plasticine was determined from the mass difference between the pure core sample and the core sample including the plasticine extensions. Thus, the complement volume to the salt core was calculated using the plasticine's bulk density. In turn, the bulk density of the plasticine could be determined via its weight and its volume which was measured using an "Excellence Dichte-Waage" from Mettler Toledo.

$$V_{\text{cylinder}} = \pi \cdot r^2 \cdot L \quad (3.39)$$

where V – Volume of the core cylinder
 r – Radius of the core cylinder
 L – Length of the completed core

$$m_{\text{cylinder}} = m_{\text{dry salt}} + m_{\text{plasticine}} \quad (3.40)$$

$$V_{\text{plasticine}} = \frac{m_{\text{plasticine}}}{\rho_{\text{plasticine}}} \quad (3.41)$$

$$V_{\text{core}} = V_{\text{cylinder}} - V_{\text{plasticine}} \quad (3.42)$$

$$V_{\text{salt}} = \frac{m_{\text{dry salt}}}{\rho_{\text{dry salt}}} \quad (3.43)$$

where $\rho_{\text{dry salt}}$ – Particle density of the pure material (Helium pycnometry)

$$n = \frac{(V_{\text{core}} - V_{\text{salt}})}{V_{\text{core}}} \cdot 100\% \quad (3.44)$$

where n – Total porosity of the salt core [%]

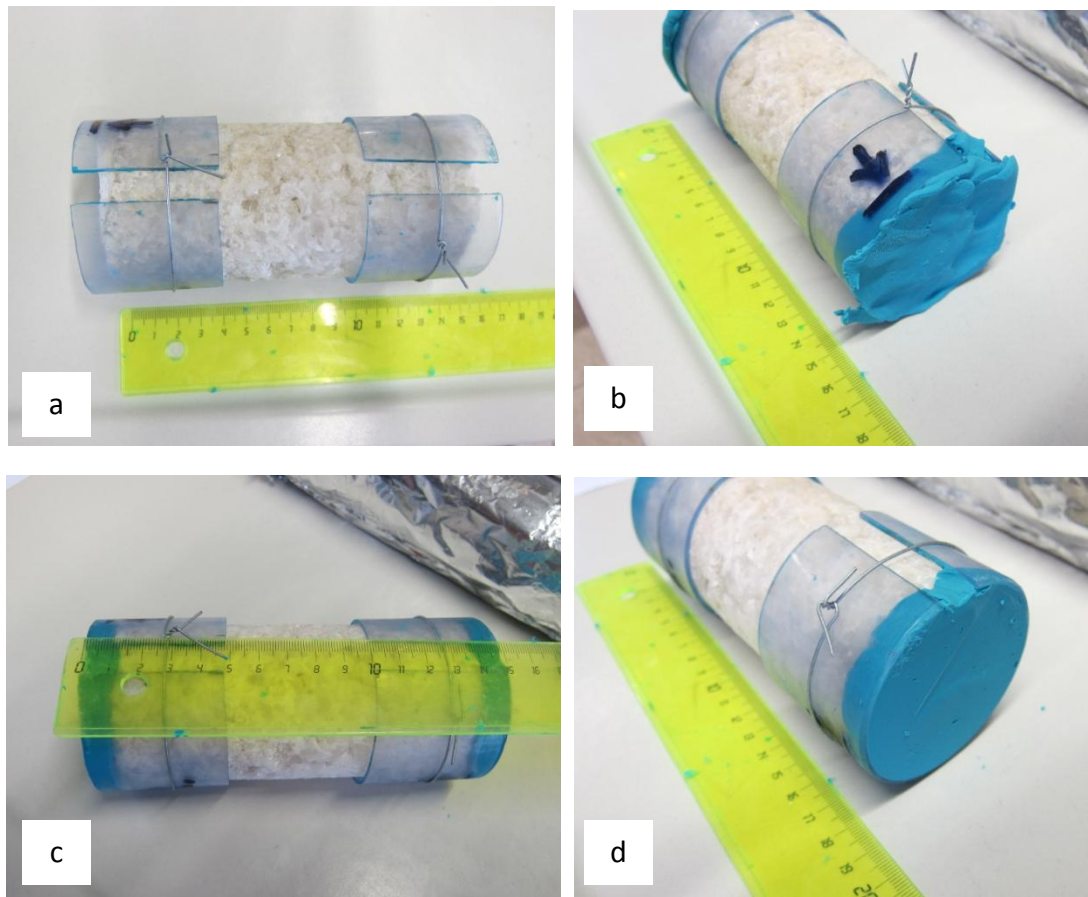


Figure 23: Completion of the cylindrical shape of the salt core in order to determine gravimetrically the total porosity of the core sample.

The particle density of the pure materials without pores (ρ_{salt}) was measured on six selected sediment samples representing the variability of salt appearance and main composition (in the following called master samples) using **helium pycnometry** at the Institute of Drilling Engineering and Fluid Mining (IBF, TUBAF). First, the master samples were crushed and dried at 105°C for 48 hours. Afterwards, measurements of the particle density were accomplished with a multi-volume gas pycnometer with integrated automatic temperature control (Pycnomatic ATC, Porotec GmbH/Thermo Electron Corporation). The average standard deviation of at least 4 measurements was always less than 0.015%.

Subsequently, the particle density of each salt core sample was estimated by visual inspection and comparison of the appearance of each core sample with the measured master samples.

In addition to the procedure described above, the porosity of large salt cores with diameters of 185 mm was calculated from the bulk volume of the salt core (which in turn was calculated from the cylindrical shape of the core) and the total mass of the core as follows:

$$n_{\text{total}} \% = \left(1 - \frac{m_{\text{core}} \rho_{\text{salt}}}{V_{\text{core}}}\right) \cdot 100\% \quad (3.45)$$

where m_{core} – Mass of the dried core
 ρ_{salt} – Particle density of the pure material resulting from helium pycnometry for similar salt samples (with comparable phenotype)
 V_{core} – Calculated bulk volume of the cylindrical shaped salt core

3.3 Data Evaluation

3.3.1 Resource estimation

The total amount of lithium occurring in the Salar de Uyuni was estimated on the basis of lithium concentrations in the brine, the thickness and the porosity of the upper salt crust. The surface area of the salt flat was digitized from a Landsat satellite image downloaded from USGS Earth Explorer¹⁴. Small islets within the salt flat were digitized separately and excluded from the total surface polygon. ArcGIS® 9.3 from ESRI was used as Geo Information System for resource estimation.

3.3.1.1 Map interpolation

a) *Lithium concentration map*

In order to create a 2-dimensional raster map of the lithium concentration in the brine, various interpolation algorithms were tested and compared with each other (Figure A – 7). For instance, the application of the inverse distance weighting algorithm resulted in peculiar circular areas around single data points (compare Figure A – 7, A) which seem not to be realistic.

In contrast, the application of ordinary kriging resulted in the most reliable lithium distribution map. In addition, Scharfmeister (1999) recommends to always apply the kriging algorithm if the most probable value for a certain location is sought. This is the case when creating a map of the lithium distribution in the Salar de Uyuni brine.

For ordinary kriging, the data points should be allocated in different distances so that neighboring points with short distances as well as with greater distances occur in the data set of the investigation area. The spatial distribution of the data locations is important to ease the variogram analysis.

A stationary stochastic process is assumed for kriging and the data must fulfill the requirement of having a normal distribution (Schafmeister, 1999). *SPSS for Windows*¹⁵ was used to check the lithium data for normal distribution using the Shapiro-Wilk test.

¹⁴ USGS Earth Explorer: <http://earthexplorer.usgs.gov/>, accessed on 13-01-2014. Landsat image: 30x30 m, scene recorded in June 2002, 7 bands.

¹⁵ Release 11.0.0, SPSS Inc.

Unfortunately, the data did not have a normal distribution ($N = 76$, $p\text{-value} = 0.001 < \alpha = 0.05$, therefore the null hypothesis that the lithium data are normally distributed has to be rejected). Alternatively, a normal distribution was reached by logarithmic transformation of the data. Therefore, an overestimation of high lithium concentrations can be avoided during interpolation.

Next, the spatial structure of the lithium data was examined by variogram analysis in order to find the best linear unbiased estimator which is useful for the lithium interpolation. The experimental variogram showed that the difference of the lithium concentration between two neighboring sampling locations is low but with increasing distance the difference rapidly increases. Therefore, a spherical semi-variogram model was best suited to fit the empirical variogram. For small distances, the variogram increases linearly and gradually changes into the horizontal sill (Figure 24).

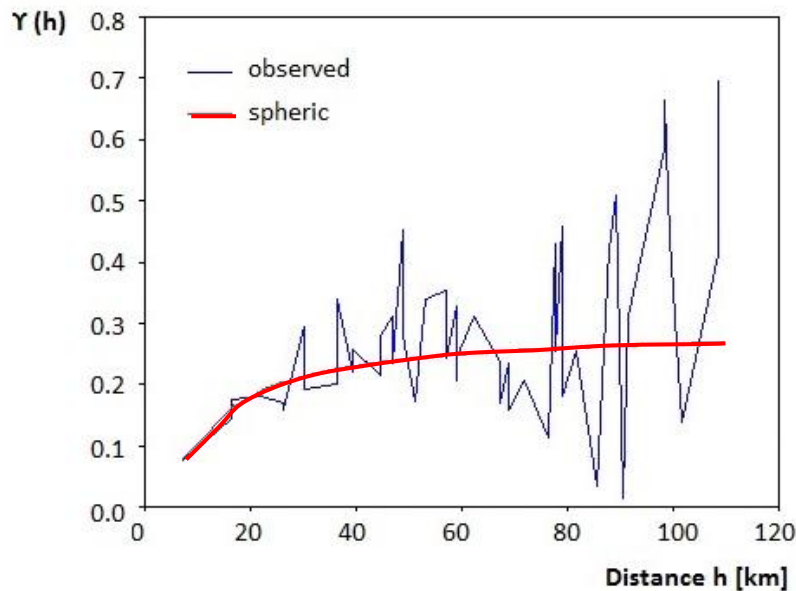


Figure 24: Variogram $\gamma(h)$ of the lithium concentrations in the Uyuni brine (blue curve) and the adapted spherical model (red curve): range = 122.5 km, sill = 0.41, nugget = 0.056.

Moreover, the data were checked for **anisotropy effects** by evaluating variograms in different search directions. A weak anisotropy was identified for lithium in the direction of 11.3° which was finally included in the model of the semi-variogram.

The average standard error of prediction with the kriging procedure accounts for 208 mg/L. This is about half of the standard deviation of the real data (STD = 409.9 mg/L).

b) Map of the salt thickness

For creating a map of the salt thickness, an additional boundary condition was assumed. At the salt flat border, the salt thickness tends towards zero. In this case, the kriging procedure would fail because interpolation exceeds the border of the salt flat. Also, kriging requires an autocorrelation of the data depending on their spatial

distance (Akin and Siemes, 1988). Therefore, even if additional data points were defined along the outer border, kriging would not be valid since this requirement would be disturbed.

Hence, interpolation of the salt thickness was performed by using the **discrete smooth interpolation** (DSI) algorithm. DSI is a unique interpolation method based on certain hard and soft mathematical constraints. The algorithm guarantees that the interpolation of a surface is as smooth as possible (Mallet, 2002).

3.3.1.2 Lithium reservoir calculation

When estimating the total mass of lithium occurring in the brine, one needs to compute the total brine volume depending on the porosity of the salt. In ArcMap, z-values of different raster data sets (maps) can be charged with each other pixel by pixel. Having maps of the lithium distribution in the brine and the total salt thickness and assuming a constant average porosity, the total mass of lithium in the Salar de Uyuni can be computed by equation 3.46.

$$Li_{total} = Li \cdot S \cdot n \quad (3.46)$$

where Li – Map of the lithium distribution in the brine [$mg/L = g/m^3$]
 S – Map of the salt thickness of the upper salt layer [m]
 n – Total porosity of the salt layer [-]

The resulting new map shows the distribution of the total lithium amount (Li_{total}) in g/m^2 .

However, in case of changing porosity properties with depth, different layers have to be defined (Figure 25). The lithium reservoir calculation is carried out according to the following steps:

- First, the total brine volume of the salt flat (V_{C1}) will be calculated assuming a homogeneous porosity in all depth (n_1).
- Then, the brine volume of layer B will be calculated with the same porosity (V_{B1} , n_1).
- The brine volume of layer A (V_A) is now obtained from the difference between V_{C1} and V_{B1} .
- Finally, the volume V_{B2} must be re-calculated but now using the real porosity of that layer (n_2).
- Thus, the total brine volume V_{C2} is the sum of V_A and V_{B2} .

In order to determine layer B, some transformations were performed on the salt thickness map. First, the original map of the salt thickness [S] has to be reduced by a certain absolute value x which corresponds to the thickness of the uppermost layer A (equation 3.47, Figure 25). Then, all values in the new map which are less than zero were defined as zero (equation 3.48, Figure 25).

$$[S'] = [S] - x \tag{3.47}$$

$$[S''] = \text{CON}([S'] < 0, 0, [S']) \tag{3.48}$$

where $[S'']$ – Transformed salt map
 $[S]$ – Initial map of the salt thickness
 x – Depth of the upper boundary layer of the respective salt horizon

Figure 25 illustrates the salt map transformation based on a cross-section of a simplified salt flat composed of two different layers.

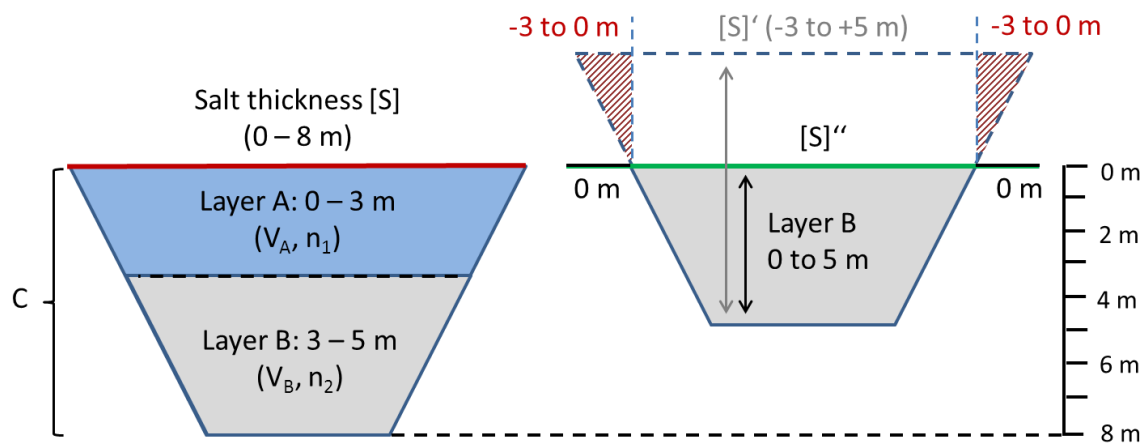


Figure 25: Schematic example illustrating the computation of different salt layers in ArcGIS (the red line symbolizes the initial salt thickness; the red dashed line is an intermediate result after the first transformation step; the green line represents the final salt map of layer B).

3.3.2 Time series analyses

Data records from the long-term monitoring of brine level, brine temperature, atmospheric pressure and air temperature were analyzed using the Tsoft software package, version 2.2.2 (Van Camp and Vauterin, 2005). Spectral analysis of the time-series was performed in the frequency domain using Fast Fourier Transform (FFT). In order to separate long-term from short-term data variations, FFT filters (high-pass and low-pass filters) were applied using different cut-off frequencies. The phase lag between each pair of time-series signals was identified by signal correlation. Furthermore, in order to make a comparison with the measured brine level data, the synthetic earth-tide at the location of the Salar de Uyuni was also computed using Tsoft. Additionally, in order to investigate the temporal changes in the frequency composition of the time-series, series of spectra in a number of time windows were created by moving window spectrum calculation.

In order to investigate the mean daily variation of a parameter, the values of each day-time (in time steps of 10 or 20 min, respectively) for a given observation period were averaged and plotted together with the standard deviation.

4 Results and Interpretation

The hydraulic properties of the Uyuni salt crust were studied using different laboratory methods applied to salt core samples as well as by pumping test evaluation. In order to characterize the total salt porosity, one has to consider the different types of pore objects that might exist in the salt. Based on the equivalent diameter of a pore object, Mays (2007) distinguishes three pores size classes: Nanopores, Micropores and Millipores (Figure 26). Additionally, all pore objects larger than 10 cm are referred to as macropores in the following.

The micro- and the millipores space can be adequately detected and quantified by different laboratory investigations on salt core samples. Since the nanopores only account for a negligible share of the total salt porosity as could be seen from the pore size distribution (chapter 4.1.2), this pore class will no longer be considered in the following.

The results of the porosity determination based on salt core investigations will be used to estimate the total lithium reserves of the Salar de Uyuni. This is presented in the first part of this chapter. Next follows the evaluation of pumping tests in the field, which also capture macropores such as cavities or fractures in the salt. In comparison with results from flow-through experiments, the salt permeability will be studied with emphasis on the brine flow conditions within the salt crust. The last part focuses on the time-series analysis of long-term observations of the brine level and the Rio Grande stream level and their conclusions on the development of the hydraulic properties of the salt crust during the year.

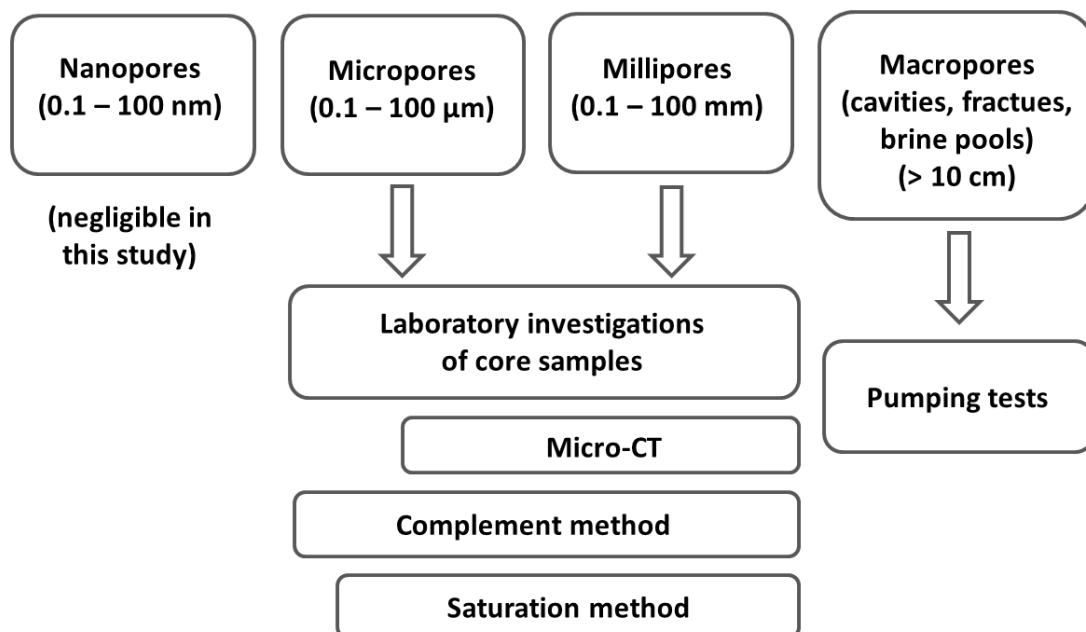


Figure 26: Pore size classification modified after Mays (2007) and applied methods of porosity quantification.

4.1 Porosity determination and lithium reservoir estimation

The porosity of Uyuni's upper salt layer was examined by three different methods: Micro-CT-analyses giving information about the total porosity as well as the pore structure and pore size distribution, direct measurement of the total porosity by the complement method, and a saturation method for obtaining the effective porosity.

4.1.1 Results and discussion of micro-CT analyses

As described in chapter 3.2.7.1 the most challenging step in CT-image processing is the segmentation procedure. While conducting the visually interpreted threshold technique, objects with intermediate gray values occurred in some CT-images of certain core samples which clearly belong neither to the pure salt matrix nor to the air-filled pore space (compare Figure 27). A possible explanation for those objects with intermediate gray values might arise from secondary crystallization in the pore space from the originally dissolved solids. Initially, the solid salt is completely saturated with brine in the natural environment of the salt flat. When extracting the core samples from the bore hole a certain amount of brine can immediately pour out of the samples. A quantification of the amount of lost brine is not possible in retrospect due to its dependence on the pore size characteristic of each core sample.

The formed secondary crystallizations have a lower density compared to the original solid salt matrix, and therefore appear in intermediate gray values in the CT-images (Figure 27). Additionally, they reduce the remaining pore space which will be accessible by the saturation method (chapter 3.2.7.2).

However, a retrospective quantification of the influence of secondary salt precipitation can only be quantified using CT-images.

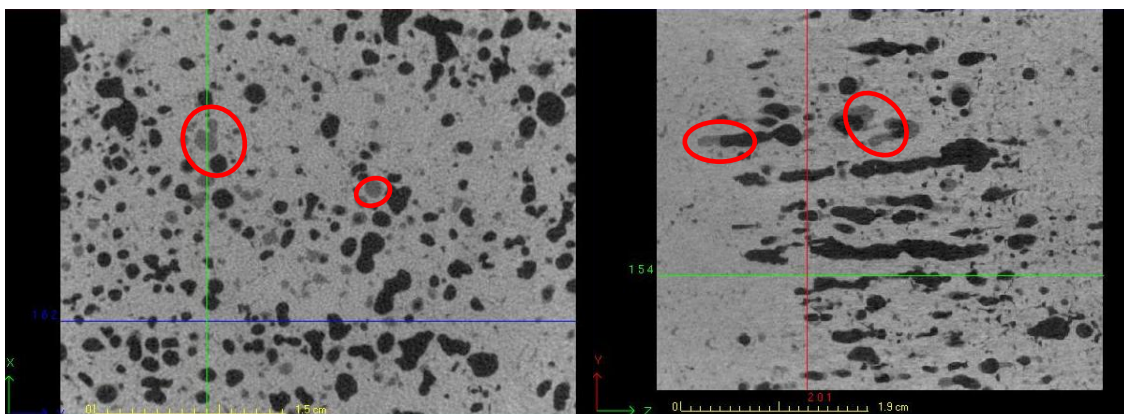


Figure 27: Example of CT-gray scale images of a core sample from the upper part of the crust (08-CEN-A, 1a) in X-Y (horizontal section) and Y-Z direction (vertical section): bright areas indicate solid salt – dark areas depict air-filled pores. Red circles mark examples of those areas with intermediate gray values probably caused by secondary crystallization after drying of the core sample.

Therefore, threshold identification was done in two ways. Once, including intermediate pore objects to the pore space and once excluding those objects from the pore space. Finally, a comparison was done with the results of the Otsu method which is based completely on mathematical algorithms.

For comparison of the different results the root mean squared error (RMSE) was calculated according to equation 4.1 (Lughofer, 2011) in order to avoid the neutralization between positive and negative differences in porosity between one and another method.

$$\text{RMSE} = \sqrt{\frac{1}{N} \sum_{s=1}^N (n_{\text{method 1}} - n_{\text{method 2}})^2} \quad (4.1)$$

where N – Total number of samples
s – Sample-ID according to Table 5
n – Porosity

In case of core sample 8a there are quite large differences between the visually determined porosity considering the voxels with intermediate gray values as real pore objects, and the other two segmentation algorithms (Table 5). The reason for this is a different clipping from the 3D CT-image of the core sample which depends strongly on the user's specifications. It shows the strong inhomogeneity of the sample material and the necessity to select exactly the same clipping in order to make any comparison. Therefore, the differences of core sample 8a are not included in the calculation of the mean or RMSE values in Table 5.

The overall average proportion of those pore objects with intermediate gray values accounts for about 5.9% of the total porosity considering black and intermediate gray voxels (Table 5). Although, the Otsu algorithm does not consider any differences between intermediate gray values or clear white or black values, the automatic segmentation procedure yields quite low differences with regard to the visual determined threshold technique including all gray pore objects (Figure 28). This means that with a root mean square error of 1.8% we can use the OTSU results as real porosity values also including those pores with secondary mineralization or intermediate CT-values.

4. Results and Interpretation

Table 5: Comparison of porosity results arising from different segmentation techniques: visually interpreted threshold technique (a) including intermediate CT gray values and (b) excluding those values, (c) Otsu segmentation algorithm. (*values in brackets are not considered in the calculations of median and RMSE (for further explanations see text above))

Sample-ID	$n_{\text{visual, without interm.}} [\%]$ (1)	$n_{\text{visual+intermed.}} [\%]$ (2)	$n_{\text{OTSU}} [\%]$ (3)	$\Delta[(2) - (1)] [\%]$	$\Delta[(3) - (2)] [\%]$	$\Delta[(3) - (1)] [\%]$
1a	10.15	17.87	17.00	7.7	-0.9	6.9
1b	32.29	37.33	34.48	5.0	-2.9	2.2
8a	7.04	(17.08)*	7.96	(10.04)*	(-9.12)*	0.9
10b	7.83	11.82	10.63	4.0	-1.2	2.8
12b	2.79	8.05	5.96	5.3	-2.1	3.2
15b	6.88	14.73	14.54	7.9	-0.2	7.7
22a	3.29	9.41	8.80	6.1	-0.6	5.5
25b	3.38	10.46	9.47	7.1	-1.0	6.1
29b	2.42	5.56	5.50	3.1	-0.1	3.1
INC-crust	24.72	33.23	30.49	8.5	-2.7	5.8
03-INC-K2	15.24	19.93	16.93	4.7	-3.0	1.7
			<i>Number</i>	10	10	11
			<i>Mean [%]</i>	5.9	-1.5	4.2
			<i>RMSE [%]</i>	6.2	1.8	4.7

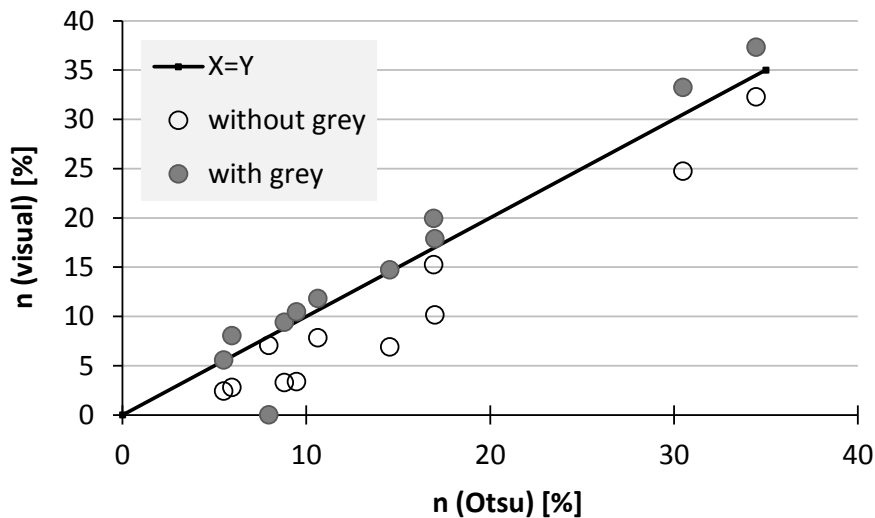


Figure 28: Comparison of the porosity determined by the Otsu algorithm and visual thresholding technique (gray circles indicate porosity values including voxels with secondary crystallization, uncolored circles do not consider voxels with intermediate gray values i.e. secondary crystallization)

In conclusion, the pore object identification according to the mathematical Otsu algorithm assigns voxel objects with intermediate gray values to the pore space. Secondary crystallizations from residual brine after recovery of the drilling cores do not significantly influence the results of porosity determination.

Obviously, a mathematical difference in the gray-value distribution occurs which can be used to clearly separate pore objects from the salt matrix within the Otsu algorithm, even if a visual distinction is not clear.

Consequently, due to its reproducibility and reliability, the Otsu algorithm forms the base of the following results.

Table 6 shows the final results of the total and effective porosity obtained with micro X-ray computed tomography for 11 studied samples from 08-CEN and 03-INC. Total porosity values range between 5.5% and 34.5% (N = 11, STD = 9.67%). For most of the samples, the proportion of connected pore objects indicating the effective porosity accounts for more than 50%, partly between 83 - 98% of the total porosity. Only one sample (08-CEN_29b) shows a very low effective porosity of 0.6% which is only 12% of the total porosity. The effective porosity is considered to be the volume of the largest pore object identified by the labeling algorithm or even those pore objects which are similar in size to the largest one.

Figure 29 shows that the highest porosities were detected within the uppermost part of the salt crust (0.2 – 2.0 m depth). With increasing depth, the porosity seems to decrease (Figure 29). However, partial large cavities of several cm in size occur in core samples from greater depth (surrounded by dense halite, Figure 30-b).

Table 6: Results of micro-CT-analysis of selected core samples (segmentation algorithm according to Otsu (1979)).

Sample-ID	depth [m]	V _{sample} [cm ³]	V _{salt/background} [cm ³]	V _{pore} space [cm ³]	V _{conn. pores} [cm ³]	n _{total} [%]	n _{eff} [%]
08-CEN_1a	0.1	79.1	65.7	13.4	7.5	17.0	9.5
08-CEN_1b	0.4	113.2	74.2	39.0	38.0	34.5	33.6
08-CEN_8a	2.8	114.1	105.0	9.1	2.7	8.0	2.3
08-CEN_10b	3.5	113.1	101.1	12.0	11.2	10.6	9.9
08-CEN_12b	4.6	115.8	108.9	6.9	4.3	6.0	3.7
08-CEN_15b	5.7	92.6	79.2	13.5	13.2	14.5	14.2
08-CEN_22a	7.7	113.8	103.8	10.0	8.3	8.8	7.3
08-CEN_25b	8.6	105.3	95.3	10.0	8.5	9.5	8.1
08-CEN_29b	10.5	38.2	36.1	2.1	0.2	5.5	0.6
03-INC_crust	0.25	100.1	69.6	30.5	29.8	30.5	29.7
03-INC_K2, 2.7-3.7	3.00	114.2	94.9	19.3	17.8	16.9	15.6

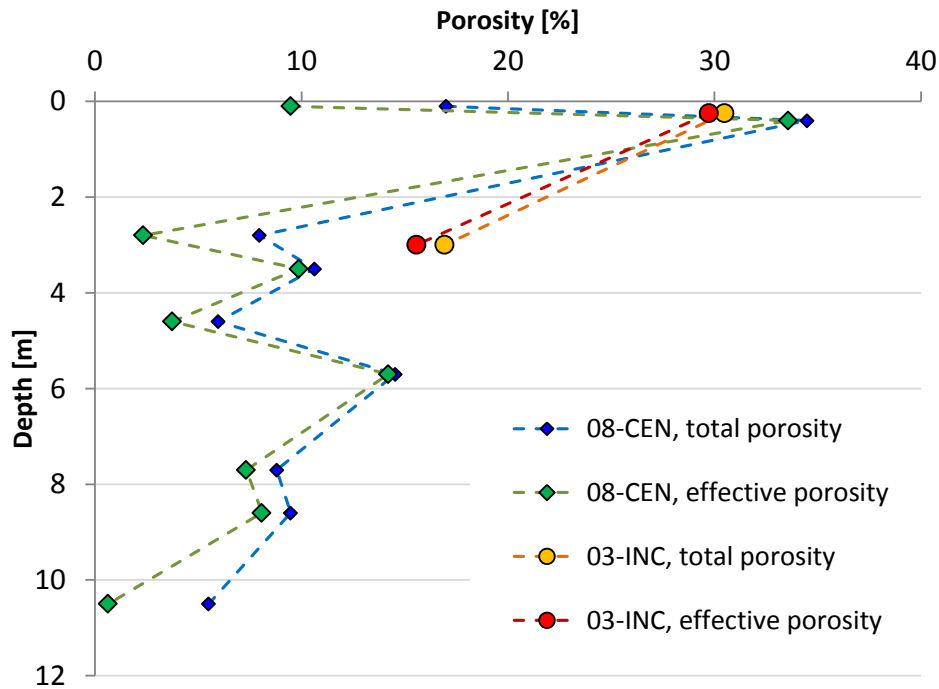


Figure 29: Porosity distribution with depth for 08-CEN and 03-INC samples arising from X-ray computed tomography analysis (Otsu algorithm).

4.1.2 Pore structure and pore size distribution

When considering the pore structure (morphological features of the pore space), the following types of pore objects have to be distinguished: closed (isolated) pores and open (connected) pores. Some open pores are only open at one side – so called blind pores or dead end pores. Open pores contribute to the brine flow and therefore belong to the effective porosity. When extracting the brine from the salt, even blind pores might be dewatered and therefore contribute to the maximum extractable volume of brine.

The sum of open and closed pores determines the total porosity.

The uppermost part of the salt crust (0.2 – 2.0 m depth) is characterized by a high total porosity and mainly roundish shaped pore objects. Especially between 0 m and 0.3 m depth, pore objects are elongated and vertically orientated (compare Figure 30-a). This is also evidenced by the shape factors calculated by MAVI which indicate prolate shapes for the ordinary pores in most of the core samples (Table 7).

This pore structure might arise from the downward movement of infiltrating water during the rainy season or rising brine due to strong evaporation. This vertical movement of unsaturated fluid leads to partial dissolution of halite in that range. In contrast, the precipitation of salts may also occur in the pore space when evaporation leads to concentration of near-surface brine to oversaturated conditions (Lowenstein and Hardie, 1985).

4. Results and Interpretation

On the contrary, core samples from greater depth show a dense halite matrix with distinct lower total porosity. The pores are usually angular due to the prevailing cubic crystal structure of the halite matrix. Some core samples include very large pore objects or little cavities, respectively. As can be seen in Figure 30-b, those pore objects extend to several cm in size and are bordered by the geometric faces of halite crystals growing into the pore object. This cavity of core sample INC-K2 ranges over the whole length of the sample and accounts for the overall cylindrical pore object character which is indicated by the shape factors (Table 7).

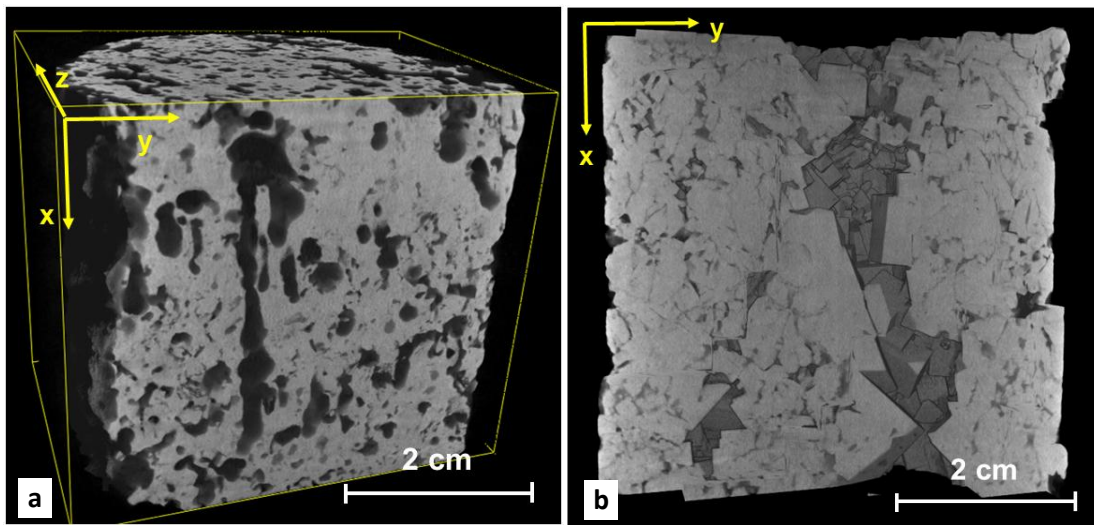


Figure 30: 3D CT-images from core samples from 03-INC from (a) 0.3 m depth (upper crust) and (b) from 3.0 m depth

Table 7: Key figures of pore morphology (mean shape factors (SF) 1, 2 and 3 for all pore objects within the measured core samples, V_{mean} – mean pore volume of all pore objects, N - number of detected pore objects).

Sample ID	SF 1	SF 2	SF 3	Shape	V_{mean} [mm ³]	STD [mm ³]	N
1a	0.91	0.77	0.86	prolate	0.70	54.5	19,105
1b	0.90	0.76	0.84	prolate	3.50	359.6	11,165
8a	0.92	0.79	0.85	prolate	0.86	35.9	10,616
10b	0.87	0.71	0.80	oblate	2.56	163.0	4,690
12b	0.91	0.77	0.84	prolate	0.68	45.8	10,220
15b	0.92	0.80	0.86	prolate	1.49	138.5	9,034
22a	0.91	0.77	0.84	prolate	0.39	51.8	25,904
25b	0.90	0.76	0.83	prolate	0.46	57.8	21,716
29b	0.91	0.79	0.85	prolate	0.32	5.9	6,525
INC-crust	0.89	0.73	0.83	prolate	4.47	360.1	6,826
INC-K2	0.84	0.66	0.77	cylinder	5.42	297.5	3,570

The presence of those well-shaped cubic crystals indicates saturated brine conditions with respect to certain mineral phases. This is confirmed by positive saturation indices of halite, magnesite, calcite and gypsum which were computed for several Uyuni brine samples by PHREEQC modeling using the Pitzer database (Heinrich, 2012). Thus, these mineral phases may crystallize within closed pores to more or less extend until equilibrium conditions are reached between the residual brine phase and the surrounding salt matrix. Beyond that, geochemical modeling in PhreeqC showed, that other typical evaporite minerals such as polyhalite, carnallite, kieserite and sylvite are undersaturated in the brine (Heinrich, 2012). Hence, they remain in solution and the pores do not crystallize completely (Merkel and Planer-Friedrich, 2008).

Small pore objects with mean single pore volumes less than 1 mm³ dominate the pore size distribution with more than 96% of the total pore object frequency in all core samples (Figure 31). Between 9% and 19% of all identified pore objects of the measured core samples are single voxel objects whose size corresponds with the resolution of the CT-image (76.5 μm x 76.5 μm x 76.5 μm = 4.4*10⁻⁴ mm³). Additionally, more than 83% of all pore objects in a salt sample are smaller than 0.1 mm³ (Figure 31). However, their contribution to the total pore volume of the samples is less than 1.1 – 8.8% (Figure 32, Table B – 4).

In contrast, less than 1% of all pore objects of a core sample are larger than 10 mm³ in size. Indeed, they account for 82-98% of the total porosity of most of the core samples (Figure 32, Table B – 4). Therefore, both the total and the effective porosity are predominated by few large pore objects as it is characteristic for instance in sample 08-CEN-8a as shown in Figure 33. Significant differences in the pore size distribution for different core samples occur only with regard to the large pore objects (Figure 31).

A defect analysis was also performed for 08-CEN-8a in order to visualize the pore size distribution in a CT-image. The red areas of the X-Y slice in Figure 33 indicate all pore objects of the 2D image which are interconnected with each other in the 3D space forming the largest pore object of the core sample. All orange regions form the second largest pore object in the 3D image. It is likely that the red and orange pore objects would be connected with each other if another or larger sample body would have been analyzed. In this specific cutting, there is no connection between both large pores either naturally or because available connections are smaller than the voxel resolution of the CT detector and therefore, could not be identified. In any case, the red and orange fields can be interpreted as one connected pore object representing the effective porosity. Blue colors represent the smallest pore objects which are obviously not interconnected with each other in 3D space.

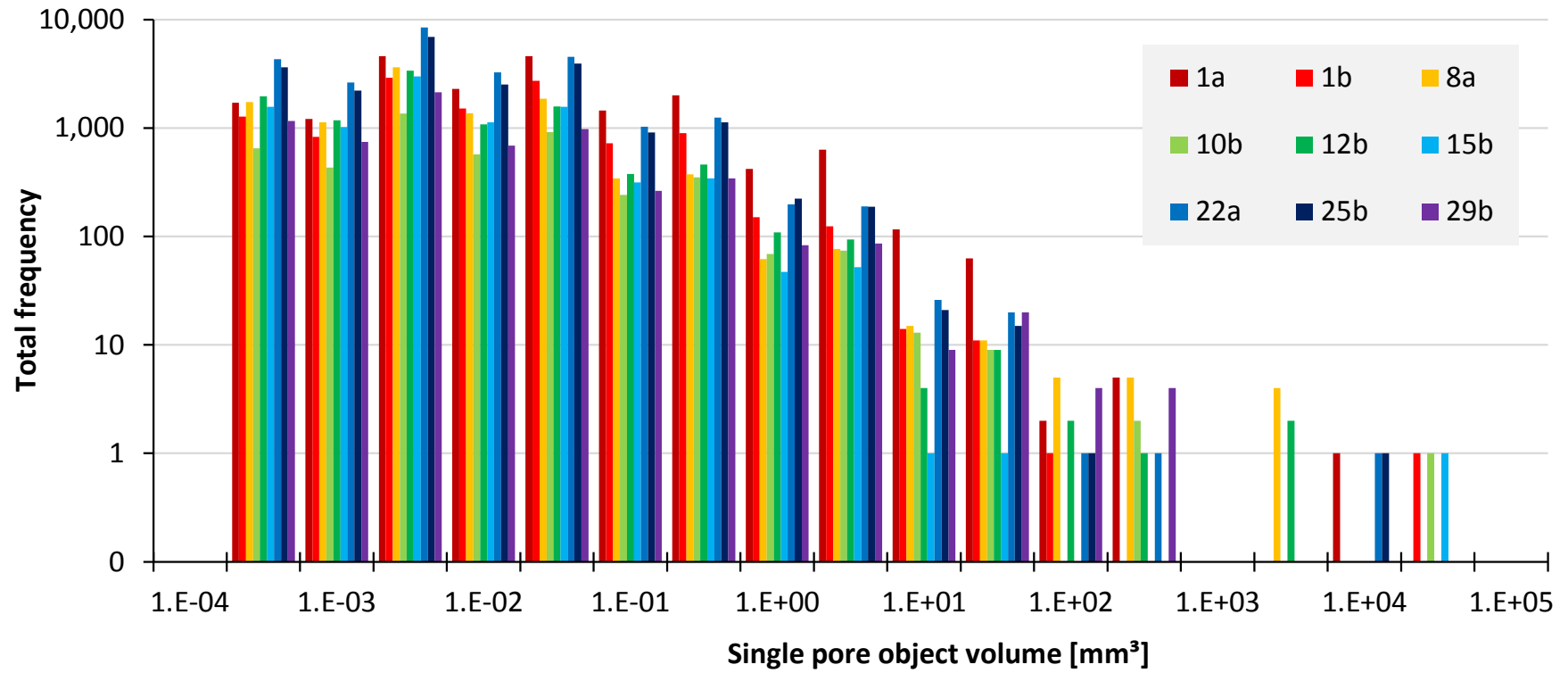


Figure 31: Logarithmic plot of the frequency distribution of single pore object volumes of the core samples from drilling 08-CEN-A (increasing numbers of core sample notations indicate increasing depth of origin).

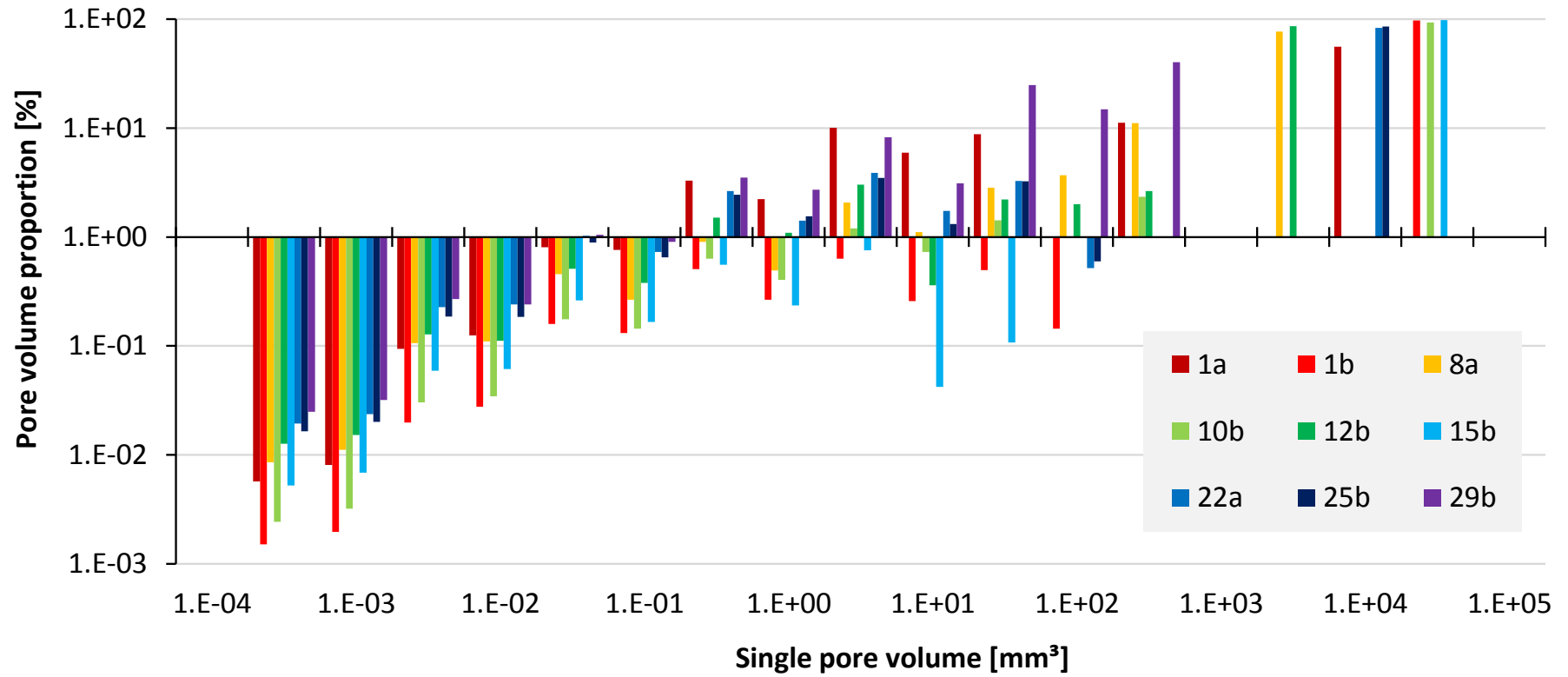


Figure 32: Logarithmic plot of the percentage of each pore size classes on the total pore volume of the samples from drilling 08-CEN-A (increasing numbers of core sample notations indicate increasing depth of origin).

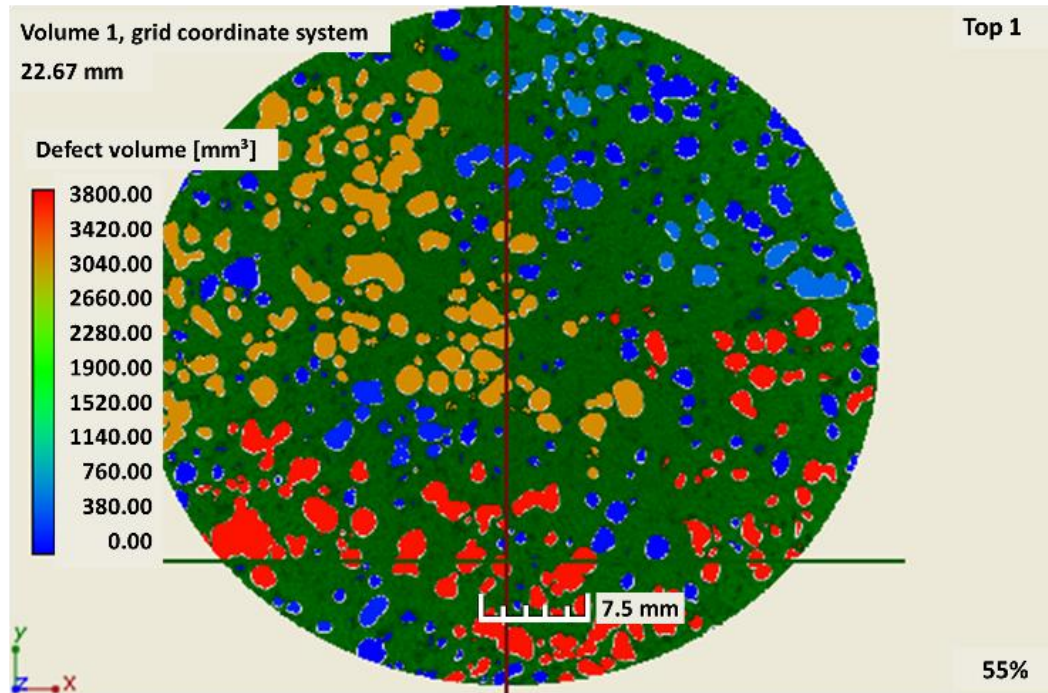


Figure 33: Horizontal representation (in X-Y direction) of a defect analysis of the core sample CEN-08-1a. Defect analysis was done with VGStudio Max. Colors indicate (connected) pore objects according to their total pore volume [mm³]: Red indicates largest single pore object, blue indicates smallest single pore object(s).

4.1.3 Total porosity of salt core samples by direct measurement

The particle density of selected core samples determined by helium pycnometry is shown in Table 8. All core samples which appeared in white do not show large differences from the particle density of pure rock salt (2.1685 g/cm³, DeFoe and Compton, 1925).

Table 8: Particle density of representative salt core samples analyzed by helium pycnometry (*mineral composition was determined by XRD at the BGR in Hannover¹⁶)

No.	Sample-ID	Depth [m]	Material description	Density [g/cm ³]
1	04-INC	3.0 m	dark/black salt	2.440
2	02-LLI-B, 11-2	4.2 m	very hard, dense gypsum* layer (characteristic layer)	2.609
3	07-SAL, 28a-b	7.1 m	white powder of halite and polyhalite*	2.140
4	13-COR, 12	8-9 m	clay mud (black/gray)	2.432
5	07-SAL, 22	6.1 m	pure white halite crumbs	2.160
6	13-COR, 29	4.4 m	dark salt gravel	2.153

¹⁶ Schramm, Michael: Federal Institute of Geosciences and Natural Resources, 30655 Hannover, personal communication from April 4, 2014.

4. Results and Interpretation

However, three of six investigated samples show significantly higher particle densities between 2.4 and 2.6 g/cm³ indicating a different mineralogical composition. These samples appear darker or denser which can be easily distinguished from normal rock salt.

The porosity results for 97 core samples according to the direct measurement under consideration of the particle density of the salt are shown in Figure 34. The distribution pattern is similar to the data previously presented for the effective porosity.

Some core samples from the uppermost 2 m depth could be analyzed only from drilling 09-RIO investigated. Unfortunately, the halite crust at this investigation site ended at a depth of approximately 4 m with a layer of lacustrine mud. Indeed, there are nearly no data points in that range from the other drillings because of the poor state of preservation of the core samples after drilling.

At greater depths (> 2m) no significant decreasing or increasing trend can be observed in the data. However, the total porosity data scatters around a median value of 13.5 ± 3.72% at depths between 2 and 10 m.

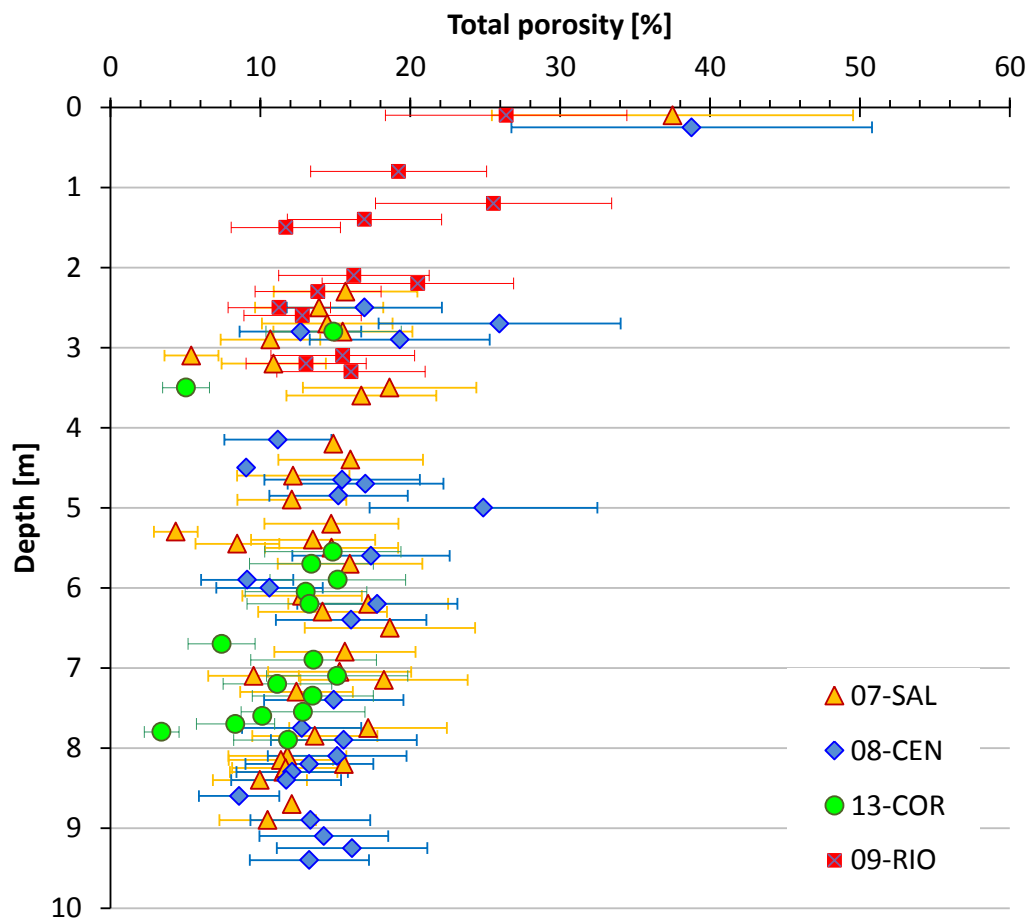


Figure 34: Total porosity determined by direct measurement of core samples from 4 different drilling sites (N = 97 samples).

4.1.4 Effective porosity determination

Saturation experiments using 2-octanol revealed effective porosity values for the core samples from five different drilling sites in the range between $1.6 \pm 0.95\%$ and $25.5 \pm 2.0\%$ (Figure 35). The *relative uncertainty* of the method was on average $\pm 13.7\%$ ($5.8 - 61.1\%$) according to the error propagation calculation after (DIN V ENV 13005, 1999, compare Text C – 3).

- The porosity data of drill 07-SAL show a slightly decreasing logarithmic trend with depth ($r = -0.905$, $\alpha = 0.02$, $R^2 = 0.92$, Figure 35). The highest porosity value was determined for the sample 07-SAL-2a from only 10 cm depth with $25.5 \pm 2.0\%$. Field observations have shown that the uppermost part of the salt crust is in general determined by high porosity. Unfortunately, due to the high porosity and fragility of the salt, most of the core samples were destroyed during the drilling procedure. Thus, only very few core samples from the uppermost 2 m of the salt crust could be recovered from the drilling and analyzed for their porosity (further details about the state of preservation of samples can be found in chapter 4.1.5). Consequently, this apparently decreasing logarithmic trend in porosity should be handled with care!
- In contrast, the effective porosity for the core samples from drill 08-CEN varied between $1.6 \pm 0.95\%$ and $12.9 \pm 1.1\%$ but do not show any systematic trend with depth.

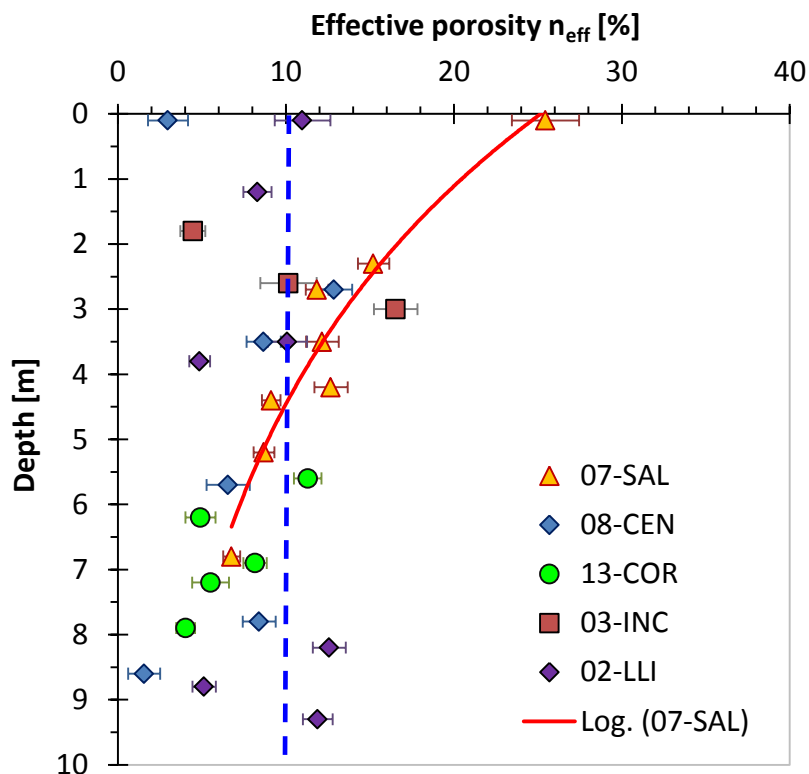


Figure 35: Results of gravimetric porosity determination according to the method of saturation with 2-octanol (N = 29). Red line indicates logarithmic trend line for core samples from 07-SAL, blue dashed line marks the median value of all data.

- At drill site 13-COR, only very few salt core samples mainly from greater depth could be selected for porosity measurements because the majority of core recovery was damaged. The reason might be a relatively high natural porosity of that salt range which makes it impossible to obtain complete core samples.
- At drilling site 03-INC the salt layer only reached a maximum thickness of 4 meters, so there is no data from greater depths. Besides, porosity data might indicate an increasing trend with depth which in turn could indicate preferential flow paths close to the assumed impermeable lacustrine mud layer. However, this hypothesis could not be verified.
- For drilling 02-LLI no data are available between 4 and 8 m depth because of the occurrence of a layer of lacustrine mud sediments which could not be used for the porosity measurement according to the saturation method.

In fact, no clear trend could be identified from the porosity data of all drillings. However, the majority of the data scatter around a median effective porosity of 8.7% with a total standard deviation of $\pm 4.83\%$ (Figure 35, Table B – 5).

4.1.5 Overall porosity distribution of the upper salt crust of Salar de Uyuni

A direct comparison of the methods used for characterizing the salt core porosity is difficult. Only two salt core samples were examined by all three methods, and only a few other samples were studied by at least two different methods. Thus, a systematic comparison with statistical certainty is not possible. However, results of the saturation method are almost lower than those from X-ray tomography or the complement method (Table 9). This is because only the connected pore space can be reached and saturated by the used organic liquid. Furthermore, sack pores containing air cannot be completely saturated because the entrapped air cannot be released.

Differences between the total porosity values from X-ray tomography and the complement method (Table 9) arise from different core segments which were included. Especially, the extracted rectangular block specimen considered in CT data evaluation is much smaller than the entire cylindrical core sample which is considered by the complement method. Therefore, a direct comparison of the results from both methods is not possible and meaningful. Only the statistical comparison of the porosity results of numerous core specimens allows for a methodological comparison.

4. Results and Interpretation

Table 9: Comparison of methods for porosity determination (n.d. – not determined).

Sample-ID	Depth [m]	X-ray tomography	Complement method	Saturation method
		n [%]	n [%]	n _{eff} [%]
1a	0.1	17.0	n.d.	3.0 ± 1.19
1b	0.25	34.5	38.8 ± 1.64	n.d.
8a	2.7	8.0	26.0 ± 1.91	12.9 ± 1.09
10b	3.5	10.6	n.d.	8.7 ± 1.02
12b2	4.5	6.0	9.0	n.d.
15b	5.75	14.5	n.d.	6.6 ± 1.29
22a	7.8	8.8	n.d.	8.4 ± 0.99
25b	8.6	9.5	8.6 ± 3.25	1.6 ± 0.95

However, total and effective porosity data from all three methods together show a common characteristic of the porosity properties of the Uyuni salt flat.

Total porosity data as well as effective porosity data from five drilling sites of the Salar de Uyuni are plotted in Figure 36. Between 2 and 10 m depth, the total porosity scatters quite uniformly around a median value of 13.5% (STD: 3.73%, N = 95).

The uppermost 2 m of the salt crust lacks of data points. This is due to the high core loss during the drilling procedure in that shallow salt horizon.

For pumping test realization, it was necessary to core the first meter using a large drill bit (8 inch or 20 cm in diameter, compare chapter 3.1.3). Fortunately, well preserved core samples could be extracted in this way from 05-TAH and 08-CEN (see Figure 37 for illustration). In accordance with the direct measurement of the porosity, these core samples were also inspected by simply measuring the outer volume and determining the total weight. The resulting total porosity varied between 30 and 39% (compare enlarged symbols in Figure 36).

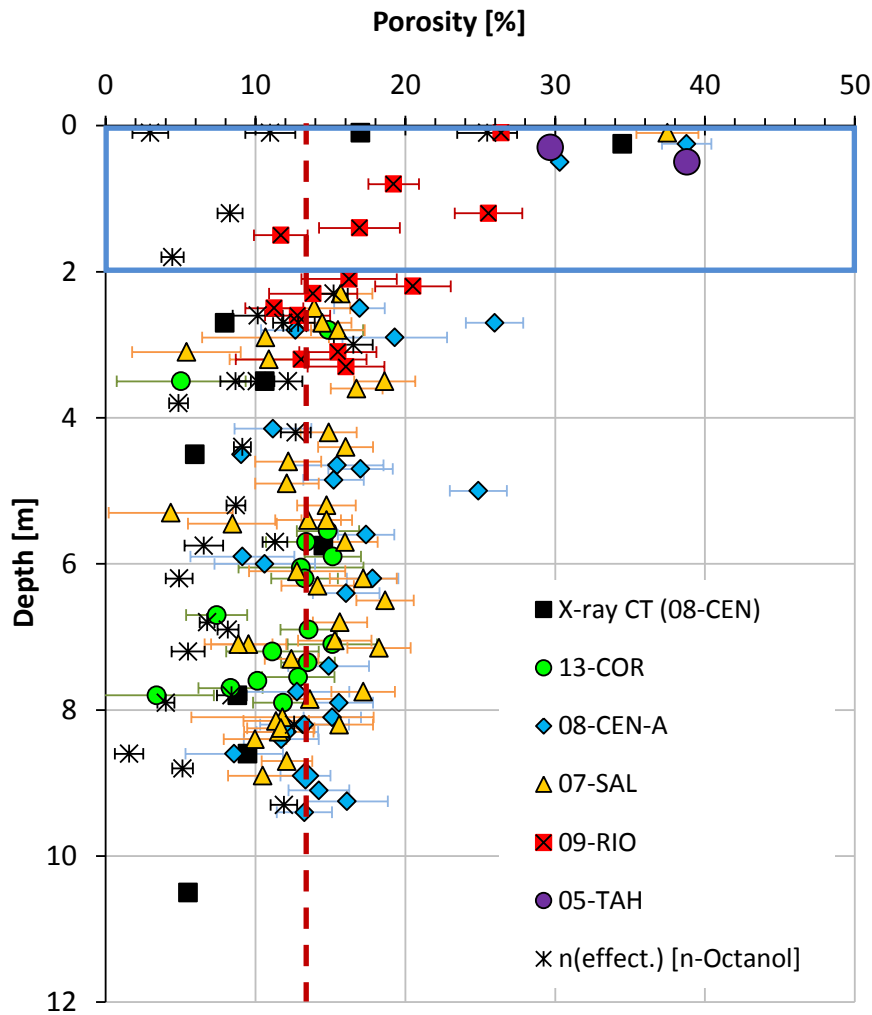


Figure 36: Porosity distribution of the upper salt crust of Salar de Uyuni based on the evaluation of core samples from 5 different drillings using three different methods (CT-analysis, saturation method, direct measurement). Results from the saturation method (using 2-octanol) represent the effective porosity (cross labels) and cannot be compared directly with the total porosity determined by the other two methods. Three enlarged symbols close to the surface mark samples drilled by 8 inch drill bit (20 cm in diameter).

Because the general drilling procedure was done with 3 inch drill bits (7.6 cm in diameter) most of the salt core samples from the highly porous zone (**friable zone**) were not stable and broke apart during the extraction (core loss). Likewise, the pore space could be larger than the core sample size leading to the same artifact of core loss. Figure 37 gives an illustration of the core recovery of two different sized core samples. The same salt horizon is well preserved when using an 8 inch drill core but could not be preserved by 3 inch drilling. Moreover, little cavities or brine pools have been discovered in some sites of the Salar de Uyuni. Here, the friable zone disappears almost completely, as it is shown on the right side of Figure 37. A systematic investigation of the porosity based on core samples is not possible due to core loss.



Figure 37: 3-inch (left) and 8-inch (middle) salt core samples from 0 – 1 m depth of the salt crust at drilling site 08-CEN. The upper approx. 20 cm are very hard and dense without high, visible porosity. Below that part there is a friable zone with very high porosity of approx. 30-40%. Right: Cross-section of the remained crust of a brine pool formed within the friable horizon of the near-surface part of the salt crust.

For that reason it can be supposed that the overall total porosity of the uppermost at least 2 m of the salt flat is higher than 30-40%.

Considering data in the literature, Risacher and Fritz (1991) assumed an average porosity for the whole salt crust of the Salar de Uyuni between 30 and 40% based on hard samples (20-30%) as well as the friable layer (40-50%). Unfortunately, no information is given about the methodology of porosity determination they used. Later on Fornari et al. (2001) describe the stratigraphy of Salar de Uyuni with (lacustrine) mud layers characterized by porosity between 30 and 50% and a salt crust having lower porosity between 15 and 30%.

In comparison, Ovejero Toledo et al. (2009) determined porosity values between 5% and 40% for the Salar de Rincon in Argentina from pumping test evaluation (storage coefficient). For the central part they actually found porosities >30%, but also lower than 10% for parts in the very east of the salt flat. Considering intergranular cavities as well as the presence of dissolution cavities, they assumed an overall porosity of 20% in order to calculate the total lithium volume in the Salar de Rincon.

Lowenstein and Hardie (1985) dealt with the recognition of halite pan deposits by specific petrographic features which were formed by different processes during the stages of the saline pan cycle. In this context they reported that a crystalline halite layer rich in druses will form with a porosity of up to 50% due to dissolution. This process certainly also occurs at Salar de Uyuni especially during the rainy season when almost the complete surface is flooded by rain and runoff water from the catchment area.

In contrast to the surface halite horizon of the salt crust of Uyuni the porosity is characterized by a marked decrease with depth (Figure 36). Casas and Lowenstein (1989) observed in different Quaternary salt pans world-wide that the porosity at depth of 10 m is usually <10%. Moreover, they found tightly cemented layers at depth of 45 m showing nearly no visible porosity anymore.

In case of the massive salt of the Salar de Atacama the porosity distribution is characterized by 30% at 0-0.5 m depths, 20% at 0.5-2 m depths, 15% at 2-25 m depths and less than 10% at >25 m depths. With increasing depths to about 35-40 m the porosity rapidly decreases to nearly zero. The overall average porosity is estimated to be about 18% for the upper 25 m of the salt crust (Garrett, 2004).

Post-depositional diagenetic cementation by clear halite is given by Baar (1977) as a possible explanation for the observed porosity loss. When pore-filling brine is exposed to day-night temperature changes the solubility of certain salt or mineral phases changes. So, salt which is deposited at night can be dissolved during the day and recrystallize again at night. This process leads to a cementation of the pore-space as described for seawater-type deposits in basins less than 6 m deep. With the additional normal packing-effect triggered by the deposition of later deposited salts and sediments, the porosity progressively decreases with depth (Baar, 1977).

According to Garrett (1970) cited in Baar (1977) a typical example of porosity values might be: "40% initially, 30% when under 15 cm of salt, 20% under 30 cm of salt, 15–20% under 60 cm of salt, 5–10% under 6–12 m of salt, and then gradually to nearly zero with deeper covering." This is in agreement with the porosity distribution with depth in Quaternary salt-deposits as illustrated in Figure 38.

In conclusion, the porosity of the Salar de Uyuni might be caused by similar processes as given in the literature. The uppermost highly porous zone might be formed by dissolution processes due to the infiltration of rain water, especially during the rainy season between December and March when the salt flat is almost completely flooded by rain and runoff water from the catchment area.

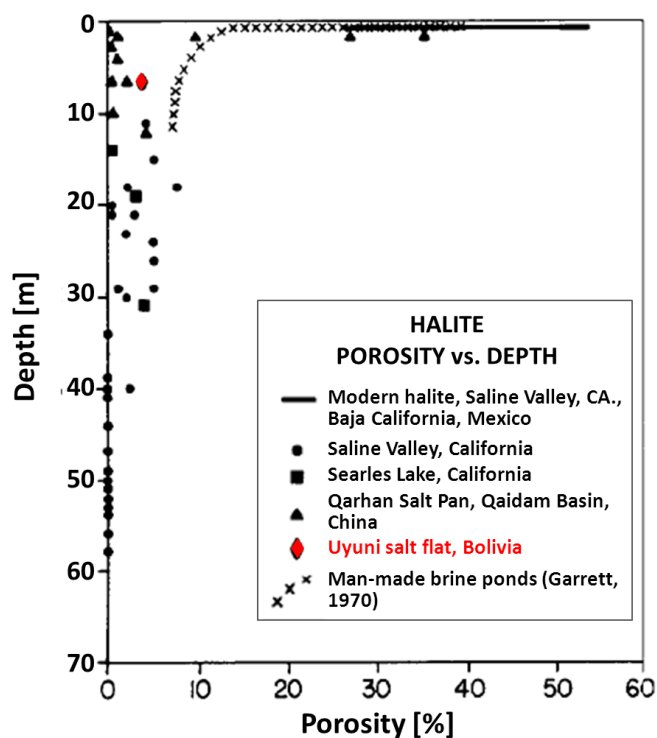


Figure 38: Porosity distribution with depth in Quaternary salt-deposits (Casas and Lowenstein, 1989): The porosity of the salt crust of Uyuni is given by <10% at a depth of 6 m (marked in red).

4.1.6 Lithium reservoir estimation

4.1.6.1 *Lithium distribution in the brine*

Between 2009 and 2012 several brine samples were taken from different depth of each investigation site. Since no clear depth-dependent differences in the lithium concentrations could be found, the results of each site were averaged for further considerations. Additionally, high-resolution sampling along different transects in the northeastern part of the salt flat was conducted in 2012.

Lithium concentrations varied between 200 mg/L up to about 1,500 mg/L (see Table B – 7). The lithium distribution pattern is similar to that published by Risacher and Fritz (1991), although absolute differences between certain sampling points are in part high. Percentage deviations between our data and those from Risacher and Fritz (1991) ranged between -36% (CEN) and +86% (YON). Some reasons for these differences include the distance between actual sampling locations of the literature and this study (approx. 4-5 km), differences in sampling techniques and preservation, analytical uncertainty (accuracy of ICP-MS analyses: $\pm 10\%$) and probably natural changes in brine geochemical composition over a time period of more than 30 years.

Nevertheless, the data show similar bias for separate locations of the salt flat (Figure 39).

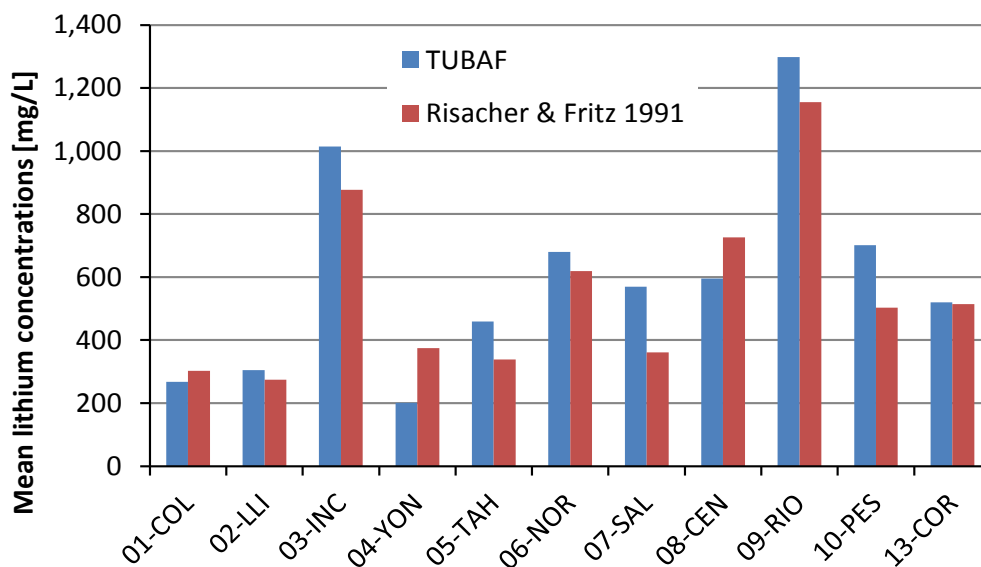


Figure 39: Comparison of lithium concentrations according to TUBAF and Risacher and Fritz (1991) for proximal sampling locations.

However, an important lithium anomaly exists in the very south of the salt flat, close to the main Rio Grande de Lipez tributary. Another high-concentration lithium anomaly occurs in the very northern part of the salt flat, close to the pampa next to *Serrania Intersalar* which separates the Salar de Coipasa from the Salar de Uyuni. The highest lithium concentrations in the brine of Salar de Coipasa were found in the southeastern part of the salt flat (Lebrun et al., 2002) which might be interconnected with Uyuni salt flat via an ephemeral stream (Quebrada Negrojahuira, Wolf, 2010) that is easily observed on satellite images (Figure 40).

To the west of the salar, the concentrations decrease systematically. Figure 41 illustrates the similarity of the lithium distribution pattern obtained by kriging interpolation of our data from sampling locations marked with red dots and previously published lithium iso-concentration patterns according to Risacher and Fritz (1991). Small differences in detail arise from different data point densities.

Due to the confirmation of the general lithium distribution pattern in the brine of the upper salt crust as already described by Risacher and Fritz (1991), data from our investigations as well as from the literature have been matched together in order to create an enhanced map of the lithium distribution (Figure 42). This final lithium distribution map forms the base for the later on lithium reservoir estimation.

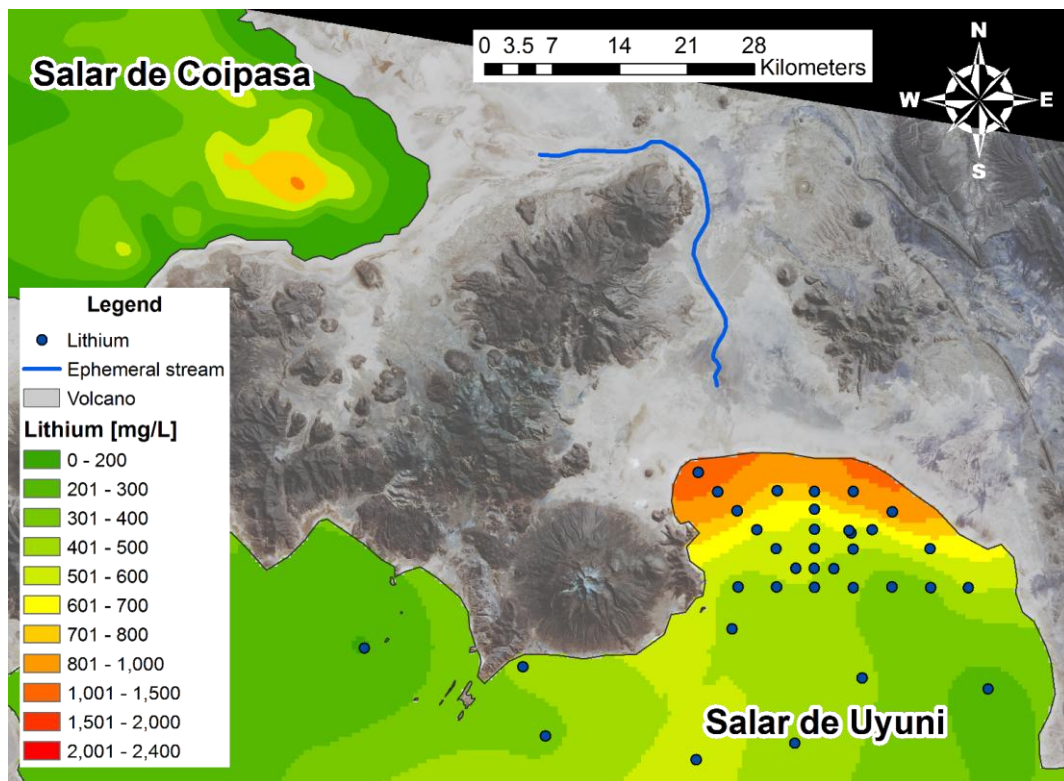


Figure 40: Landsat TM satellite image (channel 1, 2, 3) showing the dry river bed through the pampas east of the “Intersalar”. Map of lithium iso-concentrations of the Salar de Coipasa as taken from Lebrun (2002), colored map of the Salar de Uyuni illustrates lithium distribution in the brine.

4. Results and Interpretation

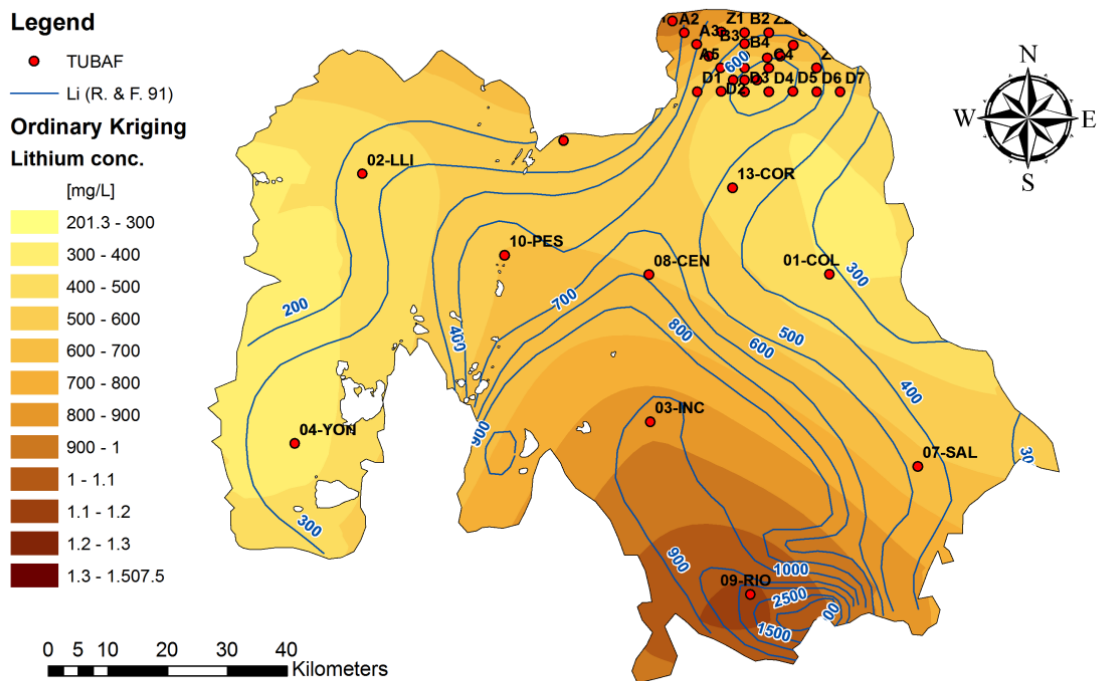


Figure 41: Lithium distribution map obtained by interpolation of lithium concentration data from own investigations (TUBAF) using ordinary kriging with spherical semi-variogram. For comparison, lithium iso-concentration lines published by Risacher and Fritz (1991) are shown.

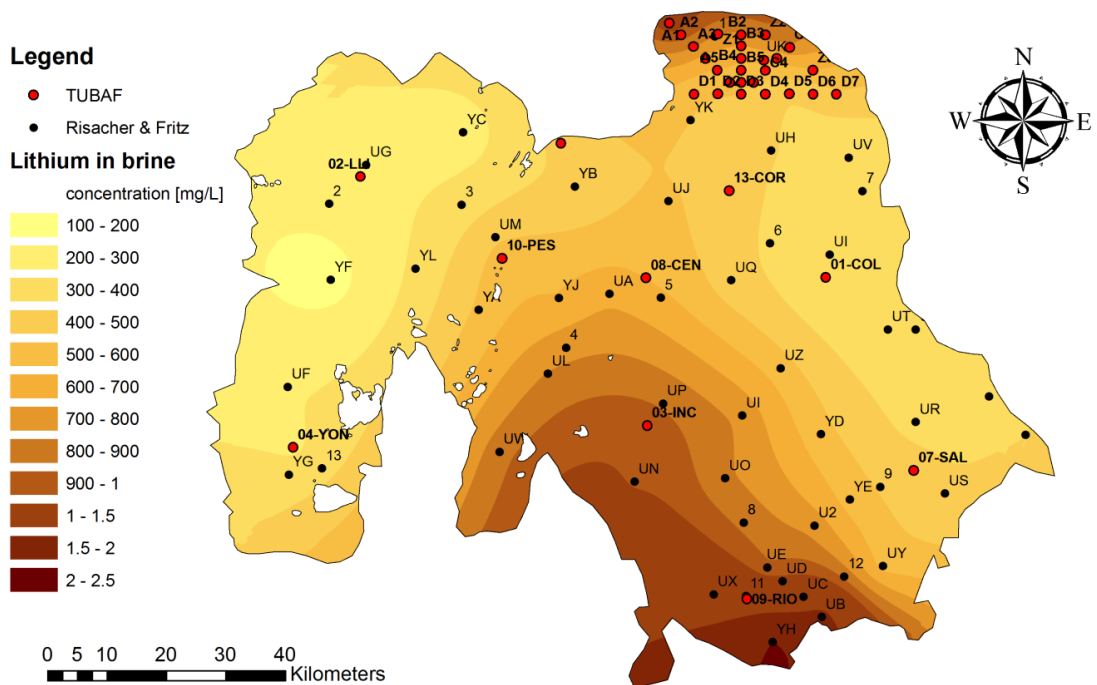


Figure 42: Lithium distribution map created by ordinary kriging with spherical semi-variogram based on logarithmic transformed lithium concentration data from TUBAF and Risacher and Fritz (1991) with consideration of anisotropy effect in direction of 11.3°. The average standard error of prediction accounts for 208.1 mg/L.

4.1.6.2 *Stratigraphy of the Salar de Uyuni*

A general stratigraphic description of exploration drill cores from Salar de Uyuni is given in Sieland et al. (2011). The upper salt crust is thickest in the central part at drilling site 08-CEN with approx. 9.5 m. Toward the borders of the salt flat, the thickness of the salt layer slightly decreases. The halite layer is underlain by a several meter thick layer of dark clayey mud which was formed during the last lacustrine phase of the evaporitic basin (Fornari et al., 2001, Fritz et al., 2004).

A second halite layer could only be reached and sampled during the drilling procedure at site 02-LLI. Both salt layers are separated by a nearly 4 m thick layer of lacustrine clay sediments.

In general, the uppermost one to three meters of the salt were characterized by extremely high porosity. The salt is crumbly and does not show well shaped cubic halite crystals but roundly shaped salt conglomerates. Consequently, the core recovery during the drilling was mostly low because of the fragility of the highly porous salt.

Beyond, a more dense and compact salt layer followed which sporadically contained small cavities of several centimeters in size within the salt core samples.

In some drillings, a particular hard and compact stratigraphic layer was found which was really difficult to drill with the drilling machine. This layer has a thickness of only 2-4 cm and is characterized by alternating foliation of whitish and dark sediment (Figure 43). XRD analysis of three selected samples yielded gypsum as the main constituent (Table 10, Figure A – 4 to A – 6).

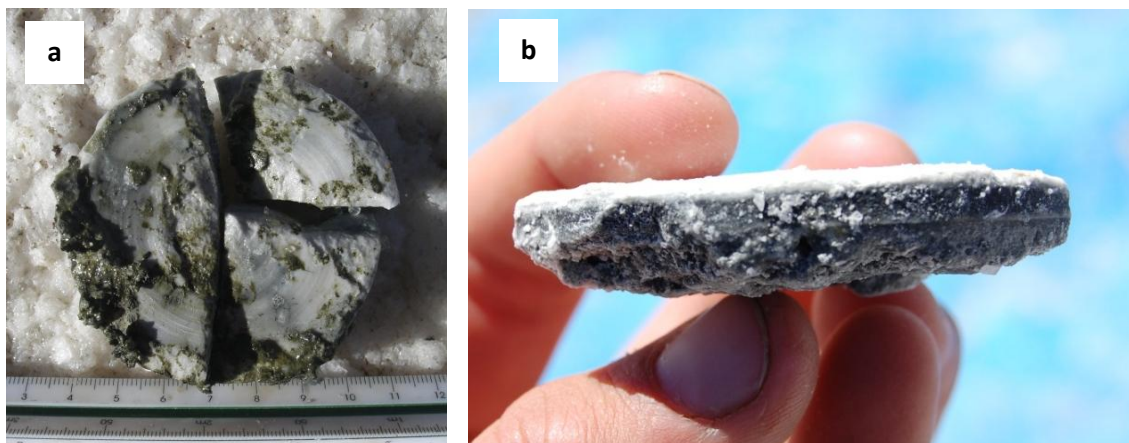


Figure 43: Thin, hard gypsum layer found in different drillings at different depth. Examples here are from (a) 09-RIO-A (3 m depth) and (b) 08-CEN-D (7 m depth).

4. Results and Interpretation

Indications of this characteristic stratigraphic layer could be found at different depths (values in brackets) at the following drilling sites:

- 02-LLI-A+B (4 m and 8 m)
- 08-CEN-A (6.5 m directly above clayey mud layer; in 10.2 m depth below 0.5 m of clay/mud layer)
- CEN-D (7 m)
- 10-PES (4.5 m)
- 09-Rio (3 m)
- TAH-A (~4.3 m)

Table 10: Mineral composition of selected sediment samples determined by XRD analysis.

Sample-ID	Depth [m]	Major and minor mineral phases	Traces
02-LLI-B, 9b	3.8	Gypsum	Halite
02-LLI-B, 11/2	4.0	Bassanite*	±Calcite?
08-CEN-A, 29c	10.2	Gypsum	Halite, ±Calcite?

**Bassanite is a conversion product of gypsum which was formed by drying the sample at 105°C for 24 hours in order to also use this sample for particle density determination by helium pycnometry.*

This stratigraphic level may indicate certain climatic conditions or a hydrological situation of the Uyuni salt flat which promoted the formation of gypsum.

At 09-RIO drilling site close to the delta of the Rio Grande main tributary in the south of the salt flat, brownish fluviatile sediments were found beneath a 20 cm thick surface salt layer. Figure 44 shows the stratigraphy of the Uyuni salt flat in different drillings. Drill profiles are arranged in north to south and west to east direction, respectively.

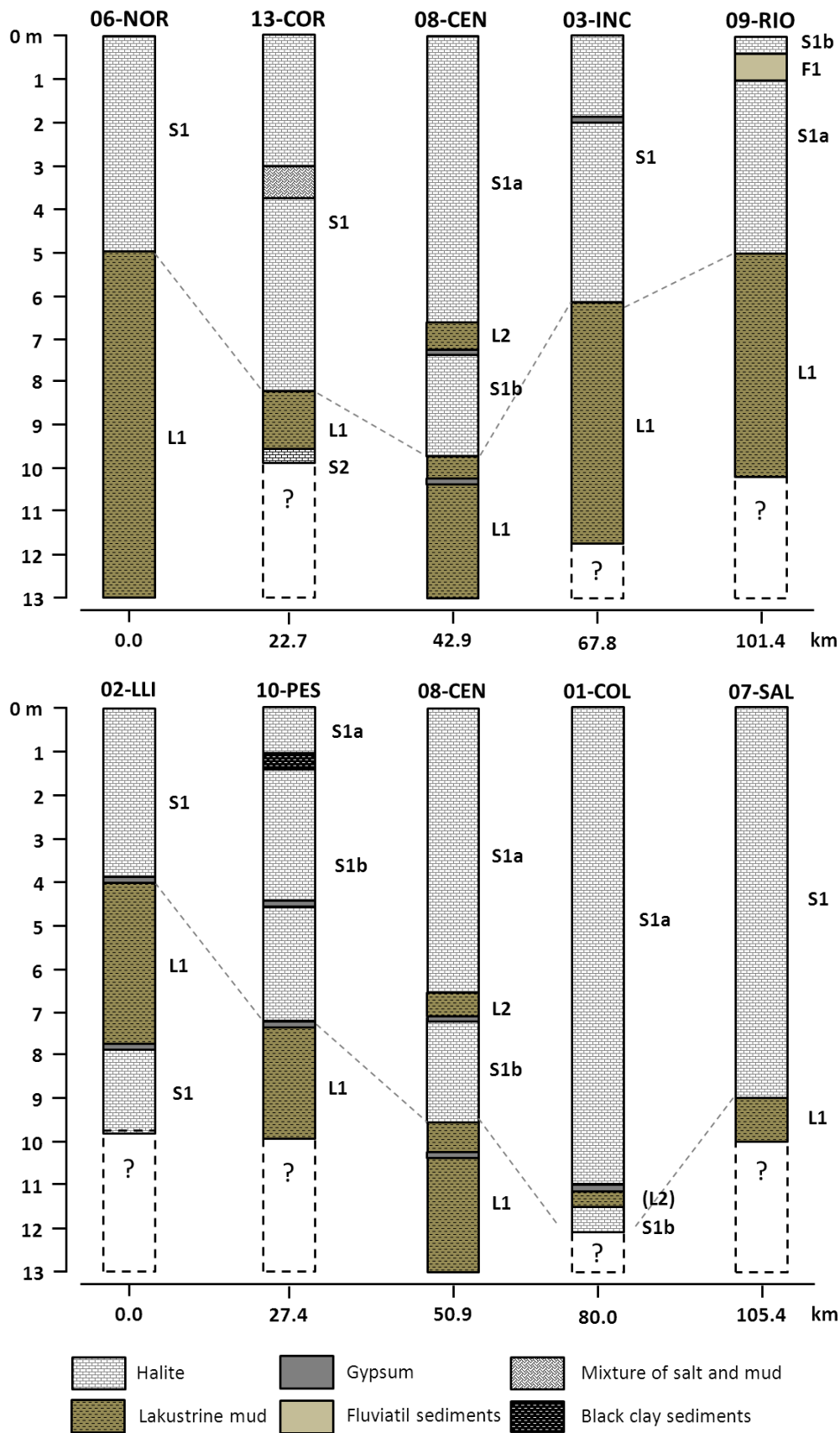


Figure 44: Drilling profiles showing the general stratigraphy of the Uyuni salt flat down to a depth of 13 meters from north to south (top) and from east to west (bottom). The label “S” indicates salt layers, while the label “L” marks lacustrine sediments. The drilling sites on the salt flat are mapped in chapter 3.1.1, Figure 10.

In order to create a continuous map of the salt thickness from the drilling data, additional information about the salt thickness from literature was used. Data were interpolated in goCad using the discrete smooth interpolation algorithm (DSI).¹⁷ The interpolation map of the salt thickness is used later on for the computation of the total lithium resources of the Uyuni salt flat.

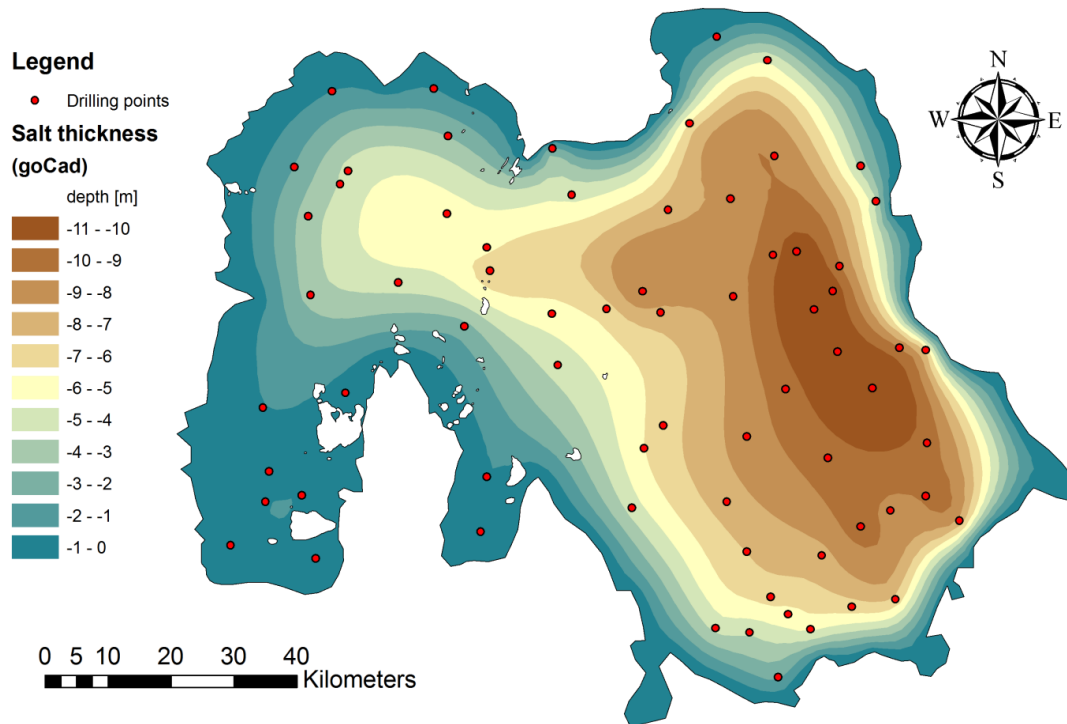


Figure 45: Salt thickness of the upper salt layer of Salar de Uyuni interpolated from own data, data from Risacher and Fritz (1991) as well as additional node points along the border.

4.1.6.3 Computation of total lithium sources

In order to calculate the total amount of lithium occurring in the brine of the Salar de Uyuni the following input parameters are necessary:

- Map of the lithium distribution in the brine (Figure 42) based on chemical data from this study (samples were taken between 2009 and 2012) and data from literature (Risacher and Fritz, 1991)
- Map of the thickness of the upper salt layer (Figure 45) based on stratigraphic data from own exploration drillings as well as from literature data (Risacher and Fritz, 1991)
- Total porosity distribution of the upper salt layer (Figure 36)

¹⁷ DSI interpolation in goCad was done by Dr. Görz, Ines: Institute of Geophysics and Geoinformatics, TUBAF, 09599 Freiberg, personal communication from January 15, 2014.

4. Results and Interpretation

As a result of the porosity distribution a two-layer model was developed. The upper two meters of the salt flat are thought to be characterized by an average porosity of 35% in accordance with previous assumptions by Risacher and Fritz (1991). The deeper part of the salt crust, from 2 m depth down to the base of the salt layer (maximum depth is around 11 meters), have shown porosity values ranging around a median value of 13.5% (N = 95 measurements).

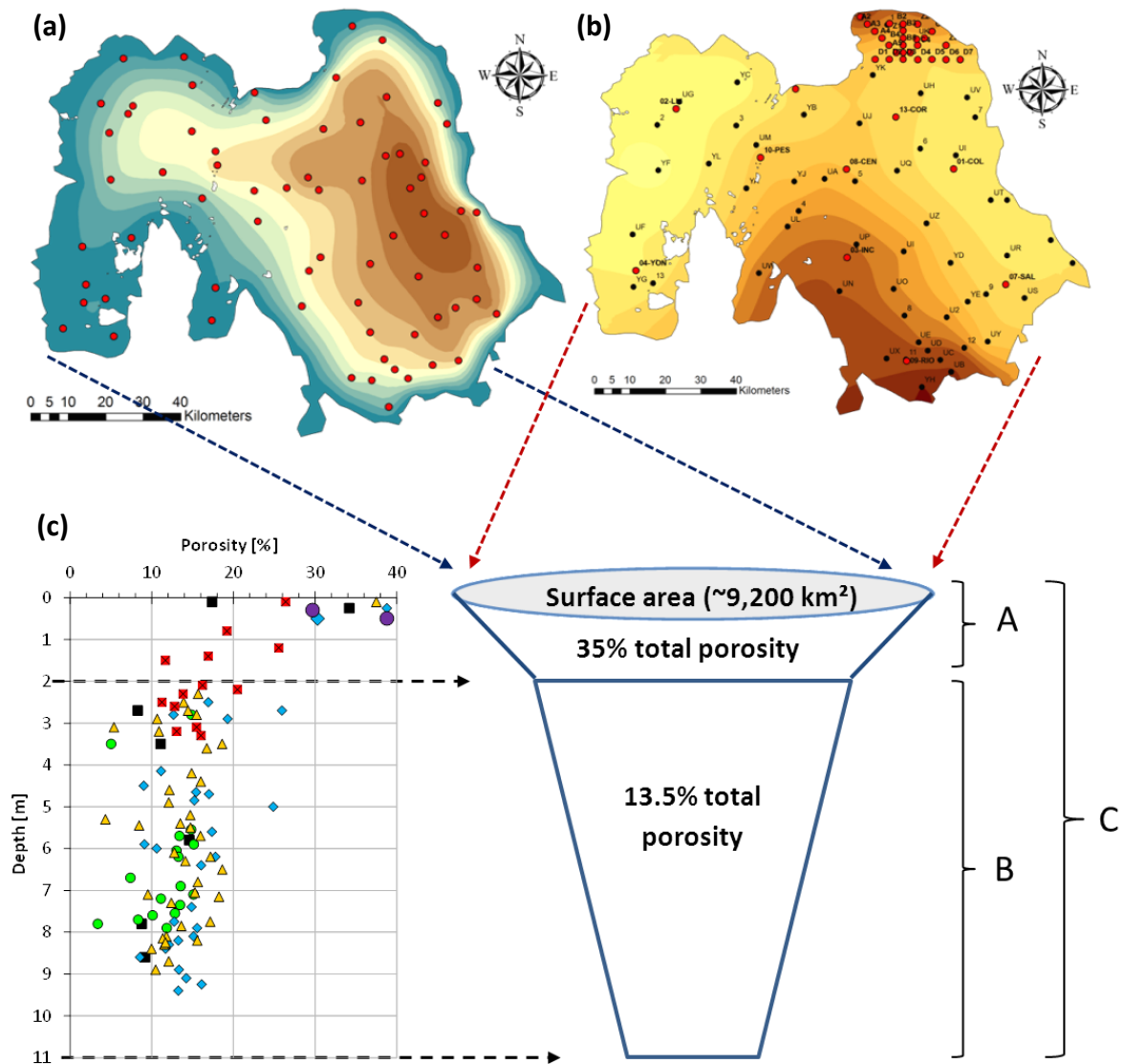


Figure 46: Model for the lithium-reservoir estimation at the Salar de Uyuni. Input data for lithium reservoir estimation in ArcMap 9.3: (a) Map of the thickness of the upper salt layer, (b) map of lithium distribution in the brine, and (c) porosity distribution with depth. Database for all maps are own investigation results and literature data from Risacher and Fritz (1991).

The computation of the total lithium amount in the entire Salar de Uyuni was carried out according to the procedure described in chapter 3.3.1.2 (Table 11).

Table 11: Results of lithium-reservoir calculations in ArcGIS® for separate layers of the model.

Layer	Properties	Li _{total} [t]
surface	Area = 9,221,311,164 m ²	
C1	0 – 11 m, 35% porosity	13,524,823
B1	2 – 11 m, 35% porosity	10,637,374
A	A = C - B	2,887,449
B2	2 – 11 m, 13.5% porosity	4,102,988
C2 (final)	C2 = A + B2	6,990,437

The reliability of the lithium estimation depends on the uncertainty of the input parameters for which following error limits are assumed:

- Laboratory analysis of lithium concentrations in the brine and interpolation by kriging: The mean error between measured and predicted lithium concentrations accounts for ±12.7%.
- Determination of the salt thickness: ±0.2 m
- Determination of the salt porosity: ±0.025% (mean absolute error of porosity determination based on error propagation estimation, Text C – 4)

Based on equation 3.46 (chapter 3.3.1.2) the total error can be estimated according to DIN V ENV 13005 (1999) to about ±15.7% (see Text C-5 for details).

Thus, the total lithium reserves in the upper salt layer of Salar de Uyuni accounts for approx. **7.0 ± 1.1 million tons** in total. This is significantly lower than previously estimated by USGS (2014) and Gruber et al. (2011) with 9 million and 10.2 million tons of lithium, respectively.

Thereby, the largest quantities are limited to a relatively small area in the southern part of the Uyuni salt flat close to the delta of the Rio Grande de Lipez (Figure 47).

However, even in deeper halite layers, lithium might occur in higher concentrations. Unfortunately there is no data available concerning the porosity of these deeper salt layers and the lithium concentrations of the brine from that depth. Thus, all of the data presented in this study relates only to the uppermost salt layer with a thickness of up to 11 m.

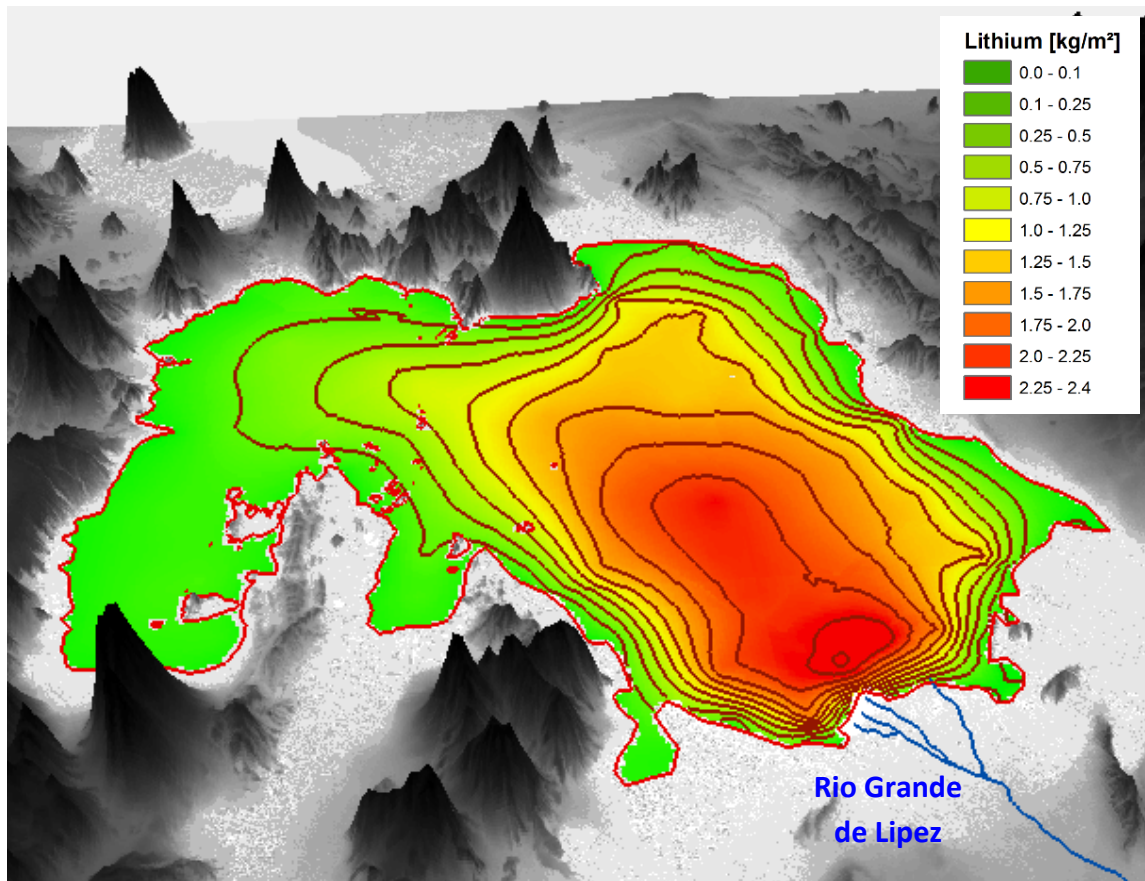


Figure 47: 3-dimensional visualization of the Uyuni basin (excessive representation) showing the distribution of the lithium reserves in the brine within the upper salt layer in kg/m².

4.2 Permeability and flow conditions within the salt crust

4.2.1 Physical properties of the brine

Density and viscosity are important parameters of the brine which have to be considered in the evaluation of the intrinsic permeability of the salt crust. Both parameters depend strongly on temperature and mineralization. Therefore, density and viscosity were determined for different brine samples in the laboratory. Moreover, field measurements of the temperature distribution with depth were conducted at different sites.

4.2.1.1 Temperature profiles

Brine temperature profiles were measured in different wells in November 2010 and December 2012 during the Bolivian spring season. The near-surface brine temperatures ranged between 12° and 15°C (Figure 48). This can be explained by the higher mean daily air temperatures in spring (10° to 12°C) in comparison to the mean annual air temperature of about 7.7°C. Furthermore, even higher temperature conditions occur during daytime when intense solar radiation heats up the salt surface and thus the near-surface brine.

In all wells, a temperature decrease with depth could be observed (Figure 48). The maximum brine temperature differences between surface and depth ranged between 3.0 K and 6.9 K for the sites 10-PES and 07-SAL, respectively. Indeed, in 02-LLI-B and 07-SAL a reversal point could be detected in a depth of 3.5 m and 6 m, respectively. At greater depth, the brine temperatures slightly increased again (Figure 48). The depth of the temperature minimum is related to the total thickness of the salt crust at the particular site. The thicker the salt crust, the deeper the temperature minimum occurs. The reason for this temperature phenomenon could be the annual air temperature fluctuation on the salt surface. The temperature minimum in the brine temperature profile might arise from the last winter period (June – July) when the average air temperature reached its annual minimum around 2.0°C (average monthly air temperature between 2001 and 2011, Table B – 3). The maximum average air temperatures occur between January and February with 12°C. Thus, the annual mean air temperature variation accounts for about 10 K between summer and winter which is more or less muted in the brine temperature profiles.

Another possible explanation for the temperature increase in greater depth of the profiles 02-LLI-B and 07-SAL could be related to a geothermal heat source beneath the salt flat. Already in September 1976, Ericksen et al. (1977) measured brine temperatures in the interior of the Uyuni salt flat. They found average temperature of 5° – 6°C for near-surface brine which corresponds to the mean air temperature in September. However, abnormally high temperatures of 9° – 12°C were detected in brine pools in the eastern part of the salt flat. They suspected, that these higher

temperatures could be the result of inflowing thermal spring water coming from beneath the salt crust.

However, due to the lack of deeper temperature measurements in this study, no clear indications could be found to support this hypothesis.

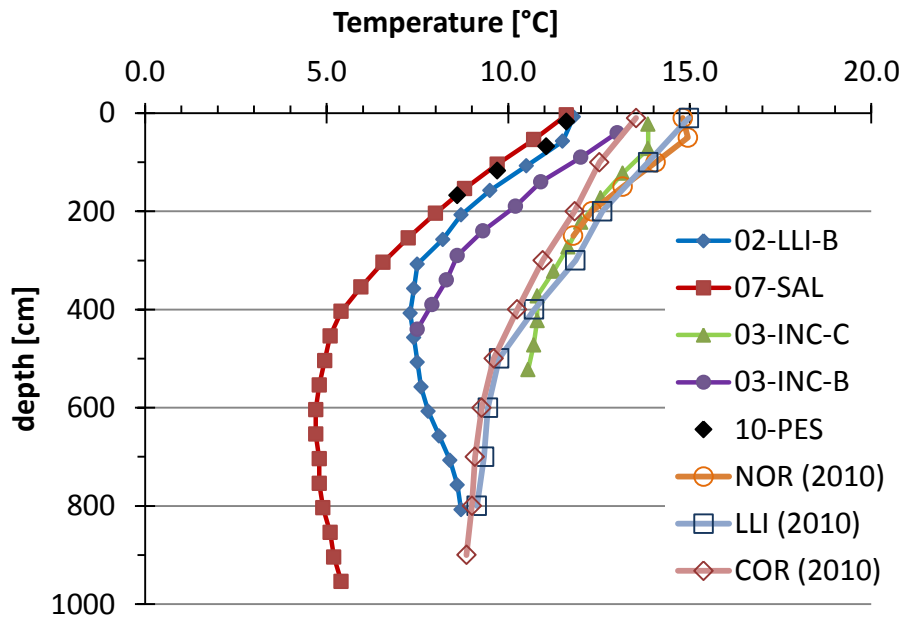


Figure 48: Temperature profiles in five different wells (measurements were performed at different times: Solid symbols indicate temperature profiles measured in December 2012 using a GMH 3350 temperature measuring device, empty symbols arise from measurements in November 2010 using a CeraDiver®).

4.2.1.2 Density of Uyuni brines

The brine density varied between 1,204 and 1,229 kg/m³ at 25°C (Table B – 9). There is a decreasing trend in density for brine samples from the south-east to north-west of the salt flat reflecting different chemical compositions and mineralizations (Figure 49). Samples from 01-COL and 06-NOR deviate strongly from the general trend because of their boundary location in the northern or eastern part of the Salar de Uyuni. As already noted, the lithium distribution has a slight anisotropy effect at 11.3° (compare chapter 3.3.1.1). This effect might be caused by two main inflow sources: Rio Grande de Lipez in the south as well as the Quebrada Intersalar which seems to be a connection between Salar de Uyuni and Coipasa in the north (compare chapter 4.1.6.1, Figure 40). Both regions are characterized by water covering for most of the year (even in the high season of dryness).

Samples from 10-PES showed the highest density in addition to those from 09-RIO. Local inhabitants reported that the area around the islet of Pescado is the first part of the salt flat which dries up after the rainy season. Therefore, it is possible that the salt crust is very hard and compact and has the highest salt enrichment due to evaporation.

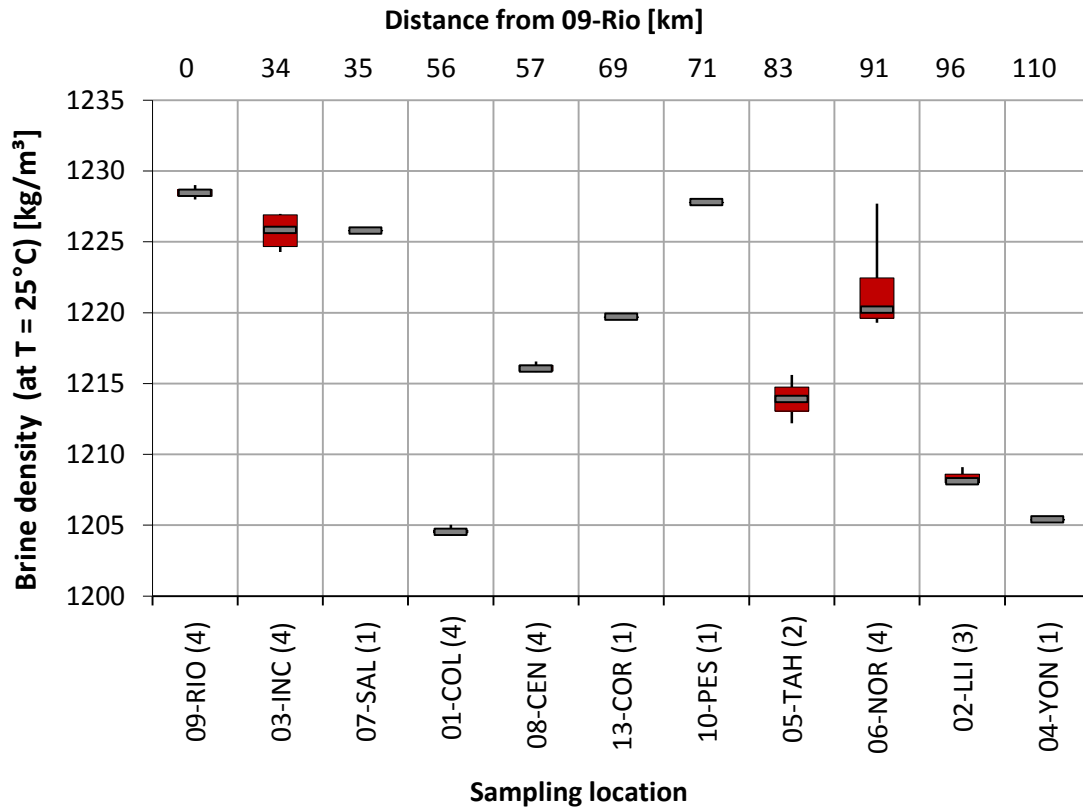


Figure 49: Box plots of brine sample density measurements from different locations at 25°C temperature condition (numbers in brackets indicate the number of data represented by each box blot). Samples are arranged in increasing distance from site 09-Rio (secondary horizontal axis).

4.2.1.3 Viscosity of Uyuni brines

As described in chapter 3.2.1 the viscosity of brine samples was determined for at least two different temperatures in the range between 15 and 22°C in order to consider the temperature dependency of the viscosity. However, due to technical limitations it was not possible to perform viscosity measurements at temperatures lower than 15°C. The stirring water bath for the experiments only consists of a heating device. The only way to cool the samples below room temperature was by adjusting the tap water flow which in turn had a minimum temperature of ~12°C. Higher temperatures were not tested because they were not representative of the field temperature conditions.

The resulting dynamic viscosity dependence on temperature of the Uyuni brine samples is shown in Figure 50 (original measurement values are given in Table B – 10). For comparison, literature data for standard salt solutions are added. The lower three blue curves indicate different concentrations of pure NaCl solutions (data taken from Kestin et al., 1981). The upper orange curve indicates a standard salt solution which consists of 4.59 moles Cl, 2.2 moles Na, 1.01 moles Ca, as well as minor amounts of K, Li, Mg and Sr (Holldorf and Baumbach, 1987).

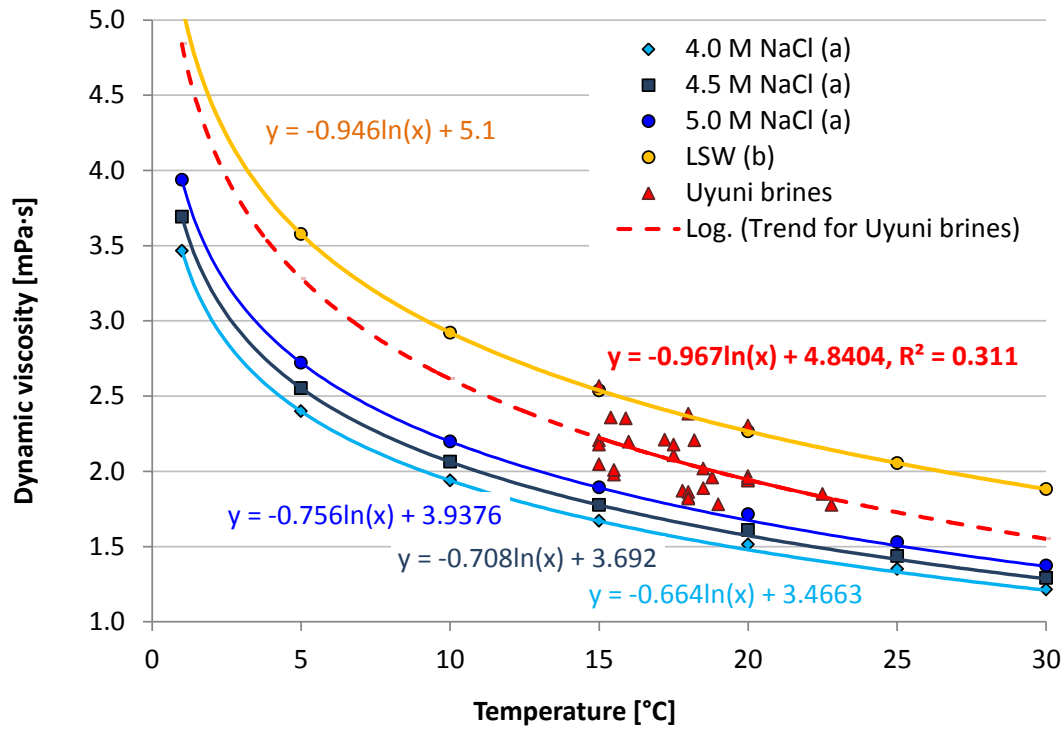


Figure 50: Dynamic viscosity of brine samples depending on temperature conditions during the measurement. For comparison, the relationship between dynamic viscosity and temperature for several standard salt solutions of different concentrations are plotted as well (according to (a) Kestin et al. 1981, (b) Hollendorf and Baumbach, 1987). LSW – Standard salt solution composed of a mixture of salts (main composition is described in the text).

In order to use the experimentally determined Uyuni brine viscosity data for further calculations, one needs to compute the respective dynamic viscosity at field temperature, for instance during pumping test completion. Hence, laboratory data must be extrapolated to the almost lower field temperature conditions ($T_{\text{field}} = 7.1$ to 15.6°C).

Due to the limited number of data points in a narrow temperature range of 2.1 to 5 K, extrapolation is subject to high uncertainty.

Even so, a logarithmic regression model was constructed for all Uyuni data points without regard of differences in mineralization (red dashed line in Figure 50). The model explains about 31% of the variability of the experimental data and plots intermediate between the viscosity curves of the standard salt solutions. This represents the average mineralization of the Uyuni brine samples ranging between 9.1 and 10.8 molar.

In order to get the logarithmic regression lines for each brine sample, the slope and Y-axis intercept of the viscosity curves from standard salt solutions were adapted so that the experimentally measured data of a certain brine sample were fit in the best way.

At this juncture, data points for each sampling site were examined separately.

Now, the dynamic viscosity of the Uyuni brine samples can be converted by means of the obtained regression equations to standard temperature conditions of 25°C for

better comparison (Table 12). At constant temperature, the viscosity increases with increasing mineralization (Busch et al., 1993). The lowest dynamic viscosity was found for the brine from 02-LLI in the northeastern part of the salt flat. On the other hand, the highest viscosity was reached for sampling site 09-RIO in the southern part.

Table 12: Dynamic viscosity η of Uyuni brine samples from different locations at standard temperature $T = 25^\circ\text{C}$.

Sample-ID	η [mPa·s]	Regression
02-LLI	1.569	$\eta = -0.850 \cdot \ln(T) + 4.305$
05-TAH	1.700	$\eta = -0.870 \cdot \ln(T) + 4.5$
06-NOR	1.844	$\eta = -0.940 \cdot \ln(T) + 4.87$
08-CEN	1.718	$\eta = -0.970 \cdot \ln(T) + 4.84$
09-RIO	2.082	$\eta = -0.947 \cdot \ln(T) + 5.13$

4.2.1.4 Input parameters for pumping test evaluation

For latter pumping test evaluation, the brine sample viscosity and density were related to the average field temperature during the pumping test, which in turn was detected by Cera-Divers (Table 13). The conversion of standard density values (at 25°C) to field temperature conditions was done using equation 3.25 in chapter 3.2.1. The required thermal expansion coefficient of the brine was determined experimentally on selected samples from 02-LLI and 09-RIO-site to be $4.2 \cdot 10^{-4} \text{K}^{-1}$ on average (for details see Table B – 8).

Brine viscosity under field temperature conditions was calculated using adapted regression equations from experimental data (see Table 12).

Table 13: Density and dynamic viscosity of the brine under field temperature conditions during pumping test completion.

Pumping test	$T_{\text{field}} [^\circ\text{C}]$	Density [kg/m ³]	Viscosity [mPa*s]
02-LLI (2010)	12.5	1214.8	2.158
02-LLI (2012)	7.1	1217.7	2.639
05-TAH (2010)	12.0	1220.7	2.338
06-NOR (2010)	15.6	1226.8	2.288
08-CEN (2010)	10.0	1224.0	2.606
08-CEN (2012)	9.3	1224.3	2.677
09-RIO (2010)	10.5	1236.1	2.903

4.2.2 Pumping tests in a highly saline environment

The transmissivity or intrinsic permeability of the upper salt layer of the Uyuni salt flat was determined in the field via pumping tests. Altogether seven pumping tests were performed at five different sites on the salt flat during two field campaigns in 2010 and 2012.

Natural challenges of the investigation site

The realization of pumping tests on the Uyuni salt flat revealed some particularities. Due to the high altitude of about 3,653 m a.s.l. the atmospheric pressure accounted for about 665 - 670 mbar on average. This is about one-third lower than the atmospheric pressure at sea level. Consequently, the partial pressure for oxygen was also strongly reduced. Together with the high density and viscosity of the highly mineralized brine (in comparison with normal fresh water) the performance of the used pumps was reduced to 1/5 and 1/10, respectively, of the originally designed performance of the pump as specified by the manufacturer (gasoline pump from HONDA and submersible pump from HOMA, respectively).

Additionally, due to the high permeability of the salt crust high pumping rates are also necessary in order to create a sufficient cone of depression during the pumping test. Unfortunately, the maximum pumping rate was limited on the one hand by the above mentioned limitations of the submersible pump to maximum discharge of $Q_{\max} \sim 2.5$ L/s. On the other hand another more powerful submersible pump could not be applied due to the limited space inside the borehole ($\varnothing = 19$ cm, max 1.5 m deep).

Therefore, high demands on preciseness were made for data correction (i.e. barometric compensation, density correction, compensation of natural daily brine level fluctuations as well as discontinuities due to fixation problems of the data loggers).

Another problem arose from the extremely flat surface morphology of the salt flat without any natural discharge system. Therefore, the pumped brine was discharged as far as possible via connected PE tubes (approximately 50 m) or a flexible tube (100 m) away from the pumping and monitoring wells. Greater distances of discharge could not be achieved because of limited equipment.

Characterization of the aquifer system and flow regime

In order to correctly evaluate the pumping test data, the general hydraulic aquifer model, including all boundary conditions, needs to be identified. For this, the main parameters for each test are summarized in Table 14 and are discussed below.

- (1) Due to the giant surface area of the salt flat ($\sim 10,000$ km²) which is situated at the lowest point of a closed drainage basin, the aquifer can be assumed to be extended virtually unlimited.

- (2) Prior to the pumping test the free groundwater table (pressure head of the groundwater) is horizontal over the entire area of the pumping test site.
- (3) The pumping test was performed with a time-constant pumping rate ($Q = \text{constant}$).
- (4) Boundary conditions of the first order due to inflows from surface waters (e.g. rivers, springs) can be excluded. Also no-flow boundaries (boundary conditions of the second order) are not likely within the respective areas influenced by the cone of depression created by the pumping tests.
- (5) The well diameter (50 mm and 180 mm, respectively) is small in relation to the area influenced by the pumping test.
- (6) The aquifer thickness (M) of the whole salt flat is not equal at all sites, however within the area influenced by a single pumping test the thickness can be assumed to be equal.
- (7) The pumping test evaluation requires the assumption of homogeneity of the aquifer. Since, the aquifer is not homogeneous, a strong vertical anisotropy can be assumed due to the stratigraphic layering of more or less porous halite horizons interrupted by fine dense gypsum or clay layers (compare chapter 4.1.6.2).

The applied pumping test evaluation procedures according to THEIS or COOPER & JACOB as well as according to guideline TGL 23864/08 (1973) require the assumption of 2-dimensional (i.e. exclusively horizontal) inflow into the pumping well. If this assumption is fulfilled, the vertical anisotropy of the aquifer can be neglected. As a consequence, all results only represent horizontal hydraulic properties.

- (8) The aquifer of the upper salt crust is characterized by confined aquifer conditions at all pumping test sites. This is indicated by the strong inverse relationship between the atmospheric pressure and brine level in several time-series records (12-day series from December 2011 at 02-LLI, 08-CEN and 01-COL sites situated in west-east direction, 269 day series at 06-NOR, 08-CEN and 03-INC sites arranged from north to south on the salt flat).

An example for the inverse relationship between brine level and atmospheric pressure is given in Figure 51 for a 12 days series at site 02-LLI.

The barometric efficiency computed from time-series records of the brine levels also give evidence for strongly confined aquifer conditions. Thereby, coefficients ranged between 0.52 and 0.80 at different salt flat sites (compare chapter 4.3.4, Table 20).

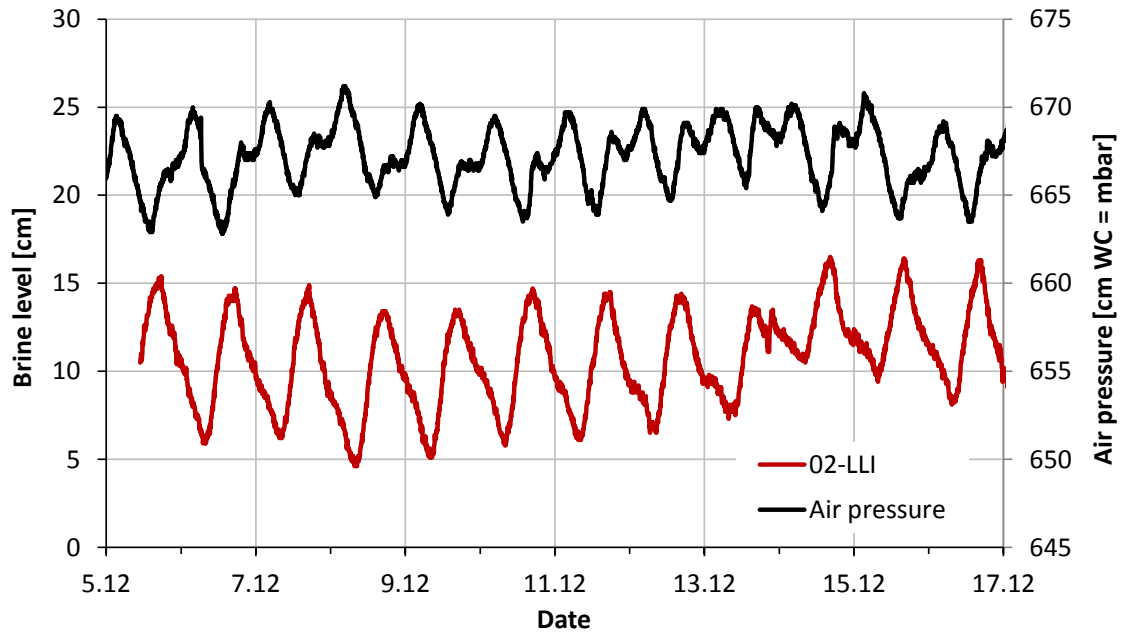


Figure 51: Brine level behavior and atmospheric pressure for a time period of about 12 days at investigation site 02-LLI in 2011.

(9) Another indicator for the hydrostatic stress is the semi-logarithmic or logarithmic plot of the drawdown versus pumping time. If the semi-logarithmic drawdown forms a straight-line and the logarithmic drawdown follows a curve with a steep slope at the beginning of the pumping test but becoming constant with time, then confined aquifer conditions exist according to Krusemann and de Ridder (2000, page 49) (compare Figure 52 and Figure 53). This is valid for the majority of the pumping tests conducted on the Salar de Uyuni.

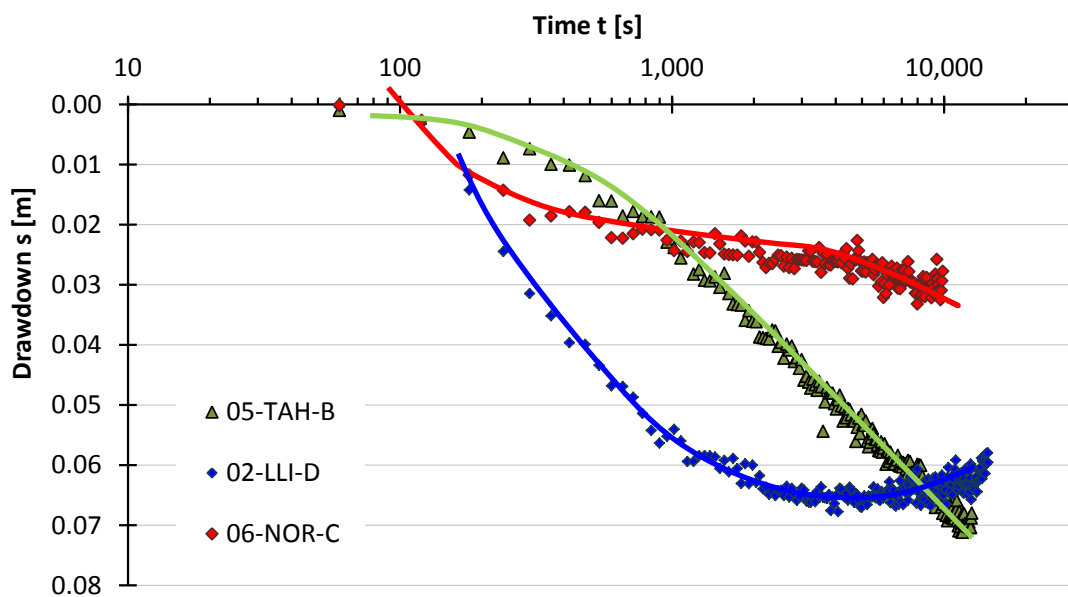


Figure 52: Semi-log plot of the time-drawdown relationships of three observation wells showing confined (05-TAH-B), leaky (02-LLI-D) and unconfined (06-NOR-C) aquifer conditions according to Kruseman and de Ridder (2000).

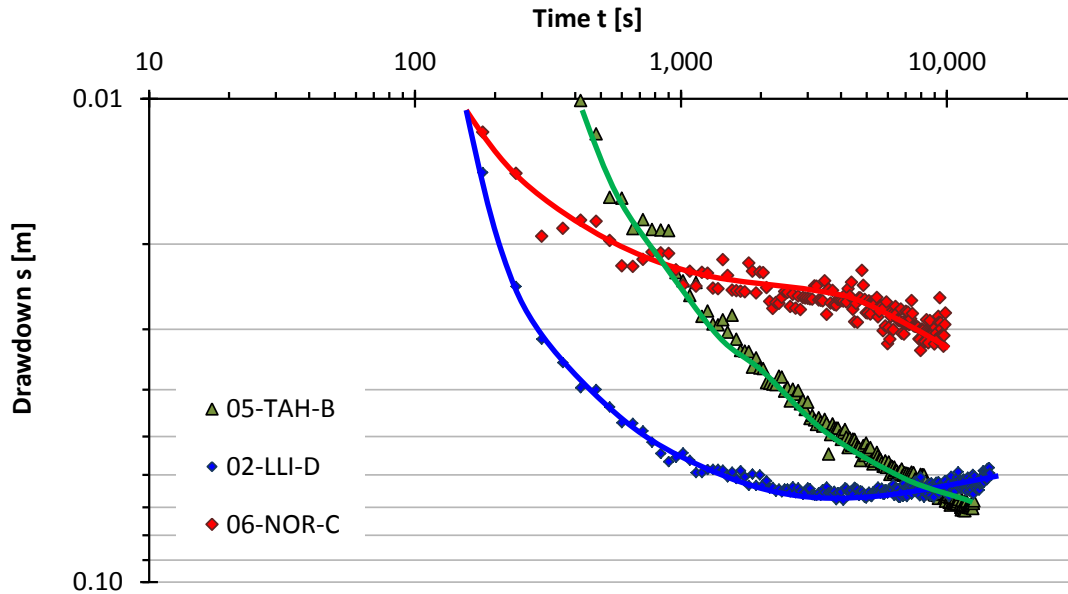


Figure 53: Logarithmic drawdown of three observation wells showing confined (05-TAH-B), leaky (02-LLI-D) and unconfined (06-NOR-C) aquifer conditions according to Kruseman and de Ridder (2000).

- One exception is the pumping test at 02-LLI site in 2010 whose drawdown resembles the influence of leakage from the second halite aquifer which was reached by one drill (02-LLI-B). At early pumping times, the drawdown curve is almost linear as for confined aquifer conditions. Then, at middle pumping times it turns into a horizontal segment which increases again to the end of the pumping test. In accordance with Kruseman and de Ridder (2000), water from the aquitard or in this case the leaky second halite aquifer would reach the pumping well with time. At late pumping times, all the pumped water would be from leakage so that the flow to the well would reach steady state conditions. However, the rerise of the brine level even during constant pumping cannot be explained by leakage effects or additional water inflow. Hence, a mistake in data compensation is likely because the average daily brine-level fluctuation used for the data correction was computed from 12-day observations in December 2011 – one year after conducting the pumping test at the same site. Probably, the brine level changes in 2011 were not equal to those appearing during the pumping test in 2010.

Nevertheless, the use of average daily brine level data from the same season of another year is the most appropriate method to fill the information gap and to execute data compensation. In order to minimize the error in the 02-LLI pumping test analysis, only drawdown data of early pumping times were considered for further evaluation (compare Figure A – 9).

4. Results and Interpretation

Table 14: Overview of the main settings of the pumping tests (pumping test numbers: PT-1 ... PT-7, all time specifications are given in Bolivia time (BOT = UTC/GMT - 4 hours).

Parameters	PT-1	PT-2	PT-3	PT-4	PT-5	PT-6	PT-7
Location	02-LLI	02-LLI	05-TAH	06-NOR	08-CEN	08-CEN	09-RIO
Date	24-Nov-10	30-Nov-12	30-Oct-10	18-Nov-10	3-Nov-10	1-Dec-12	28-Nov-10
Pumping well	A	F	A	A	A	E	A
Well depth [m]	1.0	5.0	9.0	1.0	11.3	8.0	7.0
Depth of filter screen [m]	0.3 - 1.1	0.0 - 4.0	0.0 - 0.7	0.2 - 0.9	7.5 - 9.5	0.0 - 7.5	2.0 - 3.0
Well penetration	partly	fully	partly	partly	partly	fully	partly
Observation wells	B, C, D	A, D, E	B, C, D	B, C, D	B, C, D	A, C, D	B, C, D
Aquifer thickness M [m]	4.0	4.0	4.5	5.0	9.5	6.5	4.5
Typ of pump	submersible	suction	submersible	submersible	submersible	suction	submersible
Start time [hh:min]	12:05	11:15	12:07	13:00	12:05	09:10	17:50
Const. pumping rate [hh:min]	12:15	11:45	12:07	13:05	12:15	09:20	18:10
End of pumping [hh:min]	16:05	14:47	15:35	16:05	16:13	12:08	21:36
End of observation [hh:min]	18:00	16:02	18:41	18:30	04.11.2010, 10:00	13:30	23:15
Duration of the PT [h]	4.00	3.53	3.47	3.50	4.13	2.97	3.60
Observed recovery time [h]	~ 2.0	~1.0	~ 2.0	~ 2.0	>15.0	~ 1.25	~1.67
Pumping rate Q [L/s]	1.07	1.78	1.18	2.47	1.44	2.12	1.22
Discharge distance	44 m	100 m	48 m	48 m	48 m	100 m	48 m
Assumed aquifer condition	confined	confined	confined	confined	confined	confined	confined
Steady-state conditions	steady	un(steady)	unsteady	unsteady	steady	steady	unsteady
Evaluation of drawdown	Hantush/TGL	Theis/UP32	Hantush/TGL	Hantush/TGL	Hantush/TGL	Theis/UP32	Hantush/TGL
Evaluation of recovery	Jacob, Driscoll	Jacob, Driscoll	Jacob, Driscoll				

- A second exception of confined drawdown occurs at well 06-NOR-C. Here, drawdown data may indicate unconfined aquifer conditions with delayed yield. At the beginning of the pumping, drawdown follows a similar curve as for confined aquifer conditions. At middle pumping times the curve shows a flat segment. Afterwards, it turns back into a steeper slope similar to that of confined drawdown.

The evaluation of unconfined pumping test data is carried out according to the same procedure as for confined aquifers but using the corrected drawdown instead of the measured drawdown (Jacob, 1944 cited in Ferris et al., 1962).

$$s_c = s - \frac{s^2}{2 \cdot m} \quad (4.2)$$

where s – Measured drawdown

s_c – Corrected drawdown

M – Thickness of the brine-filled aquifer

However, since the total measured drawdown is only very small ($s_{\max} = 3.6$ cm), the correction of the drawdown is negligible (less than 0.28%). Hence, pumping test evaluation for 06-NOR was carried out according to the same procedure as for confined aquifer conditions.

In the appendix (Figures A – 8, 12, 16, 20, 24, 28 and 32), all originally recorded pumping test data (barometrically compensated) are shown in comparison with the final data after all corrections were applied as described in chapter 3.1.3.1.

However, in 2010 pumping tests could be done only on **partially penetrating wells** because all wells were screened for 1 m length in order to take depth-dependent brine samples (compare chapter 3.1.2). The transmissivity results for drawdown evaluation are summarized in Table B – 11.

Only the pumping tests obtained in 2012 were performed in pumping wells whose screen **fully penetrated** the upper salt crust (i.e. 02-LLI-F, 08-CEN-E, compare Figure A – 1 (left) and Figure A – 3 (top left)). The drawdown data were primarily evaluated using the straight-line procedure according to COOPER & JACOB (Figure 54). Since the integration variable of the THEIS well function u was always larger than 0.5 for all observation wells from the pumping tests at 02-LLI and 08-CEN sites, this evaluation procedure is critical and the results may be biased.

Thus, pumping tests from 2012 were evaluated in UP32 according to the THEIS curve-matching procedure. The results of transmissivity or permeability, respectively, are given in Table B – 12.

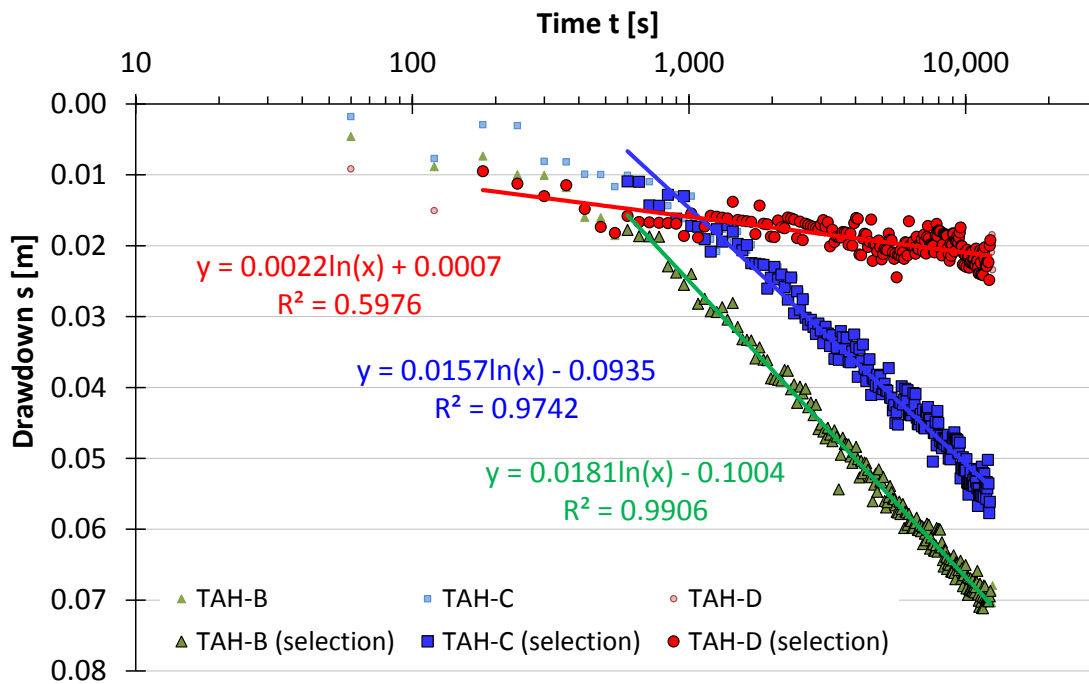


Figure 54: Semi-logarithmic brine level drawdown in three observation wells at pumping test site 05-TAH on Oct. 30, 2010. Only the linear parts of the data (bold colored symbols) were used for the construction of the regression line (light colored symbols mark original data which are not considered).

Additionally, semi-logarithmic plots of the drawdown (according to the straight-line procedure from COOPER & JACOB) and recovery (according to the evaluation procedure from JACOB and DRISCOLL, respectively) are presented in the appendix (Figures A – 8 to A – 35).

Figures of the well constellation as well as cross-sections of the wells for each investigation site can be found in Figures A – 1 to A – 3.

4.2.2.1 Evaluation of the permeability of the Uyuni salt crust

After data correction and evaluation, transmissivity results from each of the three observation wells were compared at the drawdown and recovery phases (according to different evaluation methods). The calculated transmissivity values varied between $1.2 \cdot 10^{-3}$ and $1.3 \cdot 10^{-1}$ m²/s for the different pumping test sites on the salt flat (compare Tables B – 11 to B – 14).

Certainly, these values cannot be directly compared with each other due to differences in aquifer thickness and physical properties of the brine such as density and dynamic viscosity at field temperature. For a better comparison, the transmissivity was therefore converted into intrinsic permeability which represents only the hydraulic characteristics of the hard salt crust independently of the brine properties (compare chapter 4.2.1.4, Table 13).

4. Results and Interpretation

The results of the intrinsic permeability resulting from the pumping test evaluation are summarized for all (observation) wells in Table 15. There is good agreement in the intrinsic permeability values calculated from drawdown as well as recovery of the brine by different methods.

Table 15: Intrinsic permeability K [m^2] obtained from pumping tests performed in 2010 on partly penetrating wells (drawdown evaluation was conducted according to TGL 23864/08 (1973) and in 2012 on fully penetrating wells (drawdown was evaluated by THEIS curve-matching in UP32 software). The brine level recovery was evaluated by the methods from JACOB (1963) and by DRISCOLL (1986), respectively.

Well-ID	Drawdown TGL/UP32	Recovery	
		JACOB	DRISCOLL
02-LLI-C / 2010 [#]	7.39E-10	3.47E-10	3.21E-10
02-LLI-D / 2010	7.09E-10	3.53E-10	3.57E-10
02-LLI-B / 2010 ^a	3.35E-09	1.33E-09	1.13E-09
05-TAH-B / 2010	4.98E-10	3.48E-10	3.23E-10
05-TAH-C / 2010	5.86E-10	3.01E-10	2.95E-10
05-TAH-D / 2010 [#]	4.26E-09	9.93E-10	1.04E-09
06-NOR-B / 2010 [#]	3.51E-09	9.01E-10	8.90E-10
06-NOR-C / 2010 [#]	4.78E-09	1.92E-09	2.08E-09
06-NOR-D / 2010	1.77E-09	2.20E-09	2.20E-09
08-CEN-B / 2010 [#]	8.99E-10	3.63E-10	3.79E-10
08-CEN-C / 2010 [#]	1.63E-09	4.51E-10	5.23E-10
08-CEN-D / 2010 [#]	1.47E-09	4.51E-10	4.36E-10
09-RIO-B / 2010	1.41E-09	7.82E-10	7.70E-10
09-RIO-C / 2010 [#]	1.65E-09	8.32E-10	8.32E-10
09-RIO-D / 2010	1.61E-09	8.60E-10	8.46E-10
02-LLI-F / 2012 ^b	7.18E-11	6.06E-10	2.07E-10
02-LLI-A / 2012	4.39E-10	6.30E-10	5.58E-10
02-LLI-D / 2012	5.69E-10	6.35E-10	5.79E-10
02-LLI-E / 2012 ^a	1.60E-09	n.d.	n.d.
08-CEN-A / 2012 [#]	9.94E-10	4.88E-10	4.88E-10
08-CEN-C / 2012	9.12E-10	6.28E-10	5.90E-10
08-CEN-D / 2012	8.37E-10	5.49E-10	5.20E-10
08-CEN-E / 2012 ^b	6.28E-11	7.46E-10	2.37E-10

^a filtered in the second aquifer

^b fully penetrating pumping well (completely filtered over the total thickness of the aquifer)

[#] filter screen of observation well in different depth than in pumping well (compare well constellation in Figures A – 1 to A – 3)

Deviations from 2-dimensional horizontal flow conditions

In comparison between the results from different observation wells, main differences arise from the different filter screen depths in relation to the filter screen of the pumping well (Table 15, wells marked with “#”). Therefore, the general assumption that the well only receives water from horizontal flow is no longer valid (Kruseman and de Ridder, 2000) since vertical flow components are induced especially in the vicinity of the pumping well. Due to the high vertical heterogeneity of the aquifer caused by the fine salt stratification, the determined intrinsic permeability differs from those observation wells where only horizontal brine flow can be assumed.

Indeed, the effect is highest near the pumping well and decreases with increasing distance to the well. Certainly, this effect cannot be neglected in this study because the observation wells are located at small distances to the well. Nonetheless, if the filter screen of the pumping well is in the same depth as that of the observation well, the effect of the vertical flow component can be neglected and the normal JACOB method can be applied for evaluation. However, if pumping well and observation wells are filtered in different depths, the modification according to TGL 23864/08 (1973) should be applied for confined aquifers under unsteady-state conditions (corresponding to the HANTUSH procedure (Hantush and Ven Te, 1964)).

Statements concerning the hydraulic properties of deeper sediment layers

As described by Fornari et al. (2001) the Uyuni salt flat is composed of an alternating sequence of hard salt crusts and lacustrine sediment layers. All exploration drillings in this study reached the first lacustrine mud layer which completely underlays the upper salt crust.

A second hard salt crust below the 3.5 m thick lacustrine sediments could only be explored by two drillings at site O2-LLI (B and E) in the northeastern part of the salt flat. Both observation wells were filtered within the second salt horizon between 7.5 and 9.0 m depth. Due to the natural boundary to the upper salt aquifer, no horizontal 2-dimensional flow regime is given between the pumping wells (A and F, respectively) and the screens of the observation wells B and E. Therefore, the requirements for the COOPER-JACOB procedure of drawdown evaluation are not fulfilled (Kruseman and de Ridder, 2000). Hence, the calculated intrinsic permeability values are not reliable. Consequently, no information concerning the permeability of the second salt aquifer could be gained within this study.

However, a weak influence of the pumping test could be also detected in the second salt aquifer in 2010 and 2012 (compare LLI-B in Figure 55, and LLI-E in Figure A – 28). Obviously, there is no absolute hydraulic separation of both aquifers. Unfortunately, it cannot be ruled out that a hydraulic connection was induced by the drilling and the well construction procedure. Due to the lack of adequate sealing compounds (for instance clay pellets) for the restoration of the natural compactness of the lacustrine

mud layer around the well casing, a man-made connection between upper and lower salt aquifer might have been generated in retrospect.

Ultimately, no clear statement can be given about the hydraulic impermeability of the lacustrine mud layer or even leakage effects between the upper and lower salt horizon especially at investigation site 02-LLI.

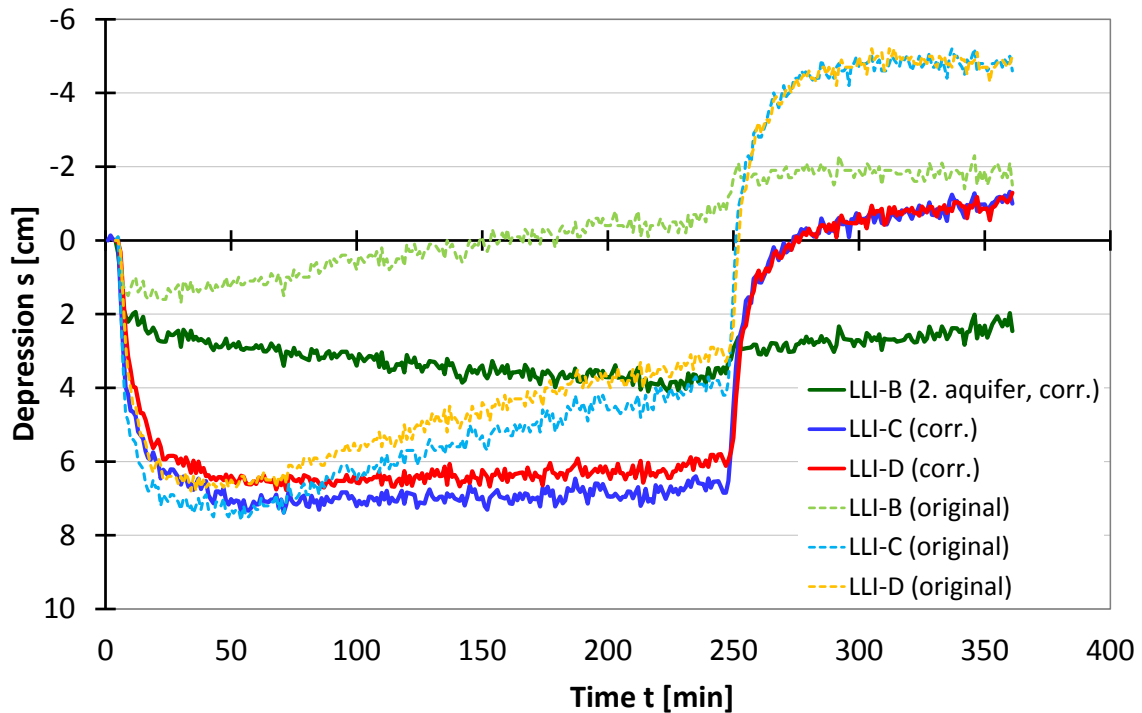


Figure 55: Pumping test data (original and corrected data) from 02-LLI on Nov. 24, 2010.

Increase of the brine level during drawdown

As can be seen from the drawdown and recovery curves for the monitoring wells C and D at site 02-LLI in 2010 (Figure 55), even after data correction (bold colored curves) there is a slight increase in the brine level during the pumping test. The final brine level after recovery is even about 1 cm higher than before starting the pumping test. This increase in the brine level can only be triggered by external factors such as immediate groundwater recharge or natural brine level fluctuations during the pumping test. Groundwater recharge within the short pumping test time interval (6 hours) can be ruled out because absolutely no rain occurred on the day of investigation or several days before, or even in the broader environment of the salt flat.

Also, a hydraulic bypass between the discharged brine water and the cone of depression created by the pumping test cannot increase the brine level during pumping. Rather, it would only accelerate the time of adjusting steady-state conditions between the discharge rate and aquifer inflow.

As described in chapter 3.1.3.1 and discussed later in chapter 4.3, the natural brine level is influenced by the atmospheric pressure and other factors. Therefore, all

pumping test data are corrected with regard to the natural brine level fluctuations observed over a longer time period. For site 02-LLI, only a time series of roughly 12 days exists from December 5 – 17, 2011. The observed period is probably not perfectly adequate in order to correct the pumping test data of Nov. 24, 2010. Anyhow, the unusual increasing behavior of the brine level during the drawdown period of the pumping test was excluded from the data evaluation by the straight-line procedure according to COOPER-JACOB in order to compute more realistic transmissivity values.

Impact of the pumping rate on drawdown in the pumping well

Another inconsistency arises from the evaluation of the drawdown directly in the pumping wells (08-CEN-E, 02-LLI-F). Here, the drawdown is strongly influenced by any fluctuations in the pumping rate (compare Figures A – 28 and A – 32) as well as the vertical component of the inflow in the vicinity of the well. That is why the results of the intrinsic permeability and also the storage coefficient determined from the drawdown in the pumping wells should be handled with care.

Assessment of further boundary conditions using a theoretical Jacob-curve

If the main assumptions of the evaluation procedure according to JACOB (1963) are fulfilled (Kruseman and de Ridder, 2000) and external impacts (for instance changes in atmospheric pressure) are sufficiently eliminated from the data, the initial brine level before starting the pumping test should be reached again after brine level recovery. Also the time of recovery should be equal to the time of the depression ($t_{\text{depression}} = t_{\text{recovery}}$). If these assumptions are valid, a comparison with the theoretical curve of depression and recovery according to the equation of JACOB (1963) may help to identify further boundary conditions in the aquifer system.

Figure 56 and Figure 57 illustrate the drawdown in the observation wells during the pumping tests performed in 2012 (fully penetrating pumping wells).

In case of the pumping test at 02-LLI, the real and theoretical drawdown data agree very well in observation well D but deviate significantly in observation well A during recovery. The reason for the faster brine recovery might arise from a reduction of the storage coefficient caused by an irreversible compaction of the halite crystal system during the pumping test. This is confirmed according to Langguth and Voigt (2004, p. 251) by ratios of $1 < \frac{t}{t'} < 2$ in all three observation wells of 02-LLI in 2012 (Table B – 13). This also explains the differences in the intrinsic permeability determined from the drawdown or recovery phase (see also Figure 58).

4. Results and Interpretation

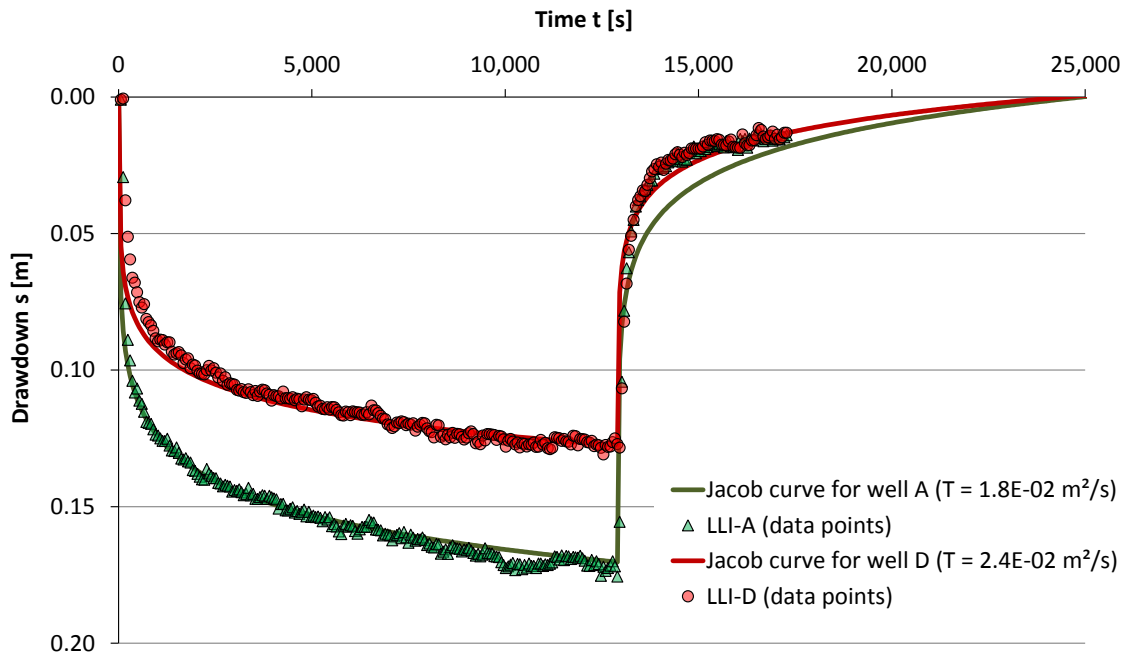


Figure 56: Measured drawdown at pumping site 02-LLI (2012) in observation wells A and D (point symbols). Two theoretical drawdown and recovery curves constructed according to the equation from Jacob are displayed for comparison with different values of transmissivity T .

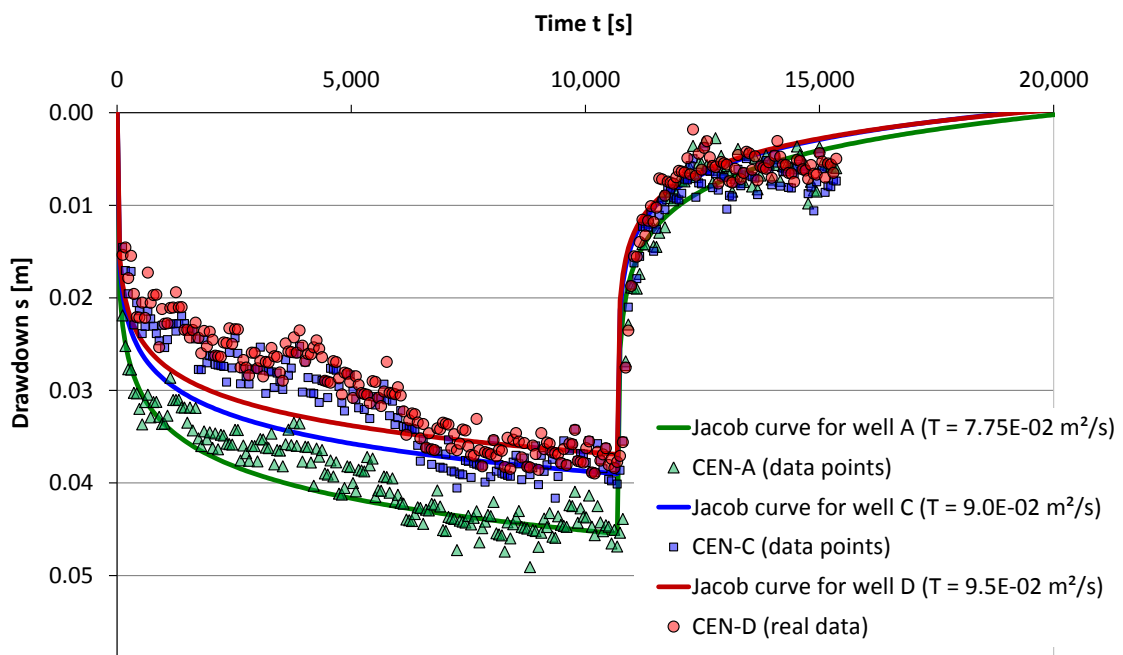


Figure 57: Measured drawdown at pumping site 08-CEN (2012) in observation wells A, C and D (point symbols). Theoretical drawdown curves according to the equation from Jacob are displayed for comparison with different values of transmissivity T .

During the pumping test at 08-CEN the pumping rate was not constant throughout the entire time of the pumping test (compare drawdown curve in the pumping well 08-CEN-E, Figure A – 32). The pumping rate was adapted several times (for instance after about 1 hour of pumping) because it seemed that the discharge rate had changed. However, the theoretical curves match quite well with the initial drawdown and with the final drawdown, as well as with the recovery indicating that no further impacts must be considered except the changing pumping rate.

Presentation of final permeability results

Figure 58 summarize the results of intrinsic permeability for the different pumping test sites. The intrinsic permeability determined for the Uyuni salt crust ranges on average between $4 \cdot 10^{-10}$ and $5 \cdot 10^{-9}$ m² (Table 15). The highest salt crust permeability occurs in the very north of the salt flat at site 06-NOR. Also 09-RIO is characterized by slightly higher permeability compared to all other pumping test sites. The reason might be connected with the flooding history of the salt flat. After the rainy season, flood water disappears in consequence of intense evaporation initially in the eastern and central part of the Salar de Uyuni. After nearly complete desiccation, residual surface water remains longest in the Rio Grande delta as well as in the very northern part to the east of volcano Tunupa. Therefore, no hard pavement can be formed and the salt surface is extremely weak and highly porous. In part, dried salt froth defines the salt’s surface.

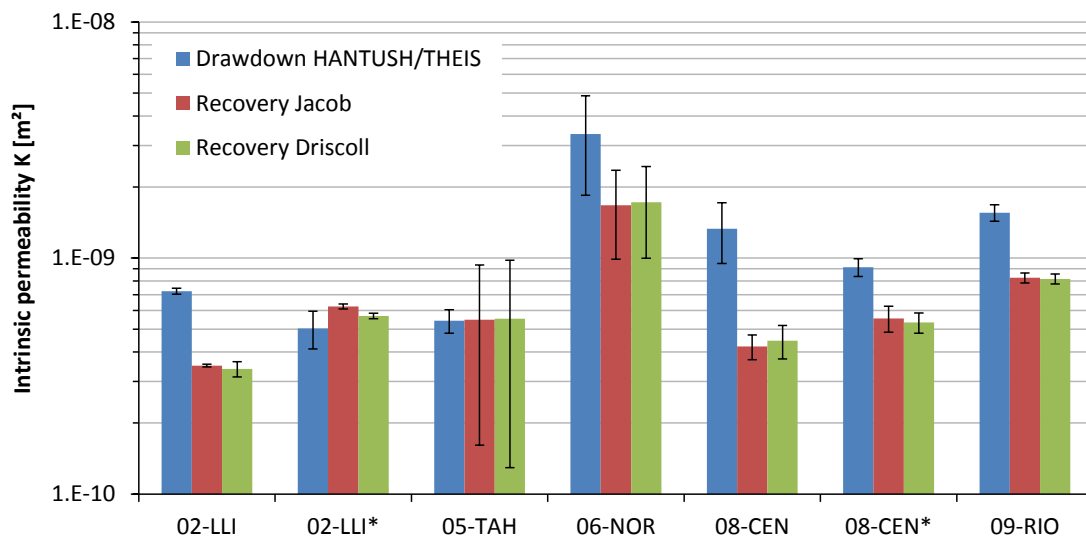


Figure 58: Intrinsic permeability of the Salar de Uyuni upper salt crust at five different sites arising from the evaluation of brine level drawdown and recovery during the pumping tests in 2010 and *2012. Mean and standard deviation from each three observation wells are shown for comparison.

4.2.2.2 Interpretation of the calculated storage coefficients

The specific storage coefficient of the underground is determined by the compressibility of the porous sediment as well as the compressibility of the fluid filling the pore space under confined aquifer conditions. Furthermore, under unconfined conditions the storage coefficient is also determined by changes in the porosity (Langguth and Voigt, 2004, Busch et al., 1993). S_0 represents the stored fluid volume per one meter pressure change and per one cubic meter aquifer volume. In natural systems the storage coefficient sometimes also represents a mixed form of both aquifer conditions.¹⁸ The calculated storage coefficients for the Uyuni pumping test sites are summarized in Table 16. The mean storage coefficients for each three observation wells at each investigation site are presented in Figure 59.

The calculation of the storage coefficient from the pumping test data is more sensitive (compared with the permeability determination) in regards to the accuracy of the pumping test data and the validity of certain requirements. It is important that the groundwater flow is strictly horizontally.

Unfortunately, the majority of the constructed wells are only partly filtered. Furthermore, most of the filter screens of the observation wells do not match in depth with that of the pumping well (Figures A – 1 to A – 3). Consequently, in most cases a vertical flow component is triggered by this well constellation leading to high uncertainty when determining the storage coefficient.

For this reason any interpretation of the results of the storage coefficients should be done with care.

Typical storage coefficients for confined aquifer conditions vary in the range of 10^{-4} to 10^{-5} which could be observed for 09-RIO and also 02-LLI (Table 16). Several coefficients are intermediate between confined and unconfined aquifer conditions. This may indicate semi-confined conditions. On the other hand, if the filter screen is located at a greater depth, the observation well reacts more like a confined well due to the depressurization at depth.¹⁸

Pumping test sites 05-TAH, 06-NOR and 08-CEN are characterized by typical storage coefficients for unconfined aquifers representing the effective salt porosity ranging between 17.3% and 30.0% on average. This is in rather good agreement with the overall effective porosity determined on salt core samples ranging between 13.5% on average for the deeper part and about 35% for the upper part of the salt crust (chapter 4.1.5).

¹⁸ Szymczak, Peter: G.E.O.S. Freiberg Ingenieurgesellschaft mbH, 09599 Freiberg, personal communication from July 3, 2013.

4. Results and Interpretation

Table 16: Storage coefficients S [-] determined from pumping tests performed in 2010 on partly penetrating wells (drawdown evaluation was conducted according to TGL 23864/08 (1973)) and in 2012 on fully penetrating wells (drawdown was evaluated by THEIS curve-matching in UP32 software). Based on the brine level recovery, the storage coefficients were computed by the method of DRISCOLL (1986).

Well-ID	Drawdown	Recovery
02-LLI-C / 2010 [#]	0.083	0.02
02-LLI-D / 2010	0.033	7.91E-04
02-LLI-B / 2010 ^a	0.000	0.40
05-TAH-B / 2010	0.906*	0.04
05-TAH-C / 2010	0.796*	0.12
05-TAH-D / 2010 [#]	0.06	0.18
06-NOR-B / 2010 [#]	0.45	0.77*
06-NOR-C / 2010 [#]	0.07	0.01
06-NOR-D / 2010	0.39	0.03
08-CEN-B / 2010 [#]	0.52	0.09
08-CEN-C / 2010 [#]	0.09	0.12
08-CEN-D / 2010 [#]	0.68*	0.32
09-RIO-B / 2010	0.014	3.43E-04
09-RIO-C / 2010 [#]	0.003	1.28E-04
09-RIO-D / 2010	0.006	1.18E-04
02-LLI-F / 2012 ^b	1.09E-06	0.00E+00
02-LLI-A / 2012	4.34E-03	3.11E-04
02-LLI-D / 2012	4.06E-03	1.93E-03
02-LLI-E / 2012 ^a	1.00	n.d.
08-CEN-A / 2012 [#]	0.13	0.39
08-CEN-C / 2012	0.13	0.08
08-CEN-D / 2012	0.60*	0.17
08-CEN-E / 2012 ^b	2.56E-06	0.00

^a filtered in the second aquifer, ^b fully penetrating pumping well (completely filtered over the total thickness of the aquifer), [#] filter screen of observation well in different depth than in pumping well (compare Figures A – 1 to A – 3), * unreliably high values

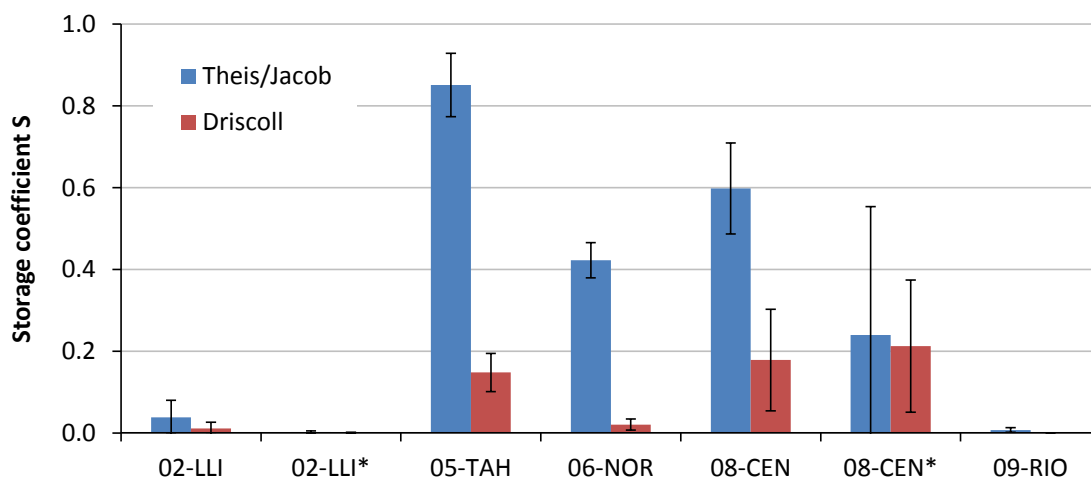


Figure 59: Storage coefficients determined from pumping test data in 2010 and *2012.

4.2.2.3 Comparison with literature data from other salt flats

Literature data concerning the hydraulic conductivity of other salt flats (i.e. salars, sabkhas or playas) were found from Chile, Argentina, USA or Saudi-Arabia (Table 17). The hydraulic conductivities of salt dominated surface-near aquifers typically vary between around $7 \cdot 10^{-2}$ and $1 \cdot 10^{-4}$ m/s which agree quite well with the results obtained for the Salar de Uyuni.

Table 17: Comparison of hydraulic conductivity k_f from different salt flats in the world (k_f values are related to freshwater).

Salt flat	k_f [m/s]	Reference
Salar de Uyuni, Bolivia	$1.2E-02$... $9.4E-04$	This study
Salar de Atacama, Chile	$1.0E-02$... $1.0E-04$	(Salas et al., 2010)
Salar de Huasco, Chile	$1.2E-04$... $4.6E-04$	(Acosta and Custodio, 2008)
Salar de Rincon, Argentina	$6.9E-02$... $2.5E-03$	(Ovejero Toledo et al., 2009)
Bonneville salt flats, USA	$2.4E-03$ (5,000 gpd/ft ²)	(Turk et al., 1973)
Coastal sabkha, Emirates of Abu Dhabi	$6.9E-04$	(Sanford and Wood, 2001)
Al-Lith Sabkha, Saudi-Arabia	$1.3E-03$	(Sabtan and Shehata, 2003)

4.2.3 Experimental permeability determination on core samples

Beside field tests, laboratory experiments were also conducted in order to measure the permeability of the salt. The vertical permeability of several salt core samples was determined by flow-through experiments using 2-octanol in order to avoid dissolution processes.

The results of experimental permeability determination on salt core samples are summarized in Figure 60 and in Table B – 15. Experimental permeability data varied between $1 \cdot 10^{-13}$ and $1.5 \cdot 10^{-10}$ m² (which corresponds to k_f between $3.8 \cdot 10^{-5}$ and $2.6 \cdot 10^{-4}$ m/s).

As can be seen, there are no clear trends depending on the depth. So, there is a quite random distribution of permeability with depth showing the large inhomogeneity of the sediment layers. Furthermore, salt core samples were selected according to the criteria of homogeneity. Therefore, fine lamina of gypsum or clay mineral deposits are not considered in these data. Due to the experimental setup all data represent only the vertical permeability of the salt and not the horizontal one.

In comparison with the intrinsic permeability determined from pumping test data (chapter 4.2.2.1), a difference of about 1 – 2 orders of magnitude occurs. On the one hand, this is caused by the vertical instead of the horizontal permeability. On the other hand, only well preserved homogenous salt core samples are selected for experimental analyses. Hence, fractures, cavities and very high porous sectors of the salt crust are not considered.

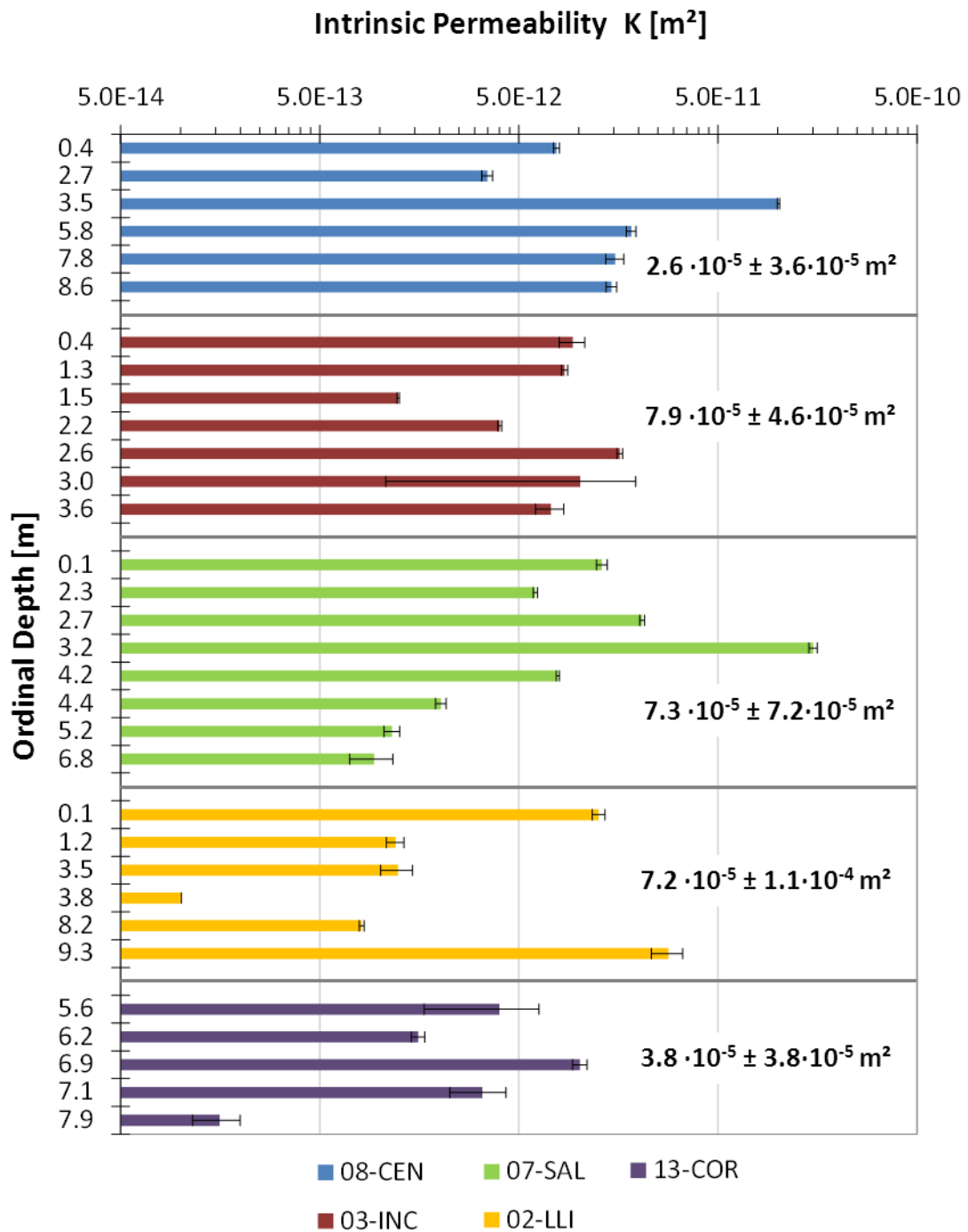


Figure 60: Intrinsic permeability (mean values and standard deviations of each four replicate measurements per core sample) versus depth of samples from five different drillings. The overall average \pm standard deviation of the hydraulic permeability related to fresh water is also given for each drilling.

4.2.3.1 Gas permeability of a gypsum layer

The strong vertical anisotropy is confirmed by a characteristic hard gypsum layer which could be identified in several drill cores from different sites (compare chapter 4.1.6.2). It is supposed that this specific gypsum layer is a stratigraphic level which occurs almost all over the salt flat formed during very specific climatic conditions immediately after a wet period with large flooding.

Due to its high density and hardness, a very low permeability is expected. Therefore, the gas permeability of a representative gypsum sample (02-LLI-B, 11/2, 4.0 m depth) was measured at the Institute of Drilling Engineering and Fluid Mining.

The measurement revealed an absolute gas permeability of around $1 \cdot 10^{-15} \text{ m}^2$ (Figure 61) which is about 3 to 4 orders of magnitude lower than the intrinsic permeability determined for several salt core samples with flow-through experiments using 2-octanol (compare chapter 4.1.6.2).

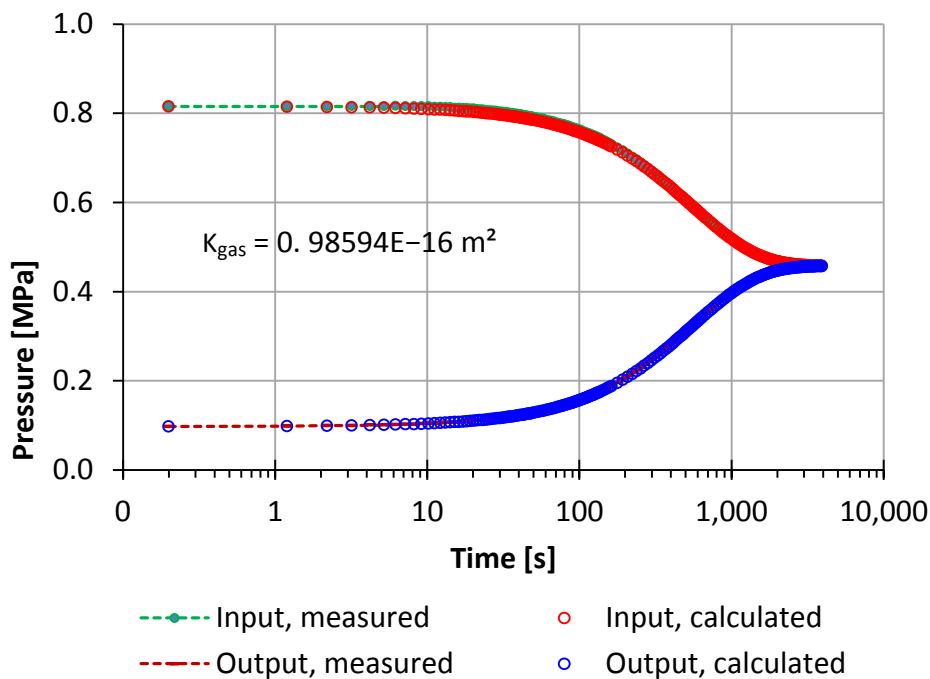


Figure 61: Pressure curves in the input and output chamber during the gas permeability measurement of the gypsum layer (sample number 11) from drilling 02-LLI-B (Measurement by Dr. Carsten Freese, Institute of Drilling Engineering and Fluid Mining, TUBAF).

4.2.4 Radiocarbon dating as brine tracer

The radiocarbon content of the brine samples is an indicator for the time of brine formation as well as vertical mixing processes between deep and shallow brine. Four brine samples were taken at different sites from different depths for radiocarbon dating. The brine samples contained between about 23.5 and 51.0 percent modern carbon (pMC, Table 18). Hence, the conventional radiocarbon ages reported by the

4. Results and Interpretation

Poznan Radiocarbon Laboratory (see chapter 3.2.5) range between approximately 5,400 and 11,600 yr BP related to the modern standard with a ^{14}C activity of 100 pMC (Table 18).

In fact, the initial ^{14}C activity of the atmosphere was not constant during the Holocene but it was subject to a systematic decrease since about 30,000 years as illustrated in Figure 62 (Clark and Fritz, 1997). Therefore, the initial ^{14}C activity a_0 was estimated from Figure 62 in consideration of the conventional radiocarbon ages of the brine samples. Then, the radiocarbon ages were calibrated using equation 4.3 assuming a half-life $T_{1/2} = 5568$ years (adapted from Clark and Fritz, 1997).

$$t = -8033 \cdot \ln \frac{a_t}{a_0} \quad (4.3)$$

where a_t – ^{14}C activity measured in the Uyuni brine samples
 a_0 – Assumed initial ^{14}C activity in accordance with Figure 62

Table 18: Conventional radiocarbon ages of Uyuni brine samples from different depths from *Nov. 2010 and Dec. 2011 (pMC – percent modern carbon). Fractionation-correction was based on the reported $\delta^{13}\text{C}$ values. The last column shows the calibrated ^{14}C ages (Age_{cal}) with respect to an assumed initial activity a_0 .

Sample-ID	Depth [m]	a [pMC]	$\delta^{13}\text{C}$ [‰ PDB]	Age [^{14}C yr BP]	a_0 [pMC]	Age_{cal} [^{14}C yr BP]
06-NOR-B*	3.3	51.0 ± 0.41	-13.5 ± 2.6	$5,410 \pm 70$	107	5,952
03-INC-C	5.0	41.5 ± 0.54	-21.6 ± 1.5	$7,070 \pm 110$	109	7,757
10-PES	5.5	40.3 ± 0.41	-19.3 ± 1.5	$7,300 \pm 90$	109	7,993
07-SAL	7.6	23.5 ± 0.16	-3.4 ± 0.3	$11,630 \pm 60$	110	12,399

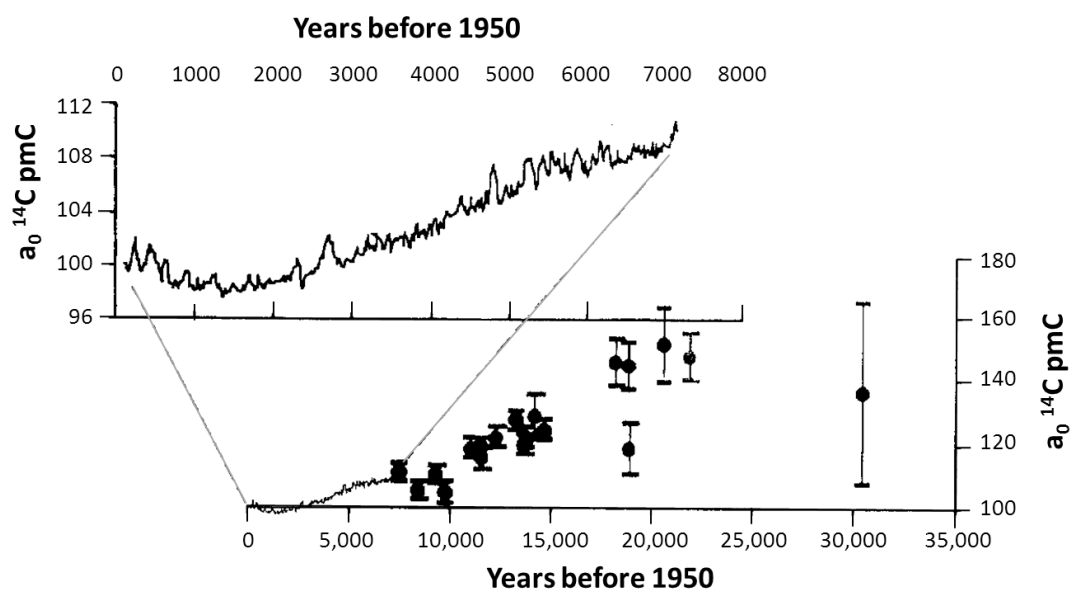


Figure 62: ^{14}C activity in the atmosphere during the Holocene based on data from tree rings and corals (from Clark and Fritz, 1997)

A linear relationship can be found when the calibrated radiocarbon ages are plotted versus the brine sampling depth (Figure 63). The age of the brine increases significantly with depth at a confidence level of 5% ($p = 0.029$).

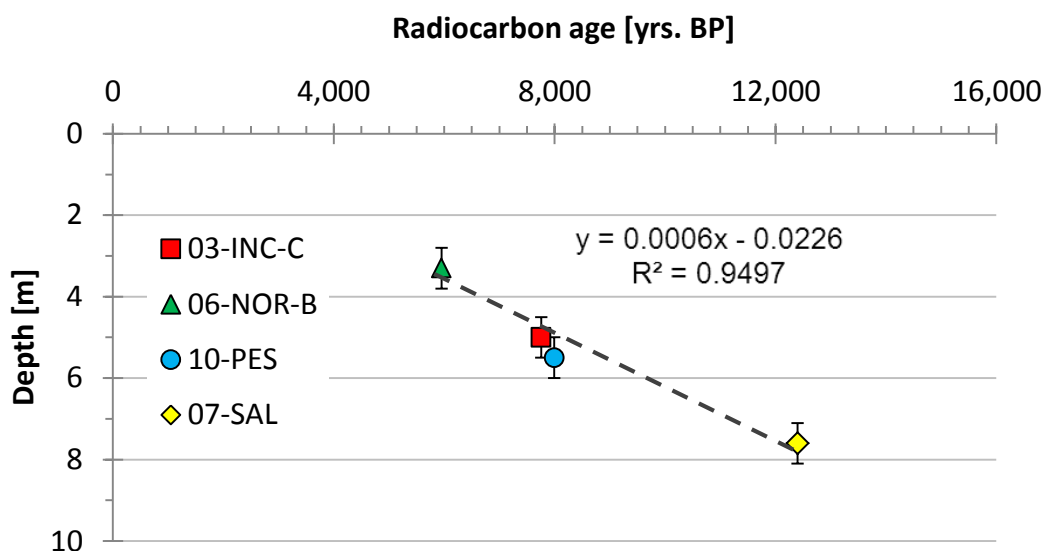


Figure 63: Calibrated radiocarbon ages of Uyuni brine samples from different depth.

Previously, Ericksen et al. (1977) published a radiocarbon age of $3,520 \pm 600$ years for an organic-rich mud sample from only 15 cm depth (sampling location was 35 km away from Colchani, total depth of the salt crust ~ 10 m). They concluded from this, that in 100 years, about 4 mm of salt accumulated due to precipitation.

According to Fornari et al. (2001) the upper salt crust of Salar de Uyuni was formed after the last palaeolake phase Tauca (12,000 – 16,000 cal. yr BP). Different studies have reported age dates based on ^{14}C analyses of solid samples of calcareous crust, carbonates, organic matter, shells or algal bioherms (summarized in Fornari et al. (2001)).

The presented age data of this study are the first based on water samples and corresponds quite well with sediment samples from the literature. This indicates that the dissolved carbon in the brine has the same age as the solid salt of the corresponding depth or the total salt crust, respectively. Since only very little carbonate is contained in the halite, it can be concluded that the brine has roughly the same “age”.

In conclusion, there might be no significant recharge from infiltrating freshwaters during or immediately after the rainy season. Radiocarbon ages also do not indicate a significant vertical mixing (brine flow) throughout the salt layer. This can be explained by the extremely high inhomogeneity of the salt crust which is formed in consequence of changing climatic conditions during the Holocene. Fine layers of clay material or gypsum may separate the highly porous halite layers. The very low gas permeability of the examined gypsum sample (compare chapter 4.2.3.1) gives evidence to this.

4.3 Natural brine level fluctuations

Changes in the natural brine level over short or long time periods give important insights into the aquifer behavior and the effect of different factors such as changes in atmospheric pressure, gravitational influence of the sun and the moon (earth tides), and groundwater recharge caused by rain events or snow melt and other related seasonal or long-term trends (Gonthier, 2007, Acworth and Brain, 2008, Bernard and Delay, 2008). Evapotranspiration of vegetation may lead to local pumping from shallow aquifers and cause diurnal water table fluctuations (Healy and Cook, 2002, Lautz, 2008). It may also indicate that brine movement within the salt flat system is probably triggered by density-driven brine flow (Fan et al., 1997, Holzbecher, 2005, Nield et al., 2008).

4.3.1 Short-term brine level records

In order to check the intended monitoring principle for long-term brine level observation of the Uyuni salt flat, some short time-series (12 days) of the brine level were recorded in December 2011. To do this, CeraDiver data loggers were installed in three different wells in varying depths (02-LLI-A, 08-CEN-D, 01-COL-B). The well locations are distributed on an imaginary line from east to west on the salt flat (compare Figure 10 in chapter 3.1.1).

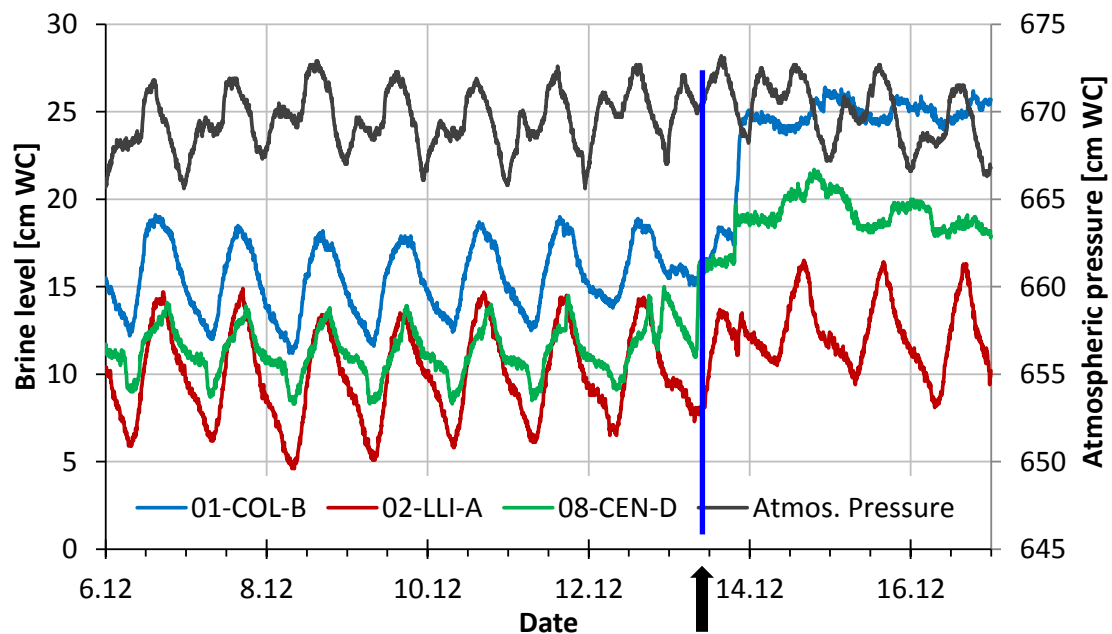


Figure 64: 12-day brine-level¹⁹ records of three wells (left axis) in comparison with the atmospheric pressure (right axis). All brine level data are baro-compensated and density corrected. Due to different depths of the CeraDivers, all data records were shifted by certain offsets for better comparison: 02-LLI-A: -65 cm WC, 01-COL-B: -225 cm WC, 08-CEN-D: -300 cm WC. Blue line indicates the onset of rain events.

¹⁹ The term “brine level” describes the position of the brine surface referred to an arbitrary reference point which is determined by the position of the Diver data-logger.

The brine levels in all three observation wells show strong periodic fluctuations each day. An inverse relationship between the atmospheric pressure and the brine-level in the wells can be stated (Figure 64): If the atmospheric pressure decreases, then the brine-level rises as it is characteristic for confined aquifer conditions (Kruseman and de Ridder, 2000).

Furthermore, during the observation period on December 13th, the first strong rainfall events occurred on the salt flat indicating the beginning of the coming rainfall period (marked by blue arrow in Figure 64). Some parts of the salt flat were completely flooded with a few centimeters of freshwater which was also confirmed by field observations (Figure 65). The effect of these rain events on the brine level or the brine pressure head can be best observed in Figure 64 for the wells 01-COL-B and 08-CEN-D. Here, the brine level pressures clearly increased above the average level of the previous days. Furthermore, the periodic character of the brine level fluctuations completely disappears. This can be explained by the partial dissolution of the uppermost salt, especially the disintegration along polygon edges due to the fresh water flooding. Therefore, a certain permeability of the uppermost salt surface is produced and the brine's pressure head is not confined anymore. The measured pressure head corresponds to the total height of the surface water and brine water column above the pressure sensor.



Figure 65: Flooded salt crust close to Incahuasi island in the central part of the Uyuni salt flat (photo taken on Dec. 14, 2012 by R. Sieland).

However, when plotting the mean daily brine level fluctuation for the time period from Dec. 06 – 12, 2011 (N = 7 days, before the onset of rain events), the minimum brine level appears between 07:00 and 08:00 and the maximum between 15:00 for 01-COL and 18:00 pm for 08-CEN, respectively (Figure 66). The increasing stage lasts for about 8.5 to 10 hours while the decreasing stage lasts for 14 to 15.5 hours.

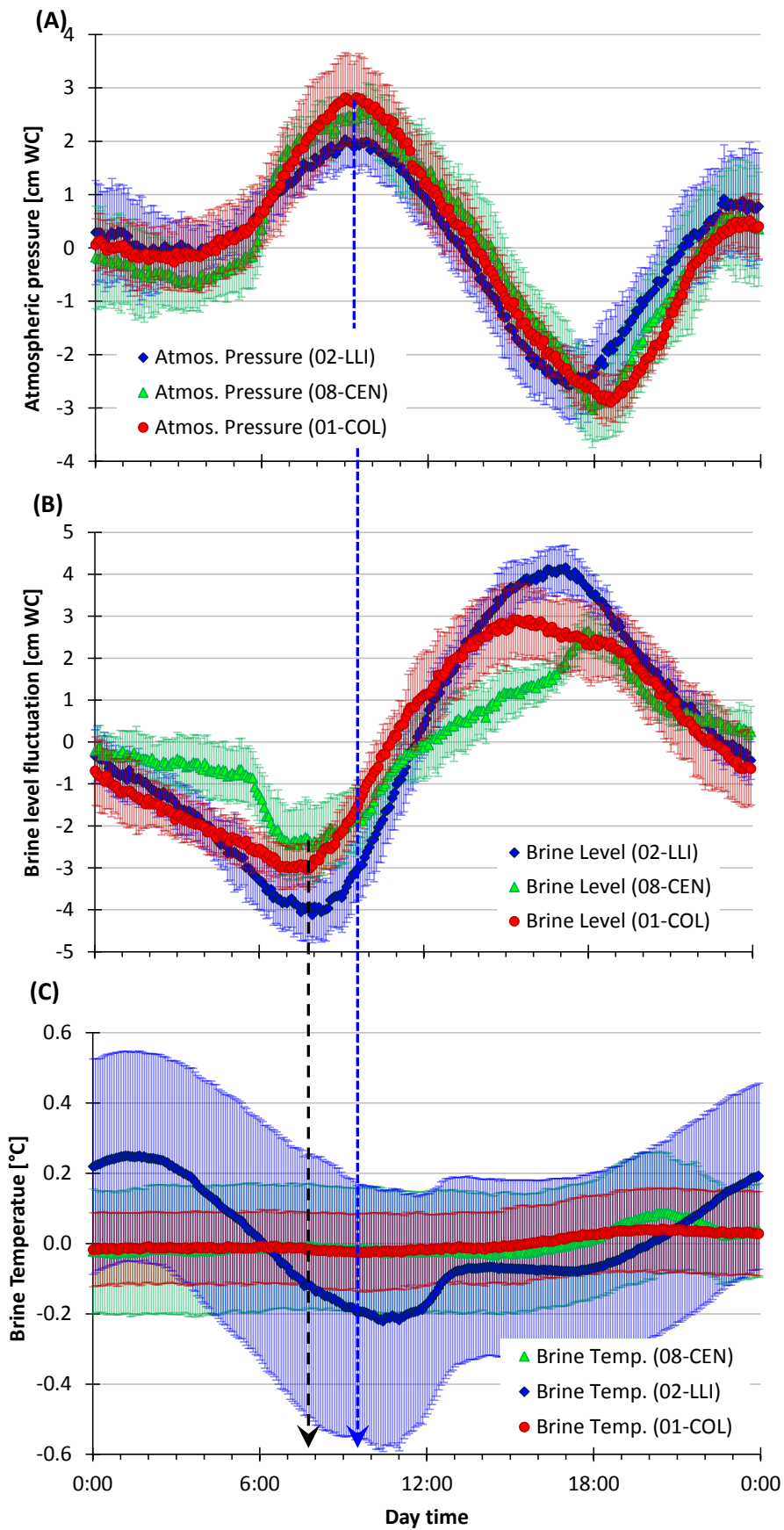


Figure 66: (A) Mean daily atmospheric pressure, (B) daily brine level fluctuation [Diver data are baro-compensated but not density corrected] in the three monitoring wells, (C) brine temperature variations [mean values from 7 complete days; time steps: 5 min]. Dashed lines mark the time lag between brine level minimum and atmospheric pressure maximum in the morning.

On the other hand, the maximum atmospheric pressure is determined in the morning at 09:00 and a minimum in the afternoon between 17:15 and 18:30.

Hence, a positive time lag of at least one hour appears between brine level minimum and atmospheric pressure peak in the morning. Even if the time lag of the brine level peak and the atmospheric pressure minimum in the afternoon does not show such a unique trend in the time lag between the different observation stations, it is obvious that the brine level changes always occur before the atmospheric pressure changes (Figure 66). Indeed, there is no logical reason that the brine level should react in advance to the atmospheric pressure. Therefore, a simple relationship between atmospheric pressure and brine level can be ruled out.

4.3.2 Time-series analyses of long-term data records

In addition to the 12-days trials of brine-level observations, long-term measurements of the brine level were conducted between December 2011 and September 2012 at three different locations from north to south on the salt flat. This time, the data loggers were not installed in the wells but directly in the salt (compare chapter 3.1.4 for detailed description of the installation procedure).

Figure 67 summarizes the brine-level records from all three monitoring stations over the entire observation period of about nine months between December 19, 2011 until September 12, 2012 (N = 269 days). The mean monthly precipitation (based on data from 2001 to 2011, Ministerio de Medio Ambiente y Agua, 2012) is also shown in the diagram for comparison.

4.3.2.1 Long-term brine level fluctuations

All three observation stations are characterized by highest brine levels in the period between January to April reflecting the large area flooding during and immediately after the rainy season of 2011/2012 (Figure 67). Lowest brine levels are detected from June to the end of the data records on September 13, 2012.

Conspicuously, two different stages of brine level behavior can be observed in all three time-series. In the rainy season, when the salt flat is assumed to be flooded, irregular and random fluctuations appear in the brine level. No periodic pattern can be observed in the brine level records. On the other side, during the dry season, the brine level follows a daily periodic pattern. The change over from one stage to the other one occurs at different times (compare Figure 67, colored arrows). At site 06-NOR, this shift took place around April 22, followed by site 03-INC on May 12. At site 08-CEN, this shift started on June 28, 2012.

The transition from random to periodic variations in the brine level records occurs at a certain threshold of absolute brine pressure. When the brine level falls below a certain minimum brine level (e.g. 31 cm WC in case of 03-INC), then the periodic brine level fluctuations can be observed as illustrated in Figure 69.

A systematic error in the installation of the CeraDivers at shallow depths (compare chapter 3.1.4.1) could have led to a complete dry up of the CeraDivers within the salt crust at certain times during the dry season leading to a completely different brine level behavior. But, this error can be strictly ruled out because the offset of the CeraDivers under atmospheric conditions accounts for -0.3 to +0.5 cm WC whereas the absolute minimum values of all brine level records were 8.0 cm WC, 10.5 cm WC, and 12.4 cm WC for 03-INC, 06-NOR, and 08-CEN, respectively.

In fact, the change in brine level behavior appears during the transition between flooding and desiccation stage of the salt flat. During evaporation and desiccation, the surface brine water becomes more and more concentrated until saturation is reached with regard to certain salt minerals (e.g. halite, compare chapter 4.1.2). At this point, salt minerals precipitate and form a hard pavement on the salt flat surface. Additionally, near-surface brine may rise due to capillary forces, evaporates and salt crystallizes within the very upper pore space. This crystallization process probably seals the upper salt crust almost completely. Kampf et al. (2005) describe a similar process responsible for the formation of a practically impermeable salt crust at the Salar de Atacama. Hence, the subsurface brine of the Salar de Uyuni becomes subject to confined aquifer conditions in the dry season.

Moreover, in the rainy season, when the salt flat is almost entirely flooded, brine temperature variations are even stronger than in the dry season (compare red curve in Figure 69). However, a significant temperature influence on the brine level cannot be observed during the rainy season. For this reason, a systematic measurement error due to the temperature dependency of the pressure measurement can generally be excluded (see chapter 3.1.4.1 for detailed discussion).

4. Results and Interpretation

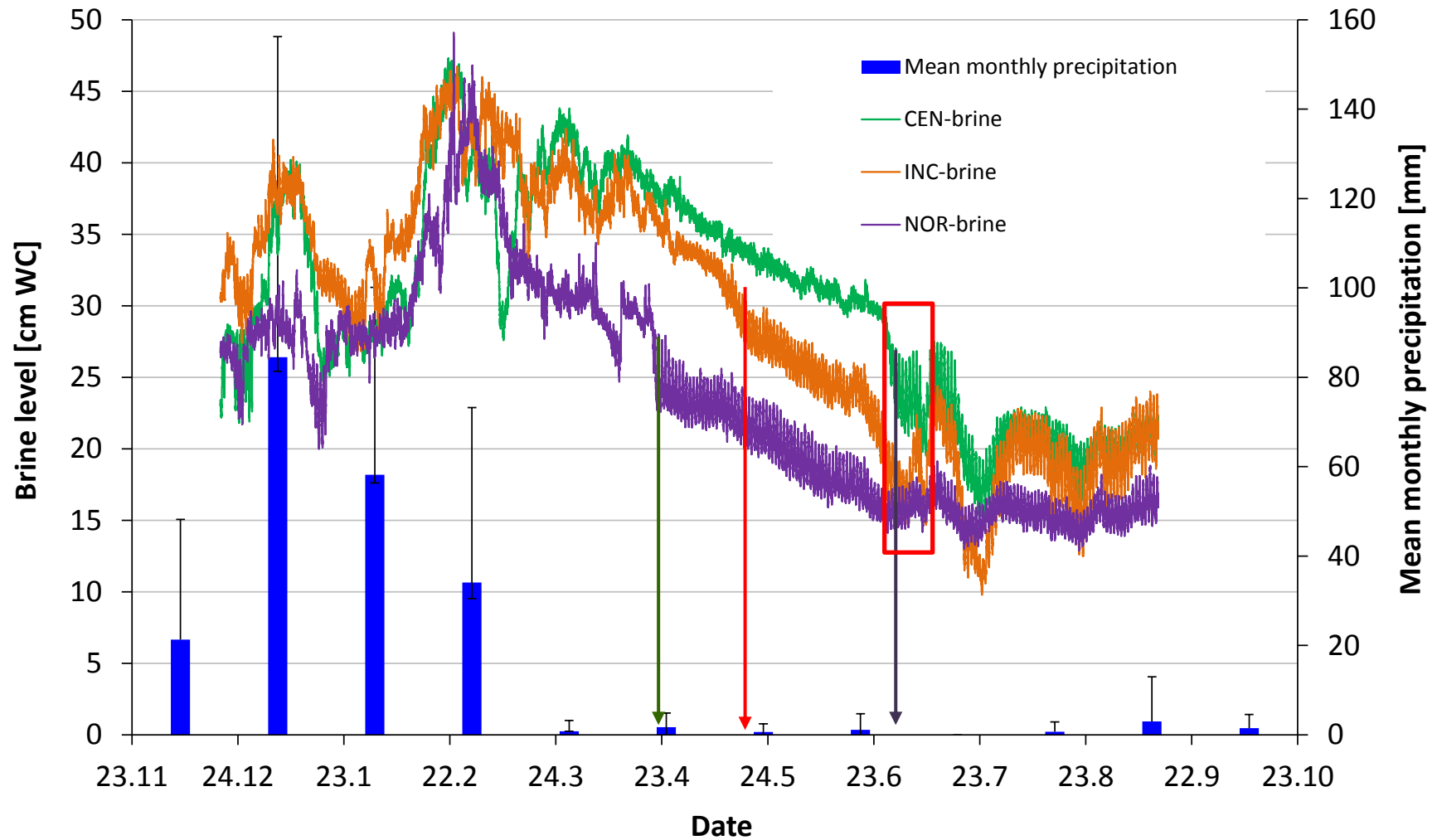


Figure 67: Brine level time-series from Dec. 19, 2011 to Sept. 12, 2012 (N = 269 days; brine level records are baro-compensated according to equation 3.1 in chapter 3.1.3.1) at three investigation points 06-NOR, 08-CEN and 03-INC (chapter 3.1.1, Figure 10) in comparison with the mean monthly precipitation based on data from 2001 – 2011. Vertical arrows mark the onset of diurnal brine level fluctuations. Details within the red rectangle are shown enlarged in Figure 68.

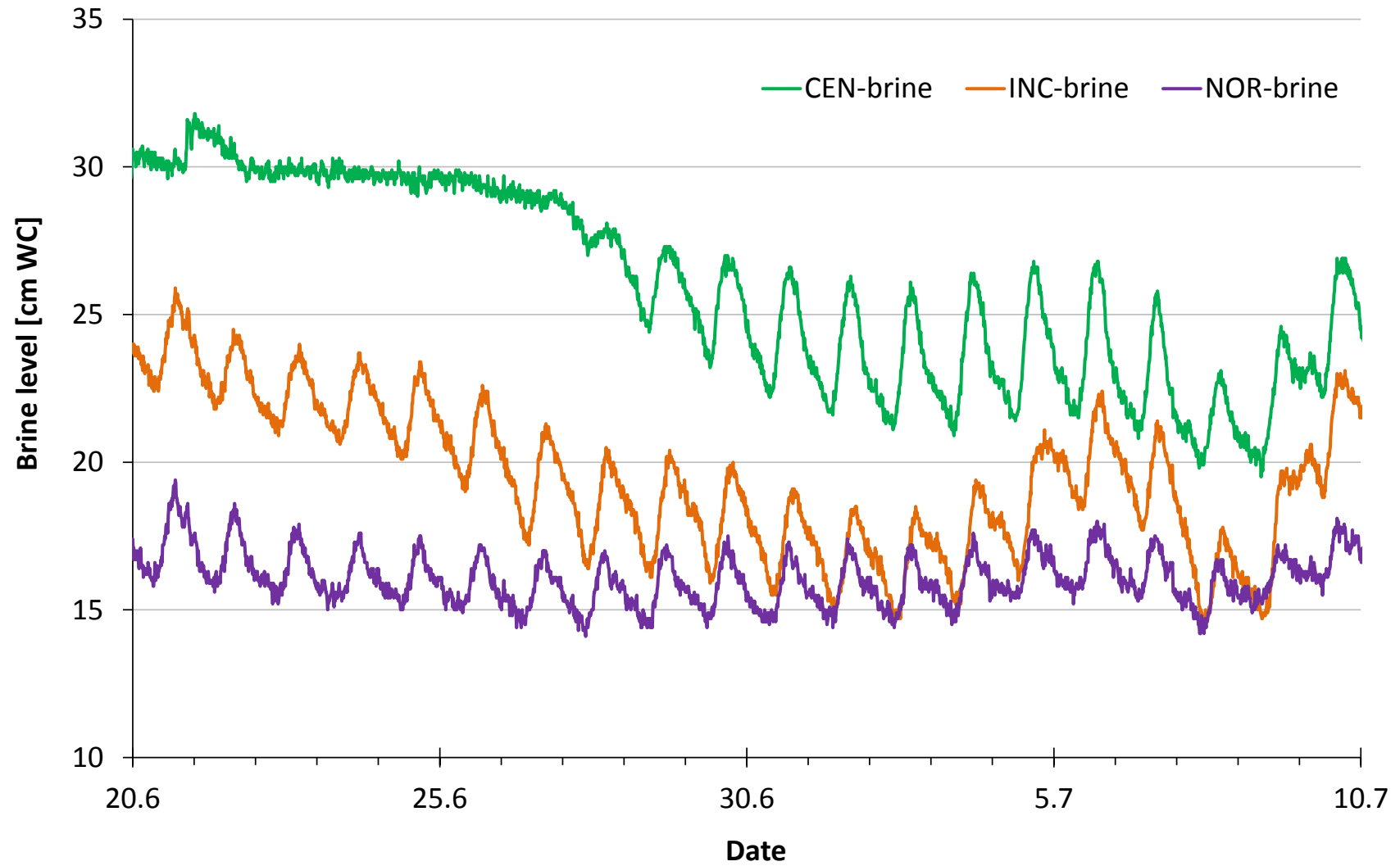


Figure 68: Enlargement of the brine level time-series showing the characteristic daily brine level variations during the dry season at the three observation stations.

4. Results and Interpretation

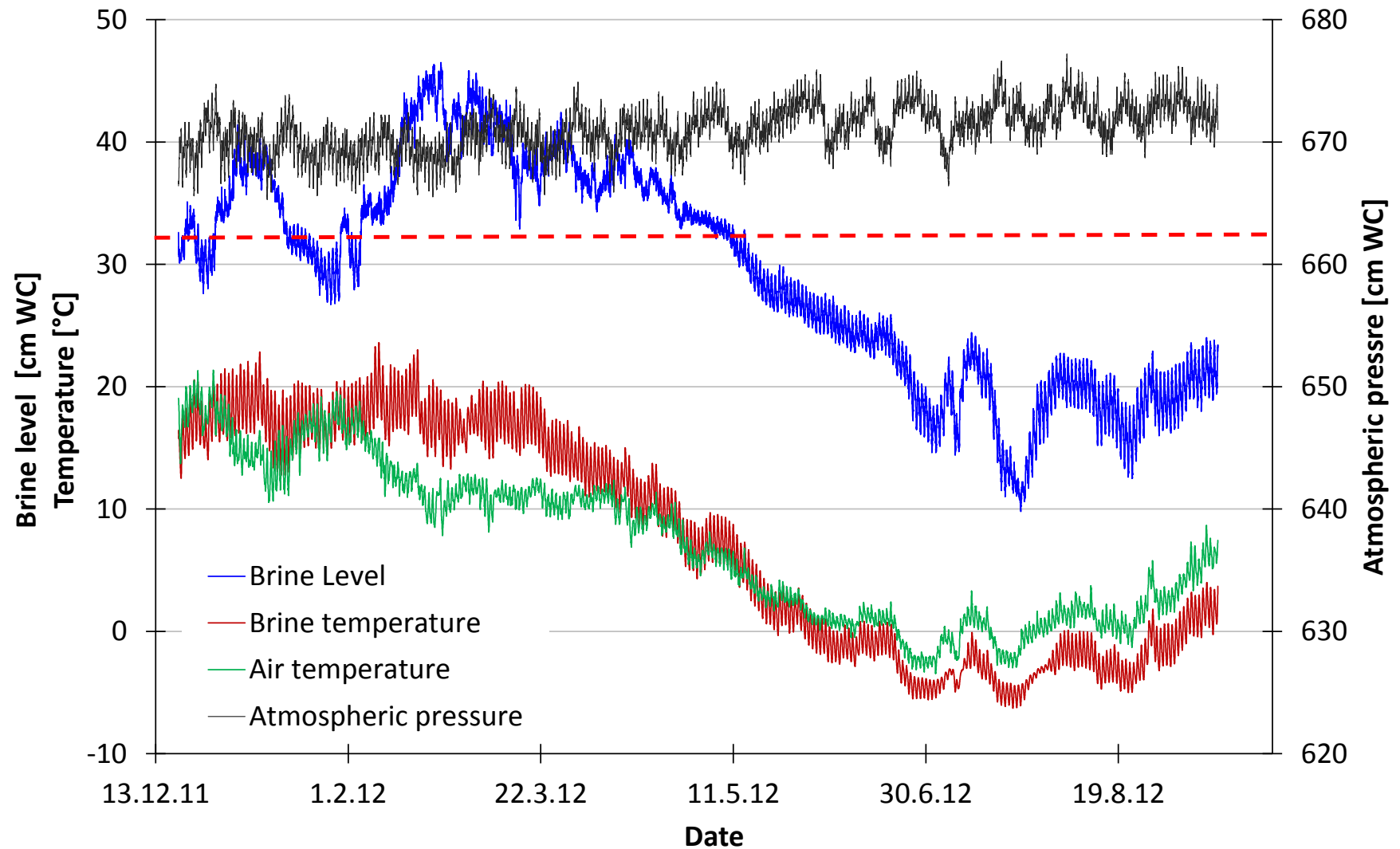


Figure 69: Time-series (N = 244 days) of brine level (baro-compensated), brine temperature, air pressure and air temperature at site 03-INC (air pressure and temperature were measured on the island of Incahuasi). The red horizontal line indicates the brine level threshold when arbitrary fluctuations change to regular diurnal fluctuations of the brine level.

4.3.2.2 Signal analyses of daily brine level fluctuations (Fourier-Analysis)

In order to evaluate the periodic variations of the brine level during the dry season, one has to remove the long-term variations from the data set. This can be done either by high-pass filtering in the frequency domain or by removing the centered daily-moving arithmetic mean (average) with a subset size of 24-hour in the time domain (Gonthier, 2007).

The power spectra computed by Fourier analysis of each time-series show certain characteristics. All parameters which are measured in the field (i.e. brine level, brine temperature, atmospheric pressure and air temperature) are dominated by very low frequencies [< 1 cycle per day (cpd)] which are caused by long-term variations over the entire observation period (Figure 70 and Figure 71).

The main reason for this is the occurrence of a rainy season and a dry season. During the South American Summer Monsoon, the Intertropical Convergence Zone is shifted southward on the Altiplano (Bräuning, 2009). There are more clouds bringing partly heavy rain falls. Direct rainfall on the salt flat and runoff from the catchment area induce large area flooding of the salt flat. Therefore, higher pressure levels (sum of brine and freshwater column above the Diver) are detected. Simultaneously, higher average air temperatures also induce higher brine temperatures. During the dry season, there is absolutely no rain and nearly no clouds. The average air temperatures are significantly lower (compare Figure 69, green curve).

The residual spectra are determined by three main frequencies (1x, 2x, 3x per day, Figure 70 and Figure 71). In comparison, the frequency spectrum of the theoretical earth tide calculated in Tsoft (Van Camp and Vauterin, 2005) for the global location of the Uyuni salt flat shows five dominant frequencies. Only two of these dominant frequencies also occur in the brine level data records. These harmonics (K1, S2) are caused by the solar oscillation of the earth containing both atmospheric-pressure and ocean-tide influences (Merritt, 2004, Acworth and Brain, 2008). Due to the lack of the other typical earth tide frequencies (O1, N2, M2) in the brine level spectrum, earth tides are no explanation for the temporal behavior of the brine-level.

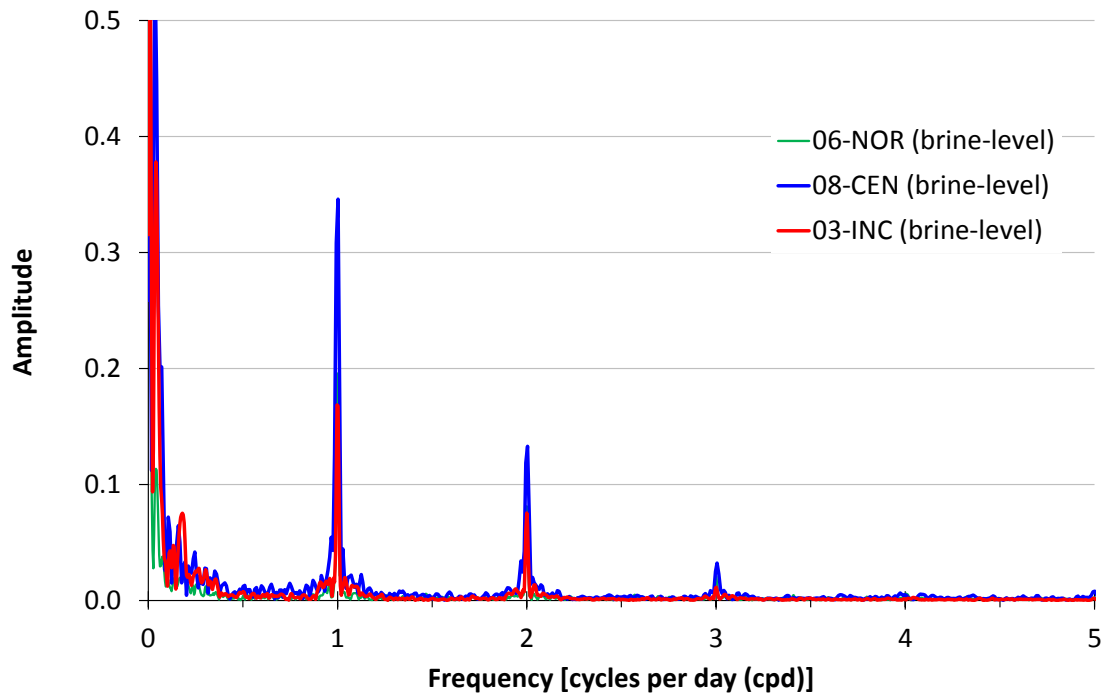


Figure 70: Fourier analysis of the brine level time-series during the dry season (all data are transformed into Z-scores according to Merkel and Planer-Friedrich (2002)).

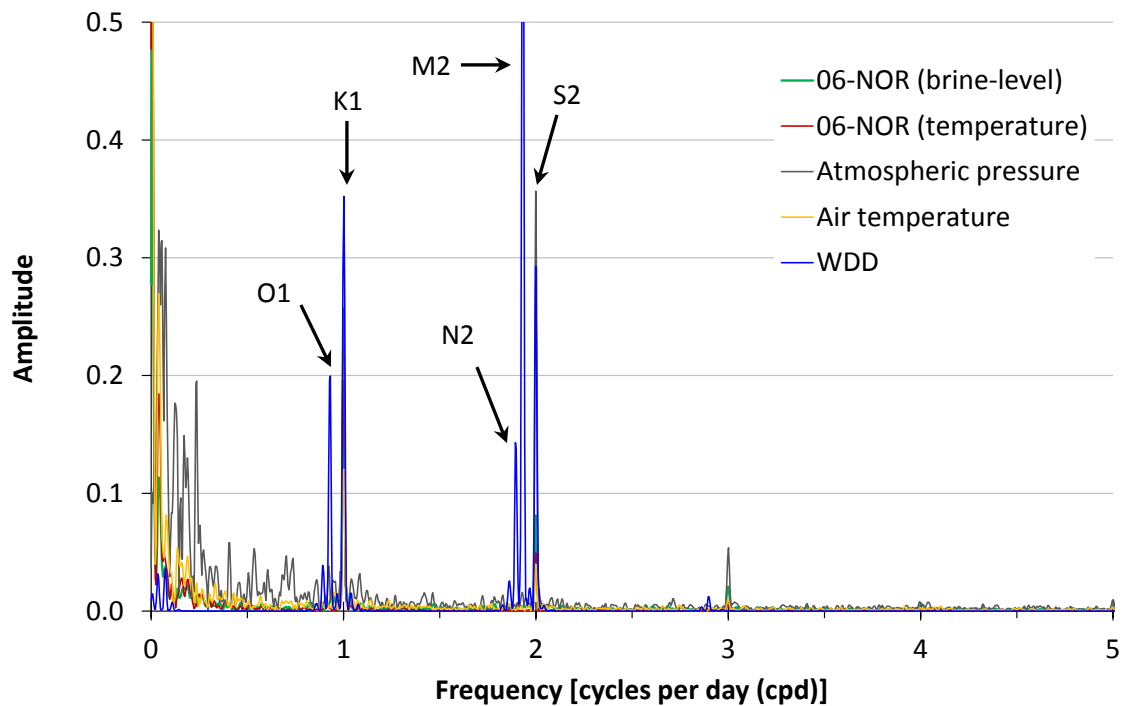


Figure 71: Fourier analysis of the time-series of brine level and brine temperature from site 06-NOR in comparison with atmospheric pressure, air temperature and synthetic earth tide (WDD) for the Salar de Uyuni [all data are transformed to Z-scores; notation of earth tide components according to Acworth and Brain (2008)].

Another method to investigate the temporal changes of the frequency spectrum is the short-time Fourier transformation (STFT). Figure 72 shows the resulting moving window spectrum of the brine level from site 08-CEN. The time of observation is indicated by the horizontal axis while the occurring frequencies are plotted on the vertical axis. The amplitude values for each point are represented by a color scale. One can clearly see the different frequency compositions of the rainy and dry season. While in the rainy season various different frequencies occur, the dry season is strongly dominated by 1 cpd and 2 cpd frequencies.

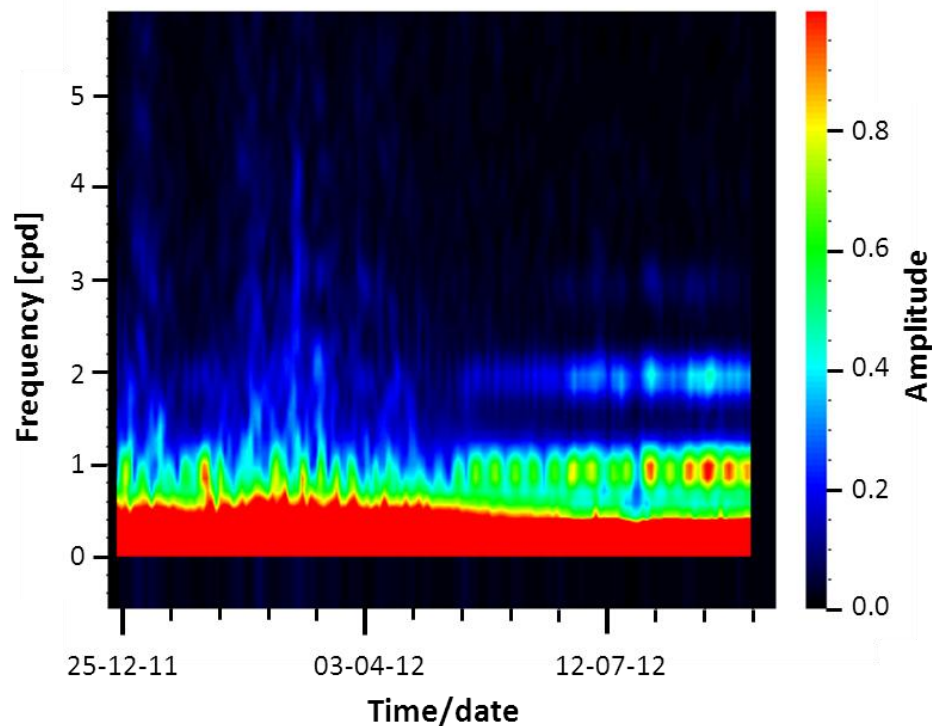


Figure 72: Moving Window spectrum of the brine level data from site 08-CEN between Dec. 12, 2011 to Sept. 13, 2012 showing the dominating frequencies in cycles per day (created in Tsoft).

4.3.3 Mean daily fluctuation

Figure 73 illustrates the mean daily fluctuation of the brine level and brine temperature of 08-CEN site as well as atmospheric pressure and air temperature during the dry season from July 28 to September 12, 2012 (N = 47 days). The daily brine level fluctuation shows a similar periodic pattern for the long-term series as compared to the 12-day series (see Figure 66 + Figure 73) with the minimum brine level in the morning around 09:00 and a maximum in the afternoon at around 17:00.

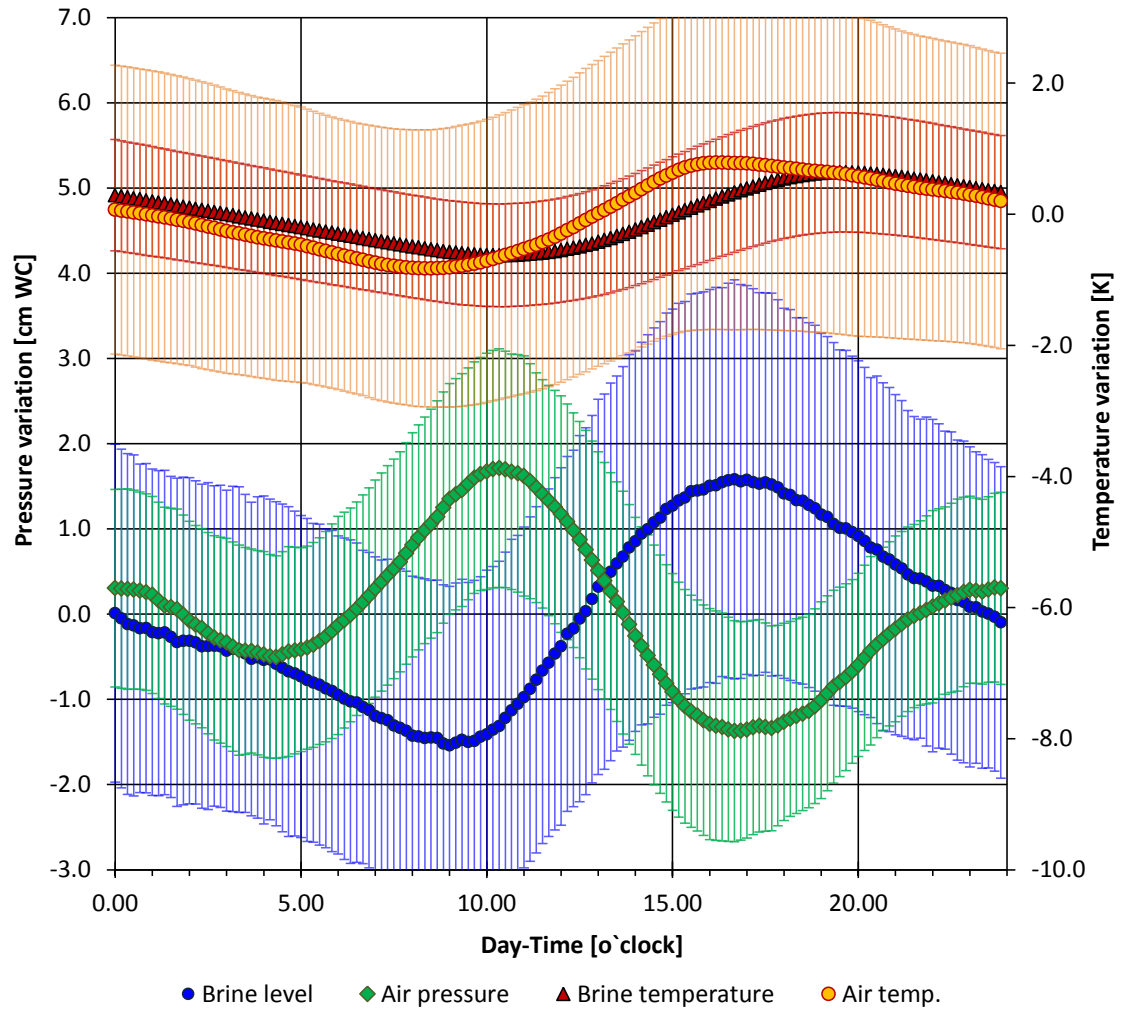


Figure 73: Mean daily brine level and brine temperature fluctuations during the dry season at site 08-CEN in comparison with the mean daily atmospheric pressure and air temperature (N = 47 days; June 28 to Sept. 12, 2012). Data variations are shown in absolute pressure or temperature units but for better clarity, the original data are shifted on the vertical axis by the mean value of the respective parameter.

The time lag between two periodic parameters, as illustrated in Figure 73 for brine level, brine temperature, atmospheric pressure and air temperature, can be calculated by correlation analysis using TSoft (chapter 3.3.2). For that purpose, one parameter signal will be shifted from a minimum time shift (e.g. -6 hours) to a maximum time shift (e.g. +6 hours) in relation to the brine level signal. For each time step, a correlation coefficient is computed. The maximum absolute correlation coefficient indicates the time delay between the brine level and another selected parameter. A summary of the resulting time lags for all parameters related to the respective brine level signals of the three observation sites are given in Table 19.

4. Results and Interpretation

Table 19: Phase lags between brine level (at different sites) and the other parameters obtained from signal correlation in Tsoft software package (*negative correlation between both parameters; in case of negative values the peak of the corresponding parameter appears in advance to that of the brine level).

Brine level	Brine temp.	Air pressure	Air temp.
06-NOR	2.5 h	80 min*	50 min
08-CEN	2.5 h	60 min*	16 min
03-INC	1.2 h	10 min*	-55 min

In order to find out if the earth tide could have an impact on the brine level, the synthetic earth tide was computed for the Salar de Uyuni coordinates in Tsoft. However, no significant correlation could be identified for the brine level and the theoretical earth tide.

A significant positive time lag occurs between brine temperature and brine level. Here, the brine temperature reacts about two hours later than the brine level itself (Table 19). Also the atmospheric pressure reached its daily maximum value about 10 min (in case of 03-INC) to 80 min (at 06-NOR) later than the brine level reached its daily minimum. This indicates that there could be no causal relationship between atmospheric pressure and brine level change.

4.3.4 Determination of the barometric efficiency

The barometric efficiency (BE) of the salt aquifer was calculated from different brine level and atmospheric pressure time-series according to the statistical procedure from CLARK (see chapter 3.1.3.1). The computed BE values which are related to the physical characteristics of the brine range between 0.52 and 0.80 (Table 20). According to Krusemann and de Ridder (2000), BE values usually vary between 0.20 and 0.75. Hence, the Uyuni brine level is under confined conditions, which is also indicated by the typical inverse relationship between atmospheric pressure and brine level (Figure 51 in chapter 4.2.2).

The BE coefficients obtained from 12-days brine level records during the dry season (December 2011) are a bit higher compared to those obtained from long-term observations. During the rainy season the upper salt layer is influenced by dissolution due to freshwater flooding. Consequently, the upper salt crust becomes permeable and thus, the brine is unconfined or only little confined.

4. Results and Interpretation

Table 20: Barometric efficiency for short-term (Dec. 2011) and long-term brine level records (Dec. 19, 2011 to Sep. 12, 2012) at different sites on the salt flat (the obtained BE values are based on the physical properties of the brine).

Site	N (days)	BE	R ²
06-NOR	269	0.5651	0,9933
08-CEN	269	0.5162	0,9929
03-INC	269	0,5499	0,9872
02-LLI	12	0.7984	0,9997
01-COL	13	0.7436	0,9996
08-CEN	14	0.7479	0,9998

4.3.5 Interpretation of diurnal variations in data records

4.3.5.1 *Salt breeze effect*

The mean daily atmospheric pressure fluctuations are characterized by a global peak which occurs in the morning at around 10:00 followed by a pressure decline until reaching its absolute daily minimum in the afternoon at around 17:00. The atmospheric pressure increases again until midnight, but decrease once more in the early morning, where it reaches a second minimum at around 04:00.

This characteristic diurnal cycle of the atmospheric pressure on the Uyuni salt flat can be explained by the salt breeze effect caused by differential heating at the edge of the salt flat (Physick and Tapper, 1990, Tapper, 1991, Davis et al., 1999, Rife et al., 2002).

The salt flat surface has a very high albedo whereby $69 \pm 2\%$ of the incoming solar radiation is reflected (Reuder et al., 2007). Furthermore, absorbed heat is more quickly conducted downward since the rock salt has a higher thermal conductivity and a slightly higher heat capacity in comparison with the surrounding sediments and rocks (compare Table 21). Therefore, the salt surface remains cooler during the day than the surrounding desert land mass. This effect is enhanced by greater evaporation along cracks and fissures of the near surface brine which induces an additional cooling effect in comparison with the dry desert surrounding.

Due to the quick heating of the surrounding landmass, the decreased air density causes the air masses close to the surface to heat up and rise. In contrast, air masses over the salt flat remain cooler and air sinks to the bottom. Thus, different atmospheric pressures are formed in the morning: High pressure over the salt flat and low pressure over the surrounding landmass (Figure 74).

4. Results and Interpretation

Table 21: Heat capacity c and thermal conductivity λ of relevant rock and fluid types at 20°C (unless otherwise indicated).

Rock/Fluid	c [kJ/(kg·K)]	λ [W m ⁻¹ K ⁻¹]	Reference
Salt rock (halite)	0.86	6.7	Gevantman (1981)
Igneous rocks (water-saturated)	~ 0.75*	2.0 – 3.6**	*Sommerton (1992) **Sundberg et al. (2009)
Sandstone (dry)	~0.7*	1.5 – 3.6** 3.3 – 6.6***	*Abid et al. (2014) **Somerton (1992) ***Nagaraju and Roy (2014)
Water (fresh)	4.19	0.6	Hölting and Coldeway (2013)
NaCl-solution (0.25 mass-%)	3.30	0.574	Somerton (1992)

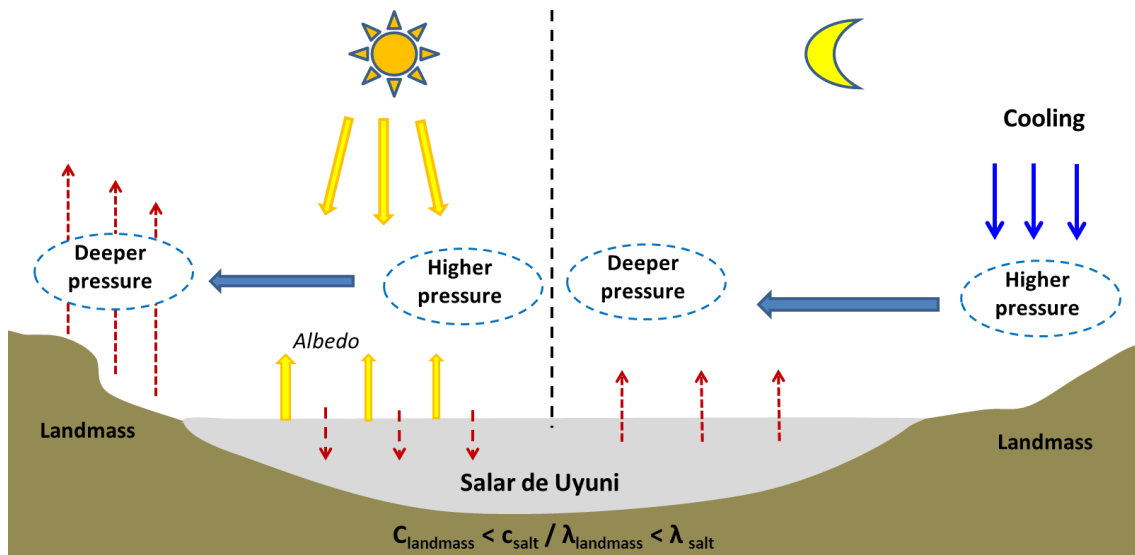


Figure 74: Principle of the salt breeze effect induced by different thermodynamic properties of the salt surface and the surrounding landmass at day and night.

In the afternoon, the salt surface also heats up due to the long-lasting intense solar radiation. The atmospheric pressure over the salt flat decreases because the heated air masses may also rise because of decreased air density. When the sun sets down and the angle of incidence decrease rapidly, the heating effect of the landmass is also less influenced. The landmass cools down more quickly than the salt surface because of the lower heat capacity and thermal conductivity. With decreasing temperatures, air masses become denser and sink down. Thus, the air pressure over the landmasses increases while the salt surface still acts as a heat source by warming up the near surface air masses, which then form a local low pressure cell (Figure 74). Therefore, on-salt flat winds of commensurate strength prevail in the late afternoon until night (Rife et al., 2002).

4.3.5.2 Effects of temperature on the brine levels

During the dry period in 2012, the daily brine level fluctuations varied between 0.9 – 9.7 cm at three observation sites. Lowest water levels occurred between 08:00 and 09:00, highest levels between 16:00 and 17:00. Similar daily water-level fluctuations were also observed in the Bonneville Salt Flats (USA) and in saline lakes in Australia. It was assumed that the observed water table fluctuations are driven both by temperature and barometric pressure effects (Turk, 1975, Macumber, 1991, Tyler et al., 2006).

The mean daily air temperature measured on the Island of Incahuasi showed a minimum in the morning between 09:00 and 10:00 whereby the maximum air temperature was reached in the afternoon at around 15:00, i.e. three hours after the zenith of the sun. However, it needs to be mentioned that the air temperature was measured at a protected place below a rock on the island of Incahuasi. This means, the measured absolute temperatures do not exactly represent the temperature conditions directly over the salt surface. However, due to the huge area of the salt flat and that the Island is completely surrounded by salt, the temperature conditions are assumed to be very similar.

Moreover, the brine temperature was measured in a depth of about 30 cm below the salt surface. Hence, it does not represent the true temperature of the salt surface which is directly heated by the incoming solar radiation. Thus, a certain time lag must occur between the fluctuations of the salt surface temperature and the brine temperature.

Due to seasonal variations, the scatter plot of brine level versus air temperature at site 03-INC is characterized by three distinct correlations (Figure 75). In the first part of the observed dry period (between May 12 and June 30, phase 1) a very strong linear relationship exists between air temperature and the brine level (correlation coefficient $r = 0.946$, coefficient of determination $R^2 = 0.93$, level of significance $p < 0.001$). However, starting in July this relation has changed significantly (phase 2). After about one month a new relationship between air temperature and brine level has adjusted ($r = 0.705$, $R^2 = 0.49$, $p < 0.001$, phase 3 in Figure 75).

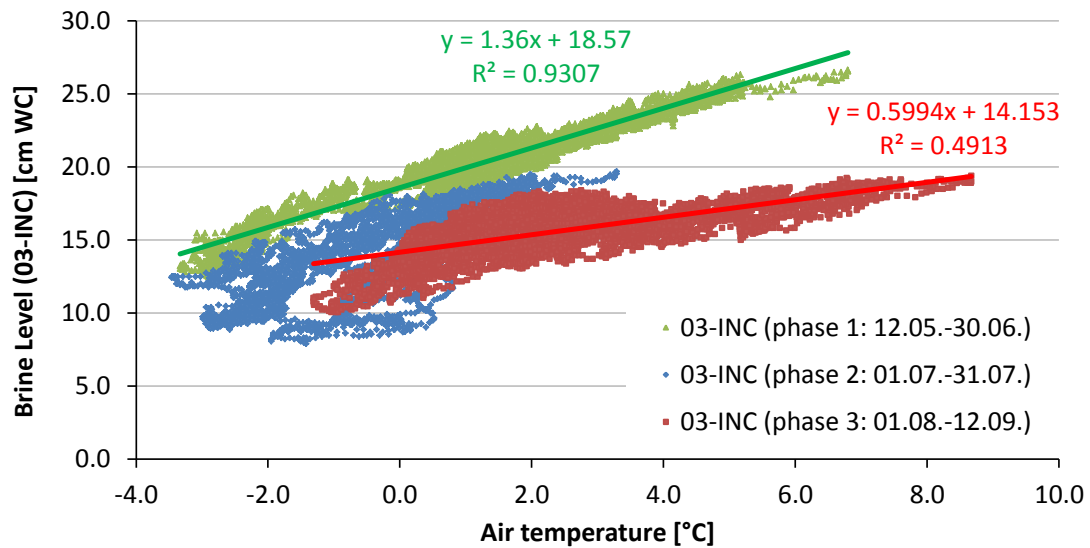


Figure 75: Linear correlation of the daily moving-averages of the air temperature and the brine level at observation site 03-INC (R^2 – coefficient of determination).

During the South American winter, the average daily air temperatures decreased from $+6.0^{\circ}\text{C}$ at the end of the rainy season (middle of May) to -2.5°C at the end of June 2012. Usually, at the end of July, air temperatures gradually increase again as can be seen from the climate diagram in chapter 1.5.2 (Figure 3). Indeed, in 2012, a short warmer period interrupted the coldest period of the year in the middle of July with average daily air temperatures of up to more than $+1^{\circ}\text{C}$ (Figure 76, top). At the end of July temperatures decreased again to the same temperature level as at the beginning of June 2012 (around -2°C). Afterwards, temperatures rose gradually until the end of the observation period.

In order to remove any seasonal effect on the correlation analysis, the daily moving-averages of air temperature and brine level were computed and plotted against each other (Figure 77). In fact, a significant linear correlation between air temperature and brine levels could be found for all three observation sites. However, the coefficients of determination (R^2) varied between 0.59 and 0.76 which means, that there must be another factor influencing the brine level beside the temperature.

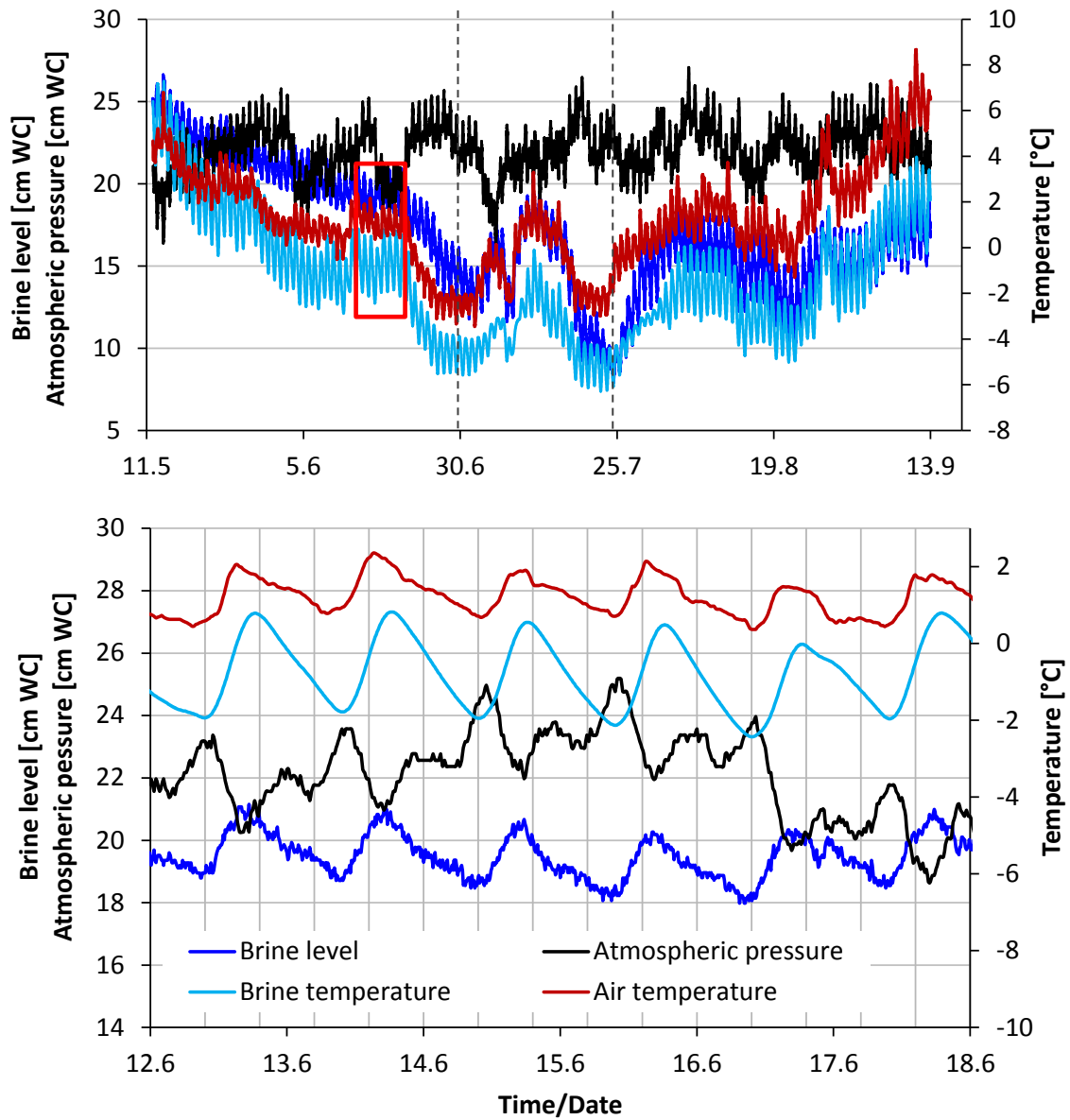


Figure 76: Illustration of the brine level, brine temperature, atmospheric pressure and air temperature at site 03-INC during the dry period between May 12 – September 12, 2012 (top) and in detail for the short period of one week in June 2012 (bottom). The original atmospheric pressure data were shifted by -650 cm WC for better graphical representation. Dashed lines (top) subdivide the observation period into three phases (for further explanations, see text).

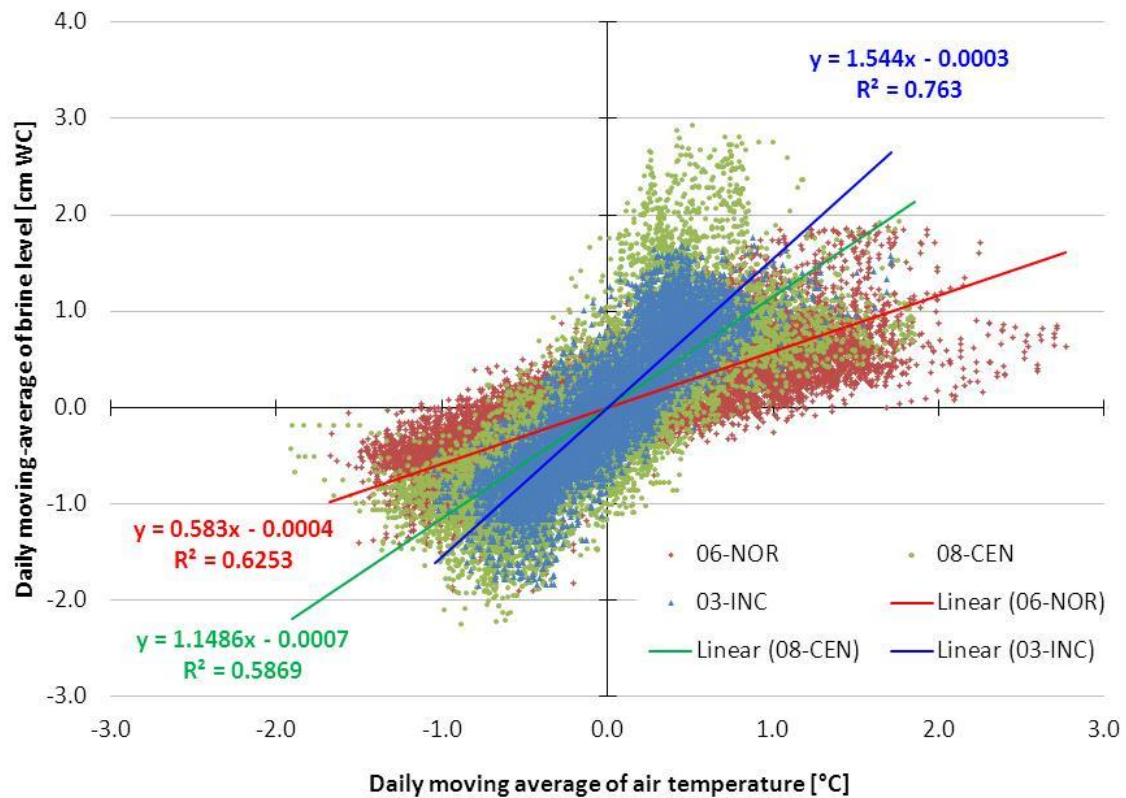


Figure 77: Correlation between daily moving averages of brine level and air temperature for the sites 03-INC, 06-NOR and 08-CEN.

Turk (1975) described a temperature dependency of brine levels in the Bonneville salt flats by two distinct effects:

- 1) In the unsaturated pore space between the brine level and salt surface, the atmospheric air can be trapped. When the near surface brine rises due to capillary forces and is followed by evaporation, the dissolved salts precipitate within the pore space as a consequence of oversaturation. This precipitation of salt minerals leads to sealing and compaction of pores in the surface-near salt crust. Thus, certain parts of the unsaturated zone can be partly or completely sealed to the atmosphere. Pore-filling air cannot escape anymore. When the sun warms the salt crust from the surface, the trapped air will also heat up during the day. Hence, the thermal expansion of the air induces higher pore pressure in the unsaturated zone. Consequently, interstitial water will be squeezed out of the unsaturated zone and into the saturated zone. The pore water contribution to the brine level leads to rising total brine levels.
- 2) With increasing temperature, the brine surface tension also decreases. Consequently, interstitial water from the unsaturated zone will also flow further downward and will feed the brine level. These two effects have been verified in detail via laboratory experiments (Turk, 1975)

Another effect mentioned by Macumber (1991) is the direct influence of changes in atmospheric pressure on the total pressure on trapped air. When atmospheric pressure rises, air trapped in the pores will be compressed. Therefore, more water can rise by capillary forces into the unsaturated zone. In contrast, when atmospheric pressure decreases, trapped air may expand and the available interstitial water will be squeezed out from the unsaturated zone and contributes to the rise in brine level.

Furthermore, in consideration of the confined aquifer conditions as shown by the calculated barometric efficiency (chapter 4.3.4), atmospheric pressure changes also directly influence the brine level. If the atmospheric pressure decreases, the brine level rises (Figure 76, bottom).

In conclusion, both the daily temperature variations and atmospheric pressure changes strongly influence the brine level of the Salar de Uyuni during the day.

4.3.6 Temporal behavior of the Rio Grande river level

The Rio Grande in the south of the Uyuni salt flat is the main tributary which discharges water all year from the catchment into the salt flat basin. Because of its complex and extensive delta region of about 300 km² (Risacher and Fritz, 1991), discharge quantification is very difficult. Thus, long-term observations of the stream level were conducted in order to indirectly get insights in the stream discharge fluctuations over time. Moreover, water temperature and specific conductivity were also recorded. The measured data are plotted in Figure 79 on the left axes.

Abnormal peaks in the water level and specific conductivity datasets were detected after about 6 months of monitoring. Figure 78 shows 13 of the altogether 15 abnormal peaks in the stream level and specific conductance data in detail. All peaks occurred in the morning between 03:00 and 10:00 and last for about 2 to 6.5 hours. The water level reached several meters of water column (between 0.8 and 8.4 m) which is enormous. In contrast, the specific conductivity showed minimum values at those times. Furthermore, it is conspicuous, that during the appearance of these peaks, the water temperature was always negative (Figure 78). Consequently, the stream water was frozen, at least around the used measurement sensor of the CTD-Diver. Hence, the specific conductivity decreased rapidly to nearly zero. The water level peaks can be explained by the volume expansion of freezing water. Especially, when water freezes in the hole of the boulder in which the CTD-Diver was installed (Figure 17 in chapter 3.1.4) the total pressure increases and thus abnormally high water levels were detected.

For further considerations, the peaks in water level and specific conductivity caused by freezing were removed by cubic interpolation using the Tsoft software package (Figure 79, right axis).

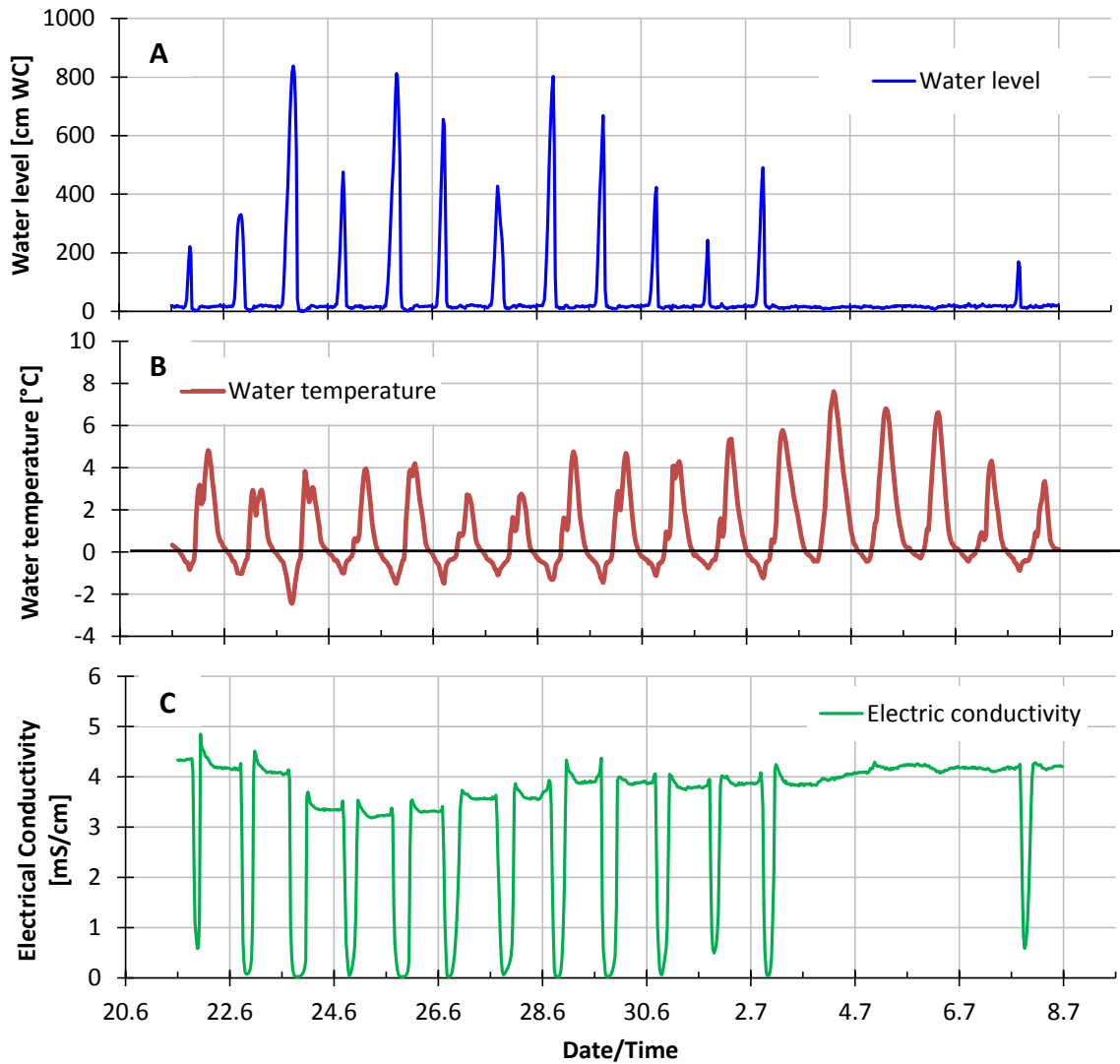


Figure 78: Anomaly of (A) water level, (B) water temperature and (C) specific conductivity in the Rio Grande data records between June 21 and July 8, 2012.

Figure 79 shows data records between Dec. 19, 2011 and Sep. 13, 2012 for water level, water temperature and specific conductivity of the Rio Grande River.

One can clearly see the high river level in the time span between December and March which is the rainy season. Here, maximum water levels of 65 cm above the CTD-Diver were recorded. The specific conductivity increased during the rainy season until February. This is in contradiction with the assumed dilution effect due to higher water supply from the catchment area. But with increased surface runoff the amount of dissolved salts and sediment transport from the surrounding mountains also increases. This is in agreement with observations from Wolf (2010) who described a stage of intense chemical weathering and erosion at the beginning and during the rainy season which he calls desert soil weathering. With decreasing precipitation and surface runoff in the winter months the specific conductivity also decreases.

4. Results and Interpretation

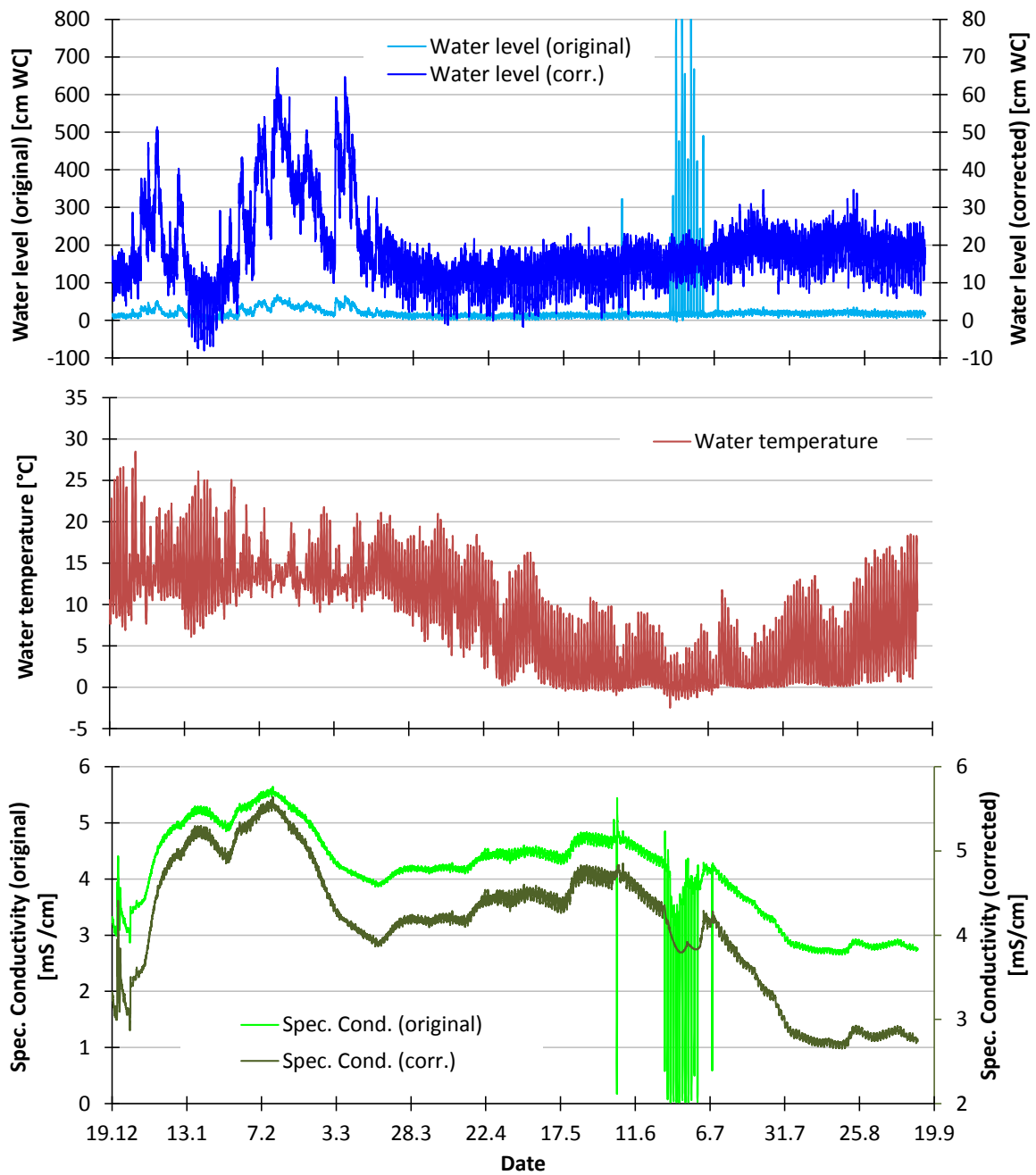


Figure 79: Water level, water temperature and electrical conductivity of the Rio Grande de Lipetz between Dec. 19, 2011 and Sept. 13, 2012. Abnormal peaks in water level and specific conductivity were removed by cubic interpolation in Tsoft (corrected data are shown on the right axis).

Starting in the middle of March when precipitation is less frequent, the Rio Grande stream level, water temperature and specific conductivity show characteristic diurnal fluctuations similar to those observed in the brine level records. In order to focus on the daily variations of the parameters, long-term variations of the data were removed by high-pass filtering. Thus, Figure 80 illustrates the mean daily fluctuations of stream level, water temperature and specific conductivity (each related to zero) for the time

period between March 18 and June 6, 2012 in Rio Grande de Lipez (Note: The chart values do not represent real measuring data).

The stream level is characterized by an early morning maximum around 07:00 and an afternoon minimum between 12:30 and 13:00 (Figure 80). In the afternoon, the water level rises again and returns to its initial level at around 20:00. It then remains nearly constant throughout the night until the next morning. The daily change in stream water level varied between 9.9 cm and 20.4 cm (mean daily amplitude = 15.3 cm) in the dry period from March 18 to June 3, 2012.

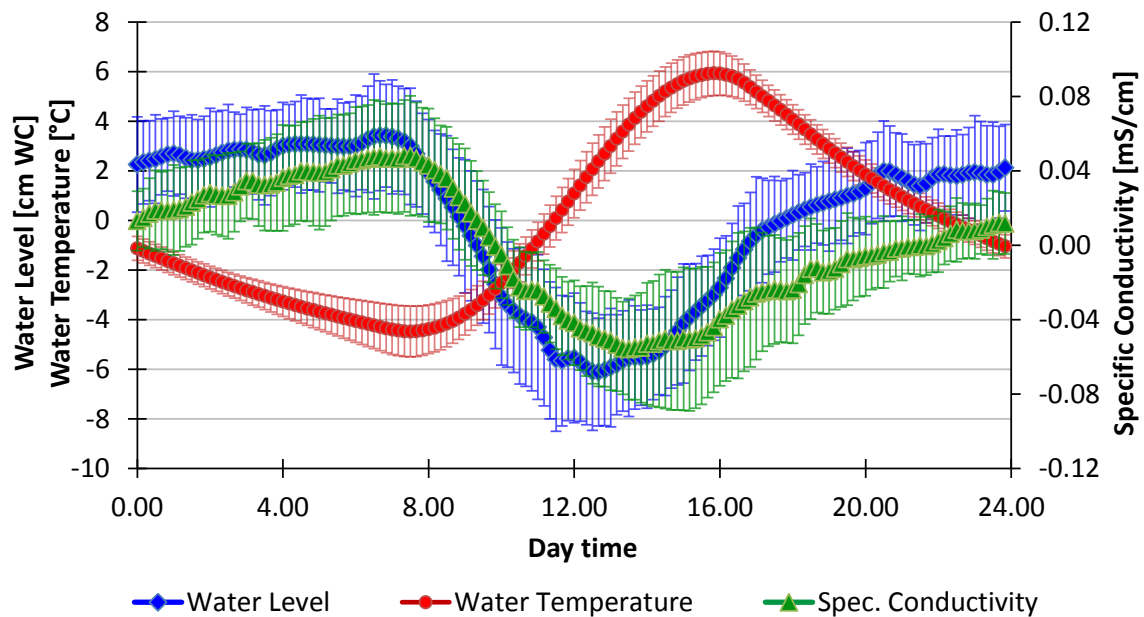


Figure 80: Mean daily fluctuations in water level, water temperature and specific conductivity of the Rio Grande River in the dry season between March 18 and June 03, 2012 ($n = 77$ days). Long-term trends were removed for all three parameters by high-pass filtering (cut-off frequency = 0.5 cpd, band width = 0.5 cpd).

Similar diurnal cycles in the stream flow rates are also described by White (1932), Lautz et al. (2008) and Gribovszki (2010) as a consequence of plant evapotranspiration in the catchment area. After sunrise, the water consumed by the vegetation from the shallow aquifers increases due to higher plant transpiration rates. During the night, vegetation transpiration is reduced and thus the net influx of groundwater induces recharge which results in maximum water levels in the early morning. Maximum changes of up to 20 cm were observed on hot summer days in consequence of the strong evapotranspiration by riparian vegetation (Gribovszki et al., 2010). This is the same order of magnitude as the daily stream level variations measured at the Rio Grande. Indeed, diurnal groundwater levels are generally described by a minimum level between 18:00 and 19:00 and a maximum level between 07:00 and 09:00 (Lautz, 2008). Thus, the ET-induced diurnal signals in the groundwater level would theoretically lag behind the measured Rio Grande stream flow rates by about 1 hour in

the morning and 4 to 5 hours in the afternoon. Such a peculiar time lag of about 1 – 1.5 h between groundwater and stream flow fluctuations was also observed by Gribovszki et al. (2008) in a small forested watershed. This is explained by temporal variations in the relative importance of local or regional hydraulic gradients (Szilágyi et al., 2008).

In fact, the stream level is influenced by the physical evaporation of the river water, capillary rising shallow groundwater from bare soils and the daytime vegetation transpiration. At night, almost all of the spring water which feeds the river network in the catchment area reaches the observation point near the Rio Grande delta into the Uyuni salt flat for long-term stream level measurements.

4.3.6.1 Estimation of long-term average evapotranspiration in the Rio Grande catchment area

From the magnitude of the daily water level fluctuations, the evapotranspiration rate of the vegetation can be estimated (White, 1932).

When using the long-term daily average Rio Grande water level fluctuations (Figure 80), even the long-term average evapotranspiration of the catchment area can be approximated.

The evapotranspiration ET [mm d⁻¹] can be calculated according to the empirical equation from White (1932).

$$ET = S_y(24 \cdot r \pm s) \quad (4.4)$$

Where S_y – Specific yield of the aquifer or soil sediments [1]

r – Slope of the tangential line drawn on the mean daily water level curve in the section between 0:00 and 04:00 in the morning [mm h⁻¹]

s – Difference in the observed mean groundwater levels over the 24-h period [mm d⁻¹]

The determination of the parameters r and s is based on Figure 81 in accordance with Gribovszki (2008). Before calculating the mean diurnal water level, all dry season water level data were high-pass filtered (cut-off frequency: 0.5 cpd) in order to avoid the impact of seasonal water level variations.

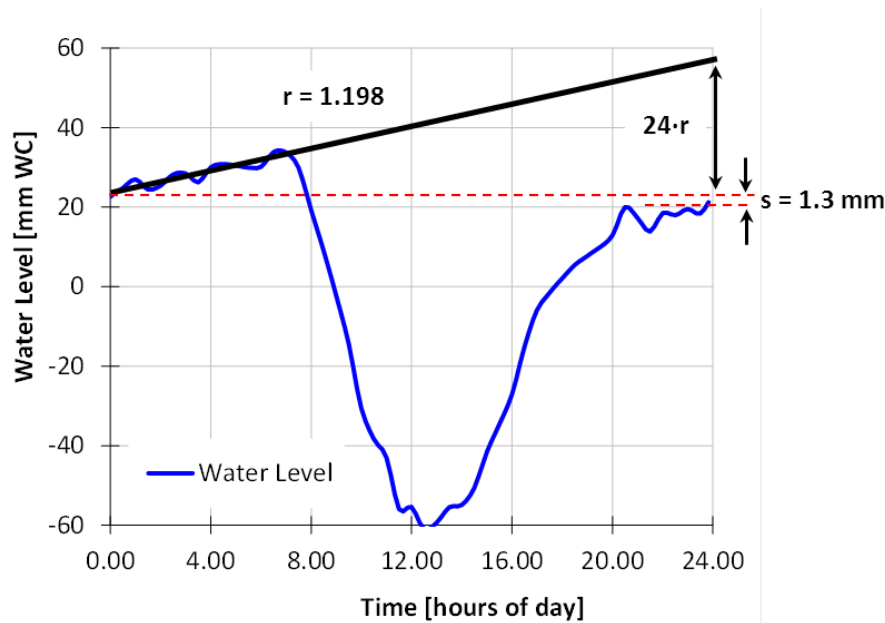


Figure 81: Mean diurnal water level fluctuation of the Rio Grande in response to evapotranspiration (water level data are high-pass filtered in Tsoft using a cut-off frequency of 0.5 cpd).

The specific yield S_y of the aquifer or soil sediments in the catchment area is the most challenging parameter to determine. Since no further hydrogeological investigations were done in the catchment area of the Rio Grande, literature data of comparable systems have to be used. Salas et al. (2010) describes the alluvial aquifer at the eastern margin of the Salar de Atacama which might be comparable with the alluvial sediment around Rio Grande de Lipez in Bolivia. They report a specific yield in the range between 10^{-1} and 10^{-4} . Assuming that evapotranspiration by plants and also the physical evaporation of capillary-rising shallow groundwater predominantly occur from shallow depths, the higher values of specific yield can be also assumed. Thus, most realistic values for the Rio Grande catchment area seem to be close to the upper limit of the given range (i.e. close to $S_y < 0.1$).

Sediments with higher specific yield, such as sandy sediments, only show muted water-level fluctuations due to ET. “In coarser sediments, small water-table fluctuations release a greater volume of water than in finer sediments, and therefore, equal evapotranspiration rates from the water table will generate smaller water-table fluctuations in coarser sediments” (Lautz, 2008).

Hence, two different scenarios will be considered in the following discussion.

- | | | |
|-------------|--------------|--------------------|
| Scenario 1: | $S_y = 0.1$ | → ET = 3.01 mm/day |
| Scenario 2: | $S_y = 0.01$ | → ET = 0.30 mm/day |

If enough water is supplied, lysimeter grass evapotranspiration on the Altiplano for four different stations revealed an average ET of 4.3 mm/day for optimal grass cropping during the period between April and October (Garcia et al., 2004). Since no optimal water supply is available for the evapotranspiration of plants on the Altiplano

especially in the dry season, real evapotranspiration values need to be lower than 4.3 mm/day which is also given by scenario 1.

However, scenario 2 is comparable with previous studies reported by Turk (Turk, 1975) for the Great Salt Lake where pure physical evaporation (without plants) was determined to be $ET = 0.76$ mm/day directly on the salt surface, and about 0.13 mm/day for the mud areas (Turk, 1975). At the Salar de Atacma, Kampf et al. (2005) also determined evaporation rates of similar magnitude (0.4 ± 0.0 mm/day) for the partially vegetated wetland margin in August 2001 (during the South American winter).

In accordance with Turk (1975), the maximum expected daily stream-flow fluctuation can be estimated by:

$$\Delta h_{\max} = \frac{ET}{n_{\text{eff}} - n_{\text{capill.}}} \quad (4.5)$$

Where Δh_{\max} – Maximum expected stream-level fluctuation [mm]
ET – Evaporation rate [mm/day]
 n_{eff} – Effective porosity of the unsaturated zone [-]
 $n_{\text{capill.}}$ - Pore space occupied by capillary water [-]

When assuming a specific yield of 0.05, which corresponds to an effective porosity of 5%, and a fraction of the effective pore space occupied by water held by capillary forces of 80%, then the maximum fluctuation in the stream-water level would account for 2.7 cm.

When increasing the assumed specific yield to 0.1, then the daily fluctuation would account for 13.5 cm which matches quite perfect with the average amplitude of the daily fluctuations observed at the Rio Grande stream level.

However, the catchment area of the Rio Grande River belongs to the southern Puna ecoregion, which is a desert vegetation belt between 3,800 and 5,000 m a.s.l. in the southern part of the Andean Cordillera. The area is characterized by scarce vegetation cover, predominantly bushes, halophytic species (Ortuño et al., 2011), tropical alpine herbs and dwarf shrubs (Locklin, 2001).

Therefore, high contributions of evapotranspiration by plants to the total evaporation are not likely. Thus, physical evaporation of the near-surface groundwater especially near springs, creeks and rivers seems to be the dominant process controlling the water level of the main Rio Grande de Lipez tributary.

5 Final Discussion and Conclusions

The global demand for lithium increases due to its need as a raw material for the production of high-capacity lithium-ion batteries. These in turn are a prerequisite for the development of the electric mobility sector. The Salar de Uyuni in Bolivia is the largest salt flat in the world and is also supposed to be one of the largest lithium-rich brine deposits worldwide. Thus, in recent times, the Salar de Uyuni has become more attractive in the field of resource security.

Due to its high solubility, lithium occurs in dissolved form in brine that fills the pore space of the huge salt flat. With the background of a potential industrial lithium extraction at the Salar de Uyuni in the future, extensive hydraulic investigations were performed in this thesis with special emphasis on porosity and permeability of the upper salt layer as well as on the physical properties of the brine.

One aim of the thesis was to explore the spatial porosity distribution of the halite layer in detail in order to estimate the total amount of lithium occurring in the brine of the Salar de Uyuni. Additionally, the brine behavior and flow conditions as well as the influence of annual flooding and desiccation on the hydraulic properties should be examined.

Re-evaluation of the lithium reserves in the Salar de Uyuni

Three different laboratory approaches were used to determine the porosity of salt core samples. The application of micro-CT analysis provided information about the total porosity, the pore size distribution as well as the pore structure. Due to the limited voxel resolution in computed tomography, the smallest detectable pore object has an equivalent diameter of only 56 μm . Thus, nanopores (<100 nm) and in part also micropores (0.1 – 100 μm) cannot be detected and quantified by this method. In contrast, the direct method (complement method using plasticine, chapter 3.2.7.3) gives reliable results of the total porosity since all pores are captured regardless of their size. However, considerations of the pore size distribution within the core samples have shown that objects with a single pore volume less than 0.1 mm^3 contribute very little to the total porosity (between 1.1 and 8.8%, chapter 4.1.2). Because of the very small proportion of nanopores to the total porosity and the small hydraulic diameter, this pore class does not contribute significantly to the hydraulic flow conditions in the Uyuni salt crust and therefore can be neglected in this study.

The saturation method, which uses 2-octanol in order to avoid any dissolution processes of the salt core samples, can be used to determine the effective porosity that is available for brine flow within the salt. However, closed pores are not considered by this method.

In conclusion, after applying all three porosity determination approaches, it was found that the upper salt layer is characterized by a depth-dependent porosity distribution: The uppermost 2 m of the salt crust are characterized by very high porosity ranging

between 30 and 39%. Conversely, the salt at greater depth is characterized by a significantly lower average total porosity of about $13.5 \pm 3.7\%$.

These results are in part in contradiction with previous studies (Ericksen et al., 1977, Risacher and Fritz, 1991, Gruber et al., 2011) which assumed an overall average porosity of the entire Uyuni salt layer between 30% and 40%. These values are based on porosity estimates of hard samples that probably came from the salt surface or only shallow depth (not given in these publications).

Major challenges lie in the quantification of the macroporosity. Large pore objects several centimeters in size or even a very high total porosity cannot be properly represented by the drilled core. This is due to the limited size of the core samples in this study with a diameter of only 6.2 cm. This could also be seen by the high core loss during drilling, especially in the friable salt horizon of the uppermost 2 m of salt crust.

Cavities and preferential flow channels within the salt or even the occurrence of brine pools cannot be quantified by laboratory analyses on core samples. Rather, they require hydraulic field tests. The evaluation of pumping test data gives an integral value for the specific yield of that part of the aquifer which is influenced by the pumping test. Under unconfined aquifer conditions, the obtained specific yield corresponds to the storage coefficient (drainable porosity) which also comprises preferential flow paths, cavities or even larger brine pools occurring in the aquifer sector influenced by the pumping test.

However, the determination of the storage coefficient from the pumping test data is very sensitive to the fulfillment of boundary conditions or the necessary requirements for the data evaluation (e.g. horizontal flow conditions). Even with limitations in the reliability of the calculated storage coefficients (see chapter 4.2.2.2), there are conformities between some computed storage coefficients and the measured average porosity.

A geochemical analysis of brine samples confirmed that the general spatial lithium distribution in the brine coincided with previously described values. Hence, our data could be used to refine the knowledge about the lithium distribution. Finally, stratigraphic information from the exploration drillings provided insights in the salt layer thickness.

Based on the results of porosity, lithium distribution and salt thickness, the total lithium reserves of the upper salt layer of the Uyuni salt flat was computed to be about 7.0 ± 1.1 million tons. This is considerably lower than estimates by previous studies which estimated about 9.0 to 10.2 million tons lithium (Risacher and Fritz, 1991, USGS, 2014, Gruber et al., 2011).

However, it should be noted that deeper salt horizons were not considered in the reserve estimation due to the lack of information concerning the porosity and lithium-concentrations in the brine of deeper halite layers. Therefore, future research should focus on the recovery and investigation of salt core samples from deeper salt layers. However, modern shallow buried saline pan halites show a strong decline in porosity converging to nearly zero at depth below 40 m of burial by cementation and

compaction (Casas and Lowenstein, 1989). Thus, it can be concluded that deeper salt horizons of the Salar de Uyuni do not significantly contribute to the total lithium sources even if lithium concentrations of deeper brines would be higher compared to those in the uppermost salt layer. Hence, no large lithium quantities may exist in deeper layers which are economically worth to extraction.

Implications from permeability properties on brine flow conditions

Pumping tests on the salt flat revealed a rather high horizontal intrinsic permeability of the upper salt layer which is a positive aspect in consideration of a possible future lithium extraction from the Uyuni brines. Though, due to the characteristic layering of the salt flat sediments a distinct vertical anisotropy occurs with respect to the permeability properties. Thus, the average vertical permeability examined by laboratory experiments is orders of magnitude smaller than the horizontal one due to the presence of thin layers of gypsum or clay sediments interbedded in the halite formation. For instance, the extremely low gas permeability measured for instance for a sample from a 2 cm thick gypsum layer confirms the large heterogeneity in vertical sediment permeability.

The pore structure was inspected visually as well as by X-ray computed tomography on salt core samples. The predominant round to elliptical shape of the pore objects in core samples from the uppermost two meters indicates dissolution processes. These are probably caused by the entrance of freshwater from rainfall or surface runoff, especially during the rainy season leading to mixing and dilution of the near-surface brine. Hence, a highly porous friable salt zone is formed by dissolution. This highly porous part of the salt layer is a prerequisite for any significant brine movement over large areas.

In contrast, in greater depth the core samples were mostly dense and compact but often contain little cavities of several centimeters in size that are closed by cubic halite crystals. From this, one can conclude, that the brine must be saturated or even in equilibrium with the salt. Consequently, no influence of dilution by freshwater input from the surface has been identified in greater depth. Thus, the vertical anisotropy in the sediment permeability and/or the higher density of the mature brine at depth avoid any significant vertical brine movement or mixing at greater depth.

Considerations of the occurrence of brine recharge and density-driven circulation

The average amount of rainfall at the Salar de Uyuni can be assumed to be 200 mm/a. Furthermore, permanent inflow of varying discharge is coming through the main tributary Rio Grande de Lipez all the year. However, the potential evaporation is estimated to about 1500 mm per year (chapter 1.5.2). Indeed, calculating a net recharge from the available data is a challenge.

During the dry season, the brine surface is only a few centimeters to decimeters below the salt surface. Hence, it can be stated that on average there is no loss of water from

the brine through evaporation, because the brine level can be considered to be static in accordance with Houston (2011).

It can even be assumed that the salt crust becomes nearly impermeable and the impact of evaporation on further brine level drawdown is consequently limited. This could be explained by the evaporation of near-surface brine which rises to the salt surface by capillary forces. Hence, dissolved salts from the brine would precipitate in the pore space of the salt crust. Thus, the permeability of the uppermost centimeters of the salt crust would be greatly reduced.

Unfortunately, no evidence could be found for this assumption in this study due to a lack of well-preserved core samples from the uppermost centimeters of salt for inspection by X-ray tomography or flow-through experiments. Under the assumption of the existence of a nearly impermeable thin crust portion, it could be concluded that the evaporation of the brine is limited or even completely suppressed. This would be in strong agreement with investigations by Kampf et al. (2005). They measured nearly zero evaporation over the rugged halite salt crust of the interior of the Salar de Atacama which is comparable with that of the Salar de Uyuni. Therefore, the brine level remains nearly constant over a long-time average and a dynamic equilibrium is assumed to be established in this way.

Nevertheless, considering that the salt surface of the Uyuni salt flat is increasing by 4 mm per 100 years (Ericksen et al., 1977, chapter 4.2.4) a net recharge of 0.014 mm/a can be assumed (assuming an average total porosity of 35%). However, if one assumes that the porosity in deeper parts of the salt crust (2-3 m) is steadily decreasing by cementation through precipitation of halite (and other minerals) on the one side (Casas and Lowenstein, 1989) and compaction (through the overburden) on the other side (Baar, 1977), the net recharge could be as well close to zero. In that case only dissolved constituents, colloids and sediment are added to the salt flat by means of the annual flooding.

Radiocarbon dated brine samples from different depths have shown that the brine from a certain depth is nearly as old as the salt layer of that depth. Therefore, it can be concluded that no significant vertical brine movement or mixing occurs within the upper salt aquifer. Hence, the net annual brine recharge is probably very low under natural equilibrium conditions.

Furthermore, no clear evidence for the occurrence of density-driven brine flow within the upper salt layer has been identified. Nevertheless, further research is recommended in this special topic.

Reasons for temporal brine level fluctuations

Long-term observations of the brine level, brine temperature, atmospheric pressure and air temperature on the Uyuni salt flat, as well as of the water level, water temperature and specific conductivity of the Rio Grande tributary, gave insight in the annual cycle of flooding and desiccation of the Salar de Uyuni. Besides the influence of

the rainy season when almost the entire salt flat was flooded, distinct daily brine level changes occurred in the dry season. It was found that the diurnal (1 cpd frequency) variations in the brine level cannot be explained by a simple atmospheric pressure effect under confined aquifer conditions because of a positive time lag between brine level minimum and atmospheric pressure peak.

Alternatively, in accordance with observations by Turk (1975) for the Bonneville salt flats, a temperature effect can be assumed to be responsible for the observed diurnal brine level fluctuations at the Salar de Uyuni. By heating of the salt due to intense radiation at day time, the surface tension of the brine decreases. Hence, capillary brine from the unsaturated zone contributes to the brine level and triggers a brine level rise in the early afternoon (Figure 82). Additionally, due to thermal expansion of trapped air, pore pressure rises and capillary water will be squeezed out. At night, the process is reversed and brine starts rising by enhanced capillary forces which lead to a brine level decrease (Figure 82).

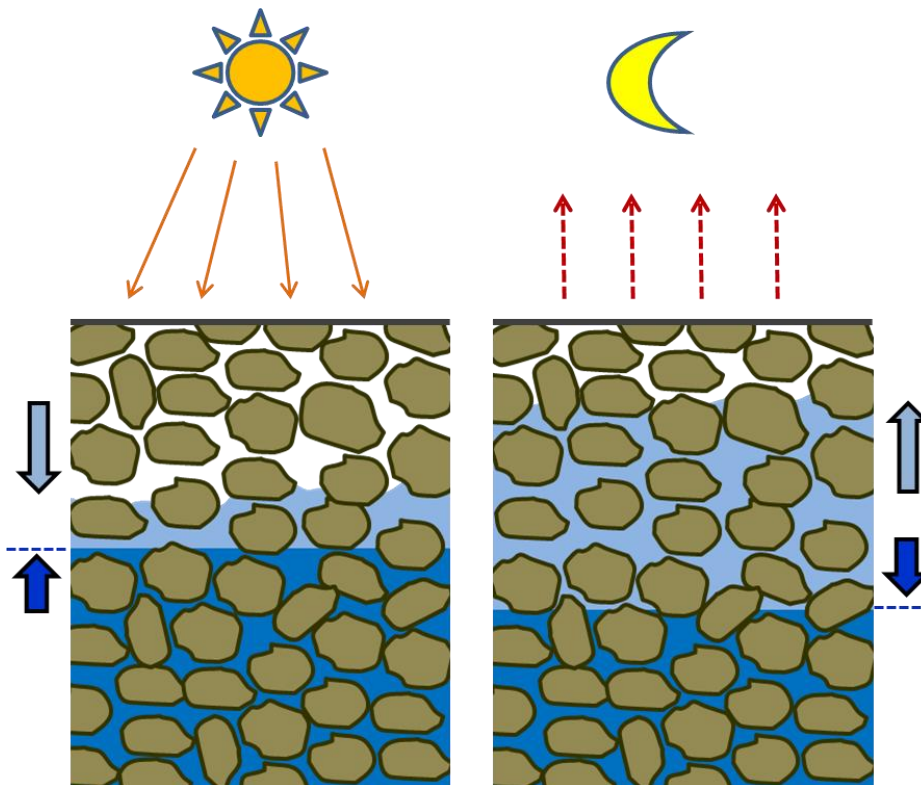


Figure 82: Sketch of the daily brine level fluctuations in consequence of a temperature effect due to warming during daytime and cooling at night (the capillary zone is marked in light blue, brine groundwater is marked in dark blue, dashed lines mark the brine head).

Unexpectedly, diurnal fluctuations were also observed in the Rio Grande water level during the dry season. In contrast to the brine level, these variations could be attributed to the influence of evaporation in the catchment area leading to a river level minimum in the early afternoon.

Recommendations for future research

As can be seen from the above conclusions, various new questions have arisen during the course of this study. The following suggested research should be undertaken to solve the following open questions at the Salar de Uyuni:

- Infiltration tests in the field or systematic high resolution computed tomography analysis of well-preserved salt core samples from the uppermost part of the salt crust have to be conducted in order to confirm the assumed salt crust impermeability, at least in the dry season. Additionally, laboratory experiments can be used to simulate the processes of capillary rise, evaporation and precipitation of salts in the unsaturated part of salt crust.
- Deeper drillings and repeated pumping tests have to be conducted in order to find out if there is possible leakage or brine flow through the lacustrine sediments between two salt aquifers.
- In order to quantify and map brine pools and preferential flow paths (channels in the salt) in the large area of the salt flat, the possibility of using geophysical methods such as ground penetrating radar (GPR) should be tested.
- Geochemical and isotopic investigations may give insight into the formation of the brine pools. They are useful to differentiate between the possible influx of deep geothermal fluids through fault zones and fractures or the incoming groundwater from the marginal zones along preferential highly permeable sediment layers.
- Further investigations are needed to determine the inflow of groundwater from the surrounding area and the interface between the Uyuni brine and the surrounding groundwater. Consequently, the hydraulic properties (porosity and permeability) of the marginal zones in the surrounding of the salt flat have to be extensively explored by core drillings, pumping tests or geophysical methods.
- The possible occurrence of density-driven brine circulation or forced free convection needs to be studied in detail. Therefore, salinity profiles, brine-level changes, and the hydraulic head of the surrounding aquifers need to be investigated for longer time periods. Seasonal temperature variations and freshwater inflow during the rainy season might also induce density gradients in the brine.
- Finally, a long-term evaluation of the hydrological balance of the Uyuni basin is necessary in order to estimate the average annual brine recharge and to improve the understanding of the dynamic equilibrium of the brine level which is supposed to be reached during the dry season.

6 References

- ABBOTT, M. B., WOLFE, B. B., ARAVENA, R. N., WOLFE, A. P. & SELTZER, G. O. (2000) Holocene hydrological reconstructions from stable isotopes and paleolimnology, Cordillera Real, Bolivia. *Quaternary Science Reviews*, 19, 1801-1820.
- ABELL, L., OPPENHEIMER, P. & SCHOOL, U. N. P. (2008) World Lithium Resource Impact on Electric Vehicles. *Plug in America*.
- ABID, M., HAMMERSCHMIDT, U. & KÖHLER, J. (2014) Thermophysical properties of a fluid-saturated sandstone. *International Journal of Thermal Sciences*, 76, 43-50.
- ACOSTA, O. & CUSTODIO, E. (2008) Impactos ambientales de las extracciones de agua subterránea en el Salar del Huasco (norte de Chile). *Boletín Geológico y Minero*, 119, 33-50.
- ACWORTH, R. & BRAIN, T. (2008) Calculation of barometric efficiency in shallow piezometers using water levels, atmospheric and earth tide data. *Hydrogeology Journal*, 16, 1469-1481.
- AKIN, H. & SIEMES, H. (1988) *Praktische Geostatistik - Eine Einführung für den Bergbau und die Geowissenschaften*, Berlin, Heidelberg, Springer.
- AMRO, M., HÄFFNER, F. & FREESE, C. (2012) Speichertechnik - Moderne In-situ- und Labormessung von Permeabilität und Porosität zum Dichtheitsnachweis von Speichern für Wasserstoff, Erdgas und CO₂ *Erdöl, Erdgas, Kohle: Aufsuchung und Gewinnung, Verarbeitung und Anwendung, Petrochemie, Kohlenveredlung*, 128, 154-160.
- ARGOLLO, J. & MOURGUIART, P. (2000) Late Quaternary climate history of the Bolivian Altiplano. *Quaternary International*, 72, 37-51.
- ARMBRECHT, J., SYCH, T. & ROBB, K. (2006) MAVI - Modular Algorithms for Volume Images V1.9.1. Fraunhofer Institut für Techno- und Wirtschaftsmathematik.
- BAAR, C. A. (1977) *Applied salt-rock mechanics*, Amsterdam, Elsevier.
- BAKER, P. A. (2001) The History of South American Tropical Precipitation for the Past 25,000 Years. *Science*, 291, 640-643.
- BAKER, P. A., RIGSBY, C. A., SELTZER, G. O., FRITZ, S. C., LOWENSTEIN, T. K., BACHER, N. P. & VELIZ, C. (2001) Tropical climate changes at millennial and orbital timescales on the Bolivian Altiplano. *Nature*, 409, 698.
- BALLIVIAN, O. & RISACHER, F. (1981) Los Salares del Altiplano boliviano - Metodos de Estudio y Estimación económica.
- BATU, V. (1998) *Aquifer hydraulics: a comprehensive guide to hydrogeologic data analysis*, New York, Chichester, Weinheim, Brisbane, Singapore, Toronto, Wiley-Interscience Publication.
- BAVEYE, P. C., LABA, M., OTTEN, W., BOUCKAERT, L., DELLO STERPAIO, P., GOSWAMI, R. R., GRINEV, D., HOUSTON, A., HU, Y., LIU, J., MOONEY, S., PAJOR, R., SLEUTEL, S., TARQUIS, A., WANG, W., WEI, Q. & SEZGIN, M. (2010) Observer-dependent variability of the thresholding step in the quantitative analysis of soil images and X-ray microtomography data. *Geoderma*, 157, 51-63.
- BERNARD, S. & DELAY, F. (2008) Determination of porosity and storage capacity of a calcareous aquifer (France) by correlation and spectral analyses of time series. *Hydrogeology Journal*, 16, 1299-1309.
- BOBST, A. L., LOWENSTEIN, T. K., JORDAN, T. E., GODFREY, L. V., KU, T.-L. & LUO, S. (2001) A 106 ka paleoclimate record from drill core of the Salar de Atacama, northern Chile. *Palaeogeography, Palaeoclimatology, Palaeoecology*, 173, 21-42.

6. References

- BRÄUNING, A. (2009) Climate variability of the tropical Andes since the late Pleistocene. *Advances in Geosciences*, 22, 13-25.
- BROBST, D. A. & PRATT, W. P. (Eds.) (1973) *United States Mineral Resources*, Washington, United States Government Printing Office.
- BUNDESREGIERUNG (2009) Nationaler Entwicklungsplan Elektromobilität der Bundesregierung.
- BUSCH, K.-F., LUCKNER, L. & TIEMER, K. (1993) *Geohydraulik*, Berlin, Stuttgart, Gebrüder Borntraeger.
- CARMONA, V., PUEYO, J. J., TABERNER, C., CHONG, G. & THIRLWALL, M. (2000) Solute inputs in the Salar de Atacama (N. Chile). *Journal of Geochemical Exploration*, 69-70, 449-452.
- CARPIO, J. M. (2007) Agua y recurso hídrico en el Sudoeste de Potosí. La Paz, Bolivia, FOBOMADE - Foro Boliviano sobre Medio Ambiente y Desarrollo.
- CASAS, E. & LOWENSTEIN, T. K. (1989) Diagenesis of saline pan halite; comparison of petrographic features of modern, Quaternary and Permian halites. *Journal of Sedimentary Research*, 59, 724-739.
- CASAS, E., LOWENSTEIN, T. K., SPENCER, R. J. & PENGXI, Z. (1992) Carnallite mineralization in the nonmarine, Quaidam Basin, China: Evidence for the early diagenetic origin of potash evaporites. *Journal of Sedimentary Petrology* 62, 881-898.
- CHEPSTOW-LUSTY, A., BUSH, M. B., FROGLEY, M. R., BAKER, P. A., FRITZ, S. C. & ARONSON, J. (2005) Vegetation and climate change on the Bolivian Altiplano between 108,000 and 18,000 yr ago. *Quaternary Research*, 63, 90-98.
- CLAPPERTON, C. M., CLAYTON, J. D., BENN, D. I., MARDEN, C. J. & ARGOLLO, J. (1997) Late Quaternary Glacier Advances and Palaeolake Highstands in the Bolivian Altiplano. *Quaternary International*, 38/39, 49-59.
- CLARK, I. & FRITZ, P. (1997) *Environmental Isotopes in Hydrogeology*, Lewis Publishers.
- CNUDDE, V. & BOONE, M. N. (2013) High-resolution X-ray computed tomography in geosciences: A review of the current technology and applications. *Earth-Science Reviews*, 123, 1-17.
- COMIBOL (2011) Memoria 2011. Generencia Nacional de Recursos Evaporíticos, <http://www.evaporiticos.gob.bo/wp-content/uploads/2012/06/memoria2011.pdf>, accessed on 15-03-2012.
- CROSS, S. L., BAKER, P. A., SELTZER, G. O., FRITZ, S. C. & DUNBAR, R. B. (2001) Late Quaternary Climate and Hydrology of Tropical South America Inferred from an Isotopic and Chemical Model of Lake Titicaca, Bolivia and Peru. *Quaternary Research*, 56, 1-9.
- DANE, J. H. & TOPP, G. C. (Eds.) (2002) *Methods of Soil Analysis - Part 4 Physical Methods*, Madison, Wisconsin, Soil Science Society of America, Inc.
- DAVIS, C., WARNER, T., ASTLING, E. & BOWERS, J. (1999) Development and application of an operational, relocatable, mesogamma-scale weather analysis and forecasting system. *Tellus*, 51A, 710-727.
- DAVIS, J. R., HOWARD, K. A., RETTIG, S. L., SMITH, R. L., ERICKSEN, G. E., RISACHER, F., ALARCON, H. & MORALES, R. (1982) Progress report on lithium-related geologic investigations in Bolivia. *Open File Report*. U.S. Geological Survey.
- DE LAS CUEVAS, C. (1997) Pore structure characterization in rock salt. *Engineering Geology*, 47, 17-30.
- DEFOE, O. K. & COMPTON, A. H. (1925) The Density of Rock Salt and Calcite. *Physical Review*, 25, 618-620.

6. References

- DIN 51562-3 (1985) Messung der kinematischen Viskosität mit dem Ubbelohde-Viskosimeter - Relative Viskositätsänderung bei kurzen Durchlaufzeiten. DIN Deutsches Institut für Normung e.V.
- DIN EN 993-1 (1995) Prüfverfahren für dichte geformte feuerfeste Erzeugnisse - Teil 1: Bestimmung der Rohdichte, offenen Porosität und Gesamtporosität. DIN Deutsches Institut für Normung e.V.
- DIN EN ISO 2811-1 (2011) Beschichtungsstoffe – Bestimmung der Dichte – Teil 1: Pyknometer-Verfahren. DIN Deutsches Institut für Normung e.V.
- DIN V ENV 13005 (1999) Leitfaden zur Angabe der Unsicherheit beim Messen. DIN Deutsches Institut für Normung e.V.
- DONSELAAR, M. E., CUEVAS GOZALO, M. C. & MOYANO, S. (2013) Avulsion processes at the terminus of low-gradient semi-arid fluvial systems: Lessons from the Río Colorado, Altiplano endorheic basin, Bolivia. *Sedimentary Geology*, 283, 1-14.
- EICHLER, H. J., KRONFELDT, H.-D. & SAHM, J. (2001) *Das Neue Physikalische Grundpraktikum*, Berlin, Heidelberg, Springer-Verlag.
- ERICKSEN, G. E. & SALAS, R. (1987) Geology and Resources of Salars in the Central Andes. *Open File Report*. U.S. Geological Survey.
- ERICKSEN, G. E., VINE, J. D. & BALLON, R. (1977) Lithium-rich brines at Salar de Uyuni and nearby Salars in Southwestern Bolivia. *Open File Report*. Denver, U.S. Geological Survey.
- ERICKSEN, G. E., VINE, J. D. & RAUL BALLÓN, A. (1978) Chemical composition and distribution of lithium-rich brines in salar de Uyuni and nearby salars in southwestern Bolivia. *Energy*, 3, 355-363.
- EVANS, R. K. (2008a) An Abundance of Lithium.
- EVANS, R. K. (2008b) An Abundance of Lithium - part two.
- FALLICO, C., DE BARTOLO, S., TROISI, S. & VELTRI, M. (2010) Scaling analysis of hydraulic conductivity and porosity on a sandy medium of an unconfined aquifer reproduced in the laboratory. *Geoderma*, 160, 3-12.
- FAN, Y., DUFFY, C. J. & OLIVER, D. S. (1997) Density-driven groundwater flow in closed desert basins: field investigations and numerical experiments. *Journal of Hydrology*, 196, 139-184.
- FERRIS, J. G., KNOWLES, D. B., BROWN, R. H. & STALLMAN, R. W. (1962) *Ground-Water Hydraulics: Theory of Aquifer Tests*, Washington, U.S. Geological Survey.
- FLINT, L. E. & FLINT, A. L. (2002) Porosity. IN DANE, J. H. & TOPP, G. C. (Eds.) *Methods of soil analysis, Part 4 - Physical Methods*. Madison Wisc., Amer. Soc. of Agronomy.
- FORNARI, M., RISACHER, F. & FÉRAUD, G. (2001) Dating of paleolakes in the central Altiplano of Bolivia. *Palaeogeography, Palaeoclimatology, Palaeoecology*, 172, 269-282.
- FRITZ, S. C., BAKER, P. A., LOWENSTEIN, T. K., SELTZER, G. O., RIGSBY, C. A., DWYER, G. S., TAPIA, P. M., ARNOLD, K. K., KU, T.-L. & LUO, S. (2004) Hydrologic variation during the last 170,000 years in the southern hemisphere tropics of South America. *Quaternary Research*, 61, 95-104.
- FRITZ, S. C., BAKER, P. A., SELTZER, G. O., BALLANTYNE, A., TAPIA, P., CHENG, H. & EDWARDS, R. L. (2007) Quaternary glaciation and hydrologic variation in the South American tropics as reconstructed from the Lake Titicaca drilling project. *Quaternary Research*, 68, 410-420.
- GARCIA, M., RAES, D., ALLEN, R. & HERBAS, C. (2004) Dynamics of reference evapotranspiration in the Bolivian highlands (Altiplano). *Agricultural and Forest Meteorology*, 125, 67-82.

- GARRETT, D. E. (2004) Handbook of Lithium and Natural Calcium Chloride - Their Deposits, Processing, Uses and Properties, Amsterdam, Elsevier Academic Press.
- GEVANTMAN, L. H. (Ed.) (1981) *Physical Properties Data of Rock Salt - National Bureau of Standards monograph 167*, Washington, U.S. Department of Commerce - National Bureau of Standards.
- GODFREY, L. V., CHAN, L. H., ALONSO, R. N., LOWENSTEIN, T. K., MCDONOUGH, W. F., HOUSTON, J., LI, J., BOBST, A. & JORDAN, T. E. (2013) The role of climate in the accumulation of lithium-rich brine in the Central Andes. *Applied Geochemistry*, 38, 92-102.
- GOERZ, I. TU Bergakademie Freiberg, Institute of Geophysics and Geoinformatics, D-09596 Freiberg, personal communication from 05-01-2014.
- GONTHIER, G. J. (2007) A Graphical Method for Estimation of Barometric Efficiency from Continuous Data - Concepts and Application to a Site in the Piedmont, Air Force Plant 6, Marietta, Georgia. *Scientific Investigation Report 2007-5111*. Reston, Virginia, U.S. Department of the Interior, U.S. Geological Survey.
- GOODALL, T. M., NORTH, C. P. & GLENNIE, K. W. (2000) Surface and subsurface sedimentary structures produced by salt crusts. *Sedimentology*, 47, 99-118.
- GOSLAR, T. Poznan Radiocarbon Laboratory, PL-61612 Poznan, Poland, personal communication from 29-07-2014.
- GOSLING, W. D., BUSH, M. B., HANSELMAN, J. A. & CHEPSTOW-LUSTY, A. (2008) Glacial-interglacial changes in moisture balance and the impact on vegetation in the southern hemisphere tropical Andes (Bolivia/Peru). *Palaeogeography, Palaeoclimatology, Palaeoecology*, 259, 35-50.
- GRIBOVSZKI, Z., KALICZ, P., SZILÁGYI, J. & KUČSARA, M. (2008) Riparian zone evapotranspiration estimation from diurnal groundwater level fluctuations. *Journal of Hydrology*, 349, 6-17.
- GRIBOVSZKI, Z., SZILÁGYI, J. & KALICZ, P. (2010) Diurnal fluctuations in shallow groundwater levels and streamflow rates and their interpretation – A review. *Journal of Hydrology*, 385, 371–383.
- GROVE, M. J., BAKER, P. A., CROSS, S. L., RIGSBY, C. A. & SELTZER, G. O. (2003) Application of strontium isotopes to understanding the hydrology and paleohydrology of the Altiplano, Bolivia-Peru. *Palaeogeography, Palaeoclimatology, Palaeoecology*, 194, 281-297.
- GRUBER, P. W., MEDINA, P. A., KEOLEIAN, G. A., KESLER, S. E., EVERSON, M. P. & WALLINGTON, T. J. (2011) Global Lithium Availability - A Constraint for Electric Vehicles? *Journal of Industrial Ecology*, 00, 16.
- HANTUSH, M. S. & VEN TE, C. (1964) *Hydraulics of Wells*. *Advances in Hydroscience*. Elsevier.
- HEALY, R. W. & COOK, P. G. (2002) Using groundwater levels to estimate recharge. *Hydrogeology Journal*, 10, 91-109.
- HEINRICH, J. (2012) Chemical and isotopic investigation of lithium-rich brine from the Salar de Uyuni (Bolivia). *Institute for Geology, Department of Hydrogeology*. Freiberg, TU Bergakademie Freiberg, unpublished.
- HERING, E., MARTIN, R. & STOHRER, M. (2009) *Taschenbuch der Mathematik und Physik*, Berlin, Heidelberg, Springer.
- HERKLOTZ, K. TU Bergakademie Freiberg, Interdisziplinäres Ökologisches Zentrum, D-09596 Freiberg, personal communication from 14-05-2014.
- HERKLOTZ, K. TU Bergakademie Freiberg, Interdisziplinäres Ökologisches Zentrum, D-09596 Freiberg, personal communication from 26-03-2014.

6. References

- HOLLDORF, H. & BAUMBACH, U. (1987) Bilanzierung der Totaleindampfung der Erdgasbegleitwässer bei Siedetemperatur *Lithiumgewinnung aus Erdgasbegleitwässern, Laborbericht 25*. Freiberg, Bergakademie Freiberg.
- HÖLTING, B. & COLDEWAY, W. G. (2013) Hydrogeologie - Einführung in die Allgemeine und Angewandte Hydrogeologie, Springer Spektrum.
- HOLZBECHER, E. (2005) Groundwater flow pattern in the vicinity of a salt lake. *Hydrobiologia*, 532, 233-242.
- HOUSTON, J., BUTCHER, A., EHREN, P., EVANS, K. & GODFREY, L. (2011) The Evaluation of Brine Prospects and the Requirement for Modifications to Filing Standards. *Economic Geology*, 106, 1225-1239.
- JACOBS, P., SEVENS, E. & KUNNEN, M. (1995) Principles of computerised X-ray tomography and applications to building materials. *Science of The Total Environment*, 167, 161-170.
- KAMPF, S. K., TYLER, S. W., ORTIZ, C. A., MUNOZ, J. F. & ADKINS, P. L. (2005) Evaporation and land surface energy budget at the Salar de Atacama, Northern Chile. *Journal of Hydrology*, 310, 236-252.
- KESTIN, J., KHALIFA, H. E. & CORREIA, R. J. (1981) Tables of the Dynamic and Kinematic Viscosity of Aqueous NaCl Solutions in the Temperature Range 20-150 °C and the Pressure Range 0.1~5 MPa. *Journal of Physical and Chemical Reference Data*, 10, 71-88.
- KLUTE, A. & DIRKSEN, C. (1986) Hydraulic conductivity and diffusivity: laboratory methods. IN KLUTE, A. (Ed.) *Methods of Soil Analysis, Part I - Physical and Mineralogical Methods*. 2nd ed. Madison, WI., Am Soc. Agron.
- KRUSEMAN, G. P. & DE RIDDER, N. A. (2000) *Analysis and evaluation of pumping test data*, Wageningen, International Institute for Land Reclamation and Improvement.
- KUMAR, R. & BHATTACHARJEE, B. (2004) Assessment of permeation quality of concrete through mercury intrusion porosimetry. *Cement and Concrete Research*, 34, 321-328.
- KUSSMAUL, S., HÖRMANN, P. K., PLOSKONKA, E. & SUBIETA, T. (1977) Volcanism and structure of southwestern Bolivia. *Journal of Volcanology and Geothermal Research*, 2, 73-74.
- LANDIS, E. N. & KEANE, D. T. (2010) X-ray microtomography. *Materials Characterization*, 61, 1305-1316.
- LANGGUTH, H. R. & VOIGT, R. (2004) *Hydrogeologische Methoden*, Berlin, Heidelberg, New York, Springer-Verlag.
- LAUTZ, L. (2008) Estimating groundwater evapotranspiration rates using diurnal water-table fluctuations in a semi-arid riparian zone. *Hydrogeology Journal*, 16, 483-497.
- LEBRUN, V., PACOSILLO, P., GUTIERREZ, J., CACERES, F., POOL, E. & PIRARD, E. (2002) Geochemistry of bitter brines in the Salar de Coipasa – Bolivia. *Aardkundige Mededelingen*, 12, 185-188.
- LOCKLIN, C. (2001) Central Andean dry puna. Terrestrial Ecoregions - Neotropcis 1001 (peer review in process; June 12, 2014).
- LOWENSTEIN, T. K. & HARDIE, L. A. (1985) Criteria for the Recognition of Salt-Pan Evaporites. *Sedimentology*, 32, 627-644.
- LUGHOFER, E. (2011) *Evolving Fuzzy Systems - Methodologies, Advanced Concepts and Applications*, Berlin, Heidelberg, Springer-Verlag.
- MACUMBER, P. G. (1991) *Interactions between groundwater and surface systems in northern Victoria*, East Melbourne, Victoria, Australia, Department of Conservation and Environment.
- MALLET, J.-L. (2002) *Geomodeling*, Oxford [u.a.], Oxford University Press.

6. References

- MAYS, T. J. (2007) A new classification of pore sizes. *Studies in Surface Science and Catalysis*, 160, 57-62.
- MCGEARY, S. (2001) Near-surface seismic reflection study of Quaternary neotectonics and stratigraphy on the Bolivian Altiplano. *Abstracts with Programs - Geological Society of America*, 33, pp. 346.
- MCGEARY, S., BILLS, B. G. & JIMENEZ, G. (2003) Shallow seismic reflection imaging of the Salar de Uyuni, Bolivia; Quaternary neotectonics and stratigraphy. IN EOS, T. (Ed.) *American Geophysical Union 2003 fall meeting (AGU)*. San Francisco, CA, United States, American Geophysical Union, Washington, DC, United States (USA).
- MCGEARY, S., BILLS, B. G., JIMENEZ, G., BLACK, J. D., RAJKOVIC, D. G. & CASLER, C. (2000) High-resolution seismic reflection profiling of the Salar de Uyuni, Bolivia, core site for paleoclimatology and neotectonic history of the Altiplano. *Abstracts with Programs - Geological Society of America*, 32, pp.273-274.
- MERIDIAN INTERNATIONAL RESEARCH (2008) *The Trouble with Lithium 2 - Under the Microscope*. Martainville, France, Meridian International Research.
- MERKEL, B. J. & PLANER-FRIEDRICH, B. (2002) Integrierte Datenauswertung Hydrogeologie. *Freiberg Online Geology*, 7, 61.
- MERKEL, B. J. & PLANER-FRIEDRICH, B. (2008) *Grundwasserchemie. Praxisorientierter Leitfaden zur numerischen Modellierung von Beschaffenheit, Kontamination und Sanierung aquatischer Systeme*, Berlin Heidelberg, Springer
- MERRITT, M. L. (2004) Estimating Hydraulic Properties of the Floridan Aquifer System by Analysis of Earth-Tide, Ocean-Tide, and Barometrie Effects, Collier and Hendry Counties, Florida. *Water-Resources Investigations Report 03-4267*. U.S. Geological Survey.
- MINISTERIO DE MEDIO AMBIENTE Y AQUA (2012) Meteorological data from the Uyuni weather station for the years 2001 - 2011 (SNHM/SNIHM/189/199/2012). La Paz, 01-11-2012, Ministerio de Medio Ambiente y Aqua, Servicio Nacional de Meteorología e Hidrología, Sistema Nacional de Información Hidrometeorológica (unpublished data).
- NAGARAJU, P. & ROY, S. (2014) Effect of water saturation on rock thermal conductivity measurements. *Tectonophysics*, 626, 137-143.
- NIELD, D. A., SIMMONS, C. T., KUZNETSOV, A. V. & WARD, J. D. (2008) On the evolution of salt lakes: Episodic convection beneath an evaporating salt lake. *Water Resources Research*, 44.
- OECD/IEA (2013) *Global EV Outlook - Understanding the Electric Vehicle Landscape to 2020*. Paris, International Energy Agency (IEA), Electric Vehicles Initiative of the Clean Energy Ministerial (EVI).
- OESTREICHER, R. UTK - EcoSens GmbH, D-06712 Zeitz, personal communication from 13-05-2014.
- ORECCHINI, F., SANTIANGELI, A. & DELL'ERA, A. (2014) 10 - EVs and HEVs Using Lithium-Ion Batteries. *Lithium-Ion Batteries*. Amsterdam, Elsevier.
- ORRIS, G. J. (1995) Bibliography and Summary of Data available for the Salar de Uyuni, Bolivia *Open File Report*. U.S. Geological Survey.
- ORTUÑO, T., LEDRU, M.-P., CHEDDADI, R., KUENTZ, A., FAVIER, C. & BECK, S. (2011) Modern pollen rain, vegetation and climate in Bolivian ecoregions. *Review of Palaeobotany and Palynology*, 165, 61–74.
- OSTU, N. (1979) A Treshold Selection Method from Gray-Level Histograms *IEEE Transactions on Systems, Man and Cybernetics*, 9, 62-66.

- OVEJERO TOLEDO, A., ALONSO, R. N., RUIZ, T. D. V. & QUIROGA, A. G. (2009) Evapofacies halítica en el Salar del Rincón, departamento Los Andes, Salta. *Revista de la Asociación Geológica Argentina*, 64, 493-500.
- PHYSICK, W. L. & TAPPER, J. (1990) A Numerical Study of Circulations Induced by a Dry Salt Lake. *Monthly Weather Review, American Meteorological Society*, 118, 1029-1042.
- PLACZEK, C., QUADE, J. & PATCHETT, P. J. (2006) Geochronology and stratigraphy of late Pleistocene lake cycles on the southern Bolivian Altiplano: Implications for causes of tropical climate change. *Geological Society of America Bulletin*, 118, 515-532.
- PLACZEK, C. J., QUADE, J. & PATCHETT, P. J. (2013) A 130 ka reconstruction of rainfall on the Bolivian Altiplano. *Earth and Planetary Science Letters*, 363, 97-108.
- RETTIG, S. L., JONES, B. F. & RISACHER, F. (1980) Geochemical evolution of brines in the Salar of Uyuni, Bolivia. *Chemical Geology*, 30, 57-79.
- REUDER, J., GHEZZI, F., PALENQUE, E., TORREZ, R., ANDRADE, M. & ZARATTI, F. (2007) Investigations on the effect of high surface albedo on erythemally effective UV irradiance: Results of a campaign at the Salar de Uyuni, Bolivia. *Journal of Photochemistry and Photobiology B: Biology*, 87, 1-8.
- RIFE, D. L., WARNER, T., CHEN, F. & ASTLING, E. (2002) Mechanisms for Diurnal Boundary Layer Circulations in the Great Basin Desert. *Monthly Weather Review, American Meteorological Society*, 130, 921-938.
- RIGSBY, C. A., BRADBURY, J. P., BAKER, P. A., ROLLINS, S. M. & WARREN, M. R. (2005) Late Quaternary palaeolakes, rivers, and wetlands on the Bolivian Altiplano and their palaeoclimatic implications. *Journal of Quaternary Science*, 20, 671-691.
- RISACHER, F. & FRITZ, B. (1991) Quaternary geochemical evolution of the salars of Uyuni and Coipasa, Central Altiplano, Bolivia. *Chemical Geology*, 90, 211-231.
- RISACHER, F. & FRITZ, B. (2000) Bromine geochemistry of salar de Uyuni and deeper salt crusts, Central Altiplano, Bolivia. *Chemical Geology*, 167, 373-392.
- RISACHER, F. & FRITZ, B. (2009) Origin of Salts and Brine Evolution of Bolivian and Chilean Salars. *Aquatic Geochemistry*, 15, 123-157.
- RISACHER, F., FRITZ, B. & ALONSO, H. (2006) Non-conservative behavior of bromide in surface waters and brines of Central Andes: A release into the atmosphere? *Geochimica et Cosmochimica Acta*, 70, 2143-2152.
- SABTAN, A. A. & SHEHATA, W. M. (2003) Hydrogeology of Al-Lith Sabkha, Saudi Arabia. *Journal of Asian Earth Sciences*, 21, 423-429.
- SALAS, J., GUIMERÁ, J., CORNELLÁ, O., ARAVENA, R., GUZMÁN, E., TORE, C., VON IGEL, W. & MORENO, R. (2010) Hidrogeología del sistema lagunar del margen este del Salar de Atacama (Chile). *Boletín Geológico y Minero*, 121, 357-372
- SANFORD, W. & WOOD, W. (2001) Hydrology of the coastal sabkhas of Abu Dhabi, United Arab Emirates. *Hydrogeology Journal*, 9, 358-366.
- SCHAFMEISTER, M.-T. (1999) *Geostatistik für die hydrogeologische Praxis* Berlin, Heidelberg, Springer.
- SCHMIDT, N. (2010) Hydrogeological and hydrochemical investigations at the Salar de Uyuni (Bolivia) with regard to the extraction of lithium. *FOG - Freiberg Online Geoscience*, 26, 1-131.
- SCHRAMM, M. Federal Institute for Geosciences and Natural Resources (BGR), D-30655 Hannover, personal communication from 07-04-2014.
- SIELAND, R., SCHMIDT, N., SCHÖN, A., SCHRECKENBACH, J. & MERKEL, B. (2011) Geochemische, hydrogeologische und feinstratigraphische Untersuchungen am Salar

- de Uyuni (Bolivien). IN BGR (Ed.) *Berichte aus der Lagerstätten- und Rohstoffforschung*. Hannover.
- SIMMONS, C. T., FENSTEMAKER, T. R. & SHARP JR, J. M. (2001) Variable-density groundwater flow and solute transport in heterogeneous porous media: approaches, resolutions and future challenges. *Journal of Contaminant Hydrology*, 52, 245-275.
- SOMERTON, W. H. (Ed.) (1992) *Thermal properties and temperature-related behavior of rock/fluid systems*, Amsterdam, London, New York, Tokyo, Elsevier Science Publishers B.V.
- STAMP, A., LANG, D. J. & WÄGER, P. A. (2012) Environmental impacts of a transition toward e-mobility: the present and future role of lithium carbonate production. *Journal of Cleaner Production*, 23, 104-112.
- STOERTZ, G. E. & ERICKSEN, G. E. (Eds.) (1974) *Geology of Salars in Northern Chile*, Washington, United States Government Printing Office.
- SUNDBERG, J., BACK, P. R.-E., ERICSSON, L. O. & WRAFTER, J. (2009) Estimation of thermal conductivity and its spatial variability in igneous rocks from in situ density logging. *International Journal of Rock Mechanics and Mining Sciences*, 46, 1023-1028.
- SVENDSEN, J. B. (2003) Parabolic halite dunes on the Salar de Uyuni, Bolivia. *Sedimentary Geology*, 155, 147-156.
- SYLVESTRE, F., SERVANT-VILDARY, S., FOURNIER, M. & SERVANT, M. (1996) Lake levels in the southern Bolivian Altiplano (19°–21°S.) during the Late Glacial based on diatom studies. *International Journal of Salt Lake Research*, 4, 281-300.
- SYLVESTRE, F., SERVANT, M., SERVANT-VILDARY, S., CAUSSE, C., FOURNIER, M. & YBERT, J. P. (1999) Lake-level chronology on the southern Bolivian Altiplano (18 degrees-23 degrees S) during late-glacial time and the early Holocene. *Quaternary Research*, 51, 54-66.
- SZILÁGYI, J., GRIBOVSKI, Z., KALICZ, P. & KUCSARA, M. (2008) On diurnal riparian zone groundwater-level and streamflow fluctuations. *Journal of Hydrology*, 349, 1-5.
- SZYMCZAK, P. G.E.O.S. Ingenieurgesellschaft mbH, D-09599 Freiberg, personal communication from 03-06-2013.
- SZYMCZAK, P. & BEHNKE, A. (2009) Umweltinformationssystem Sachsen / FIS Hydrogeologie - Pumpversuchsauswertung - UP32 Version 1.1. Sächsisches Landesamt für Umwelt, Landwirtschaft und Geologie; HGC Hydro-Geo-Consult GmbH, G.E.O.S. GmbH Freiberg.
- TAHIL, W. (2007) The Trouble with Lithium - Implications of Future PHEV Production for Lithium Demand. Meridian International Research.
- TAPPER, N. J. (1991) Evidence for a mesoscale thermal circulation over dry salt lakes. *Palaeogeography, Palaeoclimatology, Palaeoecology*, 84, 259-269.
- TAUD, H., MARTINEZ-ANGELES, R., PARROT, J. F. & HERNANDEZ-ESCOBEDO, L. (2005) Porosity estimation method by X-ray computed tomography. *Journal of Petroleum Science and Engineering*, 47, 209-217.
- TGL 23864/08 (1973) Hydrogeologie. Pumpversuche. geohydraulische Auswertung - unvollkommener Brunnen. Deutsche Demokratische Republik.
- TRAUTWEIN, U. (2005) Poroelastische Verformung und petrophysikalische Eigenschaften von Rotliegend Sandsteinen. Berlin, Technische Universität Berlin.
- TURK, L. J. (1975) Diurnal fluctuations of water tables induced by atmospheric pressure changes. *Journal of Hydrology*, 26, 1-16.
- TURK, L. J., DAVIS, S. N. & BINGHAM, C. P. (1973) Hydrogeology of Lacustrine Sediments, Bonneville Salt Flats, Utah. *Economic Geology*, 68, 65-78.

6. References

- TYLER, S. W., MUÑOZ, J. F. & WOOD, W. W. (2006) The Response of Playa and Sabkha Hydraulics and Mineralogy to Climate Forcing. *Ground Water*, 44, 329-338.
- USGS (2012) Mineral Commodity Summaries 2012. IN U.S. GEOLOGICAL SURVEY (Ed.) Reston, Virginia, U.S. Geological Survey.
- USGS (2014) Lithium. IN U.S. GEOLOGICAL SURVEY (Ed.) *Mineral Commodity Summaries*. <http://minerals.usgs.gov/minerals/pubs/commodity/lithium/mcs-2014-lithi.pdf>, accessed on 02-02-2014.
- VAN CAMP, M. & VAUTERIN, P. (2005) Tsoft: graphical and interactive software for the analysis of time series and Earth tides. *Computers & Geosciences*, 31, 631-640.
- VERGÉS, E., TOST, D., AYALA, D., RAMOS, E. & GRAU, S. (2011) 3D pore analysis of sedimentary rocks. *Sedimentary Geology*, 234, 109-115.
- VINE, J. D. (1980) Where on Earth is all of the Lithium. *U.S. Geological Survey, Open-File Report*, 80-1234, 107 pp.
- WARREN, J. K. (2006) *Evaporites: Sediments, resources and hydrocarbons*, Berlin, Springer.
- WARREN, J. K. (2010) Evaporites through time: Tectonic, climatic and eustatic controls in marine and nonmarine deposits. *Earth-Science Reviews*, 98, 217-268.
- WHITE, W. N. (1932) A method of estimating ground-water supplies based on discharge by plants and evaporation from soil: Results of investigations in Escalante Valley, Utah *US Geological Survey Water Supply Paper*, 659-A.
- WIDEGREN, J. A. & MAGEE, J. W. (2007) Density, viscosity, speed of sound, and electrolytic conductivity for the ionic liquid 1-hexyl-3-methylimidazolium bis(trifluoromethylsulfonyl)imide and its mixtures with water. *Journal of Chemical and Engineering Data*, 52, 2331-2338.
- WIRRMANN, D. & MOURGUIART, P. (1995) Late Quaternary Spatiotemporal Limnological Variations in the Altiplano of Bolivia and Peru. *Quaternary Research*, 43, 344-354.
- WOLF, M. (2010) Salare des Altiplano - Ihre Entstehung und wirtschaftliche Bedeutung IN WESSOLEK, G., KAUPENJOHANN, M. & RENGER, M. (Eds.) *Bodenökologie und Bodengenese*. Berlin, Technische Universität Berlin, Institut für Ökologie
- YAKSIC, A. & TILTON, J. E. (2009) Using the cumulative availability curve to assess the threat of mineral depletion: The case of lithium. *Resources Policy*, 34, 185-194.
- YAWS, C. L. (2009) *Thermophysical properties of chemicals and hydrocarbons*, Norwich N.Y., William Andrew.
- YIN, L., ZHOU, Y., GE, S., WEND, D., ZHANG, E. & DONG, J. (2013) Comparison and modification of methods for estimating evapotranspiration using diurnal groundwater level fluctuations in arid and semiarid regions. *Journal of Hydrology*, 496, 9–16.
- YU, J., GAO, C., CHENG, A., LIU, Y., ZHANG, L. & HE, X. (2013) Geomorphic, hydroclimatic and hydrothermal controls on the formation of lithium brine deposits in the Qaidam Basin, northern Tibetan Plateau, China. *Ore Geology Reviews*, 50, 171-183.
- ZAUNER, M. J. (2012) Gefügeanalyse zur Porosität des Halitits des Salar de Uyuni in Bolivien. *Institute of Mineralogy*. Freiberg, TU Bergakademie Freiberg, unpublished.
- ZHU, J., YOUNG, M., HEALY, J., JASONI, R. & OSTERBERG, J. (2011) Interference of river level changes on riparian zone evapotranspiration estimates from diurnal groundwater level fluctuations. *Journal of Hydrology*, 403, 381–389.

Appendix

Appendix A – Figures

Figure A - 1: Top view and cross-section of the well constellation at site 02-LLI.....	155
Figure A - 2: Top view and cross-section of the well constellation at sites 05-TAH and 06-NOR. .	156
Figure A - 3: Top view and cross-section of the well constellation at sites 08-CEN and 09-RIO....	157
Figure A - 4: X-ray diffractogram of sample 02-LLI-B, 9b	158
Figure A - 5: X-ray diffractogram of sample 02-LLI-B, 11/2.....	158
Figure A - 6: X-ray diffractogram of sample 07-SAL, 28 a-b	159
Figure A - 7: Comparison of different interpolation methods for creation of a lithium distribution map.	160
Figure A - 8: Brine level data during the pumping test '02-LLI' in 2010.....	162
Figure A - 9: Semi-logarithmic drawdown of the pumping test '02-LLI' in 2010.....	162
Figure A - 10: Analysis of the recovery phase of the pumping test '02-LLI' (2010) with the JACOB method.....	163
Figure A - 11: Recovery evaluation of pumping test '02-LLI' (2010) according to the procedure of DRISCOLL.	163
Figure A - 12: Brine level data of the pumping test '05-TAH' in 2010.....	164
Figure A - 13: Semi-logarithmic drawdown of the pumping test '05-TAH' in 2010.	164
Figure A - 14: Analysis of the recovery phase of the pumping test '05-TAH' (2010) with the JACOB method.....	165
Figure A - 15: Recovery evaluation of pumping test '05-TAH' (2010) according to the procedure of DRISCOLL.	165
Figure A - 16: Brine level data of the pumping test '06-NOR' in 2010.	166
Figure A - 17: Semi-logarithmic drawdown of the pumping test '06-NOR' in 2010.....	166
Figure A - 18: Analysis of the recovery phase of the pumping test '06-NOR' (2010) with the JACOB method.....	167
Figure A - 19: Recovery evaluation of pumping test '06-NOR' (2010) according to the procedure of DRISCOLL	167
Figure A - 20: Brine level data of the pumping test '08-CEN' in 2010.....	168
Figure A - 21: Semi-logarithmic drawdown of the pumping test '08-CEN' in 2010.	168
Figure A - 22: Analysis of the recovery phase of the pumping test '08-CEN' (2010) with the JACOB method.....	169

Figure A - 23: Recovery evaluation of pumping test '08-CEN' (2010) according to the procedure of DRISCOLL 169

Figure A - 24: Brine level data of the pumping test '09-RIO' in 2010..... 170

Figure A - 25: Semi-logarithmic drawdown of the pumping test '09-RIO' in 2010..... 170

Figure A - 26: Analysis of the recovery phase of the pumping test '09-RIO' (2010) with the JACOB method..... 171

Figure A - 27: Recovery evaluation of pumping test '09-RIO' (2010) according to the procedure of DRISCOLL. 171

Figure A - 28: Brine level data of the pumping test '02-LLI' in 2012. 172

Figure A - 29: Semi-logarithmic drawdown of the pumping test '02-LLI' in 2012..... 172

Figure A - 30: Analysis of the recovery phase of the pumping test '02-LLI' (2012) with the JACOB method..... 173

Figure A - 31: Recovery evaluation of pumping test '02-LLI' (2012) according to the procedure of DRISCOLL. 173

Figure A - 32: Brine level data of the pumping test '08-CEN' in 2012..... 174

Figure A - 33: Semi-logarithmic drawdown of the pumping test '08-CEN' in 2012. 174

Figure A - 34: Analysis of the recovery phase of the pumping test '08-CEN' (2012) with the JACOB method..... 175

Figure A - 35: Recovery evaluation of pumping test '08-CEN' (2012) according to the procedure of DRISCOLL. 175

Figure A - 36: Determination of the barometric efficiency (BE) by means of the curve of the sums of the increments of atmospheric pressure ($\Sigma\Delta p$) and natural brine level ($\Sigma\Delta h$) fluctuations for long-term and short-term observations at different sites on the Salar de Uyuni..... 176

Appendix B – Tables

Table B - 1:	Technical details of the drilling machine	177
Table B - 2:	Technical specifications of the CT-Alpha 225 computed tomograph	178
Table B - 3:	Meteorological data of the Salar de Uyuni from 2001 to 2011.....	179
Table B - 4:	Pore size distribution of salt core samples analyzed by X-ray computed tomography.....	181
Table B - 5:	Determination of the effective porosity by saturation with 2-octanol.	183
Table B - 6:	Results of porosity determination by direct measurement.....	185
Table B - 7:	Lithium concentrations in brine samples from different sites of the Uyuni salt flat..	189
Table B - 8:	Experimental determination of the cubic expansion coefficient for two brine samples from sites 02-LLI and 09-RIO.....	190
Table B - 9:	Density of brine samples at standard temperature (25°C) as well as at field temperature conditions.	191
Table B - 10:	Raw data of viscosity measurements.	192
Table B - 11:	Drawdown evaluation of pumping tests performed in 2010 on partially penetrating wells under confined aquifer conditions according to TGL 23864/08 (1973).....	194
Table B - 12:	Drawdown evaluation of pumping tests performed in 2012 on fully penetrating wells under confined aquifer conditions according to the THEIS curve matching procedure using the software UP32.	195
Table B - 13:	Recovery analysis of pumping tests with the JACOB method.	196
Table B - 14:	Recovery analysis of pumping tests with the DRISCOLL method.....	197
Table B - 15:	Intrinsic permeability of salt core samples determined by flow-through experiments.	198

Appendix C – Text

Text C - 1:	Error estimation according to DIN V ENV 13005 (1999)	203
Text C - 2:	Error estimation for permeability determination (flow-through experiments using 2-octanol)	204
Text C - 3:	Error estimation for effective porosity determination according to the saturation method.....	205
Text C - 4:	Error estimation for porosity determination according to the complement method..	206
Text C - 5:	Error estimation for lithium reservoir estimation.....	208

Appendix A – Figures

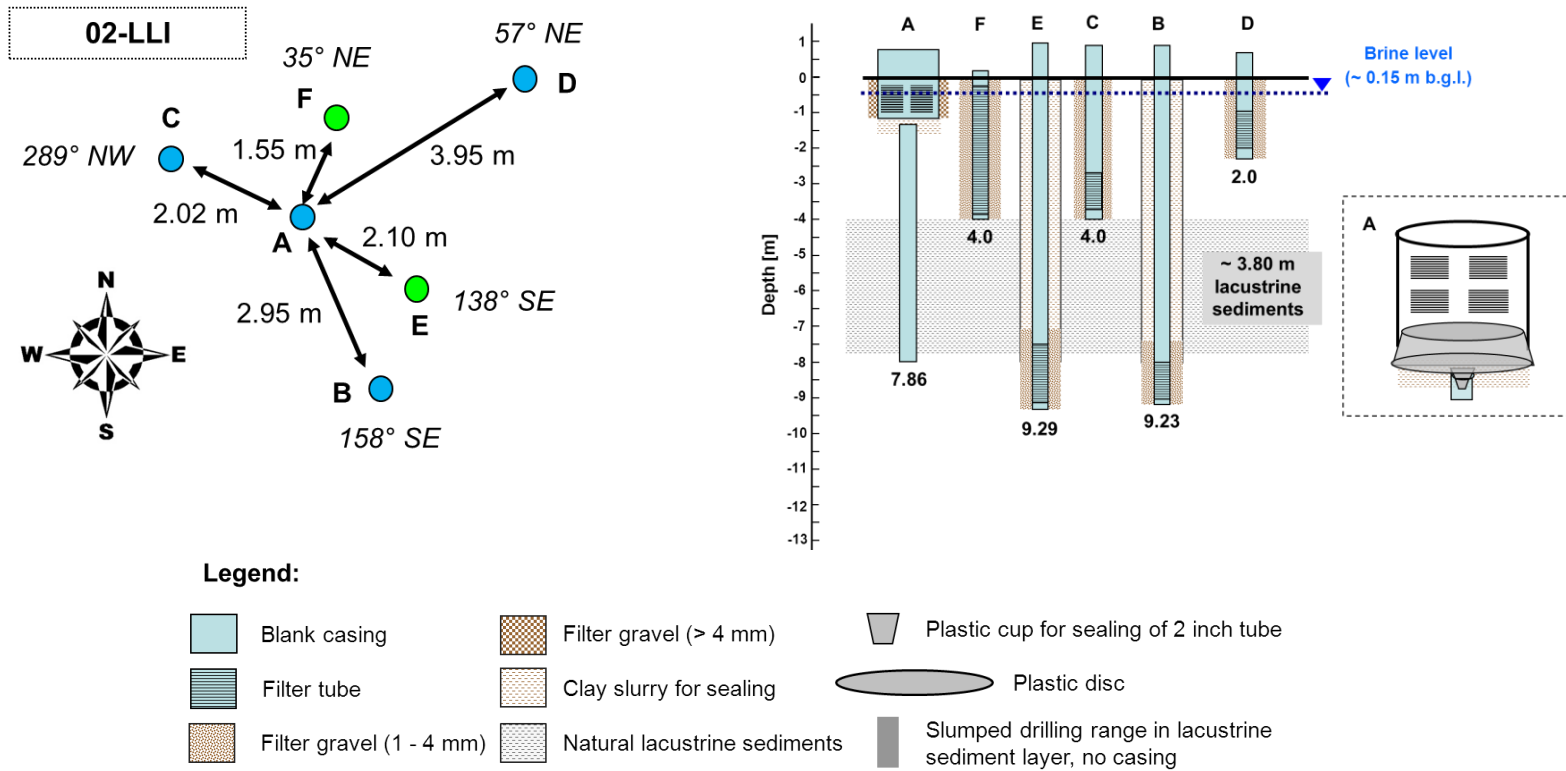


Figure A - 1: Top view (left) and cross-section of the well constellation (right) at site 02-LLI. Details of the well casing are also shown (e.g. screen (filter) depth, complete casing, back-filling material of the annular space). Wells marked with blue circles were installed in 2010, green circles indicate the wells which were installed in 2012.

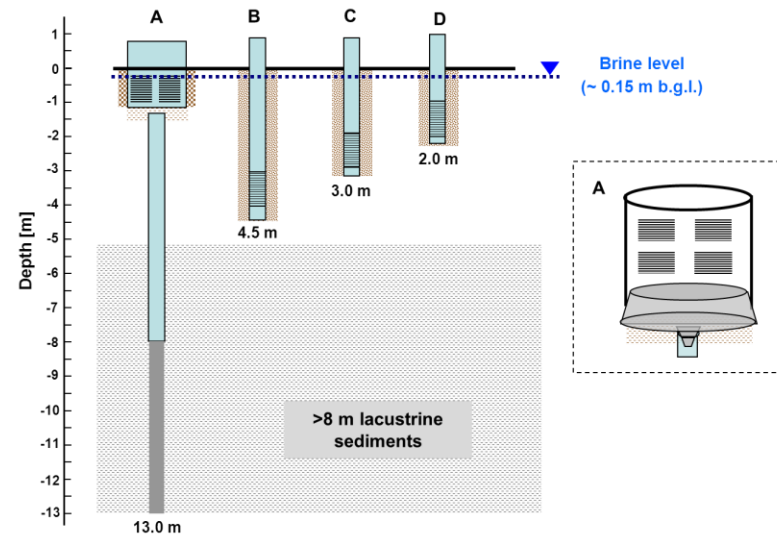
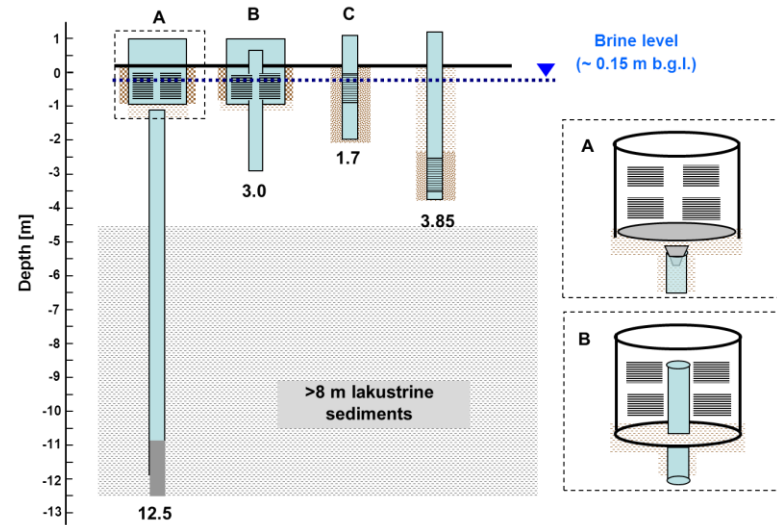
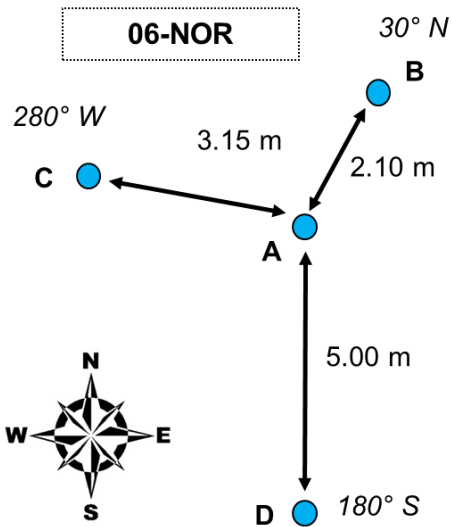
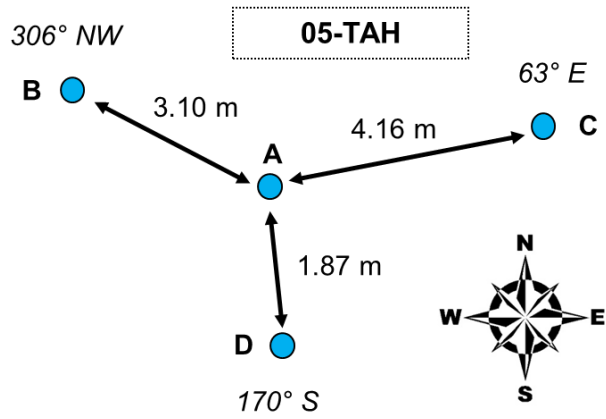


Figure A - 2: Top view (left) and cross-section of the well constellation (right) at sites 05-TAH (top) and 06-NOR (bottom). Symbols are explained in Figure A - 1.

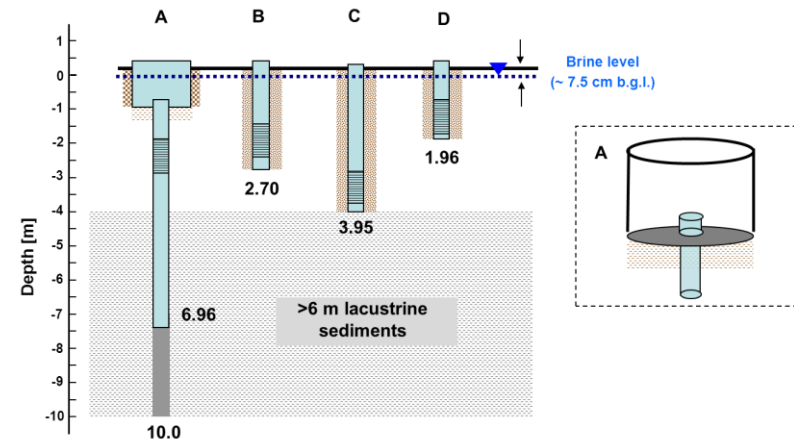
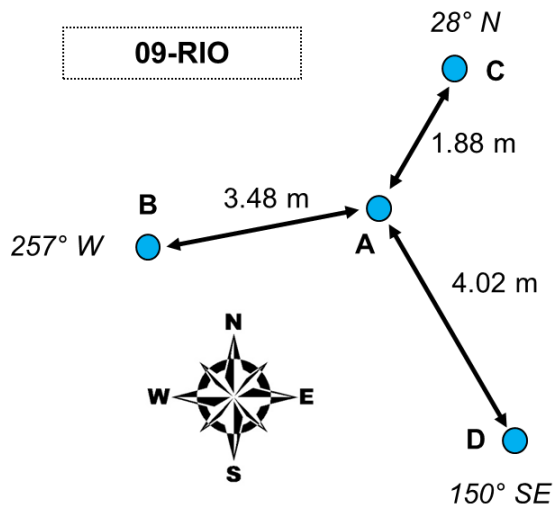
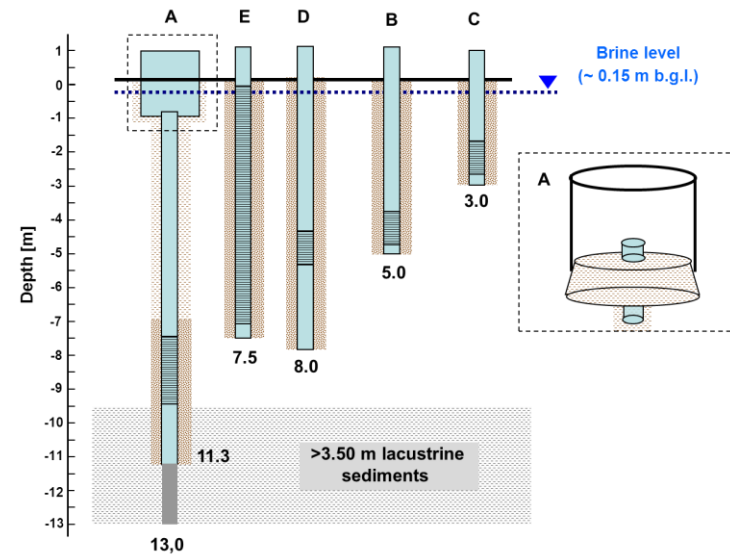
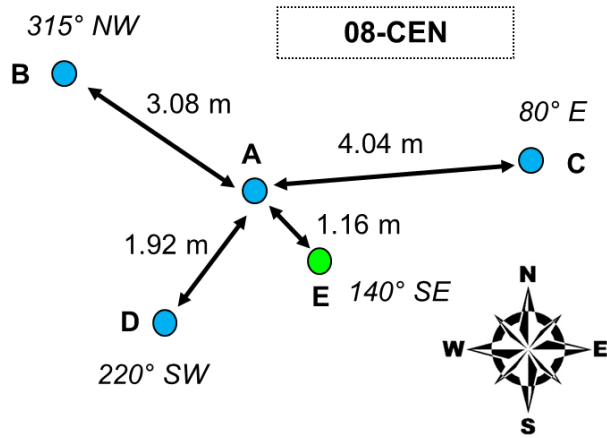


Figure A - 3: Top view (left) and cross-section of the well constellation (right) at sites 08-CEN (top) and 09-RIO (bottom). Symbols are explained in Figure A - 1.

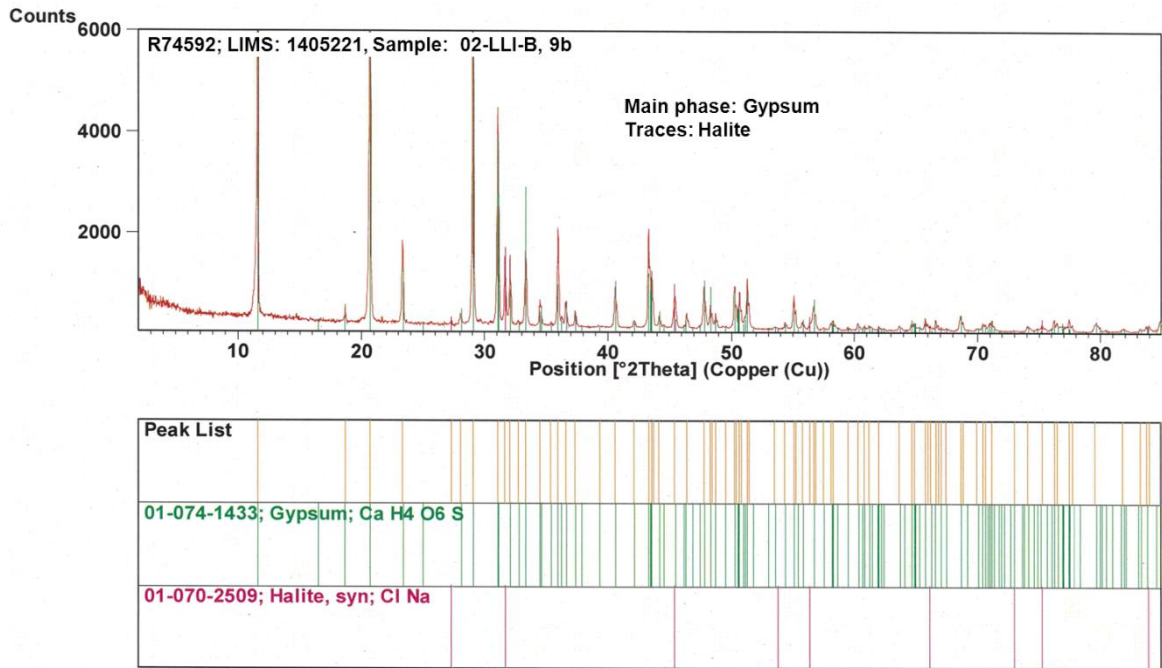


Figure A - 4: X-ray diffractogram of sample 02-LLI-B, 9b

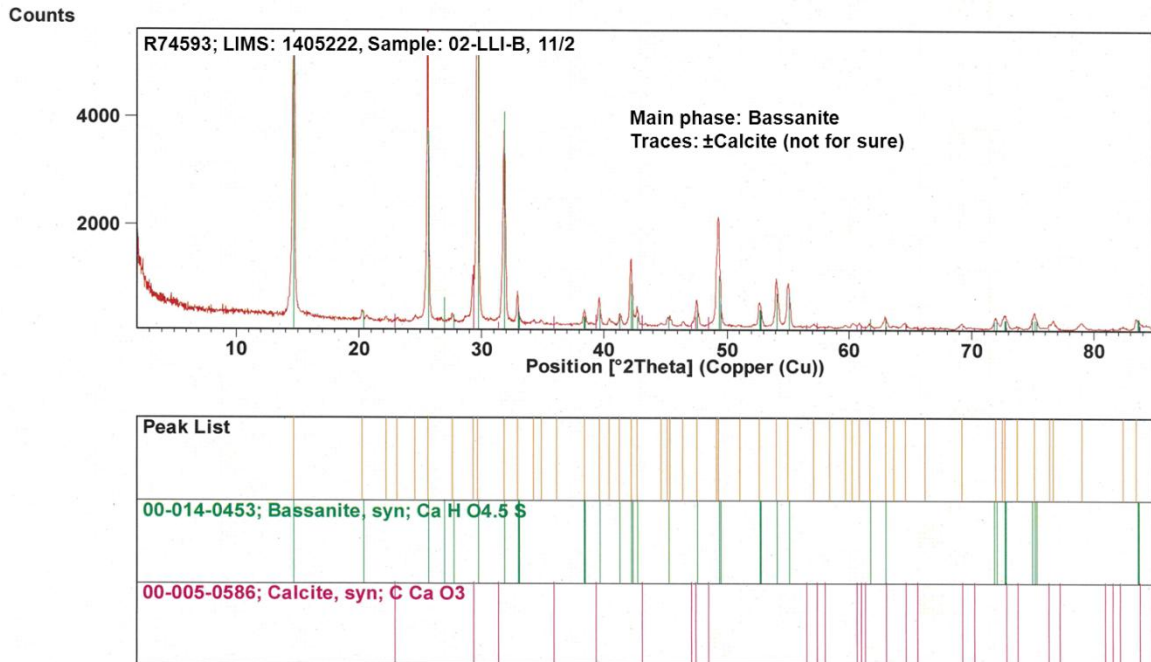


Figure A - 5: X-ray diffractogram of sample 02-LLI-B, 11/2

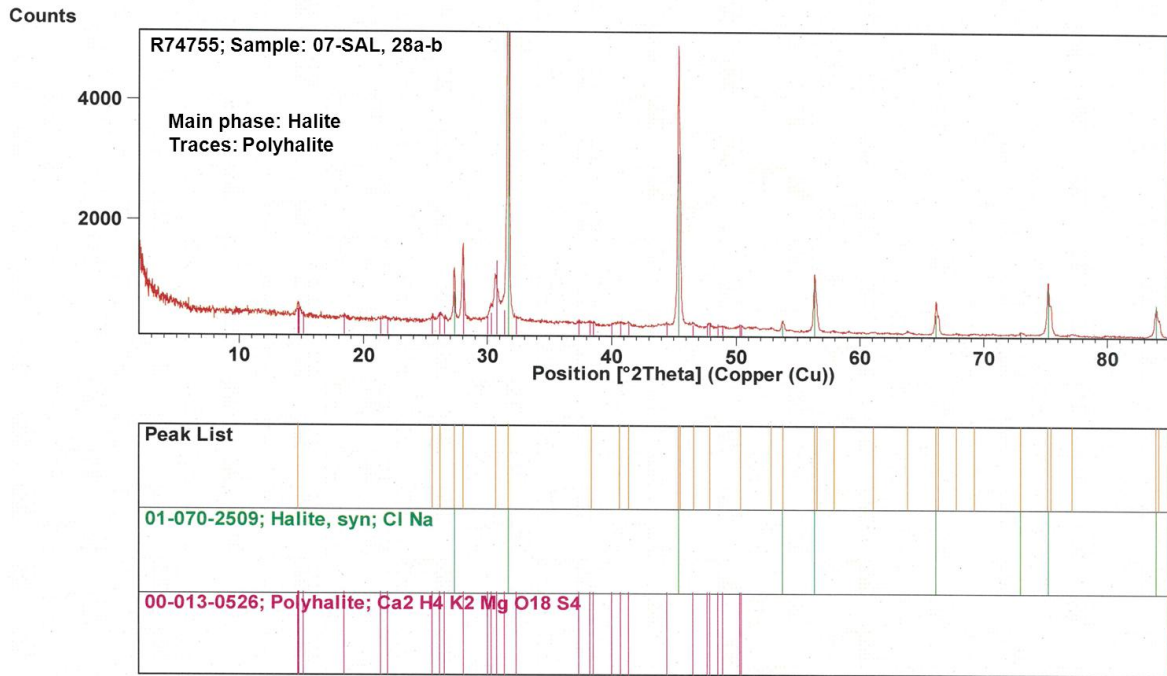


Figure A - 6: X-ray diffractogram of sample 07-SAL, 28 a-b

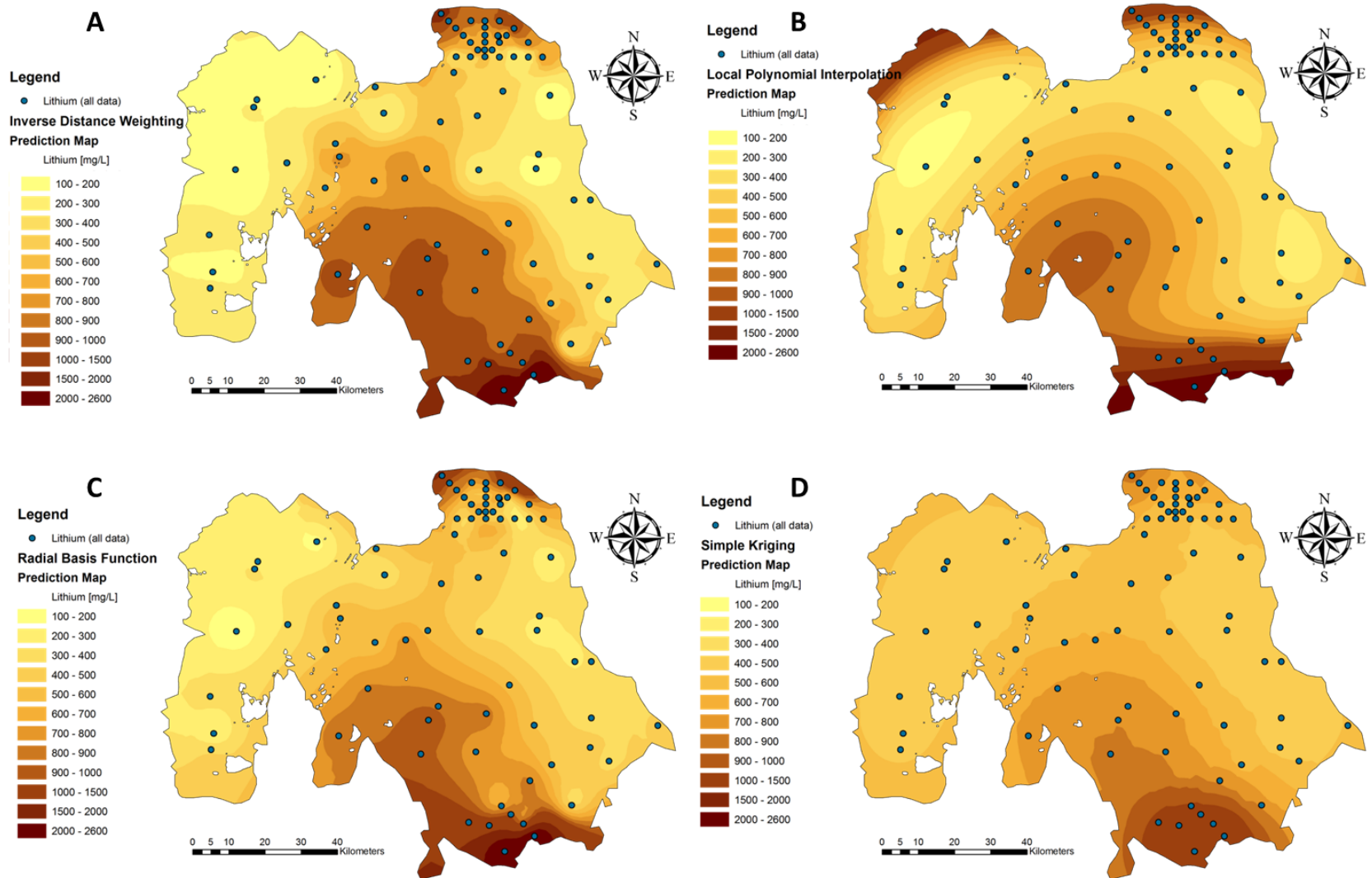


Figure A - 7: Comparison of different interpolation methods for creation of a lithium distribution map: (A) Inverse Distance Weighting, (B) Local Polynomial Function of the 4th order, (C) Radial Basis Function, (D) Simple Kriging with spherical semi-variogram.

Notes to the pumping test data

In the following, pumping test data of 7 pumping tests performed in 2010 and 2012 are summarized in diagrams.

At first, for each test site the original baro-compensated brine level data recorded by CeraDivers (illustrated by dashed lines in bright colors) are compared with the finally corrected depression data (displayed by solid lines in strong colors) which are used for actual pumping test evaluation.

Afterwards, the drawdown (s) is plotted against the logarithmic pumping time (t) for all observation wells (pumping well). Due to inconstant pumping rates occurring prevalently at the very beginning of pumping tests as well as border effects due to the well properties, first data records are generally not considered for further evaluation. Therefore, those values which are used for the COOPER-JACOB straight-line procedure (compare chapter 3.1.3.2) are highlighted in large, strong colored symbols.

For the evaluation of brine recovery after stopping the pump according to the method of THEIS and JACOB, the residual depression (s_r) in the observation wells (pumping wells) is depicted versus the ratio between total time delay since starting the pumping test (t) and the time of recovery after stopping the pump (t').

Finally, the differences between the extrapolated depression of the drawdown s and the remaining depression (s_r) are plotted versus the time of recovery (t') for all observation and pumping wells according to the procedure from Driscoll.

Pumping test 02-LLI, 24-Nov-2010

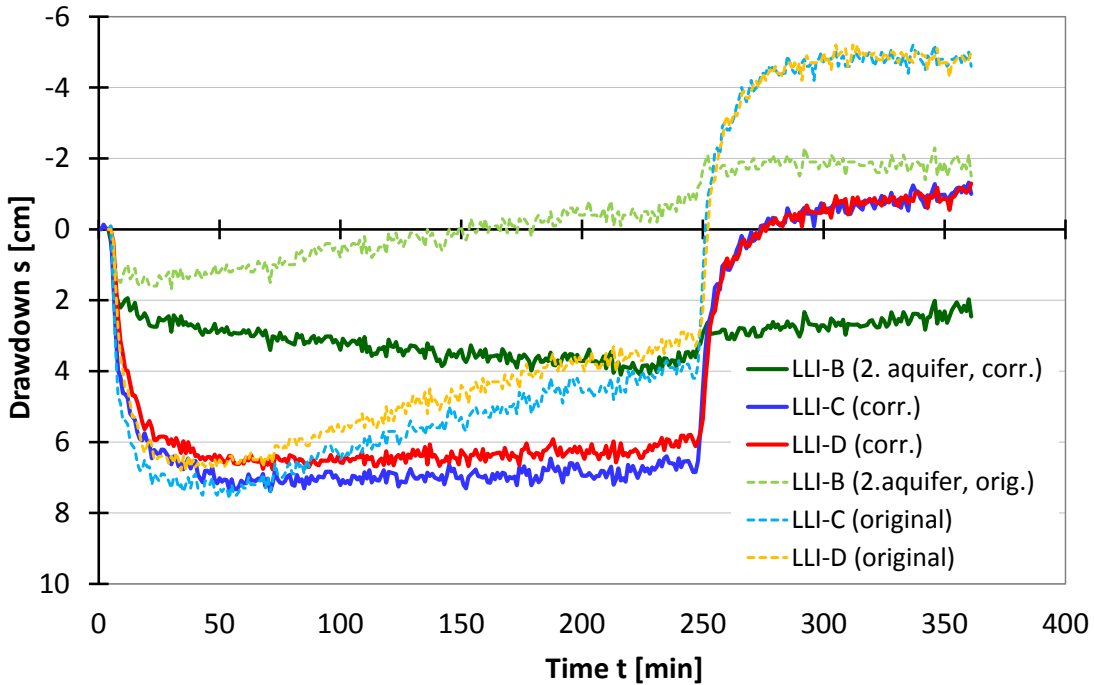


Figure A - 8: Brine level data during the pumping test ‘02-LLI’ in 2010: Dashed lines in bright colors indicate the barometric compensated data recorded by the Cera-Divers, solid lines in strong colors represent finally corrected brine level data used for pumping test evaluation (Note: Observation well B is screened in the second halite layer at depths between 8.0 and 9.0 m).

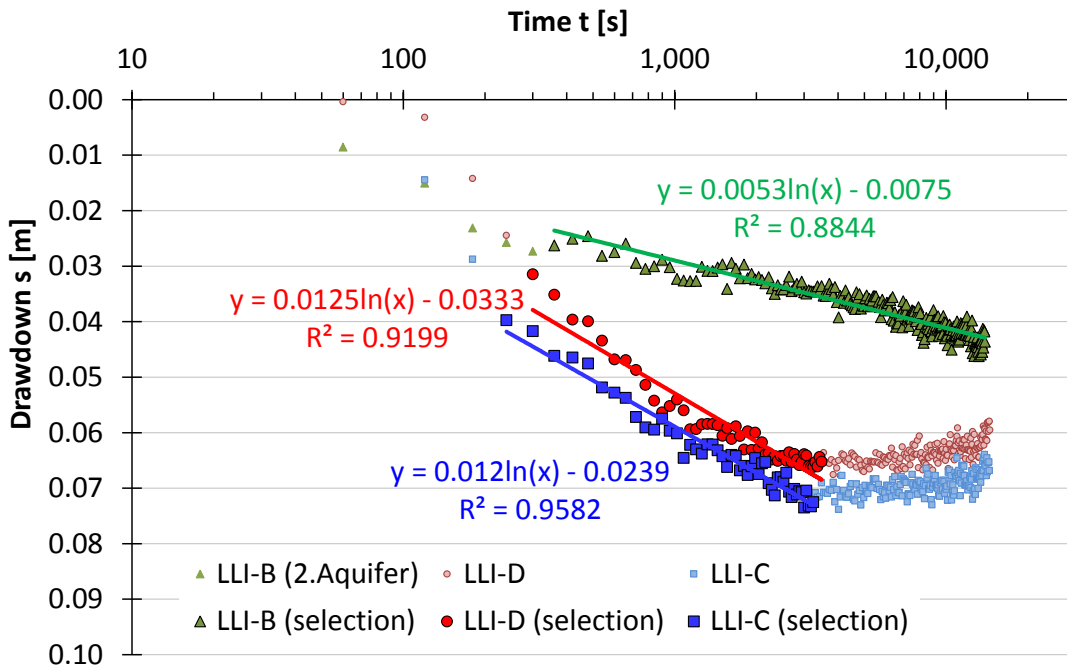


Figure A - 9: Semi-logarithmic drawdown of the pumping test ‘02-LLI’ in 2010 (Note: Observation well B is screened in the second halite layer at depths between 8.0 and 9.0 m).

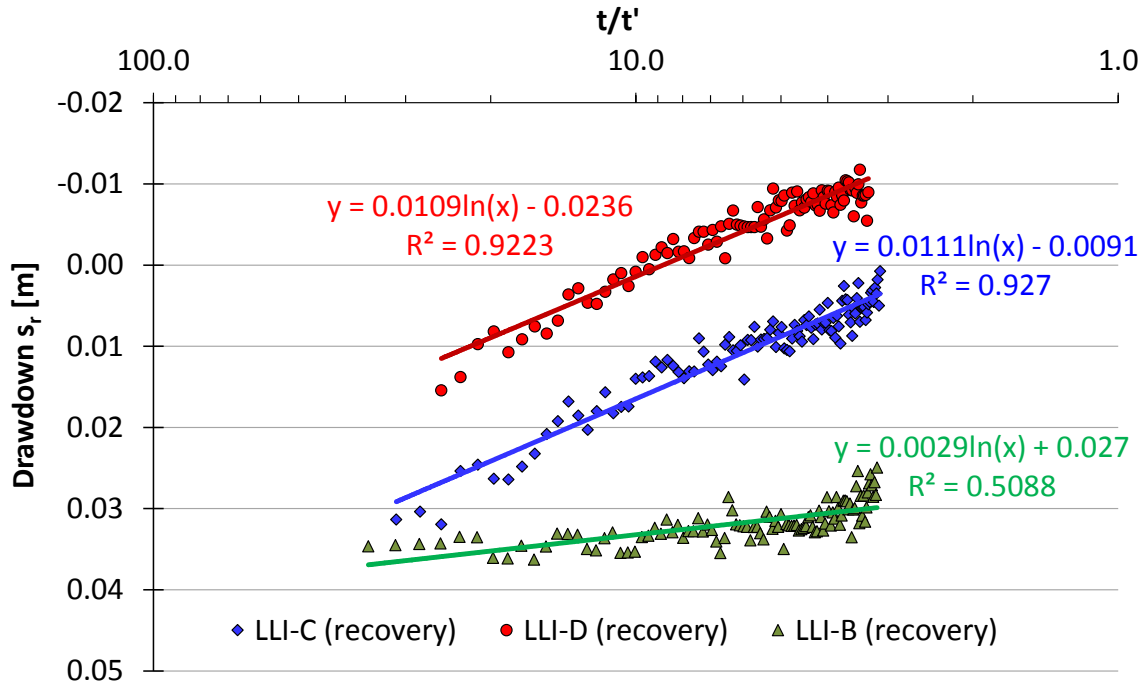


Figure A - 10: Analysis of the recovery phase of the pumping test '02-LLI' (2010) with the JACOB method.

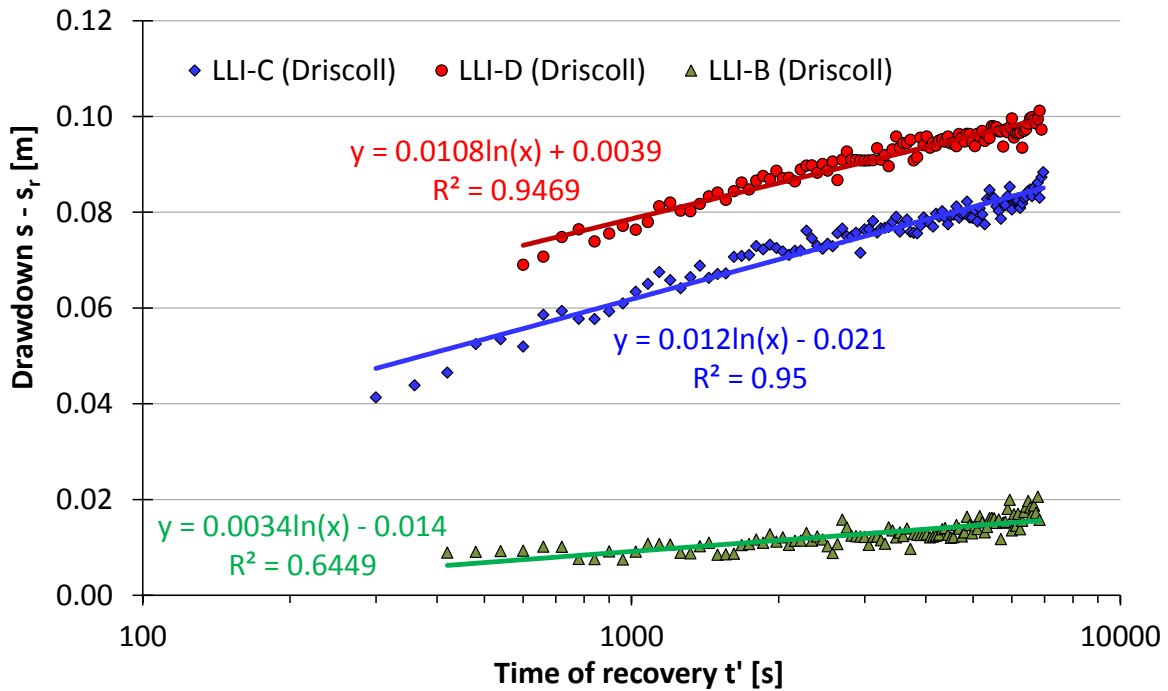


Figure A - 11: Recovery evaluation of pumping test '02-LLI' (2010) according to the procedure of DRISCOLL: Logarithmic time t' after stopping the pump vs. the difference between extrapolated drawdown (s) and residual drawdown (s_r) during recovery.

Pumping test 05-TAH, 30-Oct-2010

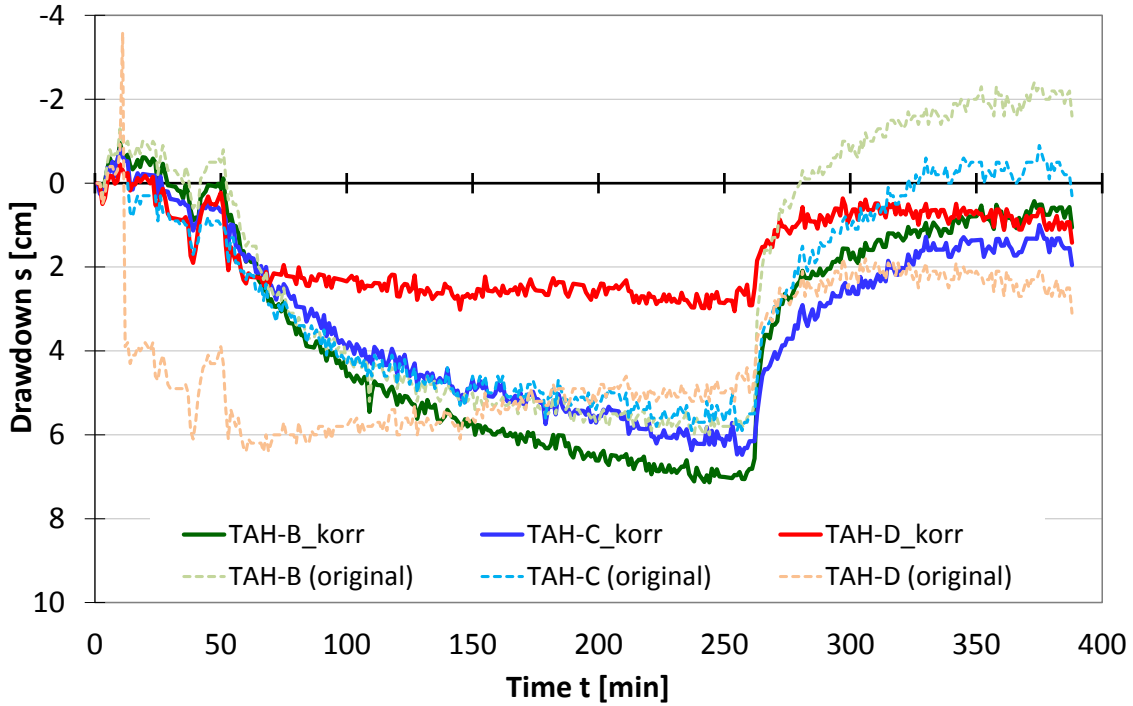


Figure A - 12: Brine level data of the pumping test '05-TAH' in 2010.

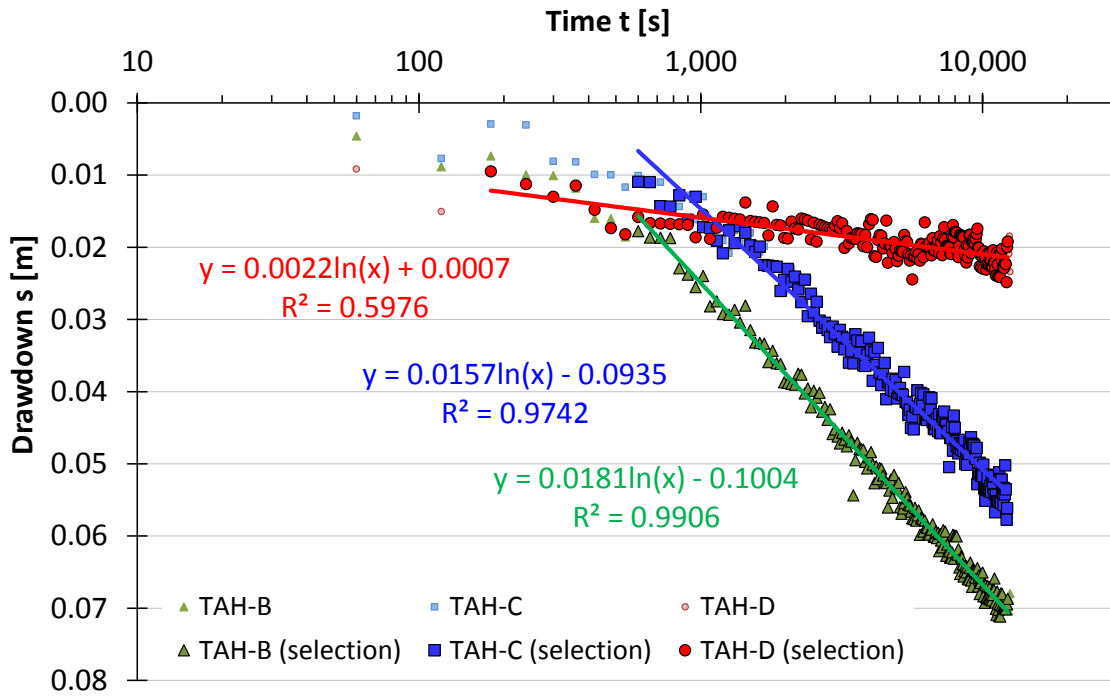


Figure A - 13: Semi-logarithmic drawdown of the pumping test '05-TAH' in 2010.

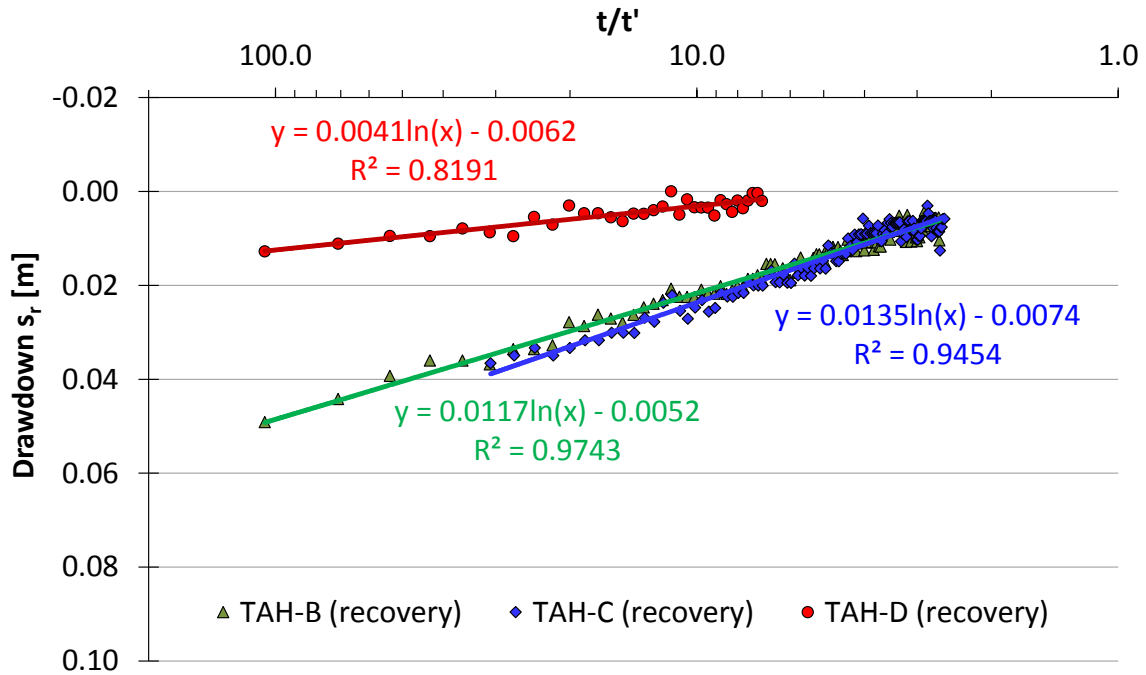


Figure A - 14: Analysis of the recovery phase of the pumping test '05-TAH' (2010) with the JACOB method.

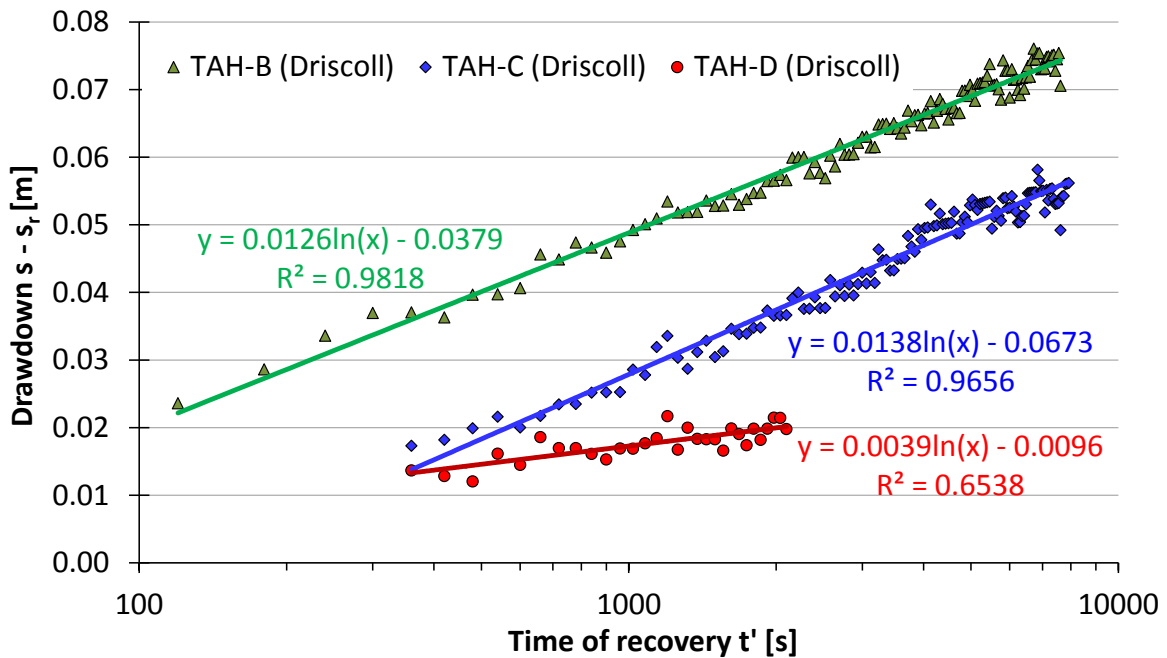


Figure A - 15: Recovery evaluation of pumping test '05-TAH' (2010) according to the procedure of DRISCOLL.

Pumping test 06-NOR, 18-Nov-2010

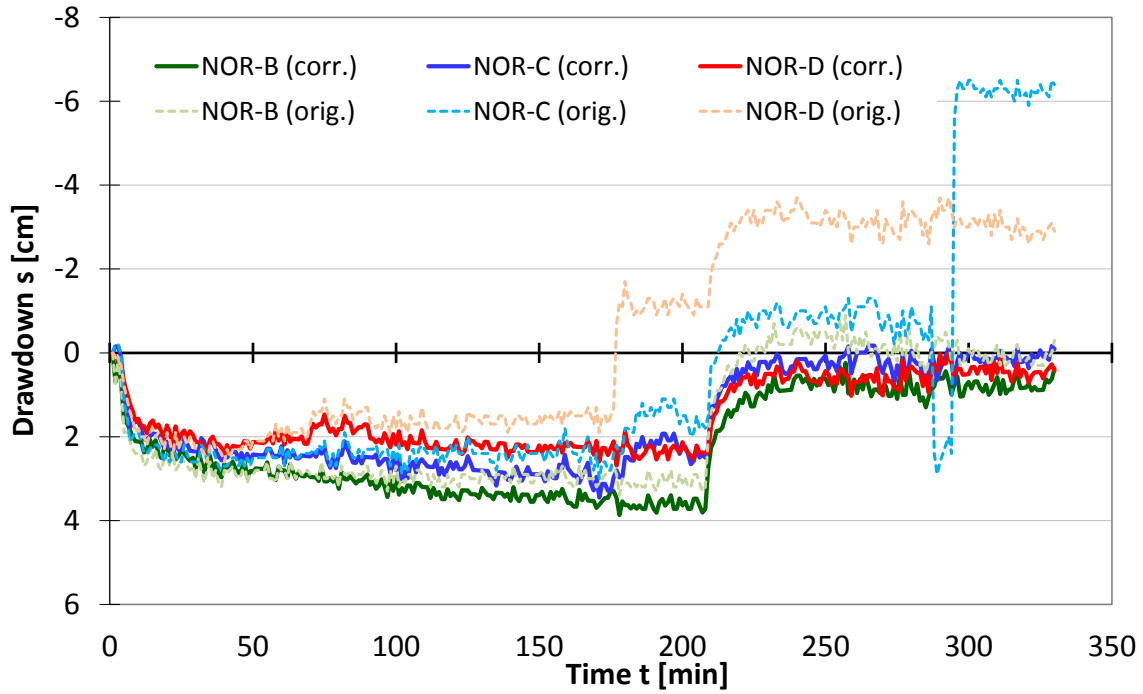


Figure A - 16: Brine level data of the pumping test '06-NOR' in 2010.

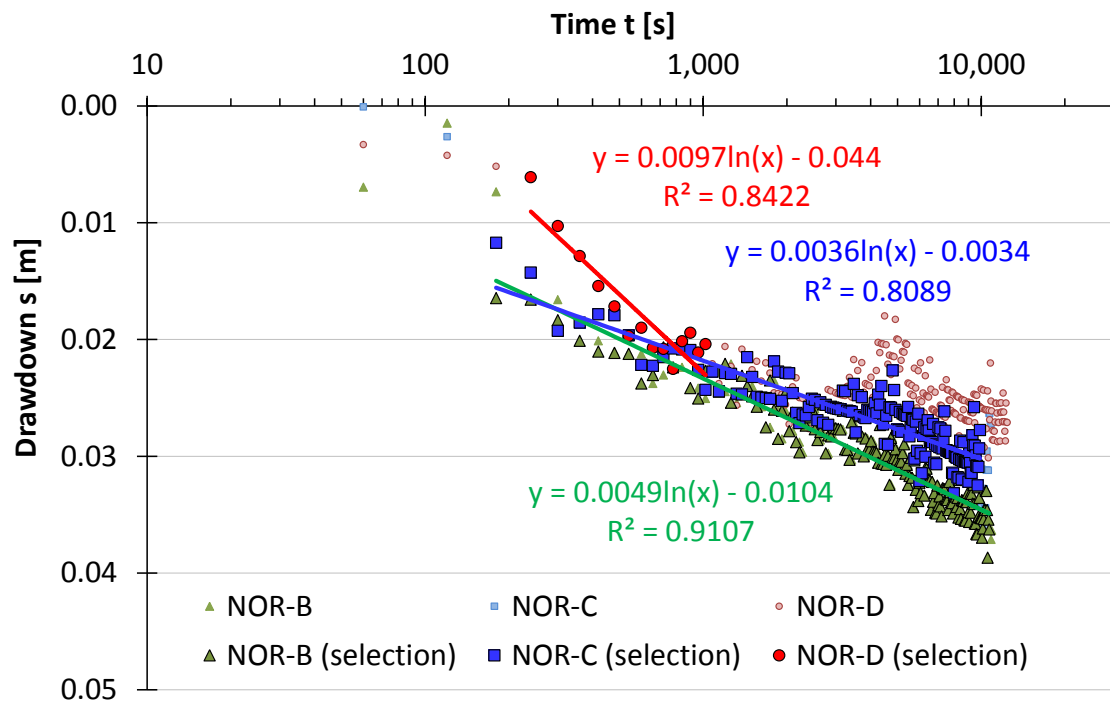


Figure A - 17: Semi-logarithmic drawdown of the pumping test '06-NOR' in 2010.

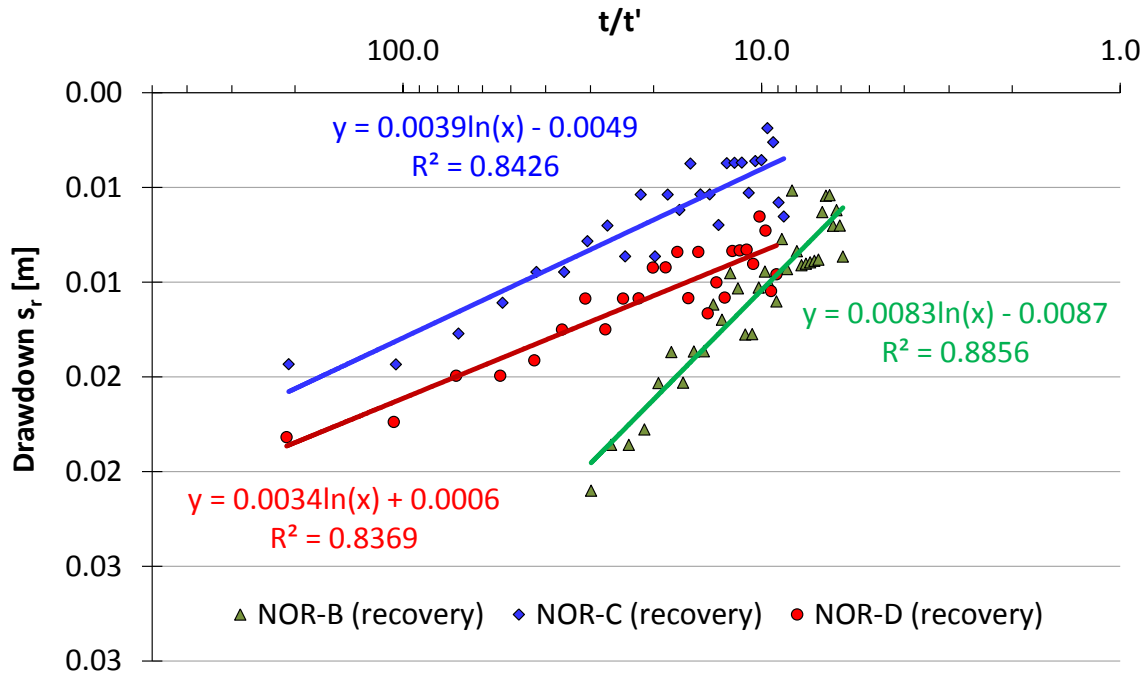


Figure A - 18: Analysis of the recovery phase of the pumping test '06-NOR' (2010) with the JACOB method.

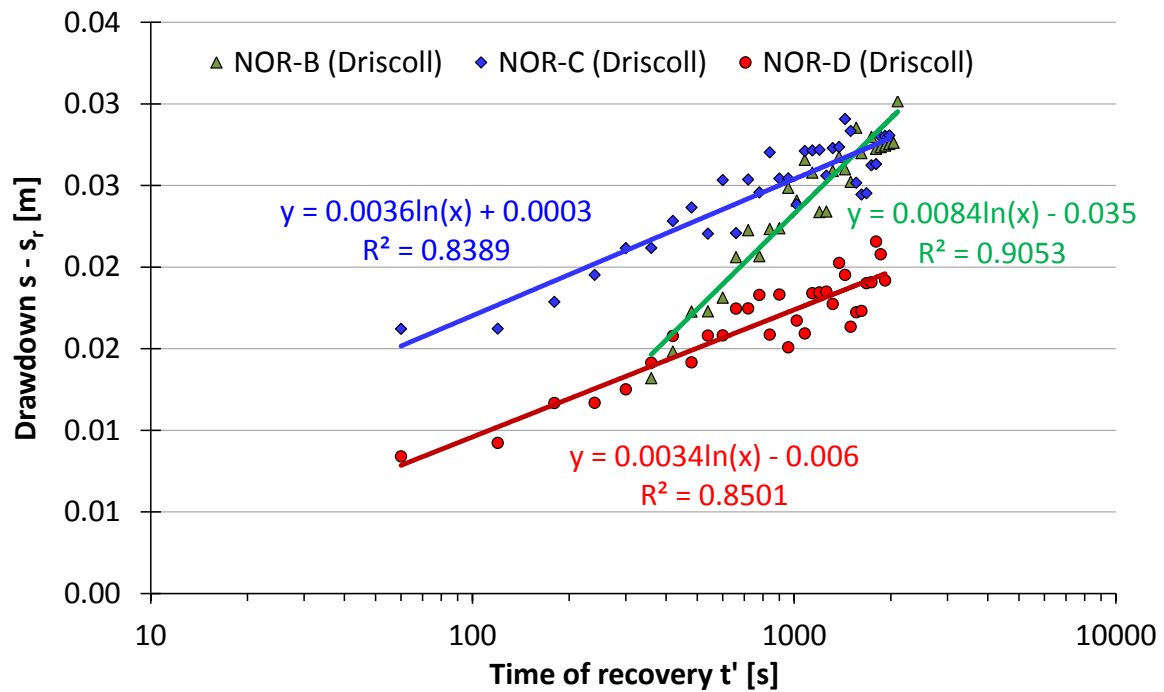


Figure A - 19: Recovery evaluation of pumping test '06-NOR' (2010) according to the procedure of DRISCOLL

Pumping test 08-CEN, 3-Nov-2010

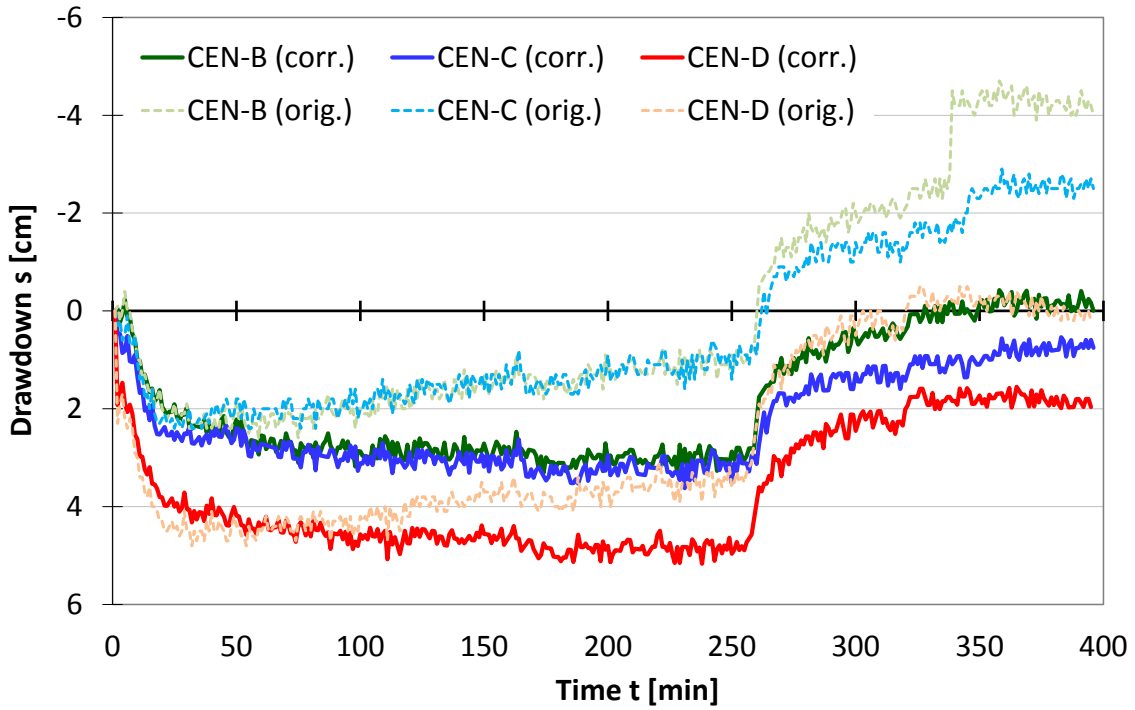


Figure A - 20: Brine level data of the pumping test '08-CEN' in 2010.

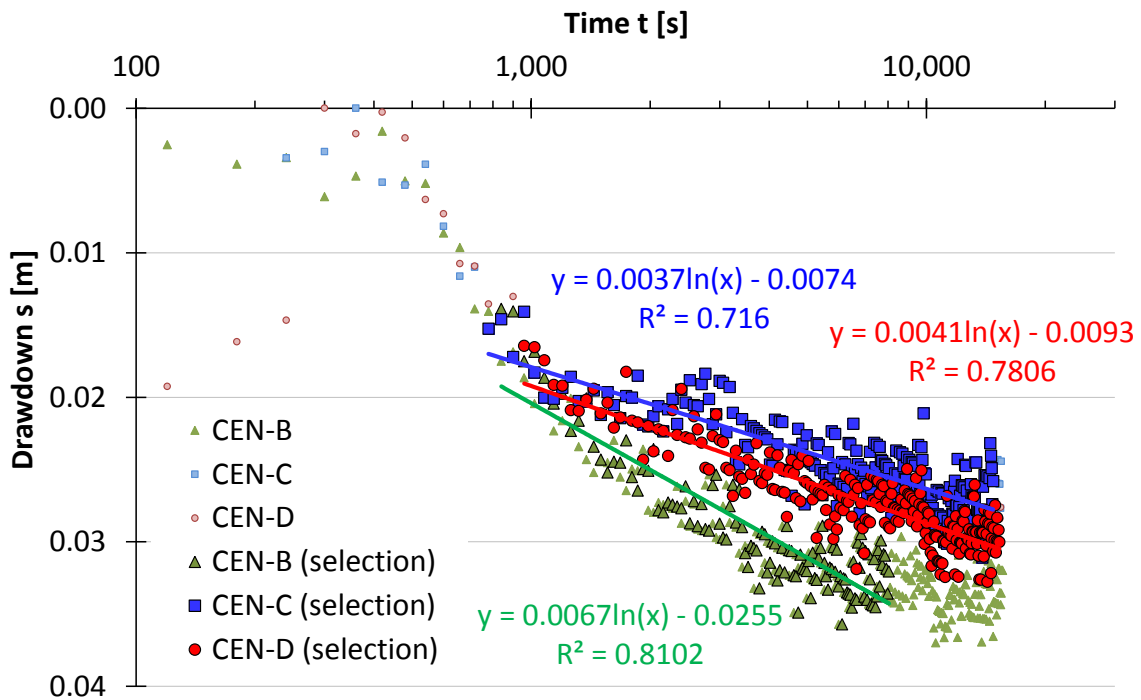


Figure A - 21: Semi-logarithmic drawdown of the pumping test '08-CEN' in 2010.

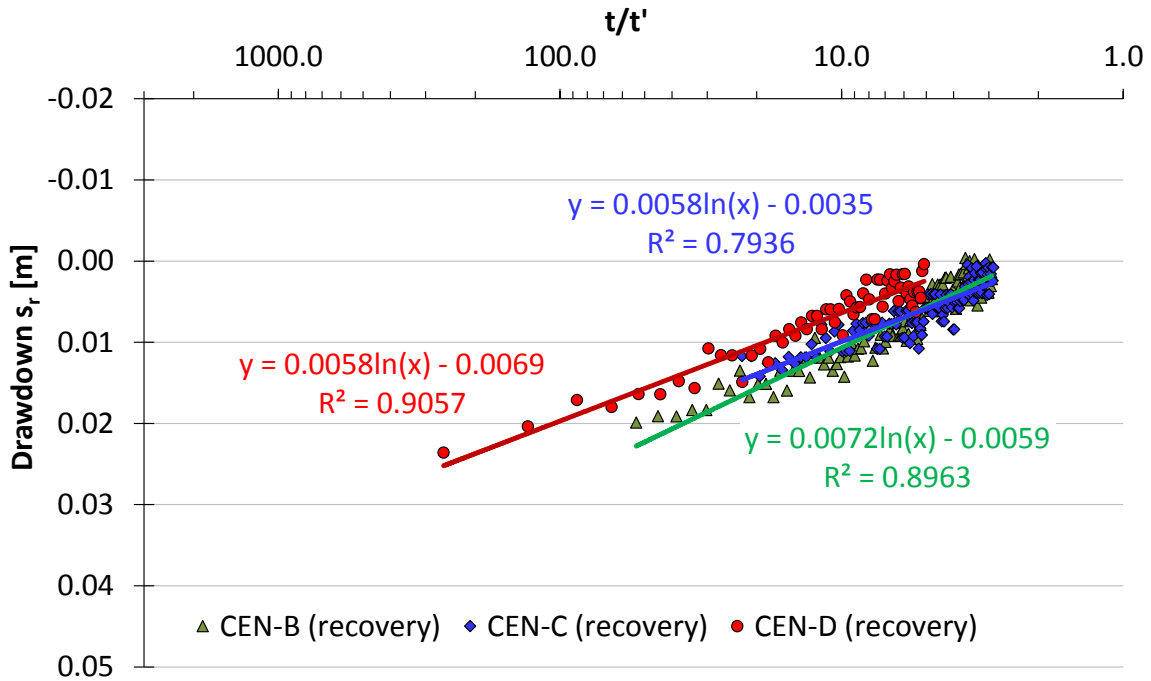


Figure A - 22: Analysis of the recovery phase of the pumping test '08-CEN' (2010) with the JACOB method.

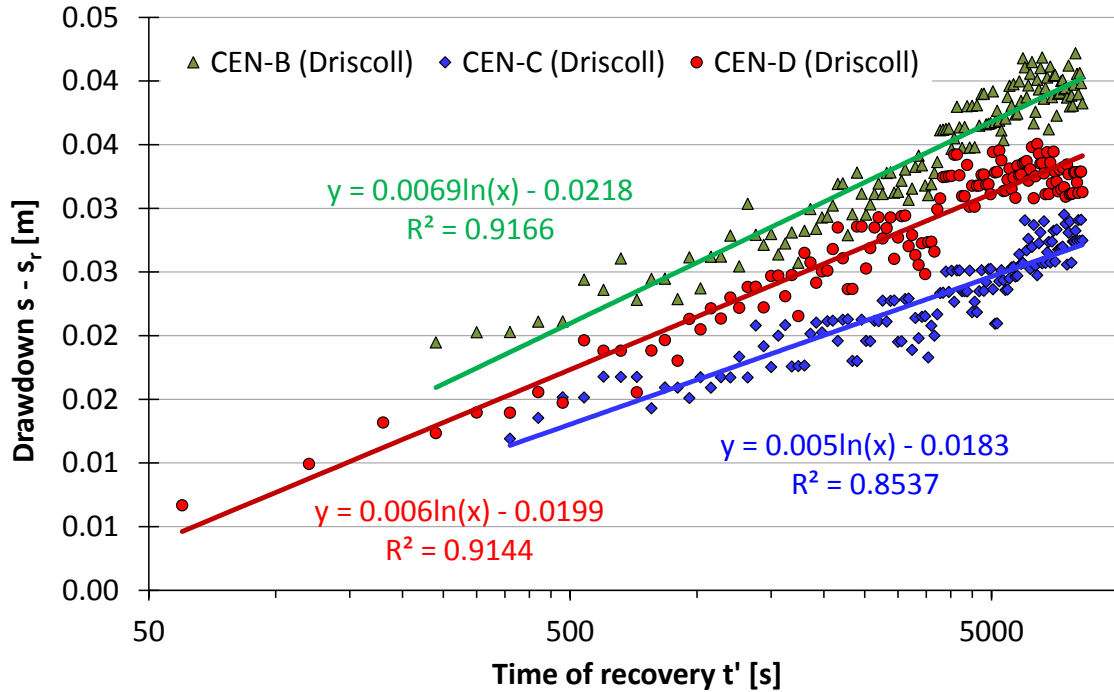


Figure A - 23: Recovery evaluation of pumping test '08-CEN' (2010) according to the procedure of DRISCOLL

Pumping test 09-RIO, 28-Nov-2010

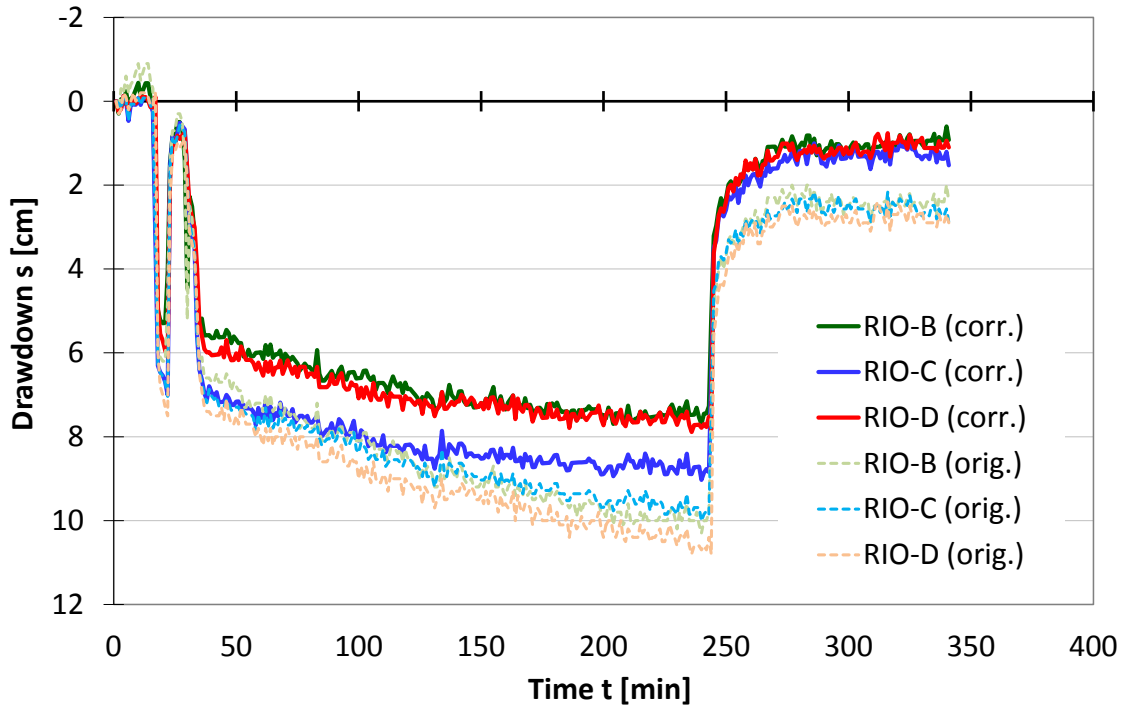


Figure A - 24: Brine level data of the pumping test '09-RIO' in 2010.

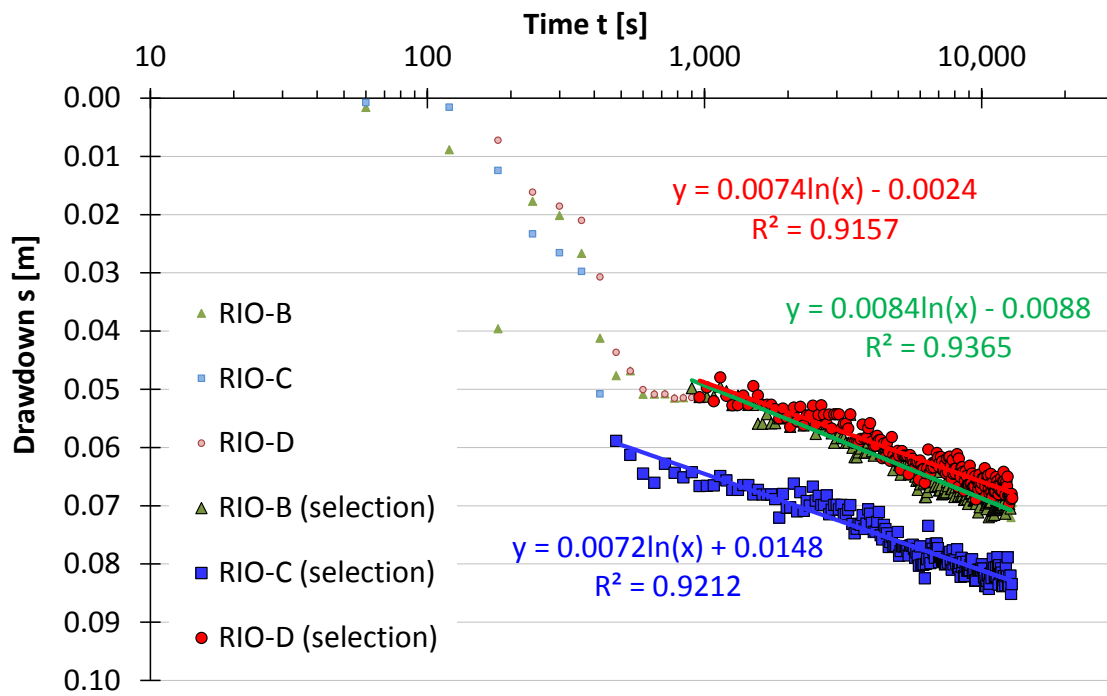


Figure A - 25: Semi-logarithmic drawdown of the pumping test '09-RIO' in 2010.

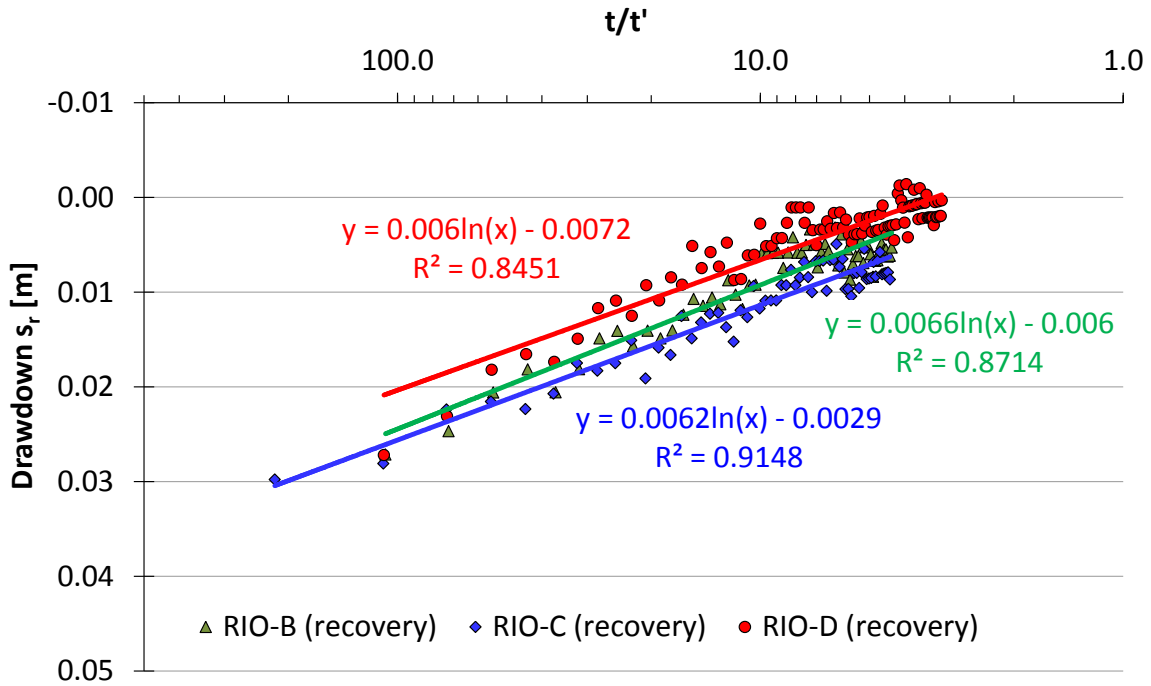


Figure A - 26: Analysis of the recovery phase of the pumping test '09-RIO' (2010) with the JACOB method.

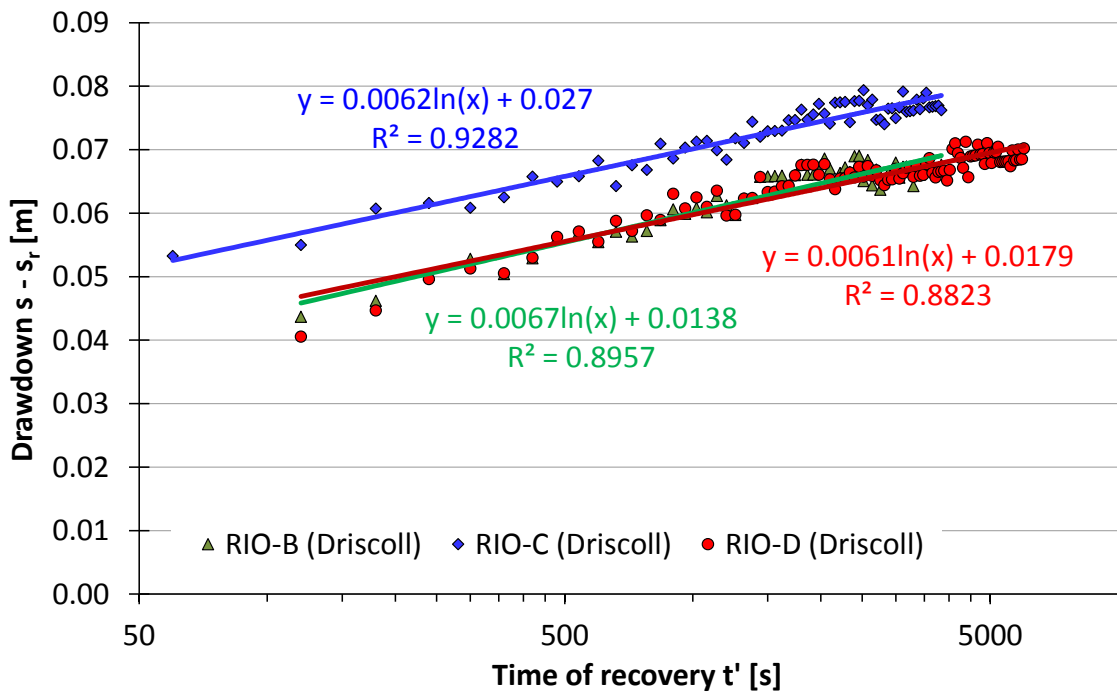


Figure A - 27: Recovery evaluation of pumping test '09-RIO' (2010) according to the procedure of DRISCOLL

Pumping test 02-LLI, 30-Nov-2012

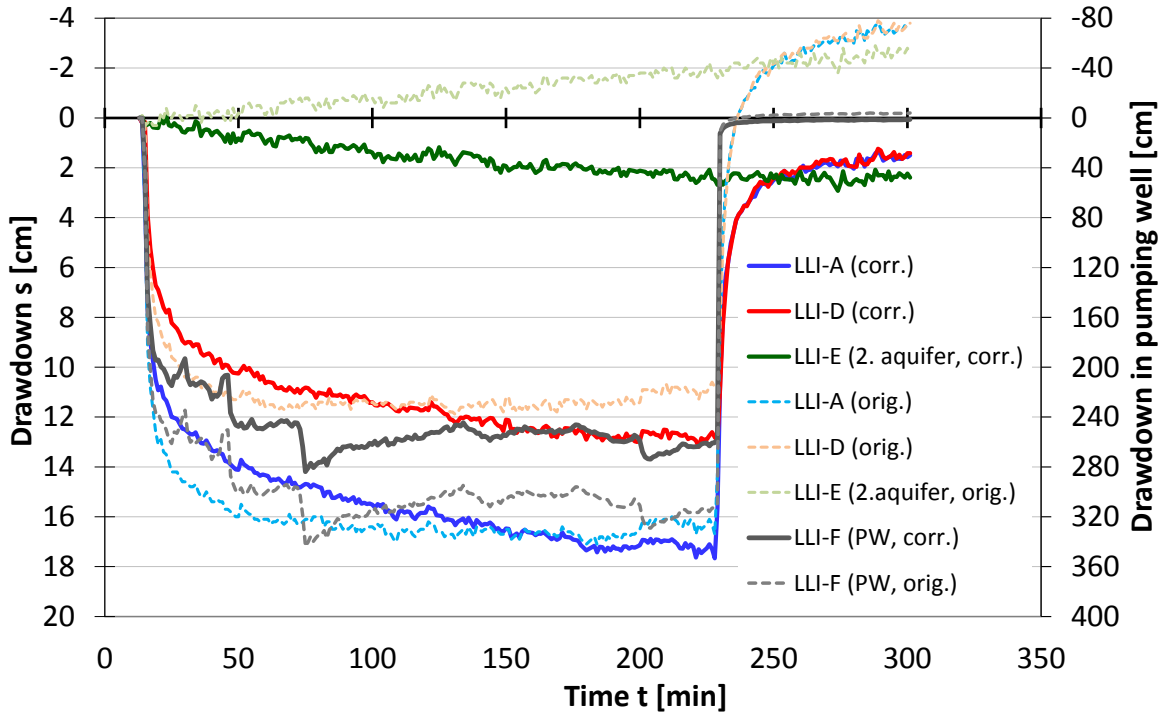


Figure A - 28: Brine level data of the pumping test '02-LLI' in 2012 (the pumping well F fully penetrates the uppermost salt layer, observation well E is filtered in the second salt layer).

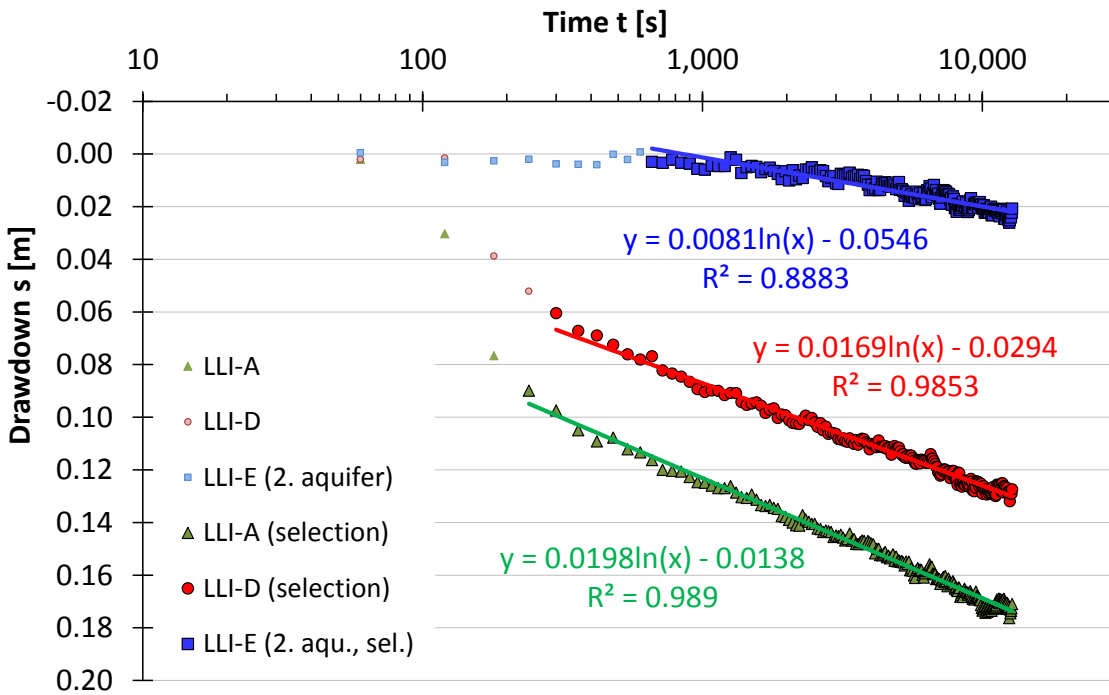


Figure A - 29: Semi-logarithmic drawdown of the pumping test '02-LLI' in 2012.

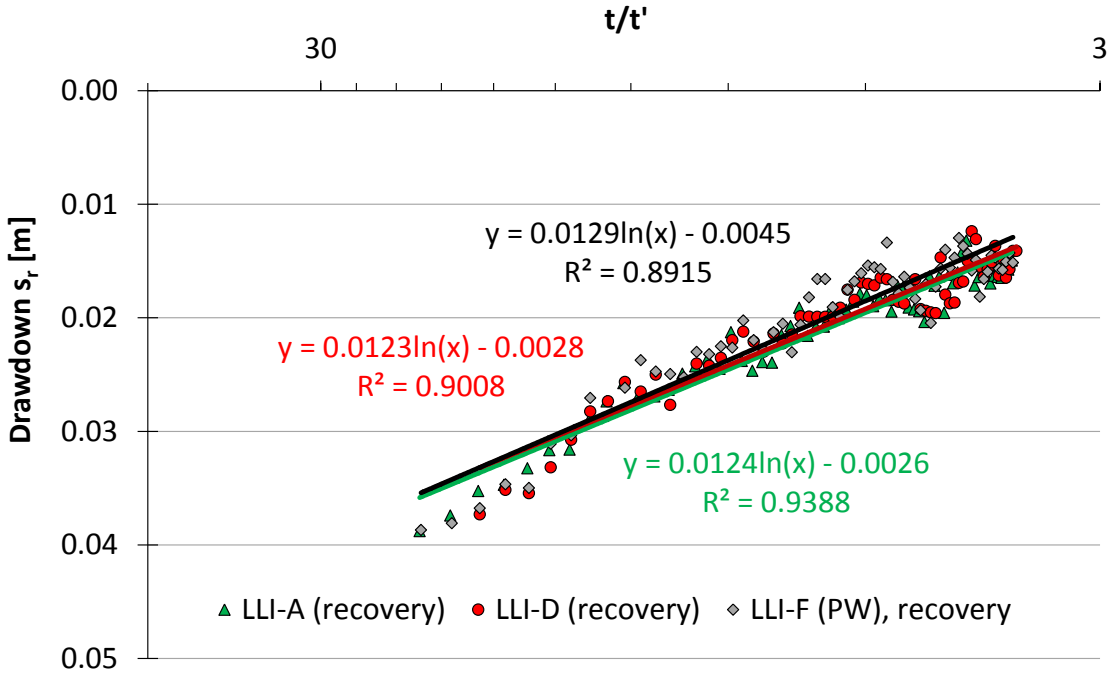


Figure A - 30: Analysis of the recovery phase of the pumping test '02-LLI' (2012) with the JACOB method (data from observation well B screened in the second salt layer are not considered here).

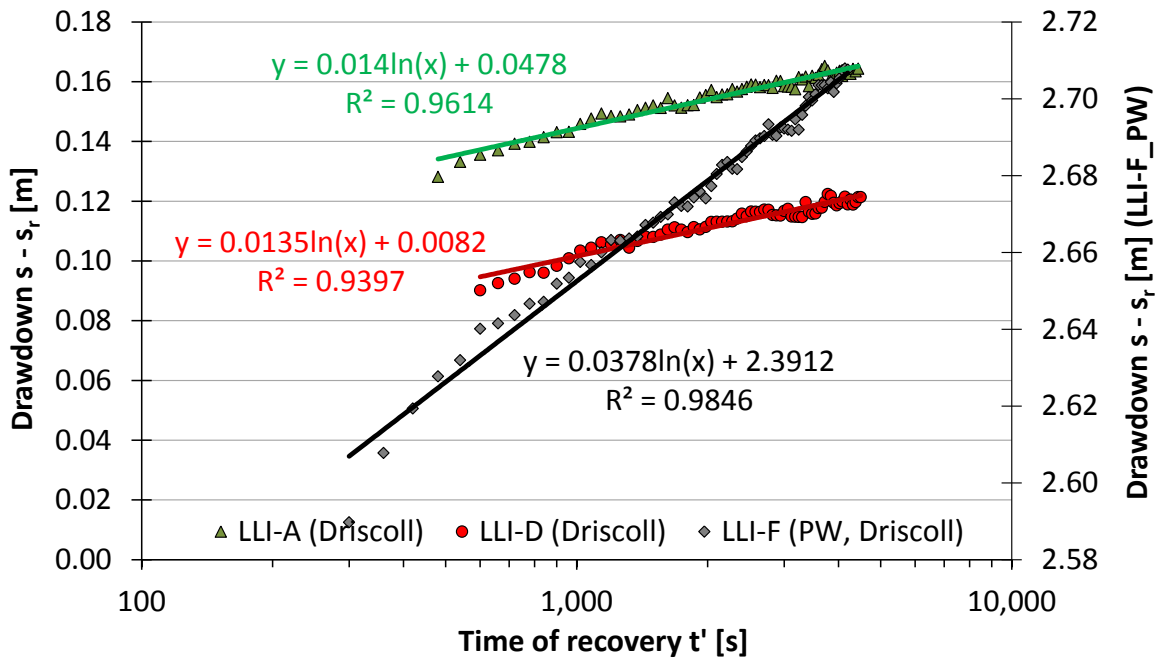


Figure A - 31: Recovery evaluation of pumping test '02-LLI' (2012) according to the procedure of DRISCOLL (recovery data observed in the pumping well F are displayed on the right axis).

Pumping test 08-CEN, 1-Dec-2012

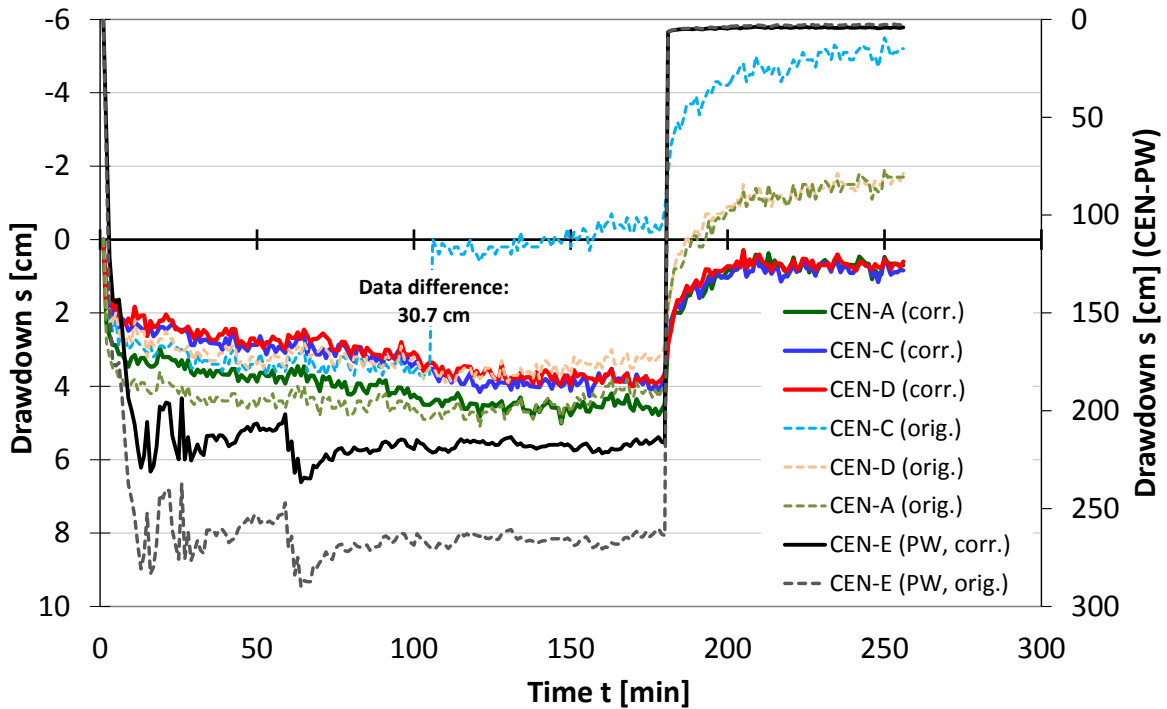


Figure A - 32: Brine level data of the pumping test '08-CEN' in 2012 (the pumping well E fully penetrates the uppermost salt layer). The original drawdown data of well 08-CEN-C showed a discontinuity of 30.7 cm after about 100 min. For better presentation, this discontinuity was reduced here.

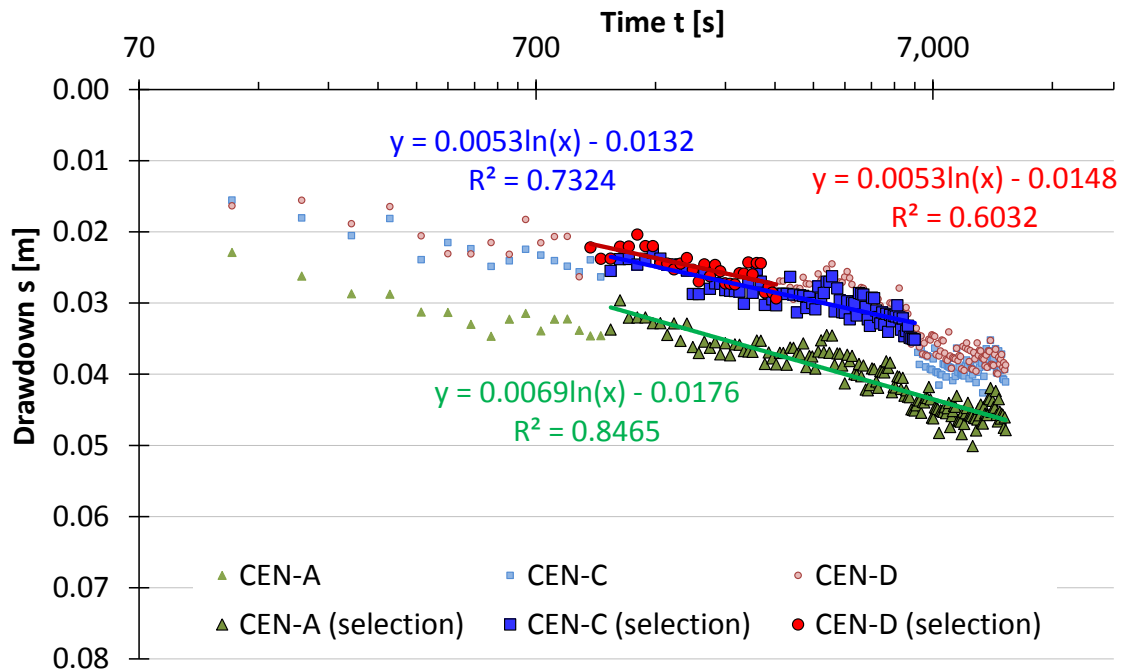


Figure A - 33: Semi-logarithmic drawdown of the pumping test '08-CEN' in 2012.

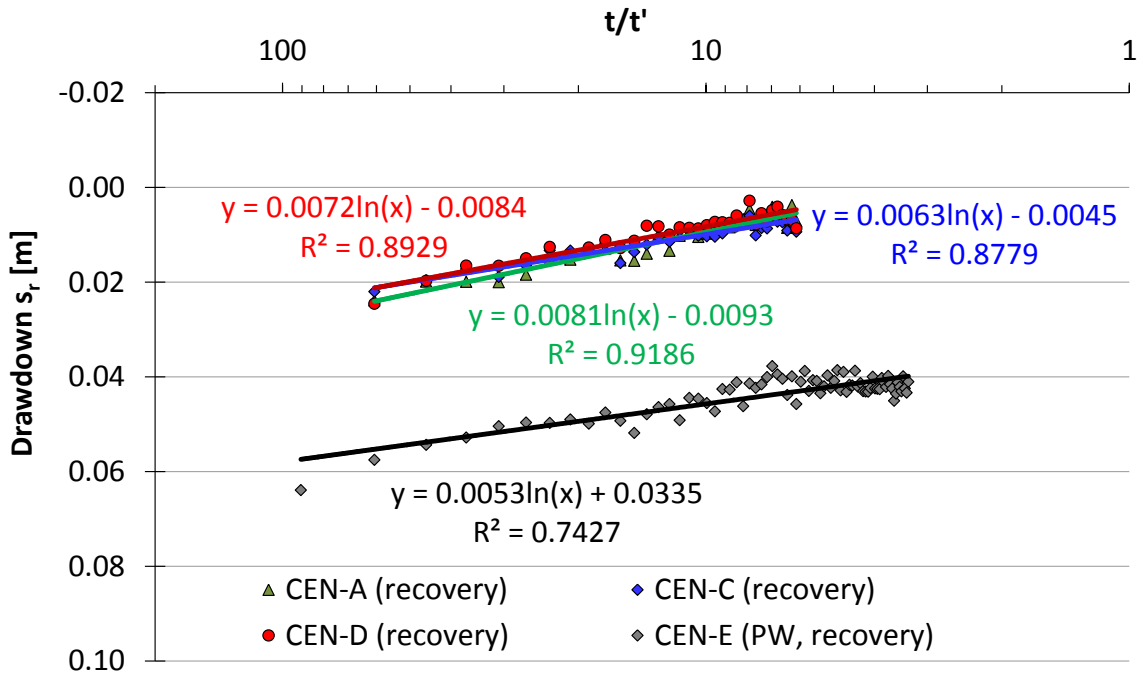


Figure A - 34: Analysis of the recovery phase of the pumping test '08-CEN' (2012) with the JACOB method.

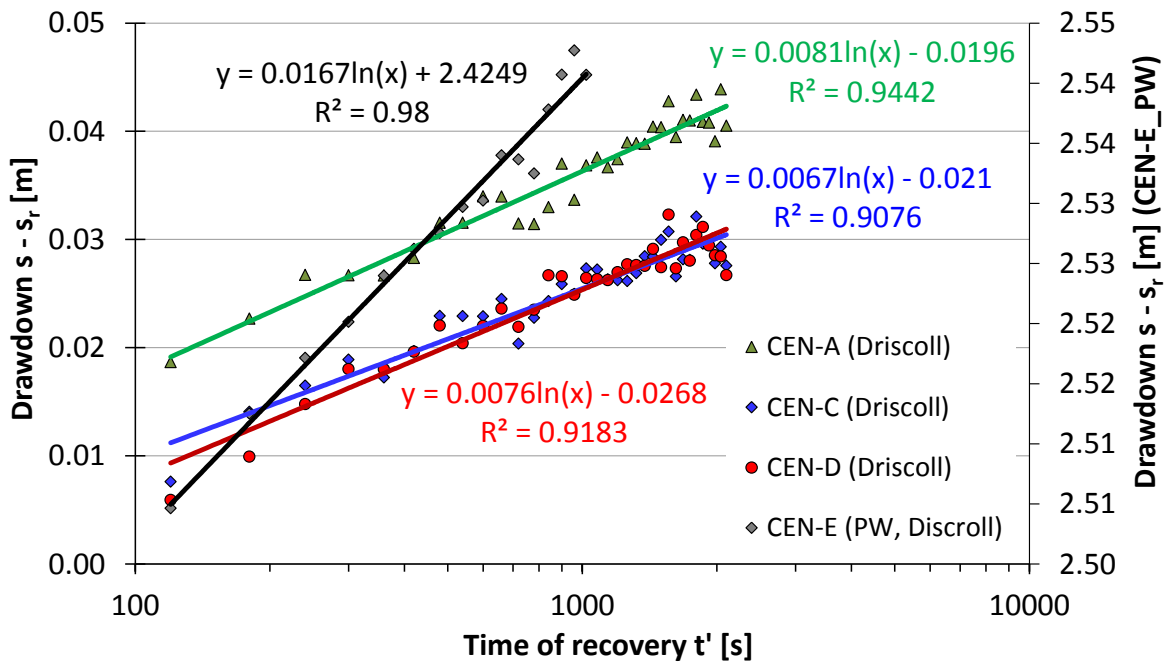


Figure A - 35: Recovery evaluation of pumping test '08-CEN' (2012) according to the procedure of DRISCOLL (recovery data observed in the pumping well E are displayed on the right axis).

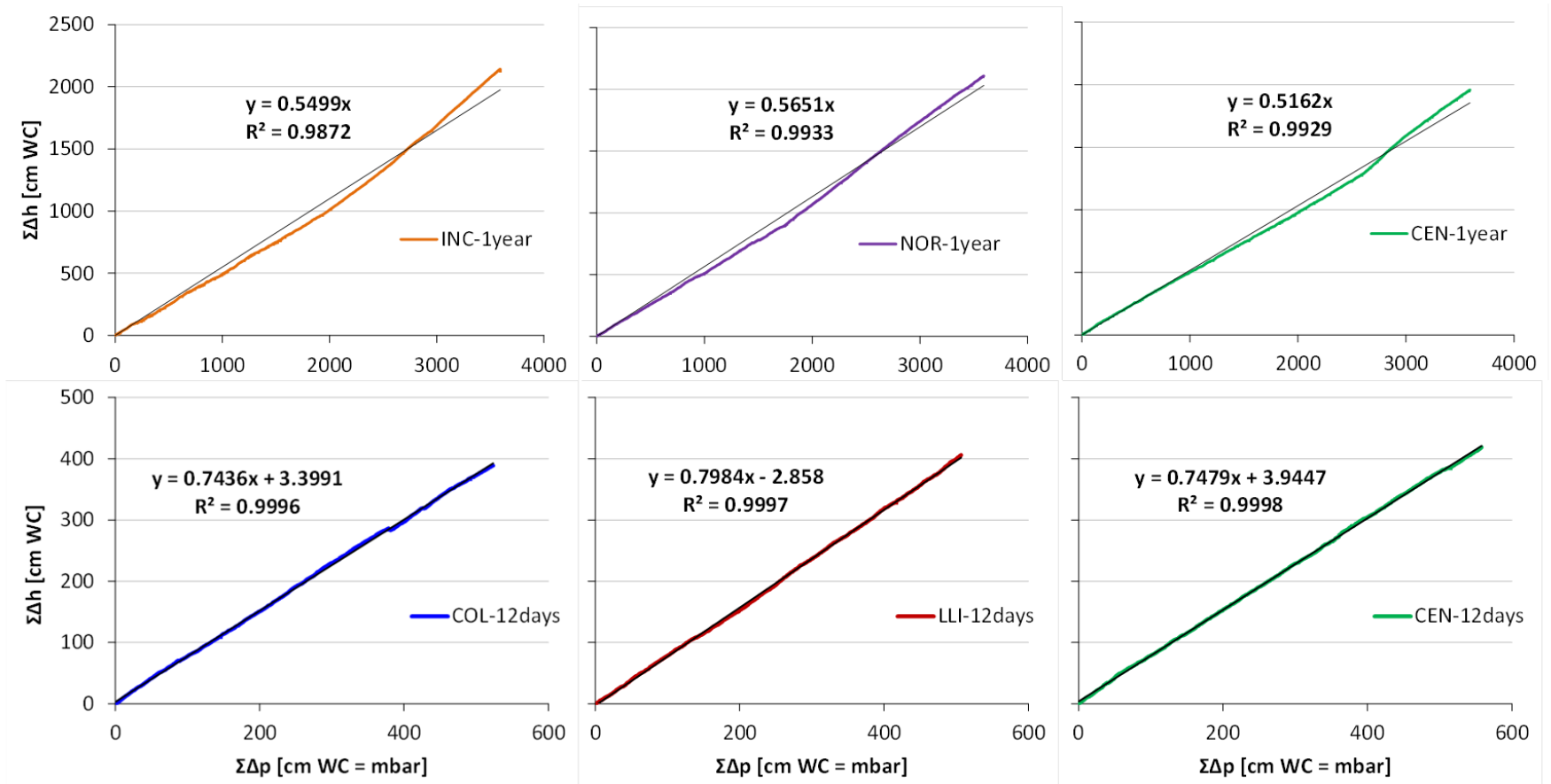


Figure A - 36: Determination of the barometric efficiency (BE) by means of the curve of the sums of the increments of atmospheric pressure ($\Sigma\Delta p$) and natural brine level ($\Sigma\Delta h$) fluctuations for long-term (top, 269 days) and short-term observations (bottom, 12 days) at different sites on the Salar de Uyuni.

Appendix B – Tables**Table B - 1: Technical details of the drilling machine (modified from Schmidt 2010)**

Technical data	
Core drill motor	Type: WEKA DK32S
Weight/length	11.9 kg / 480 mm
Power supply	3200 W / 230 V
Nominal revolution speed	1. Gear: 300 Rpm 2. Gear: 590 Rpm 3. Gear: 960 Rpm
Drill bits	Hard metal plate crown, system B, with core catcher, DRM 206x186 mm and DRM 76 mm
Drill diameter (inner/outer diameter)	186/206 mm (8 inch) 64 / 76 mm (3 inch)
Drill rig	Type: D 300 – AMB-System Total height: 1.70 m Working height: 1.00 m Total weight (without motor): 24 kg
Drill rods	Hexagonal, length: 500/1000 mm, diameter: 50 mm (aluminum / steel)
Maximum drilling depth	~ 20 m (in hard rock) (maximum total length of all drill rods: 15 m)
Drilling fluid	Local brine from the salt flat

Table B - 2: Technical specifications of the CT-Alpha 225 computed tomograph (Institute of Ceramics, Glass and Construction Materials, TU Bergakademie Freiberg)

Technical data	
Device	CT-Alpha 225
Producer:	ProCon X-Ray GmbH Garbsen, 2008
Detector	Type: PerkinElmer XRD 1620 AN CS Producer: PerkinElmer Optoelectronics, Fremont/Canada Year: 2008 No. of pixels: 2048 x 2048 Pixel size: 200 μm x 200 μm Total area: 409.6 mm x 409.6 mm
Detector parameter	Image averaging: 3 Skip: 1 Exposure time: 1.00 s
X-ray tube	Direct beam tube 225 kV Company: Feinfocus Garbsen, 2008
Tube parameter	Mode: Micro-focus Voltage: 200 kV Amperage: 130 - 180 μA Target power: 23.2 - 33.3 W
Reconstruction	Angel number: 400 Cross-section: 50 % Bit-depth: 16 Voxel size after reconstruction: 76.5 μm

Table B - 3: Meteorological data of the Salar de Uyuni from 2001 to 2011.

Station:	Uyuni	Latitude South:	20° 27' 00"
Department:	Potosí	Longitude West:	66° 48' 00"
Province:	Antonio, Quijarro	Altitude [m a.s.l.]	3669

Total Precipitation [mm]													
Year	Jan.	Feb.	March	April	May	June	July	Aug.	Sep.	Oct.	Nov.	Dic.	Annual
2001	226.5	135.7	0.7	0.0	0.0	0.0	0.0	0.0	0.1	0.0	10.2	0.0	373.2
2002	2.8	70.0	16.7	0.7	0.0	6.1	0.0	0.0	0.0	33.1	2.9	0.5	132.8
2003	74.6	14.2	38.0	0.0	3.3	0.0	0.0	0.0	0.0	0.0	0.0	53.5	183.6
2004	98.5	33.2	16.4	0.0	0.0	0.0	0.0	0.0	0.0	0.0	0.0	59.9	208.0
2005	111.4	115.1	124.7	0.0	0.0	0.0	0.0	0.0	7.2	0.0	1.8	24.6	384.8
2006	158.9	33.2	79.8	8.0	0.0	0.0	0.0	0.0	0.0	0.0	0.0	1.7	281.6
2007	23.8	7.6	27.9	0.0	0.0	0.0	0.0	0.0	0.0	0.0	1.2	27.5	88.0
2008	143.7	****	****	0.0	0.0	0.0	0.0	0.0	0.0	0.0	0.0	0.0	****
2009	0.0	37.0	13.6	0.0	0.0	0.0	0.0	0.0	0.0	0.0	0.0	0.0	50.6
2010	27.9	72.8	0.0	0.0	7.5	0.0	0.0	0.0	0.0	0.0	0.0	0.0	108.2
2011	61.4	63.7	23.4	0.0	8.2	0.0	12.0	****	0.0	0.0	0.0	66.3	****
SUM	929.5	582.5	341.2	8.7	19.0	6.1	12.0	0.0	7.3	33.1	16.1	234.0	1810.8
MEAN	84.5	58.2	34.1	0.8	1.7	0.6	1.1	0.0	0.7	3.0	1.5	21.3	201.2

Table B - 3: Meteorological data of the Salar de Uyuni from 2001 to 2011 (continuation).

Mean temperature [°C]													
Year	Jan.	Feb.	March	April	May	June	July	Aug.	Sep.	Oct.	Nov.	Dic.	Annual
2001	11.5	12.5	10.9	6.0	0.9	-0.2	1.4	4.2	7.3	10.0	12.4	11.9	7.4
2002	12.4	12.7	12.8	11.4	6.9	2.3	2.7	4.5	2.8	9.0	10.0	12.2	8.3
2003	14.2	13.4	11.4	7.6	3.8	0.5	1.6	-0.8	2.9	7.9	9.8	12.3	7.0
2004	12.5	13.0	14.3	10.1	1.8	-1.6	0.2	3.3	7.7	6.8	9.3	12.1	7.5
2005	13.6	13.0	11.2	9.7	4.8	4.3	2.3	3.1	5.9	6.7	9.7	12.5	8.1
2006	15.0	12.9	10.8	9.8	8.4	4.7	5.8	7.2	7.9	8.0	11.8	13.9	9.7
2007	12.9	12.4	12.6	11.4	11.0	5.0	4.8	6.8	9.4	9.3	11.3	13.8	10.1
2008	15.0	****	****	5.5	2.0	0.7	1.4	1.3	3.9	4.5	11.7	11.2	****
2009	11.8	13.2	12.8	9.4	1.9	1.0	0.4	3.2	3.4	8.8	9.0	8.7	7.0
2010	8.2	12.5	11.5	9.8	5.7	3.0	2.0	4.7	3.7	4.8	5.1	5.3	6.4
2011	5.4	4.3	4.3	6.0	2.3	2.4	1.1	2.6	5.6	6.6	11.5	12.7	5.4
SUM	132.5	119.9	112.6	96.7	49.5	22.1	23.7	40.1	60.5	82.4	111.6	126.6	76.9
MEAN	12.0	12.0	11.3	8.8	4.5	2.0	2.1	3.6	5.5	7.5	10.1	11.5	7.7

Table B - 4: Pore size distribution of salt core samples analyzed by X-ray computed tomography [$V_{\text{pore class}}$ – Size classification of pore objects according to the pore volume, ΣV_p – Sum of the volume of all pore objects assigned to the respective pore size class, $V(\Sigma_{\text{pores}})$ – Total pore volume of each sample].

$V(\Sigma_{\text{pores}})$:		1.34E-05		3.90E-05		9.08E-06		1.20E-05		6.90E-06		1.35E-05	
Class	$V_{\text{pore class}}$	08-CEN-1a		08-CEN-1b		08-CEN-8a		08-CEN-10b		08-CEN-12b		08-CEN-15b	
No.	[m ³]	ΣV_p [m ³]	%										
1	1.00E-13	0.00E+00	0.00										
2	5.00E-13	7.66E-10	0.01	5.89E-10	0.00	7.76E-10	0.01	2.92E-10	0.00	8.75E-10	0.01	7.07E-10	0.01
3	1.00E-12	1.85E-09	0.01	1.36E-09	0.00	1.79E-09	0.01	6.79E-10	0.00	1.93E-09	0.02	1.63E-09	0.01
4	5.00E-12	1.45E-08	0.09	9.11E-09	0.02	1.14E-08	0.11	4.34E-09	0.03	1.07E-08	0.13	9.59E-09	0.06
5	1.00E-11	3.13E-08	0.13	1.99E-08	0.03	2.14E-08	0.11	8.48E-09	0.03	1.84E-08	0.11	1.78E-08	0.06
6	5.00E-11	1.40E-07	0.81	8.22E-08	0.16	6.27E-08	0.45	2.96E-08	0.18	5.38E-08	0.51	5.32E-08	0.26
7	1.00E-10	2.42E-07	0.76	1.33E-07	0.13	8.68E-08	0.27	4.70E-08	0.14	7.99E-08	0.38	7.56E-08	0.17
8	5.00E-10	6.84E-07	3.28	3.31E-07	0.51	1.69E-07	0.90	1.23E-07	0.63	1.84E-07	1.51	1.50E-07	0.55
9	1.00E-09	9.84E-07	2.23	4.35E-07	0.27	2.14E-07	0.49	1.72E-07	0.41	2.59E-07	1.09	1.82E-07	0.24
10	5.00E-09	2.34E-06	10.05	6.81E-07	0.63	4.01E-07	2.07	3.16E-07	1.20	4.68E-07	3.03	2.84E-07	0.76
11	1.00E-08	3.13E-06	5.93	7.82E-07	0.26	5.02E-07	1.11	4.03E-07	0.73	4.93E-07	0.36	2.90E-07	0.04
12	5.00E-08	4.31E-06	8.79	9.76E-07	0.50	7.60E-07	2.84	5.75E-07	1.43	6.45E-07	2.20	3.04E-07	0.11
13	1.00E-07	4.45E-06	1.00	1.03E-06	0.14	1.10E-06	3.69	5.75E-07	0.00	7.83E-07	2.00	3.04E-07	0.00
14	5.00E-07	5.95E-06	11.16	1.03E-06	0.00	2.11E-06	11.13	8.55E-07	2.34	9.66E-07	2.64	3.04E-07	0.00
15	1.00E-06	5.95E-06	0.00	1.03E-06	0.00	2.11E-06	0.00	8.55E-07	0.00	9.66E-07	0.00	3.04E-07	0.00
16	5.00E-06	5.95E-06	0.00	1.03E-06	0.00	9.08E-06	76.81	8.55E-07	0.00	6.90E-06	86.01	3.04E-07	0.00
17	1.00E-05	1.34E-05	55.76	1.03E-06	0.00	9.08E-06	0.00	8.55E-07	0.00	6.90E-06	0.00	3.04E-07	0.00
18	5.00E-05	1.34E-05	0.00	3.90E-05	97.36	9.08E-06	0.00	1.20E-05	92.88	6.90E-06	0.00	1.35E-05	97.74
19	1.00E-04	1.34E-05	0.00	3.90E-05	0.00	9.08E-06	0.00	1.20E-05	0.00	6.90E-06	0.00	1.35E-05	0.00
Σ [%]:		100.00		100.00		100.00		100.00		100.00		100.00	
$\Sigma(< 1 \text{ mm}^3)$:		7.32		1.11		2.35		1.43		3.76		1.35	
$\Sigma(> 10 \text{ mm}^3)$:		82.63		98.25		95.58		97.37		93.21		97.89	

Table B - 4: Pore size distribution of salt core samples resulting from X-ray computed tomography (continuation).

$V(\Sigma_{pores})$:		1.00E-05		9.97E-06		2.10E-06		3.05E-05		1.93E-05	
Class	$V_{pore\ class}$	08-CEN-22a		08-CEN-25b		08-CEN-29b		03-INC-crust		03-INC-K2	
No.	[m ³]	ΣV_p [m ³]	%								
1	1.00E-13	0.00E+00	0.00								
2	5.00E-13	1.95E-09	0.02	1.64E-09	0.02	5.24E-10	0.02	3.00E-10	0.00	1.74E-10	0.00
3	1.00E-12	4.31E-09	0.02	3.64E-09	0.02	1.20E-09	0.03	7.32E-10	0.00	4.08E-10	0.00
4	5.00E-12	2.70E-08	0.23	2.22E-08	0.19	6.86E-09	0.27	5.47E-09	0.02	2.64E-09	0.01
5	1.00E-11	5.11E-08	0.24	4.06E-08	0.18	1.19E-08	0.24	1.11E-08	0.02	5.45E-09	0.01
6	5.00E-11	1.54E-07	1.02	1.29E-07	0.89	3.39E-08	1.05	5.03E-08	0.13	2.32E-08	0.09
7	1.00E-10	2.27E-07	0.73	1.94E-07	0.65	5.29E-08	0.90	8.62E-08	0.12	4.12E-08	0.09
8	5.00E-10	4.91E-07	2.64	4.38E-07	2.45	1.27E-07	3.51	2.37E-07	0.49	1.30E-07	0.46
9	1.00E-09	6.32E-07	1.41	5.93E-07	1.55	1.84E-07	2.73	3.38E-07	0.33	2.06E-07	0.39
10	5.00E-09	1.02E-06	3.87	9.41E-07	3.50	3.57E-07	8.25	5.59E-07	0.72	5.09E-07	1.56
11	1.00E-08	1.19E-06	1.74	1.07E-06	1.32	4.22E-07	3.11	6.28E-07	0.23	6.15E-07	0.55
12	5.00E-08	1.52E-06	3.27	1.40E-06	3.24	9.43E-07	24.76	7.62E-07	0.44	1.02E-06	2.11
13	1.00E-07	1.57E-06	0.52	1.45E-06	0.60	1.25E-06	14.85	7.62E-07	0.00	1.17E-06	0.77
14	5.00E-07	1.67E-06	1.00	1.45E-06	0.00	2.10E-06	40.29	7.62E-07	0.00	1.56E-06	2.03
15	1.00E-06	1.67E-06	0.00	1.45E-06	0.00	2.10E-06	0.00	7.62E-07	0.00	1.56E-06	0.00
16	5.00E-06	1.67E-06	0.00	1.45E-06	0.00	2.10E-06	0.00	7.62E-07	0.00	1.56E-06	0.00
17	1.00E-05	1.00E-05	83.29	9.97E-06	85.40	2.10E-06	0.00	7.62E-07	0.00	1.56E-06	0.00
18	5.00E-05	1.00E-05	0.00	9.97E-06	0.00	2.10E-06	0.00	3.05E-05	97.50	1.93E-05	91.91
19	1.00E-04	1.00E-05	0.00	9.97E-06	0.00	2.10E-06	0.00	3.05E-05	0.00	1.93E-05	0.00
Σ [%]:		100.00		100.00		100.00		100.00		100.00	
$\Sigma(< 1\ mm^3)$:		6.31		5.95		8.75		1.11		1.07	
$\Sigma(> 10\ mm^3)$:		89.82		90.55		83.00		98.17		97.37	

Table B - 5: Determination of the effective porosity by saturation with 2-octanol (for remarks see next page).

No.	Sample-ID	Depth [m]	m _{dry} [g]	m _{3-way-valve} [g]	m _{3-way, sat.} [g]	m _{sat.} [g]	m _{octanol} [g]	T _{exp.} [°C]	ρ _{Octanol} [g/cm ³]	V _{pores} * [cm ³]	L [cm]	V _{core} [cm ³]	n _{eff} * [%]	± [%]
1	08-CEN, 1a	0.1	276.3	545.7	592.3	322.9	46.6	23.0	0.8185	4.93	5.50	166.0	3.0	1.19
2	08-CEN, 8a	2.7	447.4	717.9	786.9	516.4	69	24.5	0.8174	32.42	8.35	252.1	12.9	1.09
3	08-CEN, 10b	3.5	423.2	694.1	753.2	482.3	59.1	24.5	0.8174	20.30	7.75	234.0	8.7	1.02
4	08-CEN, 15b	5.7	313.8	579.9	631.3	365.2	51.4	24.5	0.8174	10.88	5.50	166.0	6.6	1.29
5	08-CEN, 22a	7.8	436.5	710.7	769.8	495.6	59.1	24.5	0.8174	20.30	8.00	241.5	8.4	0.99
6	08-CEN, 25b	8.6	386.7	657.8	702.9	431.8	45.1	24.5	0.8174	3.18	6.75	203.8	1.6	0.95
7	03-INC, K4, 0.7-1.7	1.8	528.8	801.1	854.4	582.1	53.3	23.0	0.8185	13.12	9.75	294.4	4.5	0.74
8	03-INC, K7, 1.7-2.7	2.6	265.2	530.2	583.8	318.8	53.6	23.0	0.8185	13.48	4.40	132.8	10.1	1.67
9	03-INC, K2, 3 m	3	375.2	641.7	714.5	448	72.8	23.0	0.8185	36.94	7.40	223.4	16.5	1.30
10	07-SAL, 2a	0.1	220.9	482	555.9	294.8	73.9	24.8	0.8172	38.44	5.00	151.0	25.5	2.00
11	07-SAL, 7a	2.3	666.3	937.8	1026.1	754.6	88.3	24.8	0.8172	56.06	12.20	368.3	15.2	0.94
12	07-SAL, 8a	2.7	1023.3	1322.6	1417.7	1118.4	95.1	25.1	0.8169	64.41	18.00	543.4	11.9	0.68
13	07-SAL, 11b	3.5	527.6	793.4	865	599.2	71.6	24.9	0.8171	35.63	9.70	292.8	12.2	0.97
14	07-SAL, 14b	4.2	547.2	813.2	885.8	619.8	72.6	23.8	0.8179	36.76	9.60	289.8	12.7	0.99
15	07-SAL, 15	4.4	1111.5	1407.3	1495.3	1199.5	88	24.3	0.8175	55.64	20.20	609.9	9.1	0.56
16	07-SAL, 18	5.2	887.5	1170.8	1247.7	964.4	76.9	23.6	0.8181	42.00	16.00	483.1	8.7	0.62
17	07-SAL, 26	6.8	1101.5	1396.2	1470.9	1176.2	74.7	22.6	0.8188	39.23	19.20	579.7	6.8	0.50
18	02-LLI, 1a	0.1	245.8	508.2	563.0	300.6	54.8	22.6	0.8188	14.92	4.50	135.9	11.0	1.66
19	02-LLI, 3b	1.2	526.2	802.8	865.9	589.3	63.1	22.8	0.8187	25.07	10.00	301.9	8.3	0.83
20	02-LLI, 7	3.5	408.5	673.2	732.8	468.1	59.6	21.5	0.8197	20.71	6.80	205.3	10.1	1.17
21	02-LLI, 9	3.8	726.0	1009.1	1066.3	783.2	57.2	23.5	0.8181	17.91	12.20	368.3	4.9	0.63
22	02-LLI, 15	8.2	566.4	839.6	912.1	638.9	72.5	26.2	0.8161	36.84	9.70	292.8	12.6	0.98
23	02-LLI, 17	8.8	646.7	926.0	982.5	703.2	56.5	23.0	0.8185	17.03	11.00	332.1	5.1	0.69
24	02-LLI, 19b	9.3	628.5	911.3	986.3	703.5	75	21.6	0.8196	39.51	11.00	332.1	11.9	0.89

Table B - 5: Determination of the effective porosity with 2-octanol (continuation).

No.	Sample-ID	Depth [m]	m _{dry} [g]	m _{3-way-valve} [g]	m _{3-way, sat.} [g]	m _{sat.} [g]	m _{octanol} [g]	T _{exp.} [°C]	ρ _{Octanol} [g/cm ³]	V _{pores} * [cm ³]	L [cm]	V _{core} [cm ³]	n _{eff} [%]	± [%]
25	13-COR, 25	5.6	669.0	954.4	1030.7	745.3	76.3	19.8	0.8210	40.94	12.00	362.3	11.3	0.82
26	13-COR, 22	6.2	500.6	776.6	828.8	552.8	52.2	24.3	0.8175	11.85	8.00	241.5	4.9	0.89
27	13-COR, 19b	6.9	746.3	1030.4	1098.6	814.5	68.2	25.9	0.8163	31.55	12.80	386.4	8.2	0.70
28	13-COR, 18	7.2	369.8	639.3	690.7	421.2	51.4	20.3	0.8206	10.64	6.40	193.2	5.5	1.10
29	13-COR, 14a	7.9	795.7	1082.9	1138.6	851.4	55.7	26.1	0.8162	16.25	13.40	404.6	4.0	0.56
												Max:	25.5	2.00
												Min:	1.6	0.50
												Mean:	9.4	0.98
												STD:	4.8	0.35

Remarks:

m_{3-way-valve} – Salt core enclosed in heat shrink, including 2 PVC-reductions and tube connections with 3-way-valves (complete set up)

m_{3-way, sat.} – Salt core sample in complete set up, completely saturated with 2-octanol

± – Absolute error of the effective porosity results calculated according to DIN V ENV 13005 (1999), compare Text C – 3.

Table B - 6: Results of porosity determination by direct measurement (method no. 3 / completion method).

No.	Sample-ID	Depth [m]	m _{dry salt} [g]	m _{s. + plas.} [g]	L [cm]	m _{plas.+ Pers.} [g]	m _{plasticine} [g]	V _{cylinder} [cm ³]	V _{plasticine} [cm ³]	V _{core} [cm ³]	ρ _{dy salt} [g/cm ³]	V _{salt} [cm ³]	n _{total} [%]	± [%]
1	07-SAL, 2	0.10	219.9	338.5	7.1	118.6	93.1	217.1	54.0	163.1	2.157	102.0	37.5	2.07
2	07-SAL, 7a	2.30	662.7	860.0	14.7	197.1	145.7	449.5	84.5	365.1	2.153	307.8	15.7	2.11
3	07-SAL, 7b	2.50	561.3	795.3	13.3	230.5	179.1	406.7	103.9	302.9	2.153	260.7	13.9	2.40
4	07-SAL, 8a	2.70	1013.3	1229.5	21.0	213.1	161.7	642.2	93.8	548.4	2.160	469.1	14.5	1.95
5	07-SAL, 8b	2.80	1330.1	1528.5	26.5	192.2	140.8	810.4	81.7	728.8	2.160	615.8	15.5	1.79
6	07-SAL, 9	2.90	288.9	614.0	10.1	325.4	274.0	308.9	158.9	150.0	2.157	134.0	10.7	4.23
7	07-SAL, 10a	3.10	242.9	329.1	5.0	84.6	58.7	152.9	34.0	118.9	2.160	112.5	5.4	3.63
8	07-SAL, 10b	3.20	379.2	483.9	7.8	103.3	77.8	238.5	45.1	193.4	2.200	172.4	10.9	2.62
9	07-SAL, 11b	3.50	519.4	665.7	11.4	142.2	90.8	348.6	52.7	296.0	2.157	240.9	18.6	2.03
10	07-SAL, 11a	3.60	1542.9	1748.7	30.8	193.8	142.4	941.9	82.6	859.3	2.157	715.5	16.7	1.73
11	07-SAL, 14b	4.20	545.3	n.d.	9.7	n.d.	n.d.	296.6	n.d.	296.6	2.160	252.5	14.9	1.87
12	07-SAL, 15	4.40	1104.9	1291.2	22.4	186.3	134.9	683.5	78.2	605.3	2.174	508.3	16.0	1.83
13	07-SAL, 16	4.60	631.0	806.3	13.1	171.7	120.3	400.6	69.8	330.9	2.172	290.5	12.2	2.20
14	07-SAL, 17	4.90	993.4	1263.7	21.2	267.3	215.8	648.3	125.1	523.2	2.160	459.9	12.1	2.13
15	07-SAL, 18b	5.20	874.8	1068.2	18.1	186.8	135.4	553.5	78.5	475.0	2.160	405.0	14.7	1.96
16	07-SAL, 19a	5.30	214.1	313.0	4.8	97.3	71.8	145.3	41.6	103.6	2.160	99.1	4.3	4.14
17	07-SAL, 19b	5.40	630.7	822.9	13.7	189.1	137.7	417.4	79.9	337.6	2.160	292.0	13.5	2.20
18	07-SAL, 19c	5.45	296.3	367.3	5.7	71.1	45.2	174.3	26.2	148.1	2.186	135.6	8.5	2.97
19	07-SAL, 20a	5.40	1495.4	1605.1	27.6	106.5	55.1	844.0	32.0	812.1	2.160	692.3	14.7	1.68
20	07-SAL, 21	5.70	818.5	1113.0	19.3	291.1	239.7	590.2	139.0	451.2	2.159	379.1	16.0	2.17
21	07-SAL, 23a	6.20	493.5	676.2	11.4	176.8	125.4	348.6	72.7	275.9	2.160	228.5	17.2	2.23
22	07-SAL, 23b	6.30	660.4	955.9	16.2	291.6	240.2	495.4	139.3	356.1	2.160	305.7	14.1	2.42
23	07-SAL, 24a	6.10	353.6	608.7	10.0	255.1	203.7	305.8	118.1	187.7	2.160	163.7	12.8	3.20
24	07-SAL, 25a	6.50	725.1	906.4	15.9	178.3	126.9	486.2	73.6	412.7	2.160	335.7	18.6	1.92
25	07-SAL, 26	6.80	1059.6	1227.7	21.2	166.4	115.0	648.3	66.7	581.6	2.159	490.7	15.6	1.82

Table B - 6: Results of porosity determination by direct measurement (continuation).

No.	Sample-ID	Depth [m]	$m_{\text{dry salt}}$ [g]	$m_{\text{s. + plas.}}$ [g]	L [cm]	$m_{\text{plas.+ Pers.}}$ [g]	$m_{\text{plasticine}}$ [g]	V_{cylinder} [cm ³]	$V_{\text{plasticine}}$ [cm ³]	V_{core} [cm ³]	$\rho_{\text{dy salt}}$ [g/cm ³]	V_{salt} [cm ³]	n_{total} [%]	\pm [%]
26	07-SAL, 27a	7.10	421.4	523.1	8.5	99.2	73.7	258.4	42.7	215.7	2.160	195.1	9.5	2.51
27	07-SAL, 27a	7.10	421.4	n.d.	7.0	n.d.	n.d.	214.1	n.d.	214.1	2.160	195.1	8.9	2.26
28	07-SAL, 27(b)	7.30	1240.5	1355.8	22.7	91.9	66.0	694.2	38.3	655.9	2.159	574.6	12.4	1.78
29	07-SAL, 28a	7.05	425.8	602.9	10.0	177.2	125.8	305.8	73.0	232.9	2.159	197.3	15.3	2.46
30	07-SAL, 28b	7.15	612.2	822.5	14.3	207.2	155.8	437.3	90.4	347.0	2.158	283.7	18.2	2.11
31	07-SAL, 29	7.75	621.9	814.4	14.3	205.7	154.3	437.3	89.5	347.8	2.159	288.1	17.2	2.13
32	07-SAL, 30b	7.85	791.9	929.3	15.5	134.2	82.8	472.5	48.0	424.5	2.160	366.6	13.6	1.93
33	07-SAL, 31a	8.10	128.7	301.0	5.0	170.2	144.3	151.4	83.7	67.7	2.156	59.7	11.8	6.08
34	07-SAL, 31b	8.20	334.1	n.d.	6.0	n.d.	n.d.	183.5	n.d.	183.5	2.157	154.9	15.6	2.26
35	07-SAL, 31c	8.30	539.3	713.3	11.4	163.1	111.7	347.1	64.8	282.3	2.160	249.7	11.5	2.32
36	07-SAL, 32a	8.15	697.5	883.2	14.4	182.5	131.1	440.4	76.0	364.3	2.160	322.9	11.4	2.18
37	07-SAL, 32b	8.25	657.7	854.3	13.9	193.1	141.7	425.1	82.2	342.9	2.172	302.8	11.7	2.24
38	07-SAL, 33	8.40	589.3	664.8	10.7	67.6	41.7	327.2	24.2	303.0	2.160	272.8	10.0	2.09
39	07-SAL, 34	8.70	1387.8	n.d.	23.9	n.d.	n.d.	730.9	n.d.	730.9	2.160	642.5	12.1	1.68
40	07-SAL, 35	8.90	609.9	806.7	12.9	185.1	133.7	393.0	77.5	315.4	2.160	282.4	10.5	2.32
41	13-COR, 35	2.80	698.1	980.5	16.8	280.5	229.1	513.8	132.9	380.9	2.153	324.2	14.9	2.31
42	13-COR, 33	3.50	332.1	662.1	10.6	330.3	278.9	324.2	161.7	162.4	2.153	154.2	5.0	4.30
43	13-COR, 25a	5.55	666.4	845.9	14.2	175.6	124.2	434.3	72.0	362.2	2.160	308.5	14.8	2.08
44	13-COR, 25b	5.70	471.8	724.1	12.0	249.3	197.9	367.0	114.8	252.2	2.160	218.4	13.4	2.69
45	13-COR, 24	5.90	1345.0	1605.4	27.9	257.0	205.6	853.2	119.2	734.0	2.160	622.7	15.2	1.88
46	13-COR, 23a	6.05	279.0	607.0	10.1	327.9	276.5	308.9	160.4	148.5	2.160	129.2	13.0	4.17
47	13-COR, 22	6.20	491.4	617.9	10.0	126.4	75.0	305.8	43.5	262.3	2.160	227.5	13.3	2.22
48	13-COR, 19a	6.70	1133.2	1318.7	20.9	182.7	131.3	639.2	76.1	563.0	2.174	521.3	7.4	2.04
49	13-COR, 19b	6.90	733.4	805.7	13.7	70.7	45.2	419.0	26.2	392.8	2.160	339.5	13.5	1.88
50	13-COR, 18b	7.10	363.9	613.9	10.2	247.0	195.6	311.9	113.4	198.5	2.160	168.5	15.1	2.98

Table B - 6: Results of porosity determination by direct measurement (continuation).

No.	Sample-ID	Depth [m]	m _{dry salt} [g]	m _{s. + plas.} [g]	L [cm]	m _{plas.+ Pers.} [g]	m _{plasticine} [g]	V _{cylinder} [cm ³]	V _{plasticine} [cm ³]	V _{core} [cm ³]	ρ _{dy salt} [g/cm ³]	V _{salt} [cm ³]	n _{total} [%]	± [%]
53	13-COR, 16a	7.55	384.0	461.0	7.5	77.0	51.2	229.4	29.7	199.7	2.207	174.0	12.9	2.42
54	13-COR, 16b	7.60	366.3	n.d.	6.3	n.d.	n.d.	191.1	n.d.	188.7	2.160	169.6	10.1	<i>n.d.</i>
55	13-COR, 15a	7.70	602.6	677.7	10.9	75.1	49.2	333.3	28.5	304.8	2.157	279.4	8.3	2.14
56	13-COR, 15b	7.80	228.8	297.5	4.4	68.6	42.7	134.6	24.8	109.8	2.157	106.1	3.4	3.82
57	13-COR, 14a	7.90	777.1	927.4	15.1	147.2	95.8	461.8	55.6	406.2	2.170	358.1	11.8	2.02
58	08-CEN, 1b	0.25	361.7	534.2	11.2	169.2	117.8	342.5	69.0	273.5	2.160	167.5	38.8	1.64
59	08-CEN, 7	2.50	1031.7	1098.7	19.6	65.5	40.0	599.4	23.4	576.0	2.157	478.4	16.9	1.68
60	08-CEN, 8a	2.70	442.2	592.1	10.9	146.9	95.5	333.3	55.9	277.4	2.153	205.4	26.0	1.91
61	08-CEN, 8b-2	2.80	410.2	484.0	8.0	71.8	46.3	244.7	27.1	217.5	2.159	190.0	12.7	2.31
62	08-CEN, 8b-1	2.90	283.7	581.5	10.1	298.0	246.6	307.3	144.5	162.9	2.158	131.5	19.3	3.48
63	08-CEN, 11a	4.15	373.5	466.5	7.7	93.0	67.1	233.9	39.3	194.6	2.160	172.9	11.2	2.57
64	08-CEN, 12b2	4.50	186.5	n.d.	3.0	n.d.	n.d.	91.7	n.d.	91.7	2.235	83.4	9.0	<i>n.d.</i>
65	08-CEN, 12b1	4.65	226.6	299.0	5.0	72.5	46.6	151.4	27.3	124.1	2.160	104.9	15.5	3.09
66	08-CEN, 12c	4.70	620.3	833.2	14.4	209.8	158.4	438.8	92.8	346.1	2.160	287.2	17.0	2.15
67	08-CEN, 13a	4.85	824.2	1034.5	17.7	207.2	155.8	541.3	91.3	450.0	2.160	381.6	15.2	2.02
68	08-CEN, 13b	5.00	590.2	799.1	14.9	205.7	154.3	454.1	90.4	363.7	2.160	273.2	24.9	1.90
69	08-CEN, 15a	5.60	937.5	1139.5	20.0	198.7	147.3	611.6	86.3	525.3	2.160	434.0	17.4	1.88
70	08-CEN, 16a	5.90	230.2	306.3	4.8	75.9	50.4	146.8	29.5	117.3	2.160	106.6	9.1	3.47
71	08-CEN, 16b	6.00	234.6	314.1	5.0	79.5	53.6	152.9	31.4	121.5	2.160	108.6	10.6	3.35
72	08-CEN, 17	6.20	1312.6	1488.5	26.5	172.8	121.4	810.4	71.1	739.3	2.160	607.7	17.8	1.72
73	08-CEN, 18b	6.40	461.2	603.0	10.0	138.8	87.4	305.8	51.2	254.6	2.158	213.8	16.0	2.22
74	08-CEN, 20	7.40	391.3	598.7	9.9	204.3	152.9	302.8	89.6	213.2	2.157	181.5	14.9	2.70
75	08-CEN, 21b-2	7.75	328.9	610.0	10.1	278.1	226.7	307.3	132.8	174.5	2.160	152.3	12.8	3.49

Table B - 6: Results of porosity determination by direct measurement (continuation).

No.	Sample-ID	Depth [m]	m _{dry salt} [g]	m _{s. + plas.} [g]	L [cm]	m _{plas.+ Pers.} [g]	m _{plasticine} [g]	V _{cylinder} [cm ³]	V _{plasticine} [cm ³]	V _{core} [cm ³]	ρ _{dy salt} [g/cm ³]	V _{salt} [cm ³]	n _{total} [%]	± [%]
78	08-CEN, 23b	8.20	294.7	417.5	7.0	122.8	96.9	214.1	56.8	157.3	2.160	136.4	13.3	2.96
79	08-CEN, 24a	8.30	727.0	882.4	14.5	152.0	100.6	441.9	58.9	383.0	2.160	336.6	12.1	2.06
80	08-CEN, 24b	8.40	453.7	624.2	10.0	167.3	115.9	305.8	67.9	237.9	2.160	210.0	11.7	2.50
81	08-CEN, 25b	8.60	379.0	622.8	9.9	240.6	189.2	302.8	110.8	191.9	2.160	175.5	8.6	3.25
82	08-CEN, 26	8.90	2236.2	2317.6	40.1	79.9	54.0	1226.3	31.6	1194.7	2.160	1035.4	13.3	1.67
83	08-CEN, 27b	9.10	892.0	1111.2	18.9	215.9	164.5	578.0	96.4	481.6	2.159	413.1	14.2	2.02
84	08-CEN, 27a	9.25	383.0	603.8	10.1	217.7	166.3	308.9	97.4	211.5	2.159	177.4	16.1	2.73
85	08-CEN, 28	9.40	1300.9	1483.0	25.2	178.6	127.2	769.1	74.5	694.6	2.159	602.5	13.3	1.84
86	09-Rio-D, 1	0.10	669.7	830.7	16.1	156.8	105.4	484.6	62.0	422.6	2.153	311.1	26.4	1.69
87	09-Rio-C, 2a	0.80	551.9	792.7	14.2	240.9	189.5	428.7	111.4	317.3	2.153	256.3	19.2	2.25
88	09-Rio-A, 4c	1.20	355.0	660.0	12.3	305.0	253.6	369.8	149.1	220.8	2.160	164.4	25.6	2.70
89	09-Rio-B, 18b	1.40	925.0	1069.0	18.8	139.9	88.5	567.6	52.0	515.6	2.160	428.2	16.9	1.79
90	09-Rio-A, 7b	1.50	371.1	632.2	10.4	253.5	202.1	314.0	118.8	195.2	2.153	172.4	11.7	3.18
91	09-Rio-A, 11a	2.10	446.9	668.1	11.5	217.9	166.5	345.7	97.9	247.8	2.153	207.6	16.2	2.52
92	09-Rio-A, 11b	2.20	317.7	573.7	10.1	251.8	200.4	303.4	117.8	185.6	2.153	147.6	20.5	2.94
93	09-Rio-C, 10	2.30	890.4	1059.2	18.1	164.5	113.1	544.9	66.5	478.5	2.160	412.2	13.8	1.93
94	09-Rio-C, 11	2.50	811.8	1035.6	17.3	219.5	168.1	522.3	98.8	423.5	2.160	375.8	11.3	2.18
95	09-Rio-A, 13	2.60	582.1	865.0	14.7	278.9	227.5	443.8	133.7	310.1	2.153	270.4	12.8	2.58
96	09-Rio-A, 15a	3.10	266.6	630.3	10.9	363.8	312.4	329.7	183.6	146.1	2.160	123.4	15.5	4.37
97	09-Rio-A, 16a	3.20	520.3	759.5	12.8	239.1	187.7	387.3	110.3	277.0	2.160	240.9	13.0	2.56
98	09-Rio-A, 16b	3.30	421.4	708.2	12.2	282.7	231.3	368.3	136.0	232.4	2.160	195.1	16.0	2.87

Table B - 7: Lithium concentrations in brine samples from different sites of the Uyuni salt flat. Several brine samples from different depth were taken at each drilling site between 2009 and 2012 (The concentrations were averaged). Single samples along different transects in the northeastern part of the salt flat were taken in 2012.

Sample-ID	Longitude	Latitude	Li [mg/L]	Remarks
01-COL	679816	-2225426	262.0	Drilling site
02-LLI	601596	-2208505	303.0	Drilling site
03-INC	649792	-2250359	967.0	Drilling site
04-YON	590267	-2254038	201.0	Drilling site
05-TAH	635275	-2202878	428.0	Drilling site
06-NOR	669422	-2188929	602.0	Drilling site
07-SAL	694556	-2257921	468.0	Drilling site
08-CEN	649590	-2225520	565.0	Drilling site
09-RIO	666568	-2279531	1243.0	Drilling site
10-PES	625383	-2222230	611.0	Drilling site
13-COR	663561	-2210844	464.0	Drilling site
A1	653520	-2182646	1486.0	Transect
A2	655544	-2184651	922.6	Transect
A3	657558	-2186648	844.8	Transect
A4	659616	-2188626	568.6	Transect
A5	661613	-2190610	568.9	Transect
A6	663687	-2192627	599.1	Transect
B2	665618	-2184613	788.9	Transect
B3	665624	-2186497	601.6	Transect
B4	665620	-2188596	510.5	Transect
B5	665619	-2190572	619.4	Transect
B6	665600	-2192626	503.0	Transect
C2	673715	-2186734	1049.0	Transect
C3	671592	-2188602	495.6	Transect
C4	669631	-2190619	537.0	Transect
C5	667633	-2192644	419.8	Transect
D1	657667	-2194581	434.4	Transect
D2	661643	-2194575	448.0	Transect
D3	665617	-2194588	482.8	Transect
D4	669676	-2194629	450.0	Transect
D5	673666	-2194576	283.8	Transect
D6	677685	-2194626	350.8	Transect
D7	681631	-2194626	550.7	Transect
Z1	661721	-2184527	739.6	Transect
Z2	669663	-2184628	1008.0	Transect
Z3	677645	-2190603	681.1	Transect

Table B - 8: Experimental determination of the cubic expansion coefficient for two brine samples from sites 02-LLI and 09-RIO.

Brine sample	T [°C]	$\Delta V_{\text{added/removed}}$ [μl]	m_1 [g]	m_0 [g]	Δm [g]
02-LLI (cold)	9.6	620	174.9252	174.1953	-0.7299
02-LLI (warm)	31.4	-350	167.8295	168.2620	0.4325
09-RIO (cold)	8.2	600	171.7990	171.0014	-0.7976
09-RIO (warm)	31.5	-350	167.1426	167.5902	0.4476

Brine sample	$V_{\text{cold}} (V_0)$ [ml]	$V_{\text{warm}} (V_1)$ [ml]	ΔV [ml]	ΔT [°C]	Υ [K ⁻¹]
02-LLI	99.38	100.35	0.97	21.8	4.456E-04
09-RIO	99.4	100.35	0.95	23.3	4.082E-04
				Mean:	4.2E-04

Table B - 9: Density of brine samples at standard temperature (25°C) as well as at field temperature conditions (measurements were done at the BGR, Hannover). The depth indicates the mean depth of the filter screen. For density conversion to field temperature the experimentally determined cubic expansion coefficient was used ($\gamma = 4.269 \cdot 10^{-4} \text{ K}^{-1}$).

Sample-ID	Date	Depth [m]	ρ (25°C) [kg/m³]	T_{field} [°C]	ρ_{field} [kg/m³]
01-COL-B	Sep 09	5.0	1204.2	5.1	1214.5
01-COL-C	Sep 09	7.5	1204.5	4.6	1215.1
01-COL-E	Sep 09	7.0	1204.5	4.6	1215.1
01-COL-F	Sep 09	2.5	1205.0	7.4	1214.2
02-LLI-B	Nov 10	8.5	1207.9	12.5	1214.4
02-LLI-C	Nov 10	3.3	1209.1	16.1	1213.7
02-LLI-D	Nov 10	1.3	1208.1	16.7	1212.4
03-INC-A	Sep 09	3.0	1227.0	7.1	1236.4
03-INC-B	Sep 09	4.0	1226.9	8.2	1235.7
03-INC-C	Sep 09	4.8	1224.3	9.2	1232.6
03-INC-E	Sep 09	2.0	1224.8	7.0	1234.3
04-YON	Nov 10	7.3	1205.4	13.2	1211.5
05-TAH-A	Nov 10	0.4	1212.2	15.0	1217.4
05-TAH-D	Nov 10	3.2	1215.6	14.6	1221.0
06-NOR-A	Nov 10	0.5	1219.7	17.2	1223.8
06-NOR-B	Nov 10	3.2	1227.7	14.2	1233.4
06-NOR-C	Nov 10	2.3	1220.7	14.2	1226.4
06-NOR-D	Nov 10	1.3	1219.3	14.7	1224.7
07-SAL	Nov 10	7.6	1225.8	10.4	1233.5
08-CEN-L*	Nov 10	surface	1217.0	14.5	1222.5
08-CEN-A	Nov 10	8.5	1216.2	15.8	1221.0
08-CEN-B	Nov 10	4.3	1215.9	11.8	1222.8
08-CEN-C	Nov 10	2.3	1215.8	12.0	1222.6
08-CEN-D	Nov 10	5.0	1216.6	11.6	1223.5
09-RIO-A	Nov 10	2.5	1229.0	12.0	1235.9
09-RIO-B	Nov 10	2.0	1228.0	10.8	1235.5
09-RIO-C	Nov 10	2.3	1228.3	9.7	1236.4
09-RIO-D	Nov 10	1.2	1228.6	11.7	1235.6
10-PES	Nov 10	5.5	1227.8	13.3	1234.0
13-COR	Nov 10	5.5	1219.7	11.9	1226.6
14-BOL	Nov 10	n.d.	1219.6	12.5	1226.1
Rio-G	Dez 10	surface	998.9	18.0	1001.9

*surface brine sample from a natural brine pool

Appendix B - Tables

Table B - 10: Raw data of viscosity measurements: Cap. – Capillary tube number, **k** – capillary constant, **T_{exp}** – Temperature during the experiment, **#** - number of successful replicate measurements per temperature, **t_{mean}** – mean measured time for traversing the path from the upper to the lower reading mark, **t_{std.}**- standard deviation of the time measurements, **Θ** - Hagenbach correction time, **v** – kinematic viscosity, **ρ** – density of the brine at experimental temperature, **η** – calculated dynamic viscosity at experimental temperature.

Sample-ID	Cap	k	T_{exp} [°C]	#	t_{mean} [s]	t_{std} [s]	Θ [s]	v [mm²/s]	ρ (T_{exp}) [g/cm³]	η (T_{exp}) [mPa·s]
02-LLI-B	I	0.010023	15.5	10	163.7	0.4	0.94	1.631	1.213	1.978
	I	0.010023	17.8	8	155.0	0.3	0.99	1.544	1.212	1.870
	I	0.010023	18	1	154.3	0.0	0.99	1.537	1.212	1.862
	I	0.010023	18.5	1	156.5	0.0	0.98	1.559	1.211	1.888
02-LLI-D	I	0.010023	15.5	10	166.1	0.7	0.93	1.655	1.213	2.008
	I	0.010023	18	12	151.5	4.0	1.01	1.508	1.212	1.828
	I	0.010023	18	4	150.8	2.1	1.01	1.501	1.212	1.819
	I	0.010023	19	1	147.7	0.0	1.03	1.470	1.211	1.781
05-TAH-A	I	0.010023	15	11	168.7	4.7	0.92	1.681	1.217	2.047
	I	0.010023	20	11	160.4	13.4	0.96	1.598	1.215	1.942
05-TAH-D	I	0.010023	15	11	181.1	2.6	0.85	1.807	1.221	2.206
	II	0.099980	20	11	16.9	0.2	0.78	1.615	1.218	1.967
06-NOR-A	I	0.010023	16	4	179.8	0.9	0.86	1.793	1.224	2.196
	I	0.010023	17.5	8	172.6	4.0	0.90	1.721	1.224	2.105
	I	0.010023	18.2	3	180.7	6.7	0.86	1.803	1.223	2.205
06-NOR-B	I	0.010023	15.4	4	191.6	0.3	0.80	1.913	1.233	2.358
	I	0.010023	15.9	10	191.2	1.3	0.81	1.908	1.232	2.352
	I	0.010023	17.2	13	179.8	5.5	0.86	1.793	1.232	2.209
	I	0.010023	17.5	1	177.3	0.0	0.87	1.768	1.232	2.178

Table B -10: Raw data of viscosity measurements (continuation).

	I	0.010023	18.5	11	166.0	6.7	0.93	1.655	1.220	2.018
	I	0.010023	18.8	8	161.1	0.6	0.96	1.606	1.219	1.958
08-CEN-A	la	0.049860	20	11	32.8	0.1	0.92	1.589	1.219	1.937
	I	0.010023	22.5	8	152.5	13.1	1.00	1.518	1.217	1.848
	I	0.010023	22.8	4	146.6	0.2	1.04	1.459	1.217	1.776
08-CEN-C	I	0.010023	15	10	178.7	0.4	0.86	1.782	1.221	2.176
	I	0.010023	20	14	161.0	4.1	0.96	1.605	1.218	1.955
09-RIO-C	II	0.100000	20	12	19.5	0.1	0.75	1.872	1.231	2.304
09-RIO-D	I	0.010023	15	10	208.3	1.7	0.73	2.081	1.234	2.567
	I	0.010023	18	18	193.7	6.8	0.79	1.933	1.2323	2.3823

Table B - 11: Drawdown evaluation of pumping tests performed in 2010 on partially penetrating wells under confined aquifer conditions according to TGL 23864/08 (1973).

Well-ID	Regression	R ²	r [m]	Q [m ³ /s]	M [m]	T [m ² /s]	k _f [m/s]	T _{field} [°C]	ρ _{brine} [kg/m ³]	η _{brine} [mPa·s]	K [m ²]
02-LLI-C	y = 0.012ln(x) - 0.0239	0.9582	2.02	0.00107	4.0	1.63E-02	4.08E-03	12.5	1214.8	2.158	7.39E-10
02-LLI-D	y = 0.0125ln(x) - 0.0333	0.9199	3.95	0.00107	4.0	1.57E-02	3.92E-03	12.5	1214.8	2.158	7.09E-10
02-LLI-B^a	y = 0.0053ln(x) - 0.0075	0.8844	2.95	0.00107	2.0	3.69E-02	1.85E-02	12.5	1214.8	2.158	3.35E-09
05-TAH-B	y = 0.0188ln(x) - 0.1064	0.9909	3.10	0.00118	4.5	1.15E-02	2.55E-03	12	1220.7	2.338	4.98E-10
05-TAH-C	y = 0.016ln(x) - 0.0966	0.9753	4.16	0.00118	4.5	1.35E-02	3.00E-03	12	1220.7	2.338	5.86E-10
05-TAH-D	y = 0.0022ln(x) + 0.0007	0.5976	1.87	0.00118	4.5	9.82E-02	2.18E-02	12	1220.7	2.338	4.26E-09
06-NOR-B	y = 0.0049ln(x) - 0.0104	0.9107	2.10	0.00247	5.0	9.24E-02	1.85E-02	15.6	1226.8	2.288	3.51E-09
06-NOR-C	y = 0.0036ln(x) - 0.0034	0.8089	3.15	0.00247	5.0	1.26E-01	2.52E-02	15.6	1226.8	2.288	4.78E-09
06-NOR-D	y = 0.0097ln(x) - 0.044	0.8422	5.00	0.00247	5.0	4.67E-02	9.34E-03	15.6	1226.8	2.288	1.77E-09
08-CEN-B	y = 0.0067ln(x) - 0.0255	0.8102	3.08	0.00144	9.5	3.93E-02	4.14E-03	10	1224	2.606	8.99E-10
08-CEN-C	y = 0.0037ln(x) - 0.0074	0.716	4.04	0.00144	9.5	7.12E-02	7.50E-03	10	1224	2.606	1.63E-09
08-CEN-D	y = 0.0041ln(x) - 0.0093	0.7806	1.92	0.00144	9.5	6.43E-02	6.77E-03	10	1224	2.606	1.47E-09
09-RIO-B	y = 0.0084ln(x) - 0.0088	0.9365	3.48	0.00122	4.5	2.66E-02	5.91E-03	10.5	1236.1	2.903	1.41E-09
09-RIO-C	y = 0.0072ln(x) + 0.0148	0.9212	1.88	0.00122	4.5	3.10E-02	6.89E-03	10.5	1236.1	2.903	1.65E-09
09-RIO-D	y = 0.0074ln(x) - 0.0024	0.9157	4.02	0.00122	4.5	3.02E-02	6.70E-03	10.5	1236.1	2.903	1.61E-09

^awell is screened in the second salt aquifer

Table B - 12: Drawdown evaluation of pumping tests performed in 2012 on fully penetrating wells under confined aquifer conditions according to the THEIS curve matching procedure using the software UP32 (maximum accuracy was selected in UP32).

Well-ID	T [m ² /s]	M [m]	k _f [m/s]	T _{field} [°C]	ρ _{brine} [kg/m ³]	η _{brine} [mPa·s]	K [m ²]	S [-]	mean error [m]	rel. error
02-LLI-F (PW)	1.30E-03	4	3.25E-04	7.1	1217.7	2.639	7.18E-11	1.09E-06	±0.13	0.64
02-LLI-A	7.94E-03	4	1.99E-03	7.1	1217.7	2.639	4.39E-10	4.34E-03	±0.00	0.23
02-LLI-D	1.03E-02	4	2.58E-03	7.1	1217.7	2.639	5.69E-10	4.06E-03	±0.00	0.27
02-LLI-E ^a	2.90E-02	4	7.25E-03	7.1	1217.7	2.639	1.60E-09	1.00	±0.01	n.d.
08-CEN-A	2.90E-02	6.5	4.46E-03	9.3	1224.3	2.677	9.94E-10	0.13	±0.00	0.05
08-CEN-C	2.66E-02	6.5	4.09E-03	9.3	1224.3	2.677	9.12E-10	0.13	±0.00	0.08/0.07
08-CEN-D	2.44E-02	6.5	3.75E-03	9.3	1224.3	2.677	8.37E-10	0.60	±0.01	0.17
08-CEN-E (PW)	1.83E-03	6.5	2.82E-04	9.3	1224.3	2.677	6.28E-11	2.56E-06	±0.07	0.04

^awell is screened in the second salt aquifer

Table B - 13: Recovery analysis of pumping tests with the JACOB method.

Well-ID	Regression	R ²	s [m] (t/t' = 10)	s [m] (t/t' = 100)	Δs _r [m]	T [m ² /s]	t/t' (s = 0)
LLI-C (2010)	y = 0.0111ln(x) - 0.0091	0.927	0.0165	0.0420	0.0256	7.66E-03	2.27
LLI-D (2010)	y = 0.0109ln(x) - 0.0236	0.9223	0.0015	0.0266	0.0251	7.80E-03	8.72
LLI-B (2010) ^a	<i>not evaluable</i>	0.5088	0.0332	0.0399	0.0067	2.93E-02	0.00
TAH-B (2010)	y = 0.0117ln(x) - 0.0034	0.9743	0.0235	0.0505	0.0269	8.02E-03	1.34
TAH-C (2010)	y = 0.0135ln(x) - 0.0074	0.9454	0.0237	0.0548	0.0311	6.95E-03	1.73
TAH-D (2010)	y = 0.0041ln(x) - 0.0062	0.8191	0.0032	0.0127	0.0094	2.29E-02	4.54
NOR-B (2010)	y = 0.0083ln(x) - 0.0087	0.8856	0.0104	0.0295	0.0191	2.37E-02	2.85
NOR-C (2010)	y = 0.0039ln(x) - 0.0049	0.8426	0.0041	0.0131	0.0090	5.04E-02	3.51
NOR-D (2010)	y = 0.0034ln(x) + 0.0006	0.8369	0.0084	0.0163	0.0078	5.78E-02	0.84
CEN-B (2010)	y = 0.0072ln(x) - 0.0059	0.8963	0.0107	0.0273	0.0166	1.59E-02	2.27
CEN-C (2010)	y = 0.0058ln(x) - 0.0035	0.7936	0.0099	0.0232	0.0134	1.97E-02	1.83
CEN-D (2010)	y = 0.0058ln(x) - 0.0069	0.9057	0.0065	0.0198	0.0134	1.97E-02	3.29
RIO-B (2010)	y = 0.0066ln(x) - 0.006	0.8714	0.0092	0.0244	0.0152	1.47E-02	2.48
RIO-C (2010)	y = 0.0062ln(x) - 0.0029	0.9148	0.0114	0.0257	0.0143	1.56E-02	1.60
RIO-D (2010)	y = 0.006ln(x) - 0.0072	0.8451	0.0066	0.0204	0.0138	1.62E-02	3.32
LLI-F (PW, 2012)	y = 0.0129ln(x) - 0.0045	0.8915	0.0252	0.0549	0.0297	1.10E-02	1.42
LLI-A (2012)	y = 0.0124ln(x) - 0.0026	0.9388	0.0260	0.0545	0.0286	1.14E-02	1.23
LLI-D (2012)	y = 0.0123ln(x) - 0.0028	0.9008	0.0255	0.0538	0.0283	1.15E-02	1.26
CEN-A (2012)	y = 0.0081ln(x) - 0.0093	0.9186	0.0094	0.0280	0.0187	2.08E-02	3.15
CEN-C (2012)	y = 0.0063ln(x) - 0.0045	0.8779	0.0100	0.0245	0.0145	2.68E-02	2.04
CEN-D (2012)	y = 0.0072ln(x) - 0.0084	0.8929	0.0082	0.0248	0.0166	2.34E-02	3.21
CEN-E (PW, 2012)	y = 0.0053ln(x) + 0.0335	0.7427	0.0457	0.0579	0.0122	3.18E-02	0.00

^awell is screened in the second salt aquifer

Table B - 14: Recovery analysis of pumping tests with the DRISCOLL method.

Well-ID	Regression	R ²	s [m] (t/t' = 10)	s [m] (t/t' = 100)	Δsr [m]	T [m ² /s]	t/t' (s = 0)	r [m]	S
LLI-C (2010)	$y = 0.012\ln(x) - 0.021$	0.95	0.0343	0.0619	0.0276	7.09E-03	5.8	2.02	2.25E-02
LLI-D (2010)	$y = 0.0108\ln(x) + 0.0039$	0.9469	0.0536	0.0785	0.0249	7.88E-03	0.7	3.95	7.91E-04
LLI-B (2010) ^a	<i>(not evaluable because of to low Δs)</i>		n.d.	n.d.	n.d.	n.d.	n.d.	2.95	n.d.
TAH-B (2010)	$y = 0.0126\ln(x) - 0.0397$	0.9818	0.0183	0.0473	0.0290	7.44E-03	23.4	3.1	0.04
TAH-C (2010)	$y = 0.0138\ln(x) - 0.0672$	0.9656	-0.0036	0.0281	0.0318	6.80E-03	130.3	4.16	0.12
TAH-D (2010)	$y = 0.0039\ln(x) - 0.0096$	0.6538	0.0084	0.0173	0.0090	2.41E-02	11.7	1.87	0.18
NOR-B (2010)	$y = 0.0084\ln(x) - 0.035$	0.9053	0.0037	0.0230	0.0193	2.34E-02	64.5	2.1	0.77
NOR-C (2010)	$y = 0.0036\ln(x) + 0.0003$	0.8389	0.0169	0.0252	0.0083	5.46E-02	0.9	3.15	0.01
NOR-D (2010)	$y = 0.0034\ln(x) - 0.006$	0.8501	0.0097	0.0175	0.0078	5.78E-02	5.8	5	0.03
CEN-B (2010)	$y = 0.0069\ln(x) - 0.0218$	0.9166	0.0100	0.0259	0.0159	1.66E-02	23.6	3.08	0.09
CEN-C (2010)	$y = 0.005\ln(x) - 0.0183$	0.8537	0.0047	0.0162	0.0115	2.29E-02	38.9	4.04	0.12
CEN-D (2010)	$y = 0.006\ln(x) - 0.0199$	0.9144	0.0077	0.0215	0.0138	1.91E-02	27.6	1.92	0.32
RIO-B (2010)	$y = 0.0067\ln(x) + 0.0138$	0.8957	0.0447	0.0601	0.0154	1.45E-02	0.1	3.48	3.43E-04
RIO-C (2010)	$y = 0.0062\ln(x) + 0.027$	0.9282	0.0556	0.0698	0.0143	1.56E-02	0.0	1.88	1.28E-04
RIO-D (2010)	$y = 0.0061\ln(x) + 0.0179$	0.8823	0.0460	0.0600	0.0140	1.59E-02	0.1	4.02	1.18E-04
LLI-F (PW, 2012)	$y = 0.0378\ln(x) + 2.3912$	0.9846	2.5653	2.6523	0.0870	3.74E-03	0.0	0.0378	0.00
LLI-A (2012)	$y = 0.014\ln(x) + 0.0478$	0.9614	0.1123	0.1445	0.0322	1.01E-02	0.0	1.55	3.11E-04
LLI-D (2012)	$y = 0.0135\ln(x) + 0.0082$	0.9397	0.0704	0.1015	0.0311	1.05E-02	0.5	2.579	0.00
CEN-A (2012)	$y = 0.0081\ln(x) - 0.0196$	0.9442	0.0177	0.0364	0.0187	2.08E-02	11.2	1.16	0.39
CEN-C (2012)	$y = 0.0067\ln(x) - 0.021$	0.9076	0.0099	0.0253	0.0154	2.52E-02	23.0	4.105	0.08
CEN-D (2012)	$y = 0.0076\ln(x) - 0.0268$	0.9183	0.0082	0.0257	0.0175	2.22E-02	34.0	3.17	0.17
CEN-E (PW, 2012)	$y = 0.0167\ln(x) + 2.4249$	0.98	2.5018	2.5403	0.0385	1.01E-02	0.0	0.0378	0.00

^awell is screened in the second salt aquifer

Table B - 15: Intrinsic permeability of salt core samples determined by flow-through experiments.

Sample-ID	h_{octanol} [cm]	h_{water} [cm]	Δt [s]	ΔV [cm ³]	Q [cm ³ /s]	L [cm]	k_f [m/s]	$T_{\text{exp.}}$ [°C]	ρ_{octanol} [g/cm ³]	η_{octanol} [mPa·s]	K [m ²]	$\pm S_K$ [m ²]	$\pm S_K$ [%]
08-CEN, 1b	38.0	46.4	440	54.0	0.123	11.50	1.08E-05	21.9	0.819	6.217	8.32E-12	1.37E-12	16.4
08-CEN, 1b	38.0	46.4	440	54.0	0.123	11.50	1.08E-05	21.9	0.819	6.217	8.32E-12	1.37E-12	16.4
08-CEN, 1b	17.0	20.7	935	48.8	0.052	11.50	1.02E-05	21.9	0.819	6.217	7.91E-12	1.30E-12	16.4
08-CEN, 1b	17.0	20.7	935	48.0	0.051	11.50	1.01E-05	21.9	0.819	6.217	7.78E-12	1.28E-12	16.4
08-CEN, 8a	24.7	30.3	1182	61.0	0.052	8.35	5.03E-06	26.6	0.816	5.101	3.21E-12	6.38E-13	19.9
08-CEN, 8a	24.7	30.3	888	45.0	0.051	8.35	4.94E-06	26.6	0.816	5.101	3.15E-12	6.27E-13	19.9
08-CEN, 8a	28.9	35.4	975	58.0	0.059	8.35	4.97E-06	26.6	0.816	5.101	3.17E-12	6.30E-13	19.9
08-CEN, 8a	28.9	35.4	625	37.0	0.059	8.35	4.94E-06	26.6	0.816	5.101	3.15E-12	6.28E-13	19.9
08-CEN, 10b	3.1	3.7	390	57.0	0.146	9.50	1.32E-04	21.8	0.819	6.240	1.02E-10	1.70E-11	16.6
08-CEN, 10b	3.1	3.7	495	70.5	0.142	9.50	1.29E-04	21.8	0.819	6.240	9.98E-11	1.66E-11	16.6
08-CEN, 10b	4.6	5.6	415	90.5	0.218	9.50	1.31E-04	21.8	0.819	6.240	1.01E-10	1.67E-11	16.5
08-CEN, 10b	4.6	5.6	275	59.0	0.215	9.50	1.28E-04	21.8	0.819	6.240	9.97E-11	1.64E-11	16.5
08-CEN, 15b	6.2	7.6	585	53.0	0.091	6.25	2.64E-05	23.4	0.818	5.861	1.93E-11	3.38E-12	17.5
08-CEN, 15b	6.2	7.6	875	79.0	0.090	6.25	2.63E-05	23.4	0.818	5.861	1.92E-11	3.36E-12	17.5
08-CEN, 15b	8.2	10.0	455	54.0	0.119	6.25	2.62E-05	23.3	0.818	5.884	1.92E-11	3.34E-12	17.4
08-CEN, 15b	8.2	10.0	575	69.0	0.120	6.25	2.65E-05	23.3	0.818	5.884	1.94E-11	3.37E-12	17.4
08-CEN, 22a	11.2	13.7	515	54.0	0.105	8.50	2.31E-05	22.1	0.819	6.169	1.77E-11	2.93E-12	16.6
08-CEN, 22a	11.2	13.7	490	50.0	0.102	8.50	2.24E-05	22.1	0.819	6.169	1.72E-11	2.86E-12	16.6
08-CEN, 22a	10.4	12.7	610	54.5	0.089	8.50	2.12E-05	22.1	0.819	6.169	1.62E-11	2.69E-12	16.6
08-CEN, 22a	10.4	12.7	660	58.0	0.088	8.50	2.08E-05	22.1	0.819	6.169	1.60E-11	2.65E-12	16.6
08-CEN, 25b	11.9	14.5	510	63.0	0.124	7.00	2.11E-05	22.9	0.819	5.979	1.57E-11	2.69E-12	17.1
08-CEN, 25b	11.9	14.5	520	63.0	0.121	7.00	2.07E-05	22.9	0.819	5.979	1.54E-11	2.64E-12	17.1
08-CEN, 25b	9.9	12.1	516	54.0	0.105	7.00	2.14E-05	23.15	0.818	5.920	1.58E-11	2.73E-12	17.3
08-CEN, 25b	9.9	12.1	565	57.0	0.101	7.00	2.06E-05	23.2	0.818	5.908	1.52E-11	2.63E-12	17.3

Table B - 15: Intrinsic permeability of salt core samples determined by flow-through experiments (continuation).

Sample-ID	h_{octanol} [cm]	h_{water} [cm]	Δt [s]	ΔV [cm ³]	Q [cm ³ /s]	L [cm]	k_f [m/s]	$T_{\text{exp.}}$ [°C]	ρ_{octanol} [g/cm ³]	η_{octanol} [mPa·s]	K [m ²]	$\pm S_K$ [m ²]	$\pm S_K$ [%]
03-INC, K3, 0.0-0.7	17.0	20.8	790	60.0	0.076	11.50	1.49E-05	23.0	0.819	5.955	1.10E-11	1.89E-12	17.1
03-INC, K3, 0.0-0.7	17.0	20.8	800	54.0	0.068	11.50	1.32E-05	23.0	0.819	5.955	9.80E-12	1.68E-12	17.1
03-INC, K3, 0.0-0.7	34.0	41.5	620	74.0	0.119	11.50	1.17E-05	23.0	0.819	5.955	8.67E-12	1.48E-12	17.1
03-INC, K3, 0.0-0.7	34.0	41.5	670	73.0	0.109	11.50	1.07E-05	23.0	0.819	5.955	7.91E-12	1.35E-12	17.1
03-INC, K3, 0.7-1.7	20.2	24.6	800	51.5	0.064	13.00	1.20E-05	20.5	0.820	6.549	9.78E-12	1.53E-12	15.6
03-INC, K3, 0.7-1.7	20.2	24.6	710	44.0	0.062	13.00	1.16E-05	20.5	0.820	6.549	9.42E-12	1.47E-12	15.6
03-INC, K3, 0.7-1.7	27.2	33.2	565	45.5	0.081	13.00	1.12E-05	21.3	0.820	6.359	8.82E-12	1.42E-12	16.1
03-INC, K3, 0.7-1.7	27.2	33.2	472	38.0	0.081	13.00	1.12E-05	21.3	0.820	6.359	8.82E-12	1.42E-12	16.1
03-INC, K4, 0.7-1.7	65.0	79.4	1555	61.0	0.039	9.75	1.70E-06	23.0	0.819	5.955	1.26E-12	2.16E-13	17.1
03-INC, K4, 0.7-1.7	65.0	79.4	1490	57.0	0.038	9.75	1.66E-06	23.0	0.819	5.955	1.23E-12	2.11E-13	17.1
03-INC, K4, 0.7-1.7	88.5	108.1	1280	67.0	0.052	9.75	1.67E-06	23.0	0.819	5.955	1.24E-12	2.12E-13	17.1
03-INC, K4, 0.7-1.7	90.0	110.0	1100	58.0	0.053	9.75	1.65E-06	23.0	0.819	5.955	1.23E-12	2.10E-13	17.1
03-INC, K5, 1.7-2.7	15.2	18.5	2100	48.0	0.023	12.25	5.35E-06	20.0	0.821	6.668	4.43E-12	6.80E-13	15.4
03-INC, K5, 1.7-2.7	15.2	18.5	2100	48.0	0.023	12.25	5.35E-06	20.0	0.821	6.668	4.43E-12	6.80E-13	15.4
03-INC, K5, 1.7-2.7	15.4	18.8	1980	46.0	0.023	12.25	5.36E-06	20.0	0.821	6.668	4.44E-12	6.82E-13	15.4
03-INC, K5, 1.7-2.7	15.8	19.2	2160	54.0	0.025	12.25	5.63E-06	20.0	0.821	6.668	4.66E-12	7.15E-13	15.3
03-INC, K5, 1.7-2.7	15.8	19.2	2460	60.0	0.024	12.25	5.49E-06	20.0	0.821	6.668	4.55E-12	6.97E-13	15.3
03-INC, K7, 1.7-2.7	2.6	3.2	1570	41.0	0.026	5.00	1.46E-05	20.5	0.820	6.549	1.66E-11	2.69E-12	16.2
03-INC, K7, 1.7-2.7	2.7	3.2	1560	41.0	0.026	5.00	1.44E-05	20.5	0.820	6.549	1.64E-11	2.65E-12	16.2
03-INC, K7, 1.7-2.7	6.6	8.0	980	62.0	0.063	5.00	1.39E-05	20.5	0.820	6.549	1.58E-11	2.50E-12	15.8
03-INC, K7, 1.7-2.7	6.7	8.2	910	57.0	0.063	5.00	1.36E-05	20.5	0.820	6.549	1.55E-11	2.44E-12	15.8
03-INC, K2, 3 m	8.2	10.0	627	55.0	0.088	7.25	2.25E-05	20.0	0.821	6.668	1.86E-11	2.88E-12	15.4
03-INC, K2, 3 m	8.2	10.0	509	52.0	0.102	7.25	2.62E-05	20.0	0.821	6.668	2.17E-11	3.35E-12	15.4
03-INC, K2, 3 m	6.5	7.9	2882	32.0	0.011	7.25	3.60E-06	20.0	0.821	6.668	2.98E-12	4.62E-13	15.5
03-INC, K2, 3 m	6.5	7.9	4657	40.0	0.009	7.25	2.78E-06	20.0	0.821	6.668	2.30E-12	3.57E-13	15.5
03-INC, K5, 2.7-3.7	19.5	23.8	650	62.0	0.095	8.25	1.17E-05	24.0	0.818	5.718	8.32E-12	1.48E-12	17.8
03-INC, K5, 2.7-3.7	19.5	23.8	680	58.0	0.085	8.25	1.04E-05	24.0	0.818	5.718	7.44E-12	1.32E-12	17.8
03-INC, K5, 2.7-3.7	21.2	25.9	740	57.0	0.077	8.25	8.67E-06	24.0	0.818	5.718	6.18E-12	1.10E-12	17.8
03-INC, K5, 2.7-3.7	21.2	25.9	415	30.5	0.073	8.25	8.27E-06	24.0	0.818	5.718	5.90E-12	1.05E-12	17.9

Table B - 15: Intrinsic permeability of salt core samples determined by flow-through experiments (continuation).

Sample-ID	h_{octanol} [cm]	h_{water} [cm]	Δt [s]	ΔV [cm ³]	Q [cm ³ /s]	L [cm]	k_f [m/s]	$T_{\text{exp.}}$ [°C]	ρ_{octanol} [g/cm ³]	η_{octanol} [mPa·s]	K [m ²]	$\pm S_K$ [m ²]	$\pm S_K$ [%]
07-SAL, 2a	7.8	9.5	811	81.0	0.100	5.50	2.04E-05	24.4	0.817	5.623	1.43E-11	2.60E-12	18.2
07-SAL, 2a	7.8	9.6	890	83.0	0.093	5.50	1.90E-05	25.7	0.816	5.315	1.26E-11	2.42E-12	19.2
07-SAL, 2a	5.6	6.9	643	42.5	0.066	5.50	1.88E-05	24.8	0.817	5.528	1.29E-11	2.40E-12	18.6
07-SAL, 2a	5.6	6.9	611	38.5	0.063	5.50	1.79E-05	24.4	0.817	5.623	1.25E-11	2.29E-12	18.3
07-SAL, 7a	17.5	21.4	763	32.0	0.042	12.20	8.45E-06	24.6	0.817	5.576	5.88E-12	1.07E-12	18.3
07-SAL, 7a	16.6	20.3	736	31.0	0.042	12.20	8.95E-06	24.8	0.817	5.528	6.17E-12	1.14E-12	18.4
07-SAL, 7a	18.0	22.0	839	37.5	0.045	12.20	8.75E-06	24.9	0.817	5.504	6.01E-12	1.11E-12	18.5
07-SAL, 7a	17.7	21.7	840	38.0	0.045	12.20	9.01E-06	24.9	0.817	5.504	6.19E-12	1.14E-12	18.5
07-SAL, 8a	17.6	21.5	615	65.0	0.106	18.00	3.12E-05	24.9	0.817	5.504	2.15E-11	3.95E-12	18.4
07-SAL, 8a	17.3	21.2	578	60.0	0.104	18.00	3.12E-05	25.1	0.817	5.457	2.12E-11	3.95E-12	18.6
07-SAL, 8a	16.0	19.6	806	74.0	0.092	18.00	2.98E-05	25.2	0.817	5.433	2.02E-11	3.78E-12	18.7
07-SAL, 8a	16.0	19.6	556	51.5	0.093	18.00	3.01E-05	25.1	0.817	5.457	2.05E-11	3.81E-12	18.6
07-SAL, 11b	2.5	3.1	286	57.0	0.199	9.70	2.23E-04	25.2	0.817	5.433	1.51E-10	2.89E-11	19.1
07-SAL, 11b	2.5	3.1	406	79.0	0.195	9.70	2.18E-04	24.8	0.817	5.528	1.50E-10	2.82E-11	18.8
07-SAL, 11b	1.0	1.2	623	51.0	0.082	9.70	2.30E-04	24.7	0.817	5.552	1.59E-10	3.27E-11	20.6
07-SAL, 11b	1.1	1.3	680	55.0	0.081	9.70	2.06E-04	24.9	0.817	5.504	1.42E-10	2.88E-11	20.4
07-SAL, 14b	27.6	33.7	490	54.0	0.110	9.60	1.11E-05	23.7	0.818	5.789	8.00E-12	1.41E-12	17.6
07-SAL, 14b	27.6	33.7	512	56.5	0.110	9.60	1.11E-05	23.7	0.818	5.789	8.01E-12	1.41E-12	17.6
07-SAL, 14b	24.5	30.0	428	41.0	0.096	9.60	1.09E-05	23.8	0.818	5.766	7.80E-12	1.38E-12	17.7
07-SAL, 14b	24.5	30.0	487	47.0	0.097	9.60	1.09E-05	23.8	0.818	5.766	7.86E-12	1.39E-12	17.7
07-SAL, 14b	24.5	30.0	475	45.0	0.095	9.60	1.07E-05	23.9	0.818	5.742	7.68E-12	1.36E-12	17.7
07-SAL, 15	38.0	46.5	1052	20.5	0.019	20.20	3.00E-06	24.0	0.818	5.718	2.14E-12	3.83E-13	18.0
07-SAL, 15	38.0	46.5	688	13.5	0.020	20.20	3.02E-06	24.1	0.818	5.694	2.14E-12	3.92E-13	18.3
07-SAL, 15	39.2	48.0	960	18.0	0.019	20.20	2.79E-06	24.4	0.817	5.623	1.96E-12	3.59E-13	18.3
07-SAL, 15	39.2	48.0	960	17.5	0.018	20.20	2.72E-06	24.5	0.817	5.599	1.90E-12	3.49E-13	18.4

Table B -15: Intrinsic permeability of salt core samples determined by flow-through experiment (continuation).

Sample-ID	h_{octanol} [cm]	h_{water} [cm]	Δt [s]	ΔV [cm ³]	Q [cm ³ /s]	L [cm]	k_f [m/s]	$T_{\text{exp.}}$ [°C]	ρ_{octanol} [g/cm ³]	η_{octanol} [mPa·s]	K [m ²]	$\pm S_K$ [m ²]	$\pm S_K$ [%]
07-SAL, 18	35.0	42.8	1494	19.0	0.013	16.00	1.68E-06	23.4	0.818	5.861	1.23E-12	2.16E-13	17.6
07-SAL, 18	35.5	43.4	1392	16.0	0.011	16.00	1.50E-06	23.7	0.818	5.789	1.08E-12	1.93E-13	17.9
07-SAL, 26	34.2	41.7	1126	10.8	0.010	19.20	1.56E-06	22.0	0.819	6.193	1.20E-12	2.07E-13	17.3
07-SAL, 26	34.2	41.8	1188	10.2	0.009	19.20	1.40E-06	22.6	0.819	6.050	1.05E-12	1.86E-13	17.7
07-SAL, 26	39.5	48.2	1169	8.5	0.007	19.20	1.02E-06	22.8	0.819	6.003	7.65E-13	1.39E-13	18.2
07-SAL, 26	39.5	48.3	1293	9.0	0.007	19.20	9.79E-07	23.0	0.819	5.955	7.26E-13	1.32E-13	18.2
02-LLI, 1a	4.7	5.7	536	35.0	0.065	4.50	1.81E-05	22.6	0.819	6.050	1.36E-11	2.34E-12	17.2
02-LLI, 1a	4.7	5.7	719	45.0	0.063	4.50	1.74E-05	22.5	0.819	6.074	1.31E-11	2.24E-12	17.1
02-LLI, 1a	2.3	2.8	1133	32.0	0.028	4.50	1.60E-05	22.5	0.819	6.074	1.21E-11	2.12E-12	17.5
02-LLI, 1a	2.3	2.8	937	25.5	0.027	4.50	1.54E-05	22.6	0.819	6.050	1.16E-11	2.04E-12	17.6
02-LLI, 3b	38.0	46.4	844	16.5	0.020	10.00	1.49E-06	22.9	0.819	5.979	1.11E-12	1.93E-13	17.4
02-LLI, 3b	37.8	46.2	1296	25.0	0.019	10.00	1.48E-06	23.0	0.819	5.955	1.10E-12	1.89E-13	17.2
02-LLI, 3b	40.8	49.8	850	21.5	0.025	10.00	1.80E-06	22.7	0.819	6.027	1.35E-12	2.30E-13	17.1
02-LLI, 3b	40.8	49.8	1339	31.5	0.024	10.00	1.67E-06	22.6	0.819	6.050	1.26E-12	2.13E-13	16.9
02-LLI, 7	26.5	32.3	801	21.0	0.026	6.80	1.95E-06	21.5	0.820	6.311	1.53E-12	2.51E-13	16.4
02-LLI, 7	26.5	32.3	1424	31.0	0.022	6.80	1.62E-06	21.5	0.820	6.311	1.27E-12	2.07E-13	16.3
02-LLI, 7	29.5	36.0	923	20.0	0.022	6.80	1.45E-06	21.5	0.820	6.311	1.14E-12	1.87E-13	16.4
02-LLI, 7	29.5	36.0	1205	23.1	0.019	6.80	1.28E-06	21.5	0.820	6.311	1.01E-12	1.65E-13	16.4
02-LLI, 9	74.3	90.8	2460	7.2	0.003	12.20	1.39E-07	23.5	0.818	5.837	1.01E-13	1.94E-14	19.2
02-LLI, 15	33.0	40.4	850	12.8	0.015	9.70	1.28E-06	26.1	0.816	5.220	8.33E-13	1.66E-13	19.9
02-LLI, 15	33.0	40.4	1404	20.8	0.015	9.70	1.26E-06	26.1	0.816	5.220	8.19E-13	1.61E-13	19.6
02-LLI, 15	35.0	42.9	786	12.3	0.016	9.70	1.25E-06	26.1	0.816	5.220	8.16E-13	1.63E-13	20.0
02-LLI, 15	35.0	42.9	1573	23.8	0.015	9.70	1.21E-06	26.3	0.816	5.172	7.82E-13	1.54E-13	19.7
02-LLI, 19b	7.0	8.5	341	30.5	0.089	11.00	4.07E-05	21.6	0.820	6.288	3.19E-11	5.21E-12	16.4
02-LLI, 19b	7.0	8.5	401	34.8	0.087	11.00	3.95E-05	21.6	0.820	6.288	3.09E-11	5.05E-12	16.3
02-LLI, 19b	4.0	4.9	336	11.2	0.033	11.00	2.66E-05	21.6	0.820	6.288	2.08E-11	3.56E-12	17.2
02-LLI, 19b	4.0	4.9	658	31.0	0.047	11.00	3.76E-05	21.6	0.820	6.288	2.94E-11	4.84E-12	16.5

Table B -15: Intrinsic permeability of salt core samples determined by flow-through experiment (continuation).

Sample-ID	h_{octanol} [cm]	h_{water} [cm]	Δt [s]	ΔV [cm ³]	Q [cm ³ /s]	L [cm]	k_f [m/s]	$T_{\text{exp.}}$ [°C]	ρ_{octanol} [g/cm ³]	η_{octanol} [mPa·s]	K [m ²]	$\pm S_K$ [m ²]	$\pm S_K$ [%]
13-COR, 25	21.4	26.1	432	19.0	0.044	12.00	7.16E-06	19.8	0.821	6.715	5.97E-12	9.25E-13	15.5
13-COR, 25	21.4	26.1	521	23.2	0.045	12.00	7.25E-06	19.8	0.821	6.715	6.05E-12	9.31E-13	15.4
13-COR, 25	19.3	23.5	1041	13.9	0.013	12.00	2.41E-06	19.8	0.821	6.715	2.01E-12	3.17E-13	15.8
13-COR, 25	19.3	23.5	1061	13.8	0.013	12.00	2.35E-06	19.8	0.821	6.715	1.96E-12	3.09E-13	15.8
13-COR, 22	27.9	34.1	759	22.0	0.029	8.00	2.40E-06	24.1	0.818	5.694	1.71E-12	3.08E-13	18.0
13-COR, 22	27.9	34.1	907	25.0	0.028	8.00	2.29E-06	24.1	0.818	5.694	1.62E-12	2.92E-13	18.0
13-COR, 22	25.2	30.8	1014	23.0	0.023	8.00	2.08E-06	24.4	0.817	5.623	1.46E-12	2.66E-13	18.2
13-COR, 22	25.2	30.8	1056	24.0	0.023	8.00	2.09E-06	24.4	0.817	5.623	1.46E-12	2.67E-13	18.2
13-COR, 19b	8.5	10.4	736	28.0	0.038	12.80	1.65E-05	26.0	0.816	5.243	1.08E-11	2.11E-12	19.4
13-COR, 19b	8.5	10.4	507	18.5	0.036	12.80	1.59E-05	25.9	0.816	5.267	1.04E-11	2.04E-12	19.5
13-COR, 19b	7.0	8.6	454	12.0	0.026	12.80	1.40E-05	25.8	0.816	5.291	9.22E-12	1.82E-12	19.8
13-COR, 18	18.1	22.1	547	27.0	0.049	6.40	5.06E-06	20.4	0.821	6.573	4.14E-12	6.51E-13	15.7
13-COR, 18	18.1	22.1	764	38.5	0.050	6.40	5.17E-06	20.4	0.821	6.573	4.22E-12	6.61E-13	15.7
13-COR, 18	16.3	19.9	920	23.0	0.025	6.40	2.85E-06	20.2	0.821	6.620	2.34E-12	3.68E-13	15.7
13-COR, 18	16.3	19.9	627	16.3	0.026	6.40	2.96E-06	20.2	0.821	6.620	2.44E-12	3.87E-13	15.9
13-COR, 14a	49.8	61.0	1034	3.8	0.004	13.40	2.85E-07	26.0	0.816	5.243	1.87E-13	4.59E-14	24.6
13-COR, 14a	50.0	61.3	1426	3.6	0.003	13.40	1.95E-07	26.1	0.816	5.220	1.27E-13	3.20E-14	25.2

Appendix C – Text

Text C - 1: Error estimation according to DIN V ENV 13005 (1999)

Each measurement of a physical property is defective. Therefore, the error of the whole measuring procedure needs to be estimated via error propagation.

The general equation for the error propagation according to (DIN V ENV 13005, 1999):

$$s_X = \sqrt{\frac{\delta X}{\delta A} \cdot s_A^2 + \frac{\delta X}{\delta B} \cdot s_B^2 + \dots} \quad (\text{C-1})$$

where s_X = absolute total error of parameter X
 $\frac{\partial X}{\partial A, B}$ = partial derivation of parameter X to A or B, respectively
 s_A, s_B = absolute error of parameter A and B, respectively

Typ A error (for repeated measurement):

$$\mu_X = \frac{x_i}{n} \quad (\text{C-2})$$

$$s_X = \sqrt{\frac{1}{n-1} \cdot (x_i - \mu_X)^2} \quad (\text{C-3})$$

where μ_X = mean of all measurements of parameter X
 x_i = certain measurement value i
 s_X = absolute error of parameter X

Typ B error (error limit: $\pm\Delta$):

$$s_X = \frac{1}{3} \cdot \Delta^2 \quad (\text{C-4})$$

where Δ = positive and negative error limit

Text C - 2: Error estimation for permeability determination (flow-through experiments using 2-octanol)

Permeability determination by flow-through experiments

- Length of streamed salt core L (accuracy of reading: $\Delta L \pm 0.2$ cm) $\rightarrow s_L = 0.1155$ cm
- Cross section area A of the core sample: $A = \pi \cdot r^2$ with $\frac{\Delta A}{A} = 2 \cdot \frac{\Delta r}{r}$, where the accuracy of reading $\Delta r = \pm 0.05$ cm $\rightarrow s_r = 0.0289$ cm (value of uncertainty: 1.9%)

$$s_A = \sqrt{(2\pi r \cdot s_r)^2} \rightarrow r = 3 \text{ cm} \rightarrow s_A = 0.545 \text{ cm}^2$$

- Hydraulic gradient Δh (accuracy of reading: $\Delta h = \pm 0.2$ cm) $\rightarrow s_{\Delta h} = 0.1155$ cm
- Discharge of 2-octanol Q: $Q = \frac{V}{t}$ with V – volume of discharged 2-octanol, t – time of discharge, with $\Delta V = \pm 1$ ml, $\Delta t = 1$ sec (average uncertainty: $\pm 4.0\%$)

$$s_V = 0.577 \text{ ml}, s_t = 0.577 \text{ s}$$

$$s_Q = \sqrt{\left(\frac{1}{t} \cdot s_V\right)^2 + \left(-\frac{V}{t^2} \cdot s_t\right)^2} \quad (\text{C-5})$$

- Permeability k_f (average uncertainty: 14.2%)

$$k_f = \frac{Q \cdot L}{A \cdot \Delta h} \quad \text{with } A = \pi r^2: k_f = \frac{Q \cdot L}{\pi \cdot r^2 \cdot \Delta h} \rightarrow Q, L, r, \Delta h \quad \text{with}$$

$$s_{k_f} = \sqrt{\frac{k_f^2}{Q^2} \cdot s_Q^2 + \frac{k_f^2}{L^2} \cdot s_L^2 + \frac{k_f^2}{2r^2} \cdot s_r^2 + \frac{k_f^2}{\Delta h^2} \cdot s_{\Delta h}^2} \quad (\text{C-6})$$

- Density of 2-octanol ρ (accuracy of reading: $\Delta \rho = 0.004$ g/cm³) $\rightarrow s_\rho = 0.023$ g/cm³
- Kinematic viscosity of 2-octanol ν (STD of 10 repeated measurements: $s_\nu = 0.80$ to 1.43 mm²/s)
- Dynamic viscosity of 2-octanol η :

$$s_\eta = \sqrt{(\nu \cdot s_\rho)^2 + (\rho \cdot s_\nu)^2} \sim 1.0 \text{ mPa} \cdot \text{s} \quad (\text{C-7})$$

- Intrinsic permeability K (average uncertainty: 17.5%)

$$K = \frac{k_f \cdot \eta}{\rho \cdot g} \rightarrow k_f, \eta, \rho \quad \text{with}$$

$$s_K = \sqrt{\frac{K^2}{k_f^2} \cdot s_{k_f}^2 + \frac{K^2}{\eta^2} \cdot s_\eta^2 + \frac{K^2}{\rho^2} \cdot s_\rho^2} \quad (\text{C-8})$$

Text C - 3: Error estimation for effective porosity determination according to the saturation method

Effective porosity determination by saturation with 2-octanol

- Length of streamed salt core L (accuracy of reading: $\Delta L \pm 0.2$ cm)
 $\rightarrow s_L = 0.1155$ cm
- Diameter/Radius of the core sample (accuracy of reading: $\Delta d = \pm 0.1$ cm / $\Delta r = \pm 0.05$ cm)
 $\rightarrow s_d = 0.0577$ cm / $s_r = 0.0289$ cm (value of uncertainty for r: 0.96%)
- Density of 2-octanol ρ due to temperature variations during the experiment (accuracy of reading: $\Delta \rho = 0.004$ g/cm³)
 $\rightarrow s_\rho = 0.023$ g/cm³
- Mass of the salt core (dry) (accuracy of reading: $\Delta m_{dry} = \pm 0.1$ g)
 $\rightarrow s_{mdry} = 0.0577$ g

[Since not all salt cores have been dried completely, the weight difference between dried and moist salt core samples (data were taken from sample preparation for the complement method) will be used to estimate the uncertainty of the saturation method. The mean weight difference of 75 core samples after complete drying was 1.55% (maximum/worst case: 6.4%).]

- Mass of 2-octanol (accuracy of reading: $\Delta m_{octanol} = \pm 0.1$ g) $\rightarrow s_{3-way, sat/dry} = 0.0577$ g

$$\Delta m_{octanol} = m_{3-way,sat.} - m_{3-way,dry} \quad \text{with}$$

$$s_{\Delta m_{octanol}} = \sqrt{s_{3-way,sat.}^2 + s_{3-way,dry}^2} = 0.0816 \text{ g} \quad (\text{C-9})$$

- Volume of PE reduction (residual volume not belonging to the porosity of the core): $\Delta V_{res} = \pm 2$ ml = ± 2 cm³ $\rightarrow s_{V_{res}} = 1.155$ cm³ (total residual volume = 52 cm³ \rightarrow uncertainty: 2.22%)
- Volume of the salt core (average uncertainty: ± 2.35 %)

$$V_{core} = \pi \cdot r^2 \cdot L \quad \text{with} \quad s_{V_{core}} = \sqrt{\left(\frac{2 \cdot V}{r} \cdot s_r\right)^2 + (\pi \cdot r^2 \cdot s_L)^2} \quad (\text{C-10})$$

- Volume of pores (average uncertainty: ± 13.4 %)

$$V_{pores} = \frac{\Delta m_{octanol}}{\rho_{octanol}} - V_{res} \quad \text{with}$$

$$s_{V_{pores}} = \sqrt{\frac{1}{\rho^2} \cdot s_{\Delta m_{octanol}}^2 + \frac{\Delta m_{octanol}}{\rho_{octanol}^2} \cdot s_\rho^2 + (-s_{V_{res}})^2} \quad (\text{C-11})$$

- Effective porosity (average uncertainty: ±13.7%)

$$n_{\text{eff}} \% = \frac{V_{\text{pores}}}{V_{\text{core}}} \cdot 100\% \quad \text{with}$$

$$s_{n_{\text{eff}}} = \sqrt{\frac{1}{V_{\text{core}}} \cdot 100 \cdot s_{V_{\text{pores}}}^2 + \left(\frac{V_{\text{pores}}}{V_{\text{core}}}\right)^2 \cdot 100 \cdot s_{V_{\text{core}}}^2} \quad (\text{C-12})$$

Text C - 4: Error estimation for porosity determination according to the complement method

Total porosity determination by direct measurement using the complement method

- Length of salt core L after completion (accuracy of reading: $\Delta L \pm 0.2$ cm)
 $\rightarrow s_L = 0.1155$ cm
- Radius of the core samples (accuracy of reading: $\Delta r = \pm 0.05$ cm) $\rightarrow s_r = 0.0289$ cm
 (value of uncertainty for r: 0.96%)
- Mass of the salt core (dry): ± 0.1 g $\rightarrow s_{m_{\text{dry}}} = 0.0577$ g
 (maximum weight loss within the last 100 hours of drying: <1%)
- Particle density of the salt (He-Pycnometry): $\pm 0.015\%$ $\rightarrow s_{\rho_{\text{He}}} = \rho_{\text{He}} \cdot 0.015\%$
 [Semi-quantitative estimation of the density by visual comparison of each core sample with the master samples: uncertainty ~10%]
- Mass of plasticine: ± 0.1 g $\rightarrow s_{m_{\text{plasticine}}} = 0.0577$ g
- Volume of plasticine: ± 1 cm³ $\rightarrow s_{V_{\text{plasticine}}} = 0.577$ cm³
- Density of plasticine: (uncertainty: 0.025 g/cm³ = 1.5%)

$$\rho_P = \frac{m_P}{V_P} \quad \text{with } s_{\rho_P} = \sqrt{\frac{1}{V_P} \cdot s_{m_P}^2 + \left(\frac{m_P}{V_P}\right)^2 \cdot s_{V_P}^2} \quad (\text{C-13})$$

(According to equation C-3 for type-A error: $s_\rho = 0.0116$ g/cm³ (n= 10))

- Volume of the salt core cylinder after completion (average uncertainty: ±2.2%)

$$V_{\text{cyl.}} = \pi \cdot r^2 \cdot L \quad \text{with } s_{V_{\text{cyl.}}} = \sqrt{\left(\frac{2 \cdot V_{\text{cyl.}}}{r} \cdot s_r\right)^2 + (\pi \cdot r^2 \cdot s_L)^2} \quad (\text{C-14})$$

- Mass of the salt core cylinder after completion with plasticine (average uncertainty: 0.012%)

$$s_{m_{\text{cyl}}} = \sqrt{s_{m_{\text{dry}}}^2 + s_{m_P}^2} = 0.0816 \text{ g} \quad (\text{C-15})$$

- Volume of consumed plasticine for completion (average uncertainty: 1.5%)

$$V_p = \frac{m_p}{\rho_p} \quad \text{with } s_{V_p} = \sqrt{\frac{1}{\rho_p^2} \cdot s_{m_p}^2 + \left(-\frac{m_p}{\rho_p^2}\right) \cdot s_{\rho_p}^2} \quad (\text{C-16})$$

- Volume of the actual salt core (average uncertainty: 2.9%)

$$V_{\text{core}} = V_{\text{cyl}} - V_p \quad \text{with } s_{V_{\text{core}}} = \sqrt{s_{V_{\text{cyl}}}^2 + s_{V_p}^2} \quad (\text{C-17})$$

- Volume of pure salt without pore space (average uncertainty: ±0.02 %)

$$V_{\text{salt}} = \frac{m_{\text{dry}}}{\rho_{\text{He}}} \quad \text{with } s_{V_{\text{salt}}} = \sqrt{\frac{1}{\rho_{\text{He}}^2} \cdot s_{m_{\text{dry}}}^2 + \left(-\frac{m_{\text{dry}}}{\rho_{\text{He}}^2}\right) \cdot s_{\rho_{\text{He}}}^2} \quad (\text{C-18})$$

- Total porosity of the salt core sample (average uncertainty: ±20.7%)

$$s_n = \sqrt{\left(-\frac{1}{V_{\text{core}}}\right) \cdot s_{V_{\text{salt}}}\right)^2 + \left(\frac{V_{\text{salt}}}{V_{\text{core}}^2} \cdot s_{V_{\text{core}}}\right)^2} \quad (\text{C-19})$$

One can assume a maximum absolute deviation /error for the total porosity determination of ±6.1% (mean absolute error = 2.5%).

Text C - 5: Error estimation for lithium reservoir estimation

Lithium reservoir estimation

$$Li_{total} = Li \cdot S \cdot n \quad \text{with}$$

$$s_{Li_{total}} = \sqrt{S \cdot n \cdot s_{Li}^2 + Li \cdot n \cdot s_S^2 + (Li \cdot S \cdot s_n)^2} \quad (C-20)$$

where

- $s_n = \pm 0.025$ [-]
 - ➔ mean of all absolute errors of all porosity measurement values computed according to Text C-3 and Text C-4
- $s_S = \frac{1}{3}(\pm 0.2 \text{ m})^2 = \pm 0.115 \text{ m}$
 - ➔ salt thickness can be determined with an accuracy of $\pm 0.2 \text{ m}$
- $s_{Li} = \frac{1}{3}(\Delta Li)^2$
 - ➔ the mean difference between measured lithium concentrations and those which were predicted by interpolation with kriging = $\pm 80.1 \text{ mg/L}$, average uncertainty: 12.7% (n = 76 values)

For lithium reservoir estimation, an average absolute error of about 100 g/m^2 and a relative error of 15.4% occur (based on 11 measurement points).